U. S. Department of Energy
1000 Independence Avenue, S.W.
Washington, D.C. 20585

Fiscal Year 2021: First Quarter

Progress Reports:

Advanced Battery Materials Research (BMR) Program & Battery500 Consortium

Released March 2021
for the period of October – December 2020

Approved by

Tien Q. Duong, Manager
Advanced Battery Materials Research Program & Battery500 Consortium
Vehicle Technologies and Electrification Program
Energy Efficiency and Renewable Energy

TABLE OF CONTENTS

TABLE OF FIGURES

TABLE OF TABLES

A MESSAGE FROM THE MANAGER: ADVANCED BATTERY MATERIALS RESEARCH PROGRAM AND BATTERY500 CONSORTIUM

It is with the utmost sadness that we announce to the DOE Battery Research Community that our good friend, dear colleague, and outstanding scientist Professor Austen Angell passed away on Friday, March 12. Austen was an extremely collegial and highly influential scientist, an intellectual giant, and a scientific hero to all of us, in addition to being just an incredibly warm and wonderful human being. His contribution to battery materials and chemistries includes the breakthrough concept of "polymer-in-salt" electrolyte, which serves as the ancestor of the modern super-concentrated electrolytes for Li-metal batteries, and the development of advanced electrolytes such as sulfones and LiBOB. He also educated numerous young scientists who are now major players in various DOE programs. He will be forever missed.

The Office of Energy Efficiency and Renewable Energy (EERE) has two programs that perform cutting edge research to advance battery technology for electric vehicles. The Advanced Battery Materials Research (BMR) Program focuses on discovering high-performance materials, comprehensive modeling, and diagnostics analyses of materials and electrochemical cell behavior to address chemical, physical, and mechanical instabilities. It is composed of seven research task areas including: Liquid/Polymer Solid-State Electrolytes, Diagnostic Analysis, Modeling, Metallic Lithium, Sulfur Electrodes, Air-Electrodes/Electrolytes, and Sodium-Ion Batteries. The Battery500 program focuses on designing a cell that can achieve 500 Wh/Kg and 1000 cycles through novel cell architectures utilizing a lithium anode, a compatible electrolyte, and high-capacity cathodes. To accomplish this aggressive goal, the program is divided into 3 key areas: Materials and Interfaces, Electrode Architecture, and Cell Fabrication, Testing, and Diagnosis.

In this document, we report on the progress made on these projects from October 1, 2020, through December 31, 2020. A few notable achievements from the BMR investigators this quarter are summarized below:

- The Argonne National Laboratory / University of Illinois, Chicago, Group (L. A. Curtiss / A. Ngo / A. Salehi-Khojin) found that a conductive metal organic framework in combination with a redox mediator results in formation of a conductive amorphous Li_2O_2 that facilitates the growth and decomposition of the discharge product in a Li-O_2 battery. The battery with this configuration exhibits sustainable and efficient operation with a low charge potential and extended lifetime of 300 cycles at a capacity of 1000 mAh/g under a current density of 1 A/g.
- The University of Michigan Group (J. Sakamoto / N. P. Dasgutpa / J. B. Siegel) is using their newly developed *operando* video microscopy platform to investigate *in situ* anode formation and Li-metal cycling. The technique allows a comprehensive understanding of the factors that influence the nucleation and dynamic evolution of lithium morphology. It also provides insights into the evolution of Li-metal / solid electrolyte interfaces during extended cycling.
- The Srinivasan Group at Argonne National Laboratory has used mesoscale models to study the Li/LLZO interface and shed light on the lithium dissolution process and its effect on cycling. The model captures the impact of surface and bulk diffusion on void formation and performance and provides insights into how best to operate the cell to avoid delamination.

- The University of California, Berkeley, Group (B. McCloskey) is developing non-electrochemical methods to measure the activity coefficients of electrolytes to enable transference number measurements from lithium concentration cells. They are using freezing point depression measurements from differential scanning calorimetry to determine salt activity coefficients.
- S. Tepacevic's Group at the Argonne National Laboratory utilized a variety of *in situ* and *operando* X-ray photoelectron spectroscopy techniques, coupled with electrochemical measurements, to investigate factors impacting the interfacial stability of Al-doped LLZO in contact with lithium metal. Results revealed that lithium metal deposited onto the LLZO surface via different techniques (that is, magnetron sputtering, electron beam evaporation, and electrochemical deposition) displays different relativities and is dependent on the energetics of arriving lithium species.

Highlights from the Battery500 consortium team include the following:

Keystone Project 1: Materials and Interfaces

- The Binghamton University Team (M. S. Whittingham) and the University of Texas, Austin, Team (A. Manthiram) have shown that coatings on high-Ni NMC are effective for reducing both surface impurities and the 1st cycle loss. Phosphate and niobium coatings were found to be effective in reducing both the impact of surface impurities and the 1st cycle capacity loss.

Keystone Project 2: Electrode Architecture

- Y. S. Meng's group (University of California, San Diego) used scanning transmission electron microscopy and electron energy loss spectroscopy to probe the bonding environment evolution of nitrogen, sulfur, and carbon in sulfurized polyacrylonitrile (SPAN) cathode at the pristine, 1-cycle discharged and charged states. All three elements were found to actively participate in the electrochemical reaction. There was little redistribution of carbon and nitrogen elements, suggesting that the SPAN polymer backbone is still intact after the cycling.

Keystone Project 3: Cell Fabrication, Testing, and Diagnosis

- The University of Texas, Austin, (A. Manthiram Team) developed a model to understand the impact of non-participating radical species dissociation reaction on Li-S battery performance.

For more information of these and other BMR projects, we encourage you to attend the 2021 Annual Merit review. This year it will be a hybrid event with in-person and virtual attendance on June 21–25. Information regarding this meeting can be found online (https://www.energy.gov/eere/vehicles/vehicle-technologies-annual-merit-review). Our next report is expected to be available in August 2021.

Sincerely,

Tien Q. Duong

Tien Q. Duong
Manager, Advanced Battery Materials Research Program & Battery500 Consortium
Batteries & Electrification R&D
Energy Efficiency and Renewable Energy
U.S. Department of Energy

TASK 1 – Liquid/Polymer Solid-State Electrolytes

Summary and Highlights

The BMR Program goal is to develop long-life batteries superior to commercial Li-ion systems in terms of cost, vehicle range, and safety. The BMR Program addresses the fundamental problems of electrode chemical and mechanical instabilities that have slowed development of affordable, high-performance, automotive batteries. The aim is to identify electrode/electrolyte materials that yield enhanced battery performance and lead to greater acceptance of electric vehicles (EVs). Currently, the U. S. Department of Energy (DOE) Vehicle Technologies Office (VTO) supports 13 projects in the BMR Program under this Electrolytes Task. These projects can be categorized into four general topics:

- **Liquid.** The projects for liquid electrolyte (LE) aim to develop electrolyte formulations, based on fluoro-chemistries, to achieve significantly improved operating voltage, increased durability, and increased energy density of Li-ion batteries at a reasonable cost. Nonaqueous polyelectrolyte solutions with high Li^+ transference numbers will be developed to achieve high rate capabilities at room temperature. In addition, electrolytes with new polymer binders bearing a pentafluorophenyl group on the backbone will be designed, synthesized, and tested.
- **Polymer.** The targets of polymer electrolyte (PE) projects include inorganic/polymer and polymer/gel hybrid electrolytes that have flexibility, mechanical strength, thermal stability, high ionic conductivity, stable interfaces against lithium metal, and polysulfide-trapping capability enabling energy density Li-S batteries, with comparable cycle life.
- **Self-Forming & Self-Healing.** The self-forming, self-healing electrolyte projects are focused on developing and implementing Li-metal-based metal fluorite and metal iodide batteries, capable of energy densities > 400-500 Wh/kg and 1000 Wh/L.
- **Solid-State.** The solid-state projects are to develop high conductivities solid electrolytes (SEs) / composite SEs that are scalable, are chemically and electrochemically stable, and will enable low-cost, high-energy-density solid-state lithium batteries (SSLBs).

Highlights

At Stony Brook University (SBU; E. Takeuchi), additional characterization was conducted on LiI-containing SEs with varying $LiI{\cdot}H_2O$ content and/or preparation method. They found that the pristine, uncycled samples exhibit low levels of polyiodides. The negative face of the SE has a similar level of polyiodides present compared to the pristine. In contrast, the cathode face of the pellet shows a one-order-of-magnitude increase in intensity, indicating larger amounts of polyiodides and formation of an iodine-containing cathode. These data provide additional evidence for the formation of the cell components from the electrolyte, showing the formation of an I_2-$LiI(HPN)_2$ complex at the cathode interface.

At University of California, Berkeley (UCB; B. McCloskey), the group focused on developing alternative non-electrochemical methods for measuring the activity coefficients of electrolytes to enable transference number measurements from lithium concentration cells. Specifically, they focused on using freezing point depression measurements from differential scanning calorimetry (DSC) to determine salt activity coefficients. The team sees excellent agreement between the project's thermodynamic factor calculated from DSC to those in the literature. The plan is to extend the freezing point method to mixed solvent systems like ethylene carbonate : ethyl methyl carbonate (EC:EMC). In addition, the team continues to explore the effect of interfacial resistance on transport measurements, achieving lower interfacial resistances on the order of 100 $\Omega{\cdot}cm^2$ per electrode in lithium symmetric cells with $LiPF_6$ in 3:7 EC:EMC. They still see strong correlation between interfacial resistance and transport properties measured electrochemically.

The Stanford University (Z. Bao and Y. Cui) group built on their studies of a relative rigid poly(acrylic) backbone the team used in the past. They investigated a new polymer design utilizing a flexible poly(dimethylsiloxane) (PDMS) backbone, which efficiently lowers the polymer's glass transition temperature (Tg) to eliminate the need to introduce another fluorinated component. All of the polymer side chain can be functionalized with the Py^+ cation units. Beyond the benefit of mechanical flexibility, PDMS-based polymer is economically viable compared to any fluorinated polymer. Further, its mechanical property can be regulated via controlled crosslinking, and it is inert and electrochemically stable with lithium metal. Several key physical properties of the new polymer have been measured.

The Lawrence Berkeley National Laboratory (LBNL; N. Balsara) group has completed the "Synthesis of POSS containing single-ion copolymers" milestone. The temperature dependence of the ionic conductivity of the electrolytes has been measured.

The Iowa State University (ISU; S. Martin) group has completed the milestones of "100 cycles against Li metal with no cell shorting and < 20% degradation of other properties." They found that through the addition of LiPON in the ISU-7 series, the thermal stability of the ISU-6 composition was improved, reaching a working range (ΔT = TC-Tg) = ~ 120°C. This improvement over the ISU-6 composition is quite promising and enables these materials to be cast into preforms and drawn into films. In addition, a new grip assembly was designed, fabricated, and implemented to the draw tower system for glassy solid electrolyte (GSE) processing.

The Wildcat group (K. Carroll / C. Peebles) continued to work on decreasing interfacial resistance between the solid-state electrolyte (SSE) composite film and the Li-metal anode, using an additive material applied to the lithium metal to form an artificial solid electrolyte interface (SEI). They found that, compared to the baseline cell, several systems show smaller initial resistance. They continued to develop the composite ceramic polymer electrolyte with polyvinylidene fluoride (PVDF) instead of polyethylene oxide (PEO). They found that as one increases the salt concentration to 32 wt% for the PVDF polymer composite system, the highest ionic conductivity can be achieved, reaching close to that of the LATP ($Li_{1.3}Al_{0.3}Ti_{1.7}(PO_4)_3$).

The University of Michigan group (UM; J. Sakamoto) has developed a platform for *operando* video microscopy of *in situ* anode formation and Li-metal cycling. The new platform will enable them to quantitatively track changes in the 3D morphology of the Li-metal anode during the initial anode formation, and during extended cycling. These changes will be linked to the electrochemical signatures, and when coupled with *ex situ* characterization, they will provide valuable insights into the evolution of Li-metal/SE interfaces during extended cycling.

The University of Maryland (UMD) group (C. Wang) has developed a model to determine the critical overpotential (COP), under which the dendrite intrinsic suppression capability of different SSEs can be evaluated. In addition, experimental studies of COP of $Li_7La_3Zr_2O_{12}$ (LLZO), LPS, and Li_7N_2I-LiOH were carried out.

At UMD (E. Wachsman and Y. Mo), X-ray diffraction (XRD) experiments were performed on composite pellets of Ta-doped LLZO (LLZTO) and the NMC-532 cathode material (1:1 in weight ratio) prepared by physical mixing, mold pressing, and co-sintering at 500-1000°C for 3 hours. In addition, the reactivity of NMCs with LLZTO was investigated by DSC of the powder mixture. The data support the trend that NMC and LLZTO react more strongly with increasing nickel content. For this reason, future co-sintering experiments will not use NMC-811 and will limit the maximum co-sintering temperature to 900°C.

At University of Wisconsin, Milwaukee (UWM; D. Qu), the team has achieved the following: (1) validated cell design for long-term cell cycling tests; (2) finalized design of the *in situ* optical cell for real-time observation of dendrite growth at the SSE – lithium interface; (3) down selected SSE for long-term cell cycling; and (4) modified lithium anode for dendrite growth depression. They found that if Li-In alloy is used as an anode, dendrite growth can be suppressed, and the Li_3YC_{l6} SE becomes stable.

The team at Virginia Polytechnic Institute and State University (L. Madsen) performed a systematic study of long-term cycling stability of Li/MIC/$LiFePO_4$ cells at elevated temperatures. The data demonstrate that the SE used, which is a molecular ionic composite (MIC) material with only 10 wt% PBDT, is both mechanically and electrochemically stable at 150°C to enable successful cycling of $LiFePO_4$ batteries. They have also demonstrated that MIC electrolytes are compatible with high working potential cathodes such as NMC-622 at least up to 4.5 V. Compatibility with spinel $LiMn_2O_4$ has been confirmed.

The team at Solid Power (P. Zhang) and University of California, San Diego (UCSD; Y. S. Meng) has developed the SSE separator coating process at pilot scale. Rate capability of the cell made last quarter [containing a multifunctional SSE separator, an NMC-622 composite cathode (at 3 mAh/cm^2), and a Li-metal foil anode] was evaluated by charging and discharging symmetrically from C/10 to 1C. The cell retained 95% capacity at C/2 and 90% at 1C. The high-rate performance clearly indicates a low-resistance cell built with the multifunctional SSE.

The Pennsylvania State University (PSU; D. Wang) group worked on new S-C-M_xS_y materials (M = Li, Co, Ti, Mo, etc.) for all-solid-state Li-sulfur batteries. It was found that by replacing 20% of SE with TiS_2, initial discharge capacity would rise significantly from 1339.3 mAh g^{-1} to 1791.9 mAh g^{-1}. Such improvement is attributed to better electronic and ionic transport as well as extra capacity contribution by TiS_2 lithiation. $75Li_2S$-$25P_2S_5$ GSE was also used. In both cases, the main challenge has been cycle stability of the cells. They plan to work on optimizing sulfur cathode compositions, electrochemical window, and other parameters to achieve stable cycling of the cell.

Task 1.1 – Dual Function Solid-State Battery with Self-Forming, Self-Healing Electrolyte and Separator (Esther Takeuchi, Stony Brook University)

Project Objective. The project objective is to demonstrate a solid-state rechargeable battery based on a Li-metal anode and iodine cathode with a self-forming, self-healing electrolyte and separator with high gravimetric and volumetric energy density.

Project Impact. This program will enable demonstration of the proposed rechargeable battery with improved power capability, high energy density, and a self-forming, self-healing SSE/separator. Technical insight will be gained regarding improved conductivity of the solid LiI based electrolyte, power capability of the proposed system, the self-healing nature of the LiI layer, the nature of the electrode-electrolyte interfaces, and feasibility of the system to reach the DOE targets.

Approach. The proposed concept is a dual function rechargeable solid-state battery (SSB) utilizing LiI combined with silver iodide (AgI) as the electrolyte, with lithium metal (and small quantities of silver metal) as the anode, with iodine as the cathode, and with a self-forming, self-healing separator/electrolyte. The battery will be assembled in the discharged state, where the anode and cathode will be created during the first formation (charge) step. Initially, silver ion (Ag^{+}) will diffuse toward the negative electrode and be reduced to silver metal (Ag^{0}), and iodine ion (I^{-}) will be oxidized to elemental iodine (I_2) at the cathode side. As the formation of the battery continues, lithium ion (Li^{+}) will form a Li-metal layer at the anode, with generation of iodine at the cathode. LiI will remain and serve as both the separator and electrolyte.

Out-Year Goals. This is a multi-year program where the effort is divided into three major tasks.

- Year 1 involves electrolyte preparation and characterization including preparation of SSEs and conductivity measurements.
- Year 2 will focus on cell construction and testing including both *in situ* and *ex situ* analysis.
- Year 3 will focus on cell characterization. Under the program, cycle life, efficiency, energy density, and the functional capacity of cells will be determined.

Collaborations. This project collaborates with A. Marschilok and K. Takeuchi of SBU.

Milestones

1. Conduct destructive analysis of tested cells. (Q1, FY 2021; Completed)
2. Perform extended cycle life testing. (Q2, FY 2021; In progress)

Progress Report

To expand on characterization of SEs from recent FY 2020 milestones, additional characterization was conducted on LiI-containing SEs with varying LiI·H_2O content (Figure 1) and/or preparation methods (Figure 2). For the study with varying hydrate content, cells were constructed using a LiI-LiI(HPN)$_2$ SE, where the LiI·H_2O hydrate content of the LiI SE was either (1) 89% LiI and 11% LiI·H_2O or (2) 95% LiI and 5% LiI·H_2O. There was a difference in the morphology of the anode surface of the cycled SE with 11% LiI·H_2O (Figure 1a) compared to the 5% (Figure 1b) sample, suggesting that morphology may vary depending on the hydrate content of the material. When looking at the cross-section of cycled Li-SE cells with 11% LiI·H_2O (Figure 1c/e) and 5% (Figure 1d/f), there was a notable amount of rod-like shaped LiOH with (Figure 1c) or without (Figure 1e) LiI formed under the higher amount of LiI·H_2O. Cells using SSEs with each of the levels of LiI·H_2O were cycled for 25 cycles. Interestingly, there is minimal impact on cycling efficiency based on the amount of LiI·H_2O present in the SSE.

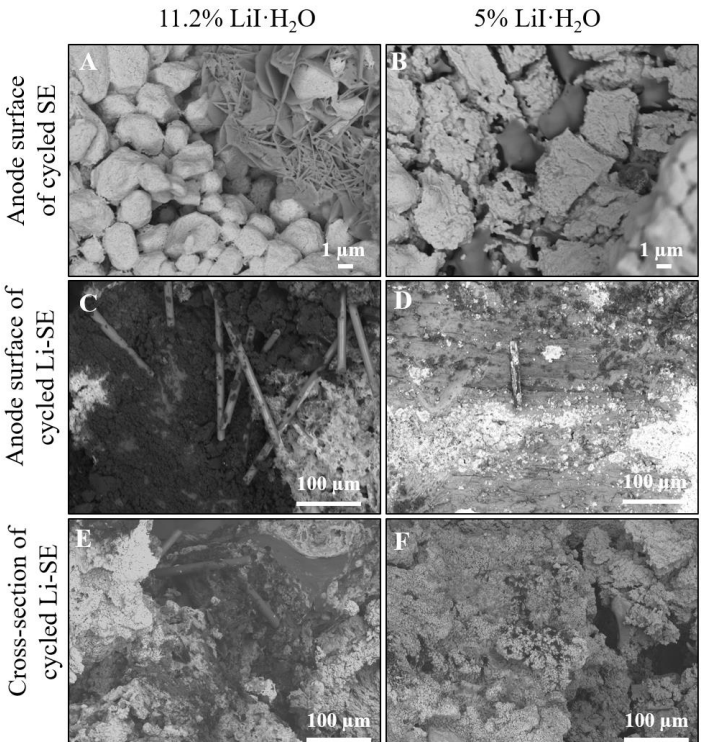

Figure 1. Backscattering scanning electron microscopy images for the cycled solid electrolyte (SE) in charged state (a-b) and cycled Li-SE (c-f) in charged state with different amounts of LiI·H_2O.

Raman spectroscopy was employed to affirm formation of an iodine-containing cathode and to assess the level of iodine formation among different preparation methods of LiI SEs (ground, and/or sonicated). The pristine, uncycled samples (Figure 2a) exhibit low levels of polyiodides, similar to the LiI(HPN)$_2$ standard. The polyiodides are strongly associated with the LiI(HPN)$_2$ complex, as evidenced by the same trend in intensity for the 2277 cm^{-1} peak, which describes the association between Li^+ and the nitrile group from the HPN. A group of cells was cycled before recovery of the SE; spectra were collected of both the negative and positive faces of the SE. Figure 2b shows that the negative face of the SE has a similar level of polyiodides present compared to the pristine. In contrast, the spectra of the cathode face of the pellet (Figure 2c) show a 1 order of magnitude increase in intensity, indicating larger amounts of polyiodides and formation of an iodine-containing cathode. These data provide additional evidence for formation of cell components from the electrolyte, building on the team's previous work showing formation of an I_2-LiI(HPN)$_2$ complex at the cathode interface.

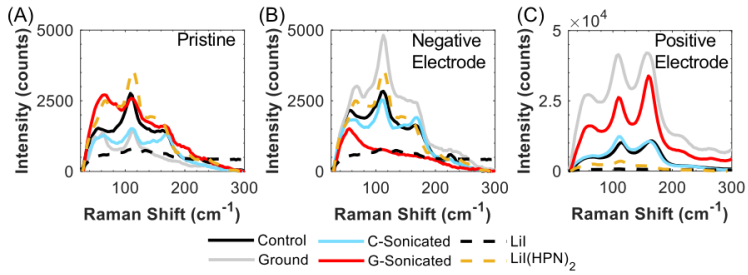

Figure 2. Raman spectra of (a) pristine solid electrolyte (SE), (b) negative side of electrolyte, and (c) positive side of electrolyte of various SE preparation methods.

Patents/Publications/Presentations

Publication

- Stackhouse, C. A.,* A. Abraham,* S. Yan, L. Wang, N. Sadique, G. Singh, A. C. Marschilok, E. S. Takeuchi, and K. J. Takeuchi. "Self-Healing, Improved Efficiency Solid State Rechargeable Li/I_2 Based Battery." *Journal of the Electrochemical Society* 168 (2021): 010519. doi: 10.1149/1945-7111/abd831.

Task 1.2 – Characterization and Modeling of Li-Metal Batteries: Characterization of Li^+ Transport in Polyelectrolytes
(Bryan D. McCloskey, University of California, Berkeley)

Project Objective. This task aims to understand lithium plating and stripping in non-traditional electrolyte systems (specifically, polyelectrolyte solutions and concentrated binary salt electrolytes) that have been proposed to reduce dendrite formation during lithium stripping and plating due to their high Li^+ transference numbers (t_+). The team will develop capabilities that allow them to understand how ion dynamics in these electrolytes impact macroscale transport properties and Li-metal plating and stripping.

Impact. Ultimately, this task will develop an understanding of how electrolyte composition and molecular interactions can be manipulated to positively impact ion transport of potential electrolytes for Li-metal batteries. This will provide a set of general design rules for novel electrolytes enabling stable, efficient high capacity Li-metal stripping and plating.

Approach. To understand various aspects of lithium plating and ion transport in these systems, the team will develop novel diagnostic and computational modeling techniques. Model polyelectrolytes, with pendant triflimide anions, will be used as polyanions, as their properties can be easily tuned via changes in the polymerization chemistry. Solution parameters that can be varied for both polyelectrolyte solutions and concentrated electrolytes include solvent and salt composition, additive inclusion, and the aforementioned polymer properties, all of which can have a profound impact on electrostatic interactions between charged species in solution, as well as interfacial stability and reaction kinetics of the lithium electrode. The team will develop capabilities that allow them to understand how molecular-level ion dynamics in these electrolytes impact macroscale transport properties and Li-metal plating and stripping. These computational simulations will be validated and refined by comparing results to experimentally measured transport properties of these electrolytes. They will optimize electrochemical methods for these electrolytes to evaluate relevant transport properties under the Newman concentrated solution theory framework, which has never been performed on these non-traditional electrolytes. ^1H and ^{19}F nuclear magnetic resonance (NMR) diffusometry will also be used to measure single-ion self diffusion coefficients without an applied electric field; solution viscosity measurements using a state-of-the-art rotating sphere viscometer can be performed under entirely air-free and water-free conditions. The team will develop capabilities to quantitatively understand degradation mechanisms of various electrolytes during Li-metal stripping and plating. Specifically, differential electrochemical MS (DEMS) will be used to study outgassing that occurs from electrolyte degradation processes.

Out-Year Goals. The ultimate goal of this project is to understand the influence of electrolytes with novel transport characteristics on the performance of Li-metal electrodes. Work will continue to build toward a complete understanding of Li-ion and counterion transport in polyelectrolyte solutions and concentrated electrolytes, as well as the impact of electrolyte transport properties on Li-metal uniformity during electrochemical stripping and plating. Outgassing measurements using DEMS will be developed to further probe the interfacial reactivity of lithium metal with electrolytes created in this project.

Collaborations. Collaborators on this project include K. Persson (atomistic and coarse-grained modeling) and N. Balsara (electrochemical characterization of PEs), both at LBNL.

Milestones

1. Establish a simple method to measure activity coefficients and thermodynamic factors for a model electrolyte. (Q1, FY 2021; Completed)
2. Synthesize very low molecular weight oligomer triflimide-based polyions (pTFSI). (Q2, FY 2021; In progress).

3. Measure conductivity, self diffusion, and concentration cells for model triflimide-based polyion (pTFSI) solutions. (Q3, FY 2021)
4. Establish electrophoretic NMR techniques for measuring the true Li^+ transference number of pTFSI solutions. (Q4, FY 2021)

Progress Report

This quarter, the team focused on developing alternative non-electrochemical methods to measure the activity coefficients of electrolytes to enable transference number measurements from lithium concentration cells. Specifically, they focused on using freezing point depression measurements from DSC to determine salt activity coefficients, $\gamma_{\pm}$. To validate the method on single salt in solvent systems, they measured the freezing point of $LiPF_6$ in DMC for concentrations ranging from neat DMC to 1 molal $LiPF_6$. This electrolyte was chosen due to the availability of high-quality activity coefficient measured in a vapor pressure manometer setup (Xin, et al., *Journal of Chemical Thermodynamics*, 2018). The team found that for a single solvent system, they can accurately predict activity of the salt using freezing point depression (see Figure 3). While there is some deviation in the predicted salt activity coefficient because part of the process of converting osmotic coefficients to activity coefficients allows shifting of the activity coefficient by an arbitrary constant, for electrolyte transport measurements the team only needs the slope of the activity coefficient as a function of concentration to determine the thermodynamic factor. They see excellent agreement between the project's thermodynamic factor calculated from DSC to those in the literature.

The team also is researching theory and experiments to extend the freezing point method to mixed solvent systems like EC:EMC. In these systems, phase behavior is significantly more complex, and the freezing point depression of the liquidus appears to be much more strongly affected than in single solvent and salt systems. They plan to continue investigating these multi-solvent systems next quarter using $LiPF_6$ in EC:EMC.

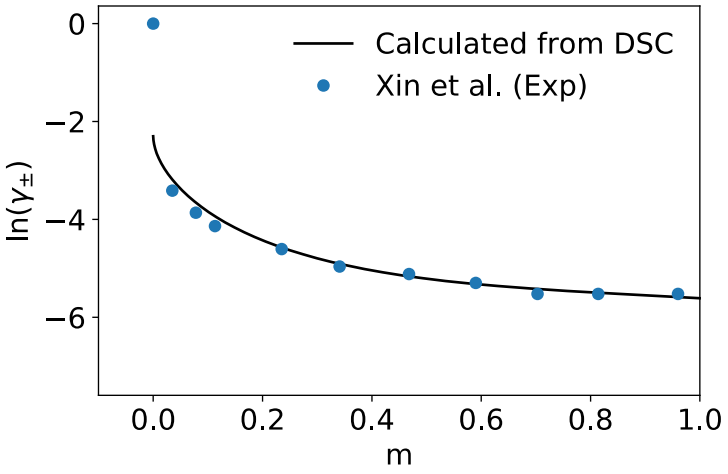

Figure 3. Salt activity coefficient versus concentration as calculated using freezing point depression from differential scanning calorimetry for $LiPF_6$ in dimethyl carbonate. Data from Xin, et al., measured using vapor pressure measurements.

The team continues exploring the effect of interfacial resistance on transport measurements. Through modifying cell pressure and electrode size, they were able to achieve lower interfacial resistances on the order of 100 $\Omega \cdot cm^2$ per electrode in lithium symmetric cells with $LiPF_6$ in 3:7 EC:EMC. They still see strong correlation between interfacial resistance and transport properties measured electrochemically. In the coming quarters, they plan to switch to an alternate measurement technique like electrophoretic NMR to characterize transference number to avoid this issue.

Patents/Publications/Presentations

Publication

- Fong, K. D., H. K. Bergstrom, B. D. McCloskey, and K. K. Mandadapu. "Transport Phenomena in Electrolyte Solutions: Nonequilibrium Thermodynamics and Statistical Mechanics." *AIChE Journal* 66, No. 12 (2020): e17091.

Presentations

- American Institute of Chemical Engineering (AIChE) Conference, Virtual (November 16–20, 2020): "Molecular Dynamics Characterization of Onsager Transport Coefficients and Transference Number in Polyelectrolyte Solutions"; K. Fong.
- AIChE Conference, Virtual (November 16–20, 2020): "Theory of Irreversible Thermodynamics and Non-Equilibrium Statistical Mechanics for Transport Phenomena in Electrolyte Solutions"; K. Fong.
- AIChE Conference, Virtual (November 16–20, 2020): "The Effect of Interfacial Phenomena on Ion Transport Characterization in Electrolyte Solutions for Li Metal and Li-Ion Batteries"; H. Bergstrom.

Task 1.3 – Advanced Polymer Materials for Batteries (Zhenan Bao and Yi Cui, Stanford University)

Project Objective. This project will develop new polymer materials for batteries. The team will develop polymer coatings with specific mechanical properties that can accommodate the volume expansion and contraction of the Li-metal anode associated with deposition and stripping (charging and discharging).

Project Impact. The cycling stability and Coulombic efficiency (CE) of Li-metal electrodes will be increased by implementation of a polymer-based protective layer that functions as an artificial SEI with desired properties. The improved performance will enable further development toward practical utilization of Li-metal anodes with higher cycling efficiency and less susceptibility to dendrite-based failure.

Approach. The project uses soft polymer coatings with dynamic crosslinking to give the resulting polymers liquid-like rheological properties and stretchable and self-healing properties. In previous work, the project has shown that such coatings resulted in uniform deposition/stripping of lithium metal and improved cycling stability of Li-metal electrodes. To understand the design rules for effective polymer coatings, the team chose a few representative polymers to systematically understand structure property relationships. Here, the team investigates the correlation between surface energy of the polymer and exchange current for lithium deposition.

Out-Year Goals. Work will progress toward the correlation between dielectric constant and exchange current. These findings will enable further understanding and development of various polymer coatings for protecting Li-metal anodes.

Collaborations. This quarter, the team is collaborating with J. Qin at Stanford University.

Milestones

1. New lithium anode coating design. Analyze potential electrochemical stability. (Q1, FY 2021; Completed)

Progress Report

The team hypothesizes that an effective method to address the lithium anodic interfacial instability is to fundamentally alter the Li-ion deposition pathways by electrostatically blocking the heterogenous surface regions that concentrate lithium ions due to high electric field. This can be experimentally implemented using electro-inactive cations at the interface that can 'shield' the inhomogeneous protrusion on the electrode surface to neutralize the electric field landscape. However, this strategy can be successful only when it is ensured that these electro-inactive cations do not undergo reduction during lithium deposition process. In other words, their reduction potential needs to be even lower than that of Li^+ ions that already have the lowest intrinsic reduction potentials among metallic cations. Previously, Ding, et al. pointed out that Cs^+ can achieve lower reduction potential than Li^+ by tuning its concentration based on Nernst Equation. Furthermore, it was shown that addition of Cs^+ ions in electrolyte resulted in improved lithium deposition morphology and battery operation. However, the concentration-dependent electrochemical stability of Cs^+ ions can be undermined by their localized aggregation at the electrode surface, resulting in the reduction of Cs^+.

Instead of using free cations, here the team proposes to tether the cations onto a polymer backbone to form a poly ionic liquid (PIL) coating that would homogenize the electric field distribution on the electrode surface and promote uniform lithium deposition. Incorporation of such cations in a polymer coating on the lithium anode is a facile method that does not alter existing manufacturing capabilities and also limits interaction with other battery components. The team will build on previous studies on anodic coating using polymers like PEO, PDMS, Nafion, single-ion conducting polymer, PVDF, and on their knowledge of designing cation-tethered polymeric coating on anode surface; in this work, they will design new coatings based on economically viable chemistry, chemically and electrochemically inert with lithium metal, possessing a conducting pathway for lithium conduction, and being mechanically robust to adapt to rapid volume changes.

Polymer Design

The schematic of Figure 4a illustrates lithium anode coated with PIL containing electro-inactive cations. In the absence of any coating, the concentrated electric field at surface protrusion triggers a self-amplified surface roughening process of lithium deposition (Figure 4b). The presence of cations is hypothesized to neutralize the radiating electric field and helps to homogenize lithium deposition pathways. Figure 4c showcases the 'cationic shielding' phenomenon where the presence of the PIL coating results in redistribution of Li^+ ions away from the surface protrusions, leading to a more uniform topology. The physio-chemical prerequisites of the PIL polymer coating for the cationic shielding mechanism are as follows: (1) the cations in the PIL backbone should have a lower reduction potential than that of Li^+, and (2) sufficient mobility of the polymer chains is essential for electric-field based response of the cations.

In previous work, the team utilized a system of random co-polymer on poly(acrylic) backbone: one co-polymer side chain contained the Py^+ (pyrrolidinium) cation units, and the other side chain was perfluoroalkyl as an inert component that can also lower the glass transition of the final co-polymer and introduce mobility to the polymer chains.

Instead of using a relatively rigid poly(acrylic) backbone, the new design (Figure 4.1d) utilizes the flexible PDMS backbone, which efficiently brings down the polymer's glass transition temperature (Tg) so that there is no longer a need to introduce another fluorinated component, and all of the polymer side chains can be functionalized with the Py^+ cation units. Beyond the benefit of mechanical flexibility, PDMS-based polymer is economically viable in comparison to any fluorinated polymer, its mechanical property can be regulated via controlled crosslinking, and it is inert and electrochemically stable with lithium metal.

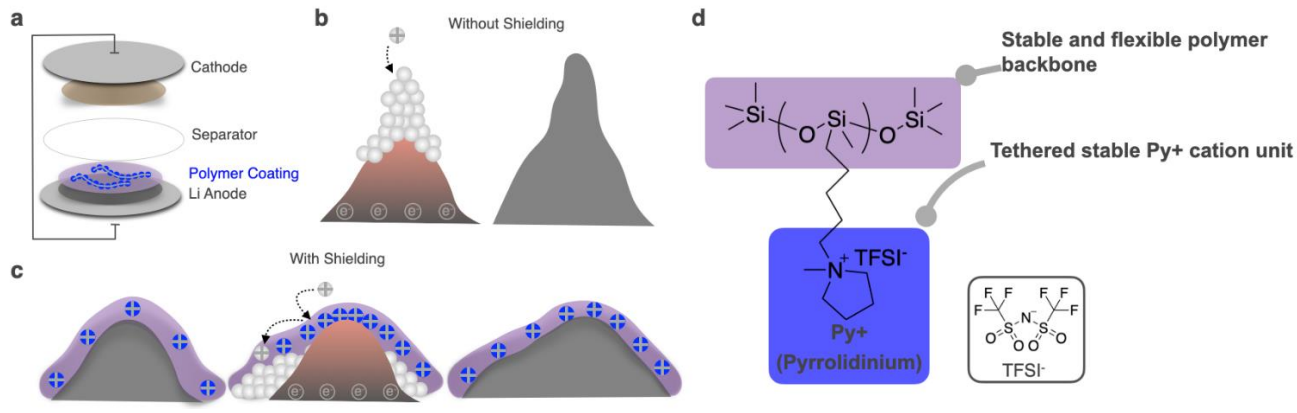

Figure 4. PDMS-Py as the anodic coating for Li-metal batteries. (a) Li-metal battery with polymer-coated anode. (b) The concentrated electric field at vicinity of surface protrusions causes the self-amplifying dendritic deposition of lithium ions. (c) Coating on Li-metal anode. During Li^+ deposition, cations in poly ionic liquid (PIL) coating remain electrochemically stable and can effectively shield the Li^+ ions, resulting in more flat and homogeneous deposition. (d) Chemical structure of the PDMS-PyTFSI coating.

Polymer Characterization

The PDMS-PyTFSI polymer was synthesized by tethering the Py^+ side chain to purchased PDMS backbone, which has controlled molecular weight with an average of 30 monomer unit per polymer chain. After the polymer was synthesized, its chemical structure was confirmed with proton NMR. As shown in Figure 5a, hydrogen containing functionality on the polymer structure are numerically numbered, corresponding to the peak signals on the NMR spectrum. The integration value of area under each peak represents the amount of hydrogen atoms for each signal peak. Through comparing the ratio among the peak integration value and the stoichiometric ratio of the hydrogen atoms at each unique chemical environment on the polymer, the team concluded that the PDMS polymer with Py^+ side chain tethered was correctly synthesized.

Other than linear polymer, the team also synthesized crosslinked PDMS-PyTFSI polymer using short-chain siloxane crosslinking agent. They added 5% (molar of crosslinking agent: molar of monomer units) of crosslinker to the polymer during polymer synthesis and then compared the resulting polymer mechanical properties and glass Tg. The mechanical properties were measured with rheology frequency sweep measurements, where the polymer samples were placed under oscillatory 1% strain; both the storage and loss moduli of the samples were measured at multiple frequencies (Figure 5b). On crosslinking, both the storage and loss moduli of the polymer increased; as indicated on the plot, the storage modulus measured at 1 Hz frequency increased by an order. The storage and loss moduli from the rheological measurement are also an indication of the solid/ liquid state of the materials; when the storage modulus is higher than the loss modulus, the material exhibits solid-like behavior, and vice versa. When there is no crosslinker, the measured polymer's loss modulus is lower than its storage modulus, indicating that the polymer is a viscous elastic liquid in the measured frequency range. On addition of the crosslinker, the polymer exhibited solid-like behavior with its storage modulus at lower frequency range, and with its storage modulus higher than the loss modulus. Beyond mechanical properties, the glass Tg of the crosslinked and linear polymer were also characterized with DSC, and the team found that the Tg of the polymer increased from -9.8°C to -2.2°C (Figure 5c). After crosslinking, the polymer's Tg was still below room temperature (25°C), indicating that the resulting polymer still has sufficient chain mobility at room temperature. Both the rheological and DSC measurements showcased that the mechanical and molecular dynamics (MD) of the PDMS-PyTFSI polymer can be tuned with minimal effect on the overall polymer chemistry through controlled crosslinking. The team believes that the polymer design based on PDMS chemistry that is reported in this work provides a synthetically accessible, economically viable, and mechanically tunable solution to the unstable Li-metal deposition at the anode/ electrolyte interface.

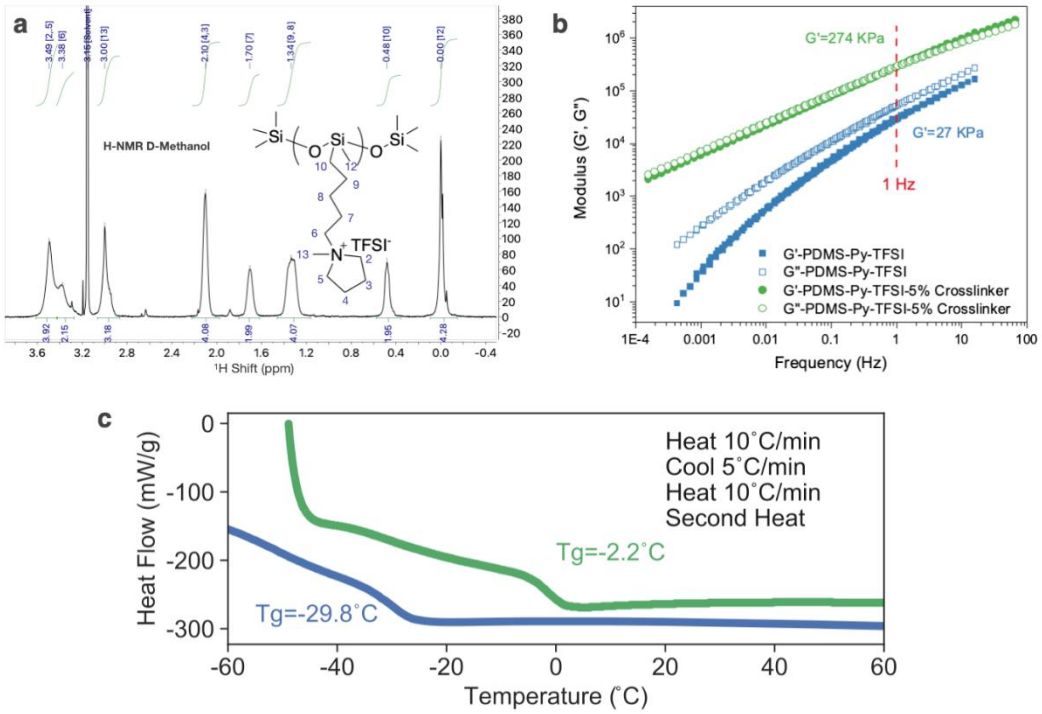

Figure 5. Characterization of PDMS-PyTFSI polymer. (a) Proton nuclear magnetic resonance (NMR) of the PDMS-PyTFSI polymer dissolved in protonated methanol. Each hydrogen containing functionality on the polymer is labeled with the number corresponding to the numbering on top of each NMR peak signal. The integration value of the area under each peak is indicated at the bottom of each signal. (b) Rheological frequency sweep of the PDMS-PyTFSI polymer conducted at room temperature with 1% strain on the polymer. The open symbol stands for loss modulus (G"), and the filled symbol stands for storage modulus (G'). Green: PDMS-PyTFSI with 5% crosslinker; Blue: PDMS-PyTFSI. (c) Glass transition (Tg) of the PDMS-PyTFSI polymer with and without the crosslinker measured with differential scanning calorimetry. Green: PDMS-PyTFSI with 5% crosslinker; Blue: PDMS-PyTFSI.

Patents/Publications/Presentations

Publication

- Huang, Z., S. Choudhury, H. Gong, Y. Cui, and Z. Bao. "A Cation-Tethered Flowable Polymeric Interface for Enabling Stable Deposition of Metallic Lithium." *Journal of the American Chemical Society* 142, No. 51 (2020): 21393–21403.

Presentation

- Storage X International Symposium, Virtual (November 13, 2020): "Molecular Design for Electrolyte Solvents and Artificial SEI for Stable Lithium-Metal Anodes"; Z. Bao.

Task 1.4 – Improving the Stability of Lithium-Metal Anodes and Inorganic-Organic Solid Electrolytes (Nitash Balsara, Lawrence Berkeley National Laboratory)

Project Objective. The project objective is to establish a new hybrid electrolyte that will be stable against cells with a Li-metal anode.

Project Impact. PEs offer increased stability in lithium batteries in comparison to more widely used LEs. Nanostructured electrolytes containing both soft, ion-conducting domains and rigid, nonconducting domains offer the opportunity to tune both mechanical and electrical properties separately. Such electrolytes are conveniently made by block copolymer self-assembly. Most of the block copolymer electrolytes studied thus far comprise organic polymer chains for both the conducting and rigid domains. The team hopes to synthesize new electrolytes that simulataneously have high transport properties and have greater stability against lithium in comparison to organic diblock copolymers.

Approach. First, the team synthesizes hybrid diblock copolymers by incorporating monomers that contain an inorganic component. Then, electrolytes are prepared by mixing these diblock copolymers with salt. Electrochemical and mechanical characterization of these materials is performed before carrying out cycling X-ray tomography (XRT) experiments and *in situ* small angle X-ray scattering (SAXS) experiments. The combination of these approaches enables rational design of materials that exhibit improved stability against lithium metal.

Out-Year Goals. The project will synthesize a new hybrid electrolyte that is designed to be stable against lithium metal. The material is a block copolymer in which one block contains acryloisobutyl polyhedral oligomeric silsesquioxane (POSS). The second block is a conventional PE (PEO). Electrochemical characterization of this polymer will include measurement of all transport properties including conductivity, diffusion coefficient, and transference number. The stability against lithium metal will be evaluated by cyclic voltammetry (CV), while its applications as an electrolyte will be evaluated and visualized using cycling XRT experiments on symmetric Li-hybrid-Li cells.

Collaborations. There are no active collaborations this quarter.

Milestones

1. Synthesize at least 2 POSS-containing single ion conductors (SICs). (Q1, FY 2021; Completed)
2. Develop the relationship between non-linear mechanical properties and ion transport in solid block copolymer electrolytes. (Q2, FY 2021)
3. Conduct *in situ* X-ray scattering experiments on Li-polymer-Li symmetric cells to quantify polymer morphology in the presence of an applied field. (Q3, FY 2021)
4. Conduct XRT experiments on Li-polymer-Li symmetric cells to quantify dendrite growth in block copolymer electrolytes. (Q4, FY 2021)

Progress Report

The following milestone has been completed: Synthesis of POSS containing single-ion copolymers.

Single-ion block copolymers containing covalently bound counter-ions can enable Li-metal anodes by eliminating concentration gradient. A series of organic-inorganic hybrid SICs, PEO-b-POSS-ran-PSLiTFSI, was synthesized. Here, PEO acts as an ion-conducting block, POSS acts as mechanically rigid non-conducting block, and the polystyrene block acts as an ionic block in which the counter ion (sulfonyl(trifluoromethane sulfonyl) imide) is covalently bonded with the benzene ring of styrene.

The synthesis was carried out via nitroxide mediated copolymerization method, as shown in Figure 6. A PEO-based macroalkoxymine initiator was synthesized using the standard procedure.[1] In the next step, the macroinitiator was reacted with POSS acrylate and lithium-4-styrenesulfonyl(trifluoromethane sulfonyl) imide, in one step in dimethyl formamide at 120°C for 24 hours to generate a random copolymer. After that reaction, the polymer was precipitated from diethyl ether and then dialysed against deionized water for 72 hours and dried to obtain the pure product. The composition of the polymer was determined by ^{1}H-NMR spectra and is shown in Table 1.

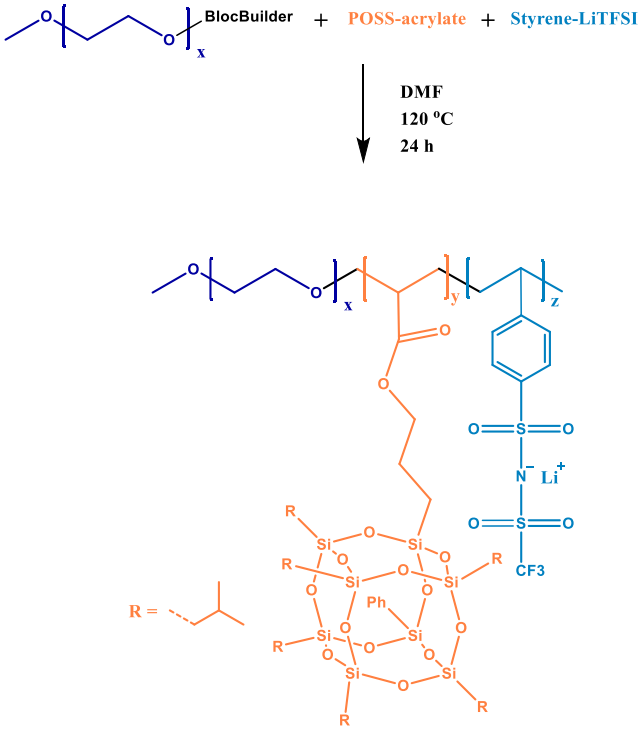

Figure 6. Scheme of synthesis of PEO-b-POSS-r-PSLiTFSI copolymer.

Table 1. Composition of the triblock copolymer PEO-b-POSS-ran-PSLiTFSI. The compositions of POSS and PSLiTSFI were determined by ^{1}H-NMR spectra. The *r* values denote the concentration of lithium ion in the polymer and are given by *r* = [Li]/[EO].

PEO-POSS-PSTFSILi	M_{PEO} (kg mol^{-1})	M_{POSS} (kg mol^{-1})	$M_{PSTFSILi}$ (kg mol^{-1})	*r*
5-2-2	5	1.9	2	0.055
5-2-4	5	1.9	4	0.11
5-2-11	5	1.9	11	0.31

Figure 7a summarizes the temperature dependence of the ionic conductivity of the electrolytes measured using a stainless-steel symmetric cell setup. The ionic conductivity of the electrolytes decreases with increasing Li-ion concentration. The current fraction ρ_+ was determined using lithium symmetric cells following the Bruce and Vincent method[2] for two of the electrolytes with r = 0.11 and 0.31. The values are 0.963 ± 0.04 and 0.96 ± 0.04, respectively, characteristic of the SICs. The effective conductivity, given by $\kappa\rho_+$, is shown in Figure 7b and compared with PEO/LiTFSI, r = 0.06, which exhibits current fraction of 0.115 ± 0.01.

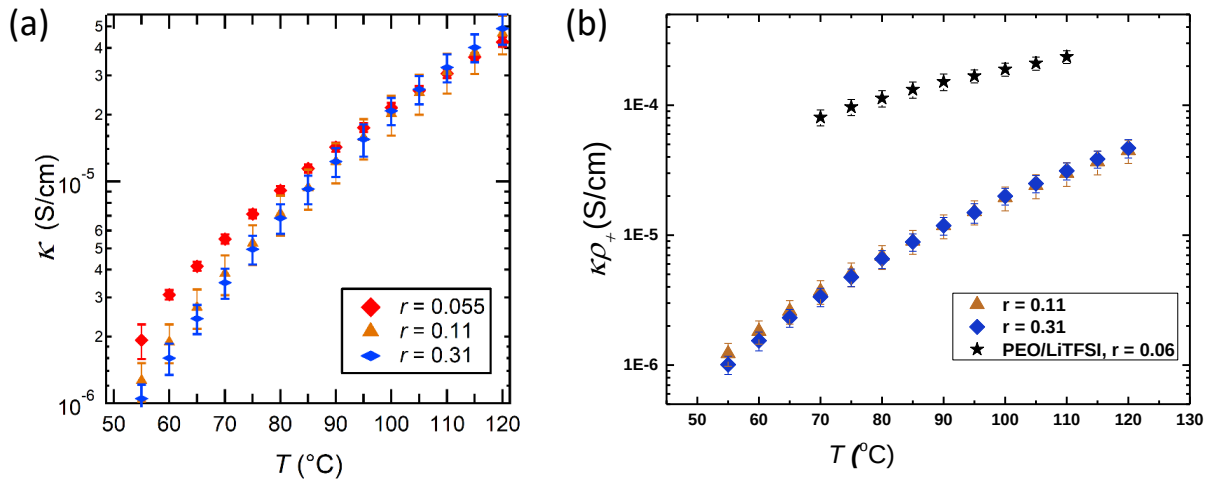

Figure 7. (a) Temperature-dependent conductivity κ is shown for three copolymers. (b) The effective conductivity $\kappa\rho_+$ is shown for two polymers with r = 0.11 and 0.31 and compared with PEO/LiTFSI, r = 0.06.

References

[1] Sethi, G. K., X. Jiang, R. Chakraborty, W. S. Loo, I. Villaluenga, and N. P. Balsara. *ACS Macro Letters* 7, No. 9 (2018): 1056.

[2] Bruce, P. G., M. T. Hardgrave, and C. A. Vincent. *Journal of Electroanalytical Chemistry and Interfacial Electrochemistry* 271, 1-2 (2002): 27.

Patents/Publications/Presentations

Publication

- Galluzzo, M. D., W. S. Loo, E. Schaible, C. Zhu, and N. P. Balsara. "Dynamic Structure and Phase Behavior of a Block Copolymer Electrolyte under dc Polarization." *ACS Applied Materials & Interfaces* 12, No. 51 (2020): 57421–5743.

Task 1.5 – Development of Thin, Robust, Lithium-Impenetrable, High-Conductivity, Electrochemically Stable, Scalable, and Low-Cost Glassy Solid Electrolytes for Solid-State Lithium Batteries (Steve Martin, Iowa State University of Science and Technology)

Project Objective. The objective of this project is to develop new Li^+-conducting mixed oxy-sulfide nitride (MOSN) GSEs that are impermeable to lithium dendrites, have high conductivities, are scalable through low-cost glass manufacturing, are chemically and electrochemically stable, and will enable low-cost, high-energy-density SSLBs. The SSLBs constructed from these new GSEs will meet and exceed all program objectives: usable specific energy @ C/3 ≥ 350 Wh/kg, calendar life 15 years, cycle life (C/3 deep discharge with < 20% energy fade) 1000, and cost ≤ $100/kWh.

Project Impact. This project will enable the team to demonstrate the following: (1) thin MOSN GSE films yield superior performance in a much safer, lower-cost, and Li-dendrite impenetrable form, and (2) high rate and long cycle life can be achieved in SSLBs using thin-film MOSN GSEs. The new GSEs in SSLBs are anticipated to increase energy density (anode basis) from ~ 300 mAhr/g to ~ 4,000 mAhr/g, enabling replacement of internal combustion engines in both light-duty and heavy-duty vehicles. Each 20% reduction in the ~ 1.6 billion liters of gasoline used per day in the United States would reduce CO_2 emissions by ~ 4 billion kg or 2 x 10^{12} l of CO_2 per day. The team will also increase scientific and engineering knowledge of thin-film GSEs in SSLBs.

Approach. The MOSN mixed glass former (MGF) glasses used for the GSEs in this project have been developed in previous work to have the necessary thermal stability and high ionic conductivity for successful use as a drawn-film electrolyte. In this project, the glass chemistry will be tuned for even more desirable properties, by investigating structure-property relationships and testing variations in glass chemistry.

Out-Year Goals. Work will progress toward developing a glass capable of being drawn to 100-micron thickness, while having high conductivity and electrochemical stability and good cycling ability.

Collaborations. There are no active collaborations this quarter.

Milestones

1. Accomplish: 100 cycles against lithium metal with no cell shorting and < 20% degradation of other properties.
   (Q8, FY 2021; Completed)
2. Accomplish: Optimize draw conditions for MOSN GSE to achieve 5 m × 5 cm x < 100-μm thin films. (Q8, FY 2021; In progress)
3. Accomplish: Fabricate MOSN MGF Li|GSE|Li cells in small area format, ~ 1 cm^2. (Q8, FY 2021; In progress)
4. *Go/No Go Decision*: Micro-sheet glass ribbon processing facility optimized/design capable of meeting the following performance requirements: Glove box enclosing preform redraw facility reaches 10 ppm O_2 and H_2O, and 3 samples of MOSN MGF GSE ribbons have been drawn at 5 m × 5 cm × 100 μm. Analysis indicates technical approach capable of achieving performance targets. (Q8, FY 2021; In progress)

Progress Report

Task 1 - Development of New MOSN MGF GSEs

Subtask 1.2 –Recipient will Continue Development of MOSN MGF GSEs with Target Properties Capable of Cycling Lithium against LM

This quarter, glasses in Table 2 were prepared and characterized. The nitrogen content in the glasses ISU-3 and ISU-4 has been determined by X-ray photoelectron spectroscopy (XPS) and CHNS combustion analysis. As a reminder, ISU-3 is a mixed oxy sulfide (MOS) glass, and ISU-4 is MOSN glass that is N-doped ISU-3 glass. Comparing ISU-3 and ISU-4 results shown in Table 3, nitrogen weight percentage increased from 0.00% N to 0.15% N. Therefore, nitrogen was successfully incorporated during synthesis of ISU-4, which is the first glass that is reported to actually be a MOSN glass, to the best of the team's knowledge. CHNS results in about 0.3 wt% of nitrogen exists in ISU-4, while ISU-3 does not have trackable nitrogen content. The XPS spectra in Figure 8a-b show that ISU-4 has two distinguishable N 1s peaks that correspond to N_t (-N<) and N_d (-N=) structures, which have been reported in LiPON glasses.[1-4]

Table 2. Compositions of glasses and glass series explored this quarter.

Sample ID	Compositional Formula
ISU-3	$0.55\ Li_2S + 0.35\ SiS_2 + 0.10\ LiPO_3$
ISU-4	$0.55\ Li_2S + 0.35\ SiS_2 + 0.07\ LiPO_3 + 0.03\ LiPO_{2.5}N_{0.33}$
ISU-5	$0.6Li_2S + 0.3\ SiS_2 + 0.1\ LiPO_3$
ISU-6	$0.58Li_2S + 0.32\ SiS_2 + 0.1\ LiPO_3$
ISU-7 (Series)	$0.58Li_2S + 0.32\ SiS_2 + 0.1[(1-x)LiPO_3 + xLiPO_{3-3y/2}N_y]$

Table 3. Nitrogen percentage in ISU-3 and ISU-4 glasses from CHNS analysis result.

	ISU-3 I	ISU-3 II	ISU-3 Avg.	ISU-4 I	ISU-4 II	ISU-4 Avg.
Mass Fraction Nitrogen	0.0000	0.0000	0.0000	0.1539	0.1556	0.1548

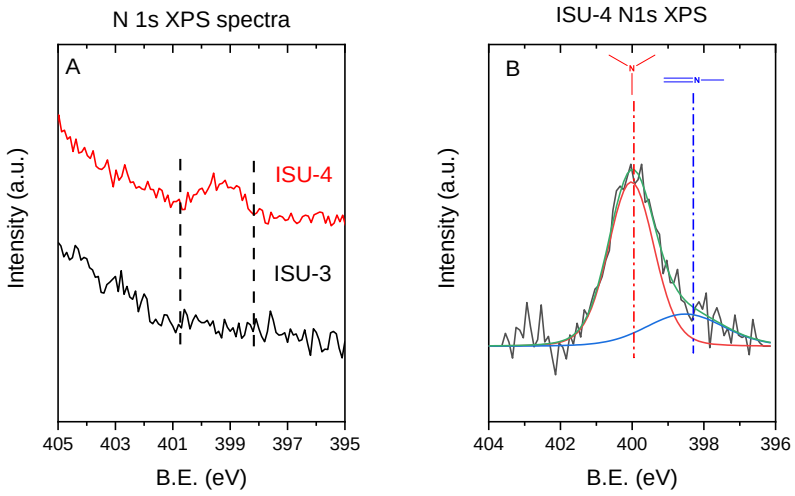

Figure 8. (a) N 1s X-ray photoelectron spectroscopy (XPS) spectra comparison between ISU-3 and ISU-4 glasses. (b) ISU-4 N 1s XPS spectrum deconvolution.

In addition, preliminary work has been completed on the ISU-7 series (Table 2) to incorporate nitrogen into the previously reported ISU-6 chemistry; see Table 3 for compositional details. As discussed in previous reports, the ISU-6 composition was found to be a promising glass composition with an ionic conductivity of ~ 7 x 10^{-4} S/cm at 25°C and a working range of approximately 114°C. Through the addition of LiPON, the thermal stability of the ISU-6 composition was improved, reaching a working range (ΔT = TC-Tg) = ~ 120°C in the x = 0.2 – 0.3 compositions, as seen in Figure 9. This improvement over the ISU-6 composition is quite promising and enables these materials to be cast into preforms and drawn into films. For this reason, the working range has been identified as an important criterion in the down-selection process. Further study will be done on this glass to determine conductivity and electrical properties.

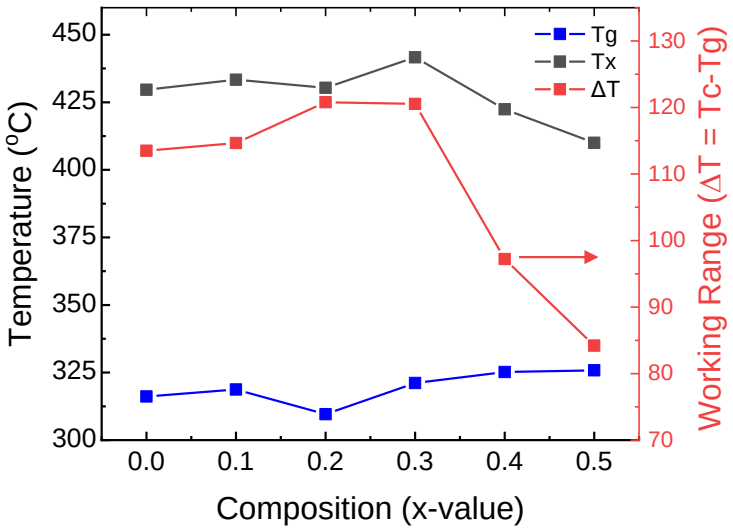

Figure 9. Composition-dependent thermal properties of the mixed oxy-sulfide nitride glasses in the ISU-7 series.

Subtask 1.3–Recipient will Initiate Development of Preforms of MOSN MGF GSEs that do not Crystallize

As seen in Figure 10a-b, 50 g and 250 g preforms were melted and cast with the ISU-6 MOS GSE chemistry, and can be seen in Figures 10-11. The raw materials for these two preforms were milled and mixed with 20% starter glass "cullet," then melted in a vertical furnace at 850°C. Precursor powders were reacted with high-energy milling using SpexMill 8000 (Figure 11a) and homogenized with a low-energy roller mill (Figure 11b). Long melting times were required due to non-homogenous powder mixing, which is the result of incomplete milling and mixing. Both melts formed a glass when cast onto 275°C plates, annealed, and cooled to room temperature. However, some regions of unmelted/unreacted raw material were present during the casting process, causing stress cracks in the large preform. In addition, many impurities were found in the glasses on cooling, which may prevent proper drawing into thin ribbon. Work is being done to increase the milling/mixing energy of larger volumes, as well as using a vacuum furnace to further purify the raw materials, with a goal of improving the final quality of the glass preform.

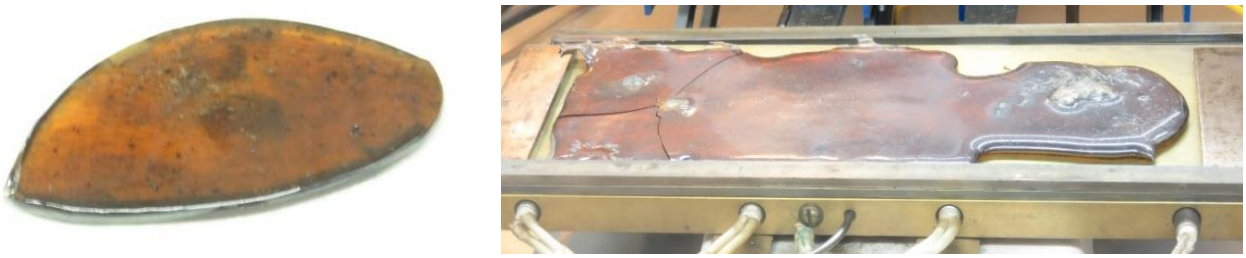

Figure 10. (a) 50 g casting of ISU-6 mixed oxy-sulfide nitride (MOSN) glassy solid electrolyte (GSE). (b) 250 g preform of ISU-6 MOSN GSE in annealing molds.

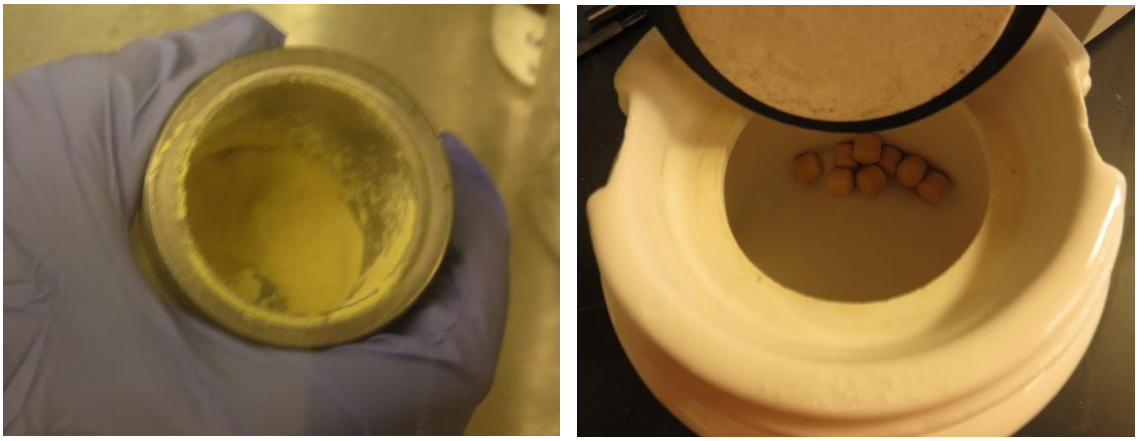

Figure 11. (a) Spex mill jar with mixed raw materials. This technique allows for high-energy milling, but a maximum of 15 g at a time. (b) Tumble mill pot, allowing for low-energy mixing of 250 g+ samples.

Task 2 - Develop Micro-Sheet Glass Ribbon Processing Facility for GSEs

As shown in Figure 12, a new grip assembly was designed, fabricated, and implemented to the draw tower system. The previous version of the grip assembly caused a large number of constraints for preform dimensions, while also failing to properly secure the preforms that were placed within it. These issues have caused approximately 30% of preforms to have some complication in the drawing process that prevented their full use. Previous size constraints required a preform be at least 8 cm in width and between 4 and 6 mm in thickness to properly fit within the grips. The new design allows preforms to fit at any width and with a new thickness range of 2 and 10 mm. Also, the previous grip assembly consistently had issues with being able to effectively acquire and maintain grip strength, often requiring the use of sandpaper to increase friction due to poor grip strength. The new design has had no issue with grip strength, eliminating the use of sandpaper to increase effective gripping ability. Additionally, the new design is made from individual components and uses standard sized screws and nuts, greatly reducing the overall cost of the item and allowing for individual parts to be easily replaced in the event of failure.

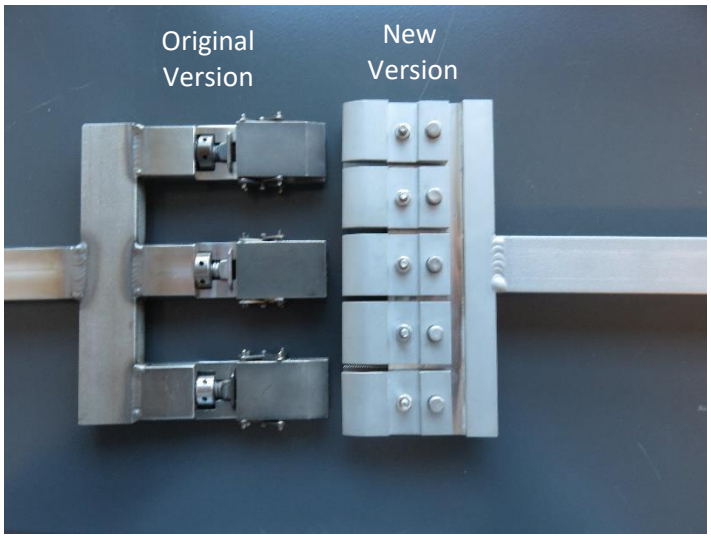

Figure 12. The two preform grip assemblies: (left) original version and (right) new version.

Task 3 - Develop Processing Conditions Micro-Sheet Ribbons of MOSN MGF GSEs

Subtask 3.1 – Complete Optimization of Draw Conditions for Oxide GSE < 500 µm

The team continued to use lithium metaphosphate ($LiPO_3$) for development of optimization techniques. This glass shows similar thermal properties to MOSN glasses and can be produced reliably and quickly for the purpose of drawing optimization. A notable insight found this quarter is that there seems to be an optimal film thickness when drawing. Generating film between the range of 40-90 µm seems to be very reliable assuming the initial conditions are appropriate, such as temperature, draw speed, and feed speed. Once film thickness is desired outside of these parameters, the drawing process becomes much more difficult, often requiring changing of multiple parameters to acquire. It has also been observed that the initial starting conditions for preforms of the same composition have a significant variance. Multiple $LiPO_3$ preforms have been drawn with furnace temperature ranging from 318°C to 333°C. This is noteworthy because once a film has reached its optimal drawing temperature, small temperature variations as low as 1°C have a very large impact on the viscosity of the glass. This difference is most likely due to variations of annealing procedures used. Measurements of film thickness have been taken to ensure consistent thickness in a 1 cm^2 area, with variation generally less than ± 10 µm. Defects within or near the surface can cause rapid changes in the thickness, causing occasional aberrant behavior in the film.

Subtask 3.2 – Complete Optimization of Draw Conditions for MOS MGF GSE < 200 µm

This work in progress will be covered in future reports. Work conducted on $LiPO_3$ is informing future work to optimize the draw conditions for MOS MGF GSE < 200 µm.

Subtask 3.3 – Complete Optimization of Draw Conditions for MOS MGF GSE < 100 µm

This work in progress will be covered in future reports. Work conducted on $LiPO_3$ is informing future work to optimize the draw conditions for MOS MGF GSE < 100 µm.

Task 4 - Fabricate and Test Li|GSE|Li Symmetric Cells in Large Area Planar Formats

Subtask 4.2 –Recipient will Complete Testing of Optimized MOSN MGF GSE in Small Cell Format Li|GSE|Li Symmetric Cells

The ISU-6 composition was tested in small cell format of less than 1 cm^2. Symmetric cells of Li|GSE|Li were fabricated in CR2032 coin cells with annealed melt quenched glass that was polished down to 2-µm polishing paper. After fabrication of the cell, it was connected to the BioLogic VMP-300, and electrochemical impedance spectroscopy (EIS) was conducted to characterize interface formation. EIS scans were collected every 30 minutes for ~ 24 hours. The cell was cycled for 100 cycles of ~ 4 hours. Additional EIS scans were conducted after every 20 cycles, as shown in Figure 13a. The bulk and interfacial resistances decrease prior to cycling; after cycling, the bulk and interfacial resistances increase slightly, but tend to stabilize or continue to decrease after 100 cycles, as shown in Figure 13b. The bulk resistance prior to cycling is 757 Ω, which increased to 889 Ω after 100 cycles. This meets the milestone of 100 cycles against lithium metal without shorting and < 20% degradation in properties. The cycling behavior in Figure 13c shows higher voltages required after the first 20 short cycles are completed, which gradually lowers to the voltage shown in the shorter cycles. This is most likely due to a conformal coating of lithium metal forming on each side of the electrolyte during these cycles. The critical current density (CCD) for this cell of ISU-6 was determined to be 0.3 mA/cm^2 under these conditions, as shown in Figure 13d.

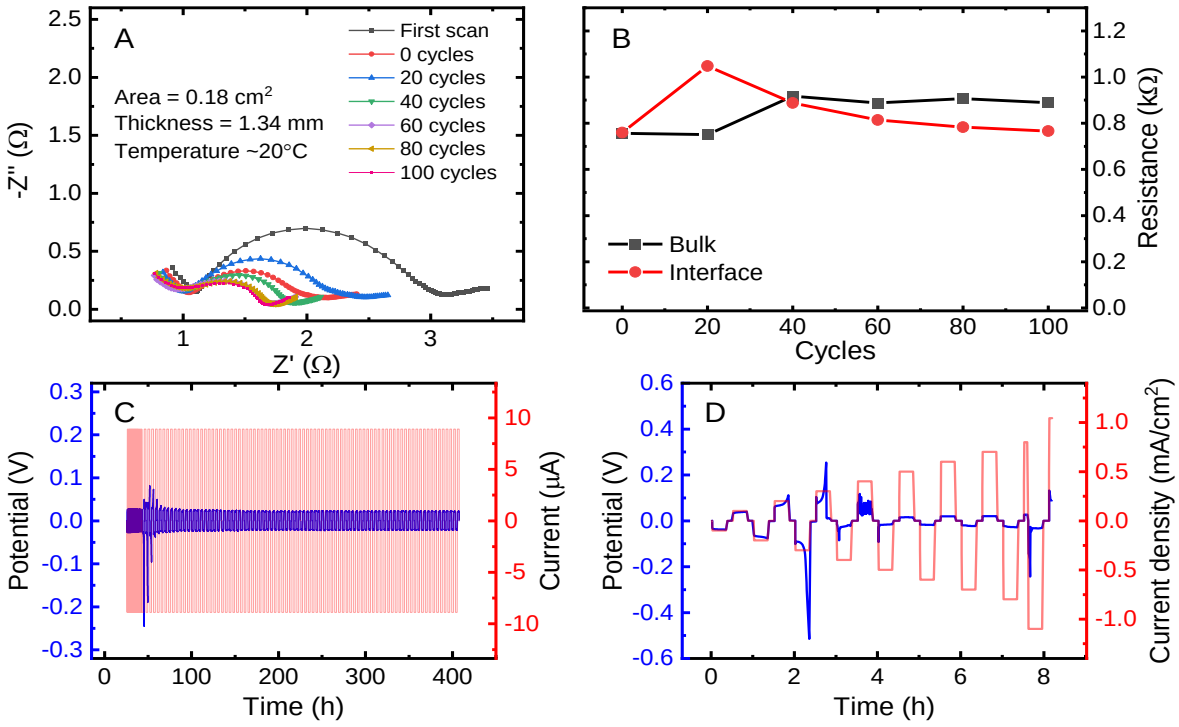

Figure 13. (a) Electrochemical impedance spectroscopy scans before, during, and after cycling of ISU-6. (b) Equivalent circuit fitted resistance values of the bulk and interfacial resistances from (a). (c) Galvanostatic cycling at 0.05 mA/cm² for 100 cycles. (d) Critical current density determination using galvanostatic cycling. (a-d) All from the same cell, with the area, temperature, and thickness specified in (a).

Small format cells have also been made using lithium metaphosphate thin films. These thin-film cells show low interfacial resistance after 4 hours (Figure 14a) and cycle well for long durations even at higher current densities (shown in Figure 14c). As expected, the film drawing process does not notably alter the conductivity of the electrolyte material, as shown in Figure 14b. The stability of oxide materials allows for stable cycling at 90°C at voltages higher than 5 V, as shown in Figure 14d. The lack of shorting under high voltages and higher current densities indicates that the thin-film oxide material has a high resistance to dendrite formation and is mechanically durable enough to prevent shorting due to fracture.

Subtask 4.3 – Recipient will Initiate Testing of Optimized MOSN MGF GSE in Intermediate Cell Format Li|GSE|Li Symmetric Cells

This work in progress will be covered in future reports. Work conducted on $LiPO_3$ in bulk and thin films is informing future work to optimize the draw conditions for intermediate-sized symmetric cells.

Subtask 4.4 –Recipient will Initiate Testing of Optimized MOSN MGF GSE in Large Cell Format Li|GSE|Li Symmetric Cells

This work in progress will be covered in future reports. Work conducted on $LiPO_3$ in bulk and thin film is informing future work to optimize the draw conditions for large-sized symmetric cells.

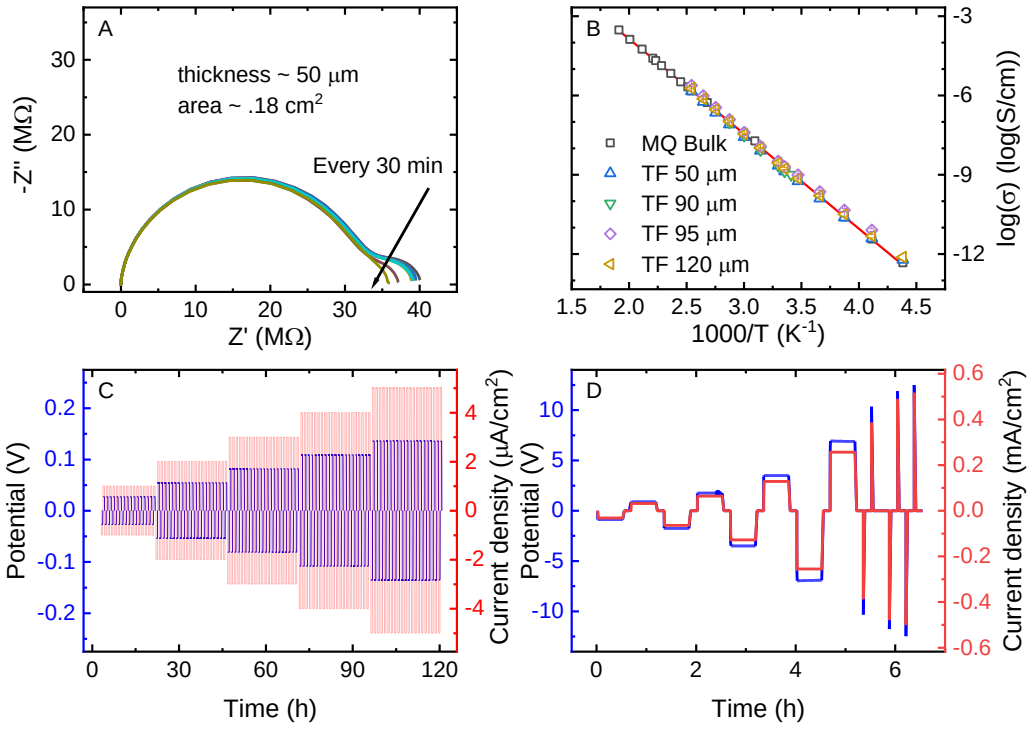

Figure 14. (a) Electrochemical impedance spectroscopy scans of 50-μm-thick thin-film symmetrical cell showing decreasing interfacial resistance with time. (b) Arrhenius plot showing conductivity of different film thicknesses and the melt quenched $LiPO_3$. (c) Cycling of thin-film $LiPO_3$ showing stable potential at 90°C. (d) Critical current density determination showing that the thin-film cell reaches maximum voltage of the potentiostat prior to shorting. (a-c) All from the same cell.

References

[1] Mascaraque, N., J. L. G. Fierro, A. Durán, and F. Muñoz. "An Interpretation for the Increase of Ionic Conductivity by Nitrogen Incorporation in LiPON Oxynitride Glasses." *Solid State Ionics* 233 (2013): 73–79. doi: 10.1016/j.ssi.2012.12.017.

[2] De Souza, J. E., et al. "LiPON and NaPON Glasses: A Study of the Ammonolysis of Lithium and Sodium Metaphosphate Melts." *International Journal of Applied Glass Science* 11 (2020): 78–86.

[3] Mascaraque, N., A. Durán, F. Muñoz, and G. Tricot. "Structural Features of LiPON Glasses Determined by 1D and 2D 31P MAS NMR." *International Journal of Applied Glass Science* 7 (2016): 69–79. doi: 10.1111/ijag.12120.

[4] Mascaraque, N., et al. "Thio-Oxynitride Phosphate Glass Electrolytes Prepared by Mechanical Milling." *Journal of Materials Research* 30 (2015): 2940–2948. doi: 10.1557/jmr.2015.128.

Patents/Publications/Presentations

Publications

- Kmiec, S., J. Lovi, A. Joyce, D. Bayko, and S. W. Martin. "Anomalously Strong Viscosity Behavior in Mixed Oxy-Sulfide $Na_4P_2S_7O_x$ Invert Glasses." *Journal of Non-Crystalline Solids* 553 (2021): 120493.
- Lazar, M., S. Kmiec, A. Joyce, and S. W. Martin. "Investigations into Reaction between Sodium and Solid-State Sodium Electrolytes." *ACS Applied Energy Materials* 3, No. 12 (2020): 11559–11569.

Task 1.6 – Composite Solid Ion Conductor with Engineered Lithium Interface (Kyler Carroll and Cam Peebles, Wildcat Discovery Technologies)

Project Objective. In this project, Wildcat seeks to perform focused, fundamental research and development on composite polymer/ceramic electrolytes and for the protection of Li-metal anodes to develop an all-solid-state Li-metal battery that achieves DOE requirements for performance to enable potential commercialization of this technology. Wildcat will leverage its high-throughput (HT) battery platform to explore a broad composite electrolyte compositional space. Additionally, the HT platform will allow the team to screen hundreds of inorganic and organic coatings for Li-metal protection and translate the best results to all solid cells.

Project Impact. Successful widespread commercialization of EVs is contingent on developing safe high-energy-density batteries capable of long cycle life. Lithium metal affords the highest theoretical capacity (3,860 mAh/g) and lowest electrochemical potential (-3.04 V versus self-healing electrolyte, or SHE), which offers the highest specific energy density of anode materials today. However, significant progress toward the passivation of lithium metal must occur before the energy density benefit can be realized. The intrinsic high reactivity between lithium metal with conventional Li-ion electrolytes (organic carbonate-based solvents) makes it extremely difficult to overcome these problems. The proposed composite polymer/ceramic electrolyte and a protected Li-metal anode will enable an all-solid-state Li-metal battery. It is expected that the outcomes from this effort will deliver a safe all-solid-state Li-metal pouch cell with over 350 Wh/kg and over 1,000 cycles (C/3) with the cost estimate below $100/kWh.

Approach. The project approach involves (1) identifying a suitable combination of solid ion conductor, polymer, and additive that minimizes overall interfacial impedance between the PE and solid ion conductor, and (2) identifying stable Li-metal protection agent or combination of agents that shows enhanced cycling performance (relative to a non-protected system) using the down-selected cell architectures.

Out-Year Goals. The out-year goals involve the screening of cathode composites to minimize interfacial resistance, the down selection of the best SSE, and the down selection of the best passivation approach for lithium metal. Following these developments, the final tasks will be to integrate these three components into a full SSB with improved cycle life.

Collaborations. All project tasks will be performed at Wildcat Discovery Technologies.

Milestones

1. Down select passivation approaches. (Q1, FY 2021; Completed)
2. Optimize SE. (Q2, FY 2021; In progress)
3. Integrate SE with cathode. (Q2, FY 2021; In progress)
4. Final Testing. (Q4, FY 2021; In progress)

Progress Report

This quarter, Wildcat utilized its HT platform to investigate further improvements in the composite polymer ceramic electrolyte. These studies involved improved processibility and film quality for higher ceramic loadings. The team was also able to optimize the polymer, salt, and ceramic composite to maximize the ionic conductivity to get closer to that of pure ceramic LATP. Additionally, Wildcat started investigating development of the SSE in the cathode composition to improve the cathode/composite SE interface. Lastly, Wildcat made progress in down selecting a passivation approach for the protected Li-metal anode.

Protected Li-Metal Additive Testing

Effort was placed on continuing to decrease the interfacial resistance between the SSE composite film and the Li-metal anode. To effectively do this, an additive material is applied to the lithium metal to form an artificial SEI that then can more favorably interact with the SSE composite. If resistance of the SSE composite / lithium metal is lowered relative to a baseline (no artificial SEI system), the interface between the artificial SEI and the SSE composite is thought to be minimized. Wildcat developed a robust process for applying the artificial SEI layer to the lithium metal, which results in repeatable and easily processable treated lithium metal to use in cell assembly. This approach to Li-metal passivation will be used in all subsequent work during this project.

A representative EIS of a Li/Li symmetric cell baseline (no Li-metal treatment) after cell assembly is shown in Figure 15. At this point, the cell is freshly made and no calendar aging or current-flow has occurred. This initial resistance must be small to successfully pass current through the cell. Using the current generation of SSE composite, a semi-circle (composed of one smaller and one larger semi-circle) with an initial resistance of ~ 530 Ohms is observed [initial resistance is measured using the point at which the end of the semi-circle crosses the x (real)-axis].

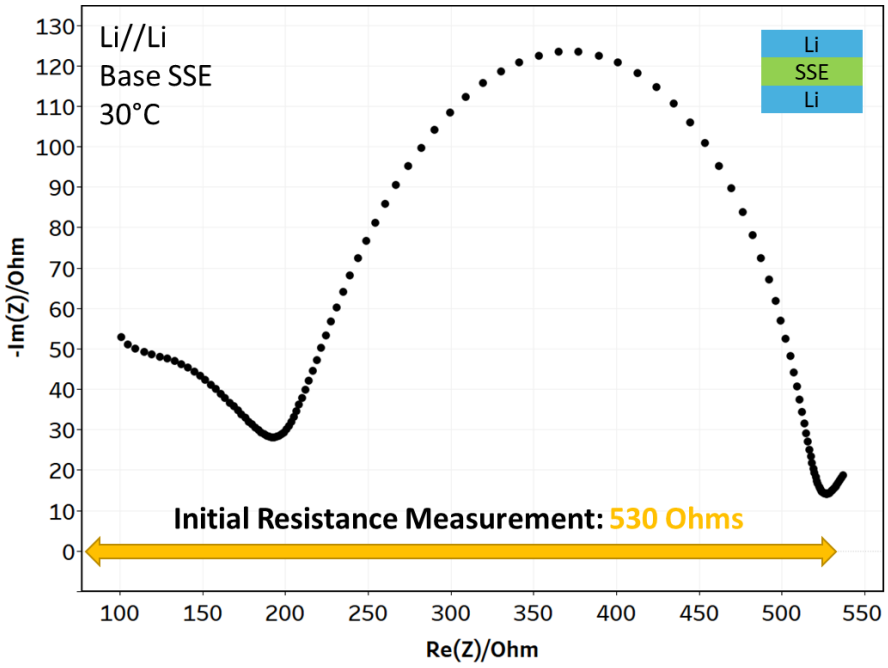

Figure 15. Representative electrochemical impedance spectroscopy of a Li/Li symmetric cell after cell assembly. The cell format is shown in the top right. The resistance is measured using the x (real)-axis.

Using learning from the initial parts of the project, lithium metal was treated with various down-selected materials to form articial SEIs that were then used in Li/Li symmetric cells. Figure 16 shows the initial resistance of various Li-metal treatments (multiple additives) color-coded by additive family (legend not shown). The average of multiple cells is shown as a colored circle, the average resistance is labeled, and the black line represents ± 1 standard deviation from the average. Some families (red Li-metal treatments) show larger cell resistance, which also shows higher cell-to-cell variation. Generally smaller resistances (green Li-metal treatments) show smaller cell-to-cell variation. Compared to the baseline cell (dark blue, no Li-metal treatment), several systems show smaller initial resistance. Next quarter, the team will continue to explore/optimize Li-metal treatments to further reduce cell initial resistance.

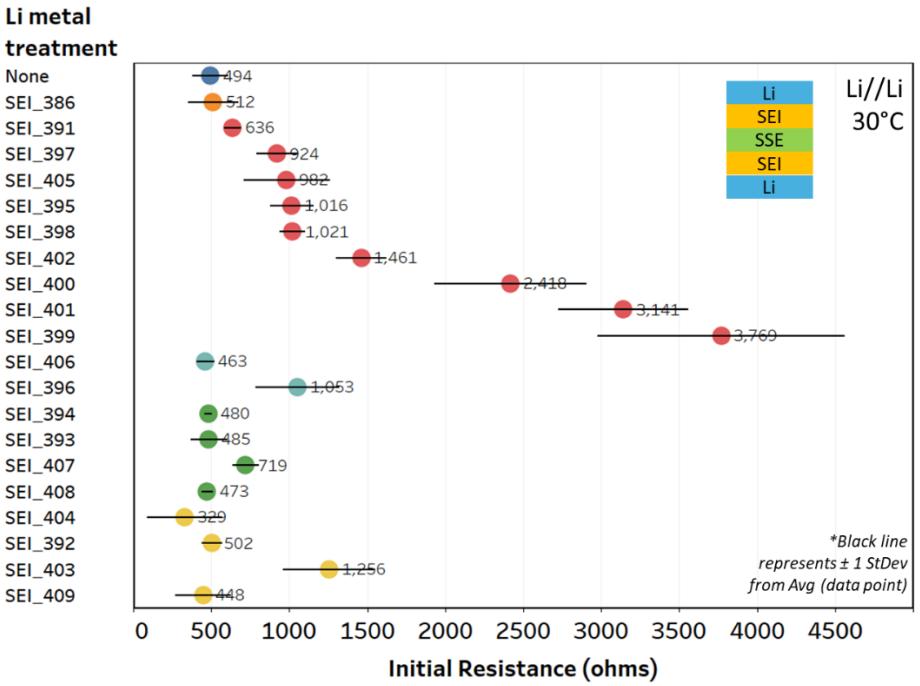

Figure 16. Electrochemical impedance spectroscopy of Li/Li symmetric cells using a solid-state electrolyte composite electrolyte with and without Li-metal protection. The cell format is shown in the top right. The average of multiple cells is shown as a colored circle, the average resistance is labeled, and the black line represents ± 1 standard deviation from the average. The various colors represent various families of additives tested (legend not shown).

Preparation of Composite Cathodes

This quarter, Wildcat began screening the integration of the SE components into the cathode composite film. The goal is to minimize the cathode / ceramic PE interface. Figure 17 shows a schematic comparing the material compositions of a conventional cathode and a catholyte, which includes the components from the ceramic PE. The use of a catholyte instead of a conventional cathode not only lowers the interfacial resistance, but also increases the accessible sites for Li^+ ions in the electrode; this therefore enhances the electrochemical performance of the SSB to a greater extent. In this context, Wildcat has begun testing several combinations of catholyte materials and the mixing conditions used to prepare them.

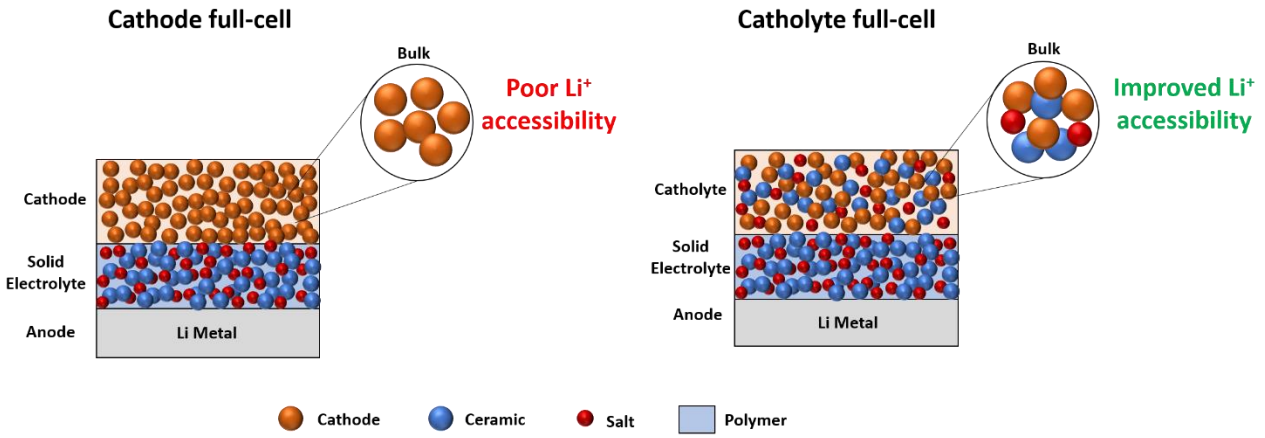

Figure 17. Schematic comparing the structures of cathode and catholyte full cells and the possible extents of their Li⁺ accessibilities.

To establish a baseline for the performance of composite cathodes, Wildcat conducted cycling tests of NMC cathodes with no SSE integrated into them. Lithium metal was used as the anode; the composite electrolyte was sandwiched between the lithium metal and the NMC cathodes. The effects of the surface treatment of the lithium metal and cathodes were also explored. A cell with the LE was used as the control. All the cells were cycled at a rate of C/20 in the voltage range of 3.0-4.3 V and at a temperature of 60°C. As shown in Figure 18a, prior to cycling, the open circuit voltage (OCV) of all the cells remained stable for a period of 12 hours. However, on cycling, it was observed that none of the solid-state cells were able to attain the charge cutoff of 4.3 V, as shown in Figure 18b. This poor performance of the baseline cathodes further cements the need for the addition of SSE into cathode to obtain catholytes.

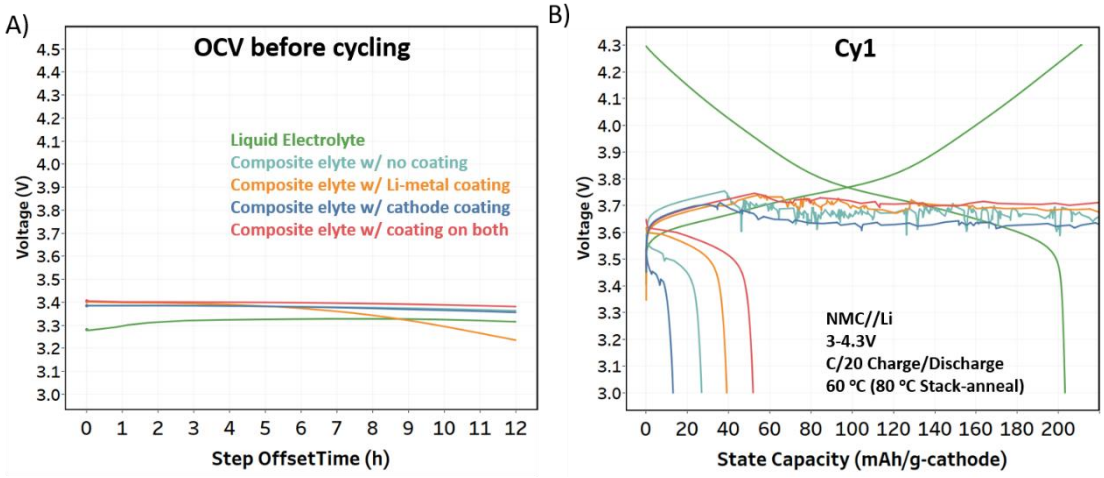

Figure 18. (a) Plot showing the evolution of the open circuit voltage of the solid-state Li//NMC cells with baseline cathodes, prior to cycling. (b) First-cycle charge/discharge voltage profiles of the solid-state Li//NMC cells with baseline cathodes.

As for catholyte composition, although the team would start by integrating this down-selected composite electrolyte with the cathode active material, they also intend to screen several other combinations of polymer, ceramic SSE, and salt with the NMC active material. To maintain the energy density advantage expected of all-solid-state batteries (ASSBs), it is desirable to have the cathode loading high (> 60 wt%) and the electrolyte wt% (< 30 wt%) low in the catholyte. However, to also obtain a reasonably good capacity retention, it is important to have an electrolyte loading that is high enough to mimic the intimate contact and accessibility seen in LE cells. Wildcat aims to test a wide range of electrolytes (5 – 50 wt%) in the catholyte to determine the optimal amount that balances energy density and capacity retention of the all-solid-state full cells.

Mixing processes and post-synthesis processing steps such as thermal annealing and stack annealing play a crucial role in improving the contact between the catholyte and the SSE. Efforts will also be made to optimize the mixing and annealing conditions used in preparing the catholyte blends.

In addition to testing the as-synthesized NMC catholytes, Wildcat will also screen coating materials to be applied on the interface between the catholyte and the SSE. Surface coating is an approach adopted to fill the voids at the cathode/electrolyte interface (CEI) using a Li^+ conductive material, and to minimize the transition metal (TM) dissolution from the cathode. Typically, used cathode coating materials include oxide materials such as Li_3BO_3, ZrO_2, $Zr_2P_2O_7$, and TiO_2. This approach has generally led to an improved interface and higher capacities in the all-solid-state cells, and therefore in the following quarter, Wildcat plans to test several coating materials to improve the performance of the catholyte-based Li//NMC full cells.

Preparation of Composite Electrolyte

This quarter, significant effort was made to optimize the high ceramic loading composite film—specifically aimed at improving the film composition, high-viscosity (HV) stability, processability, and mechanical properties. In terms of the HV stability, Wildcat screened several different polymer types; Figure 19a shows linear sweep voltammetry (LSV) plots for down-selected candidates. The LSV plots shows that the PVDF-polymer with and without the inorganic ceramic has the best HV stability. The PEO-based composite electrolyte shows the current reaction starting to proceed around 3.4 V, and then higher reactivity above 4.3 V. Based on this work, the team continued to develop the composite ceramic PE with PVDF instead of PEO. After testing the voltage stability, they also screened different concentrations of the lithium salt (Figure 19b). As shown, as the team increases the salt concentration to 32 wt% for the PVDF polymer composite system, they can obtain the highest ionic conductivity, reaching close to that of the LATP control. Work is being conducted to improve the ionic conductivity further through the use of coupling agents to minimize the interfacial impedance between the ceramic and PVDF polymer. Next, the team investigated several compositions of the PVDF polymer based composite electrolyte for their electrochemical and mechanical properties. Figure 20a shows that as the team increases the polymer concentration, they decrease the ionic conductivity of the composite electrolyte, while maintaining the same ceramic loading content. Alternatively, Figure 20b shows that as they increase the polymer concentration, they improve the sheer modulus of the films. The results suggest that there is an interplay between the ionic conductivity and the mechanical properties of the composite SE material.

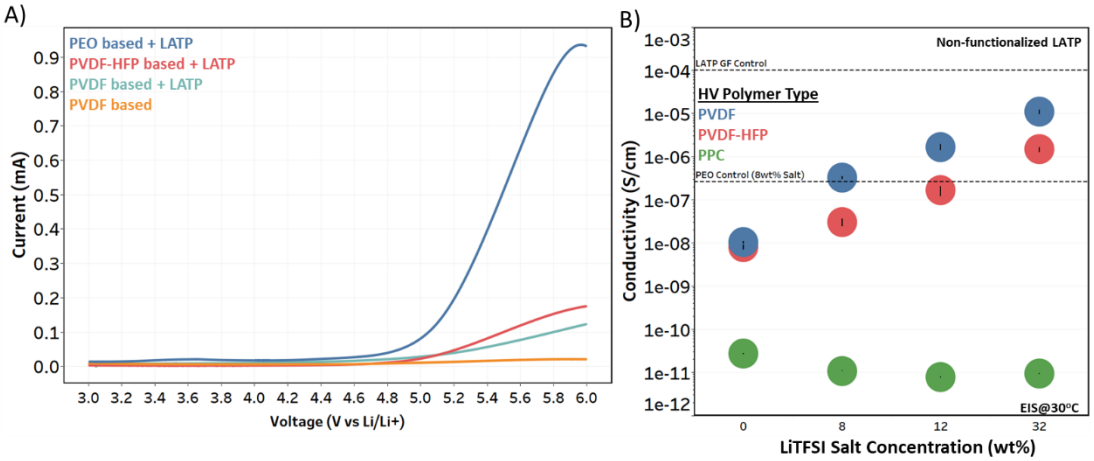

Figure 19. (a) Linear sweep voltammograms of different polymer-based composite electrolytes. (b) Ionic conductivity (30°C) results for various high-viscosity polymers with increasing salt concentration.

Following this work, next quarter the team will focus on improving both the ionic conductivity and mechanical properties of the PVDF-based polymer ceramic electrolyte through the introduction of coupling agents as well as plasticizers to help tether the ceramic and polymer while lowering the interfacial impedance.

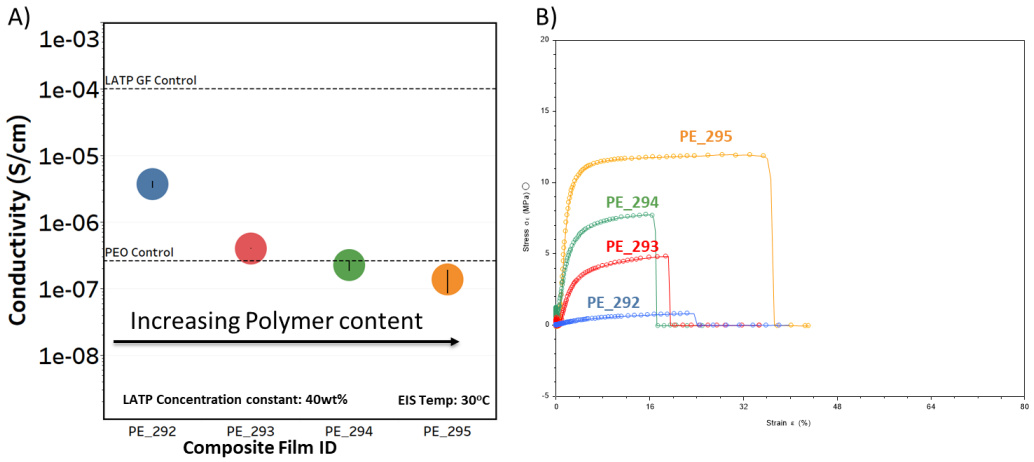

Figure 20. (a) Ionic conductivity (30°C) as a function of increasing PVDF polymer content. (b) Representative sheer modulus plots.

Patents/Publications/Presentations

The project has no patents, publications, or presentations to report this quarter.

Task 1.7 – Physical and Mechano-Electrochemical Phenomena of Thin-Film Lithium-Ceramic Electrolyte Constructs
(Jeff Sakamoto, University of Michigan)

Project Objective. While a small number of SEs exhibit high ionic conductivity (~ 1 mS cm at 298 K), few are stable against lithium metal. The garnet-type SE, based on the nominal formula LLZO, is unique in that it is a fast ion conductor and—as demonstrated in the team's recent project (DE-EE-00006821)—is stable against lithium. Moreover, the team's former project successfully demonstrated a decrease in Li-LLZO interface resistance from 12,000 to 2 Ohms cm^2 and stable cycling at 1 mA cm^2 for 100 cycles (± 15 µm of lithium per cycle). Although the past project demonstrated that LLZO is a viable SE for enabling batteries using metallic lithium, the studies used thick pellets (1 mm) and thick anodes (~ 500 µm). The goal of this project is to acquire a deep fundamental understanding of the physical and mechano-electrochemical phenomena that control the performance of cells consisting of thin LLZO (~ 10 µm), thin lithium anodes (~ 20 µm), and thin solid-state composite cathodes.

Project Impact. If successful, the project will gain knowledge to guide closely related commercialization efforts to scale the production of LLZO-based SSBs.

Approach. The team believes that to achieve a step increase in technology readiness level (TRL), the same performance characteristics previously shown should be demonstrated in technologically relevant cells, for example, thin LLZO and thin lithium.

Out-Year Goals. The out-year goals involve the following: custom thin-film composite (TFC) development, preliminary cycling studies, Vis cell development, lithium cycling, and polymer gel electrolyte screening.

Collaborations. This project collaborates with Professors N. Dasgupta and D. Siegel of UM, Mechanical Engineering.

Milestones

1. Initial design, fabrication, testing, and optimization of custom *operando* optical visualization cell. (Q1, FY 2021; Completed)

2. Initial integration of precision micro reference electrodes with thin lithium and TFC for 100 cycle tests. (Q2, FY 2021; In progress)

3. In thin lithium and thin LLZO TFC, determine the max cycling rates versus lithium thickness ranging between 2 – 17 µm. (Q2, FY 2021; In progress)

4. Refinement of custom *operando* optical visualization cell to quantify topographic lithium plating homogeneity versus cycle number. (Q4, FY 2021; In progress)

Progress Report

Co-principal investigator (PI) Dasgupta and his team have developed a platform for *operando* video microscopy of *in situ* anode formation and Li-metal cycling. The new platform will enable them to quantitatively track changes in the 3D morphology of the Li-metal anode during initial anode formation and during extended cycling. These changes will be linked to the electrochemical signatures; coupled with *ex situ* characterization, they will provide valuable insights into the evolution of Li-metal/SE interfaces during extended cycling. This, in turn, will enable prediction of long-term cell performance, accelerating the optimization process.

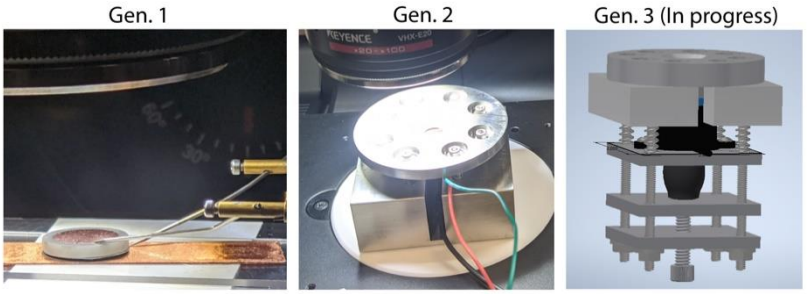

Figure 21. Photographs of generation 1 and 2 *operando* optical cells, and CAD model of new design being fabricated.

In developing the *operando* microscopy platform, special care was taken to ensure that the cell geometry, stack pressure, and electrochemical performance match those of standard *ex situ* experiments. The design has been iterated (Figure 21) based on preliminary results (Figure 22) to achieve these goals, and a 3rd generation cell is being fabricated. The electrochemical behavior (voltage curves and impedance spectroscopy) in the *operando* cells is consistent with the team's other test platforms, and thus should provide representative insights into cell performance moving forward.

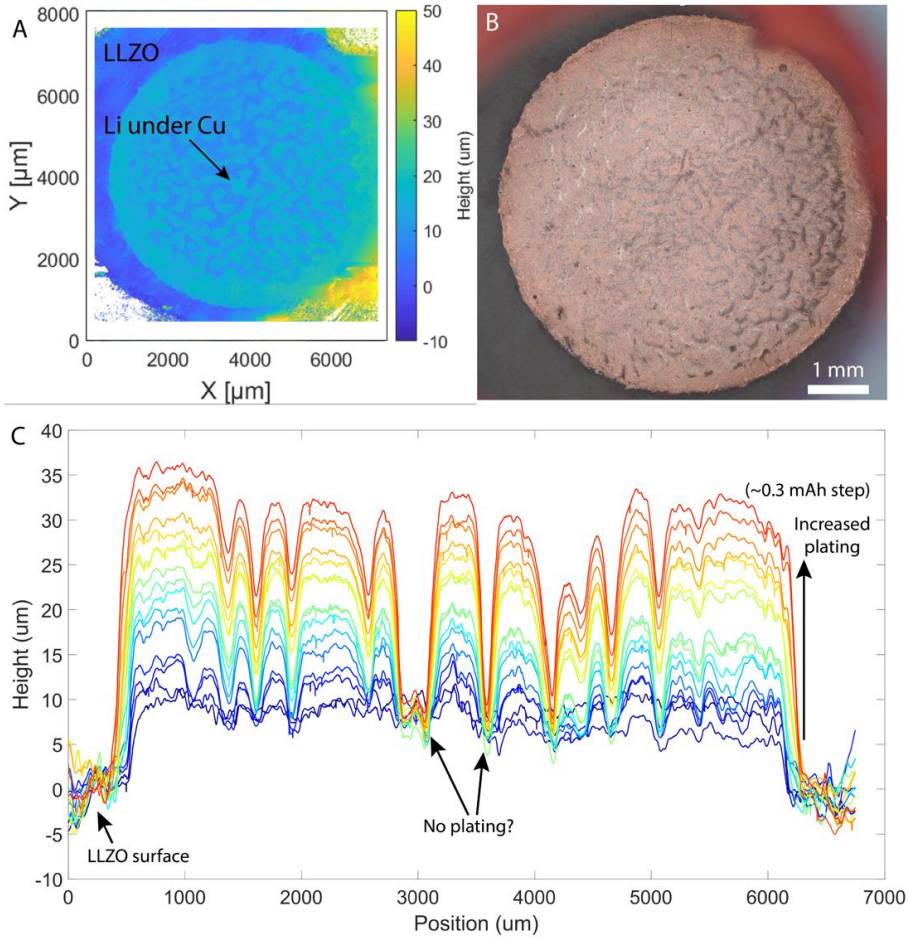

Figure 22. Preliminary results from *operando* optical cells showing (a) height map of electrode after 2 mAh/cm² of plating, (b) optical image of same electrode, and (c) series of height profiles along diameter of electrode for increasing amounts of lithium plating. Thickness of initial copper current collector was ~ 10 µm.

Patents/Publications/Presentations

Presentations

- Materials Research Society (MRS) Spring/Fall 2020 Meeting, Virtual (November 27 – December 4, 2020); J. Sakamoto. Keynote.
- Advanced Automotive Battery Conference (AABC) Meeting, Virtual; J. Sakamoto. Invited.
- ISU, Department Seminar, Virtual; J. Sakamoto; Invited.

Task 1.8 – Lithium Dendrite-Free Li_7N_2I-LiOH Solid Electrolytes for High-Energy Lithium Batteries (Chunsheng Wang, University of Maryland)

Project Objective. The objective of this project is to research, develop, and test Li-metal-based batteries that implement solid Li-ion conductors (LICs) equipped with Li_7N_2I-LiOH SE capable of achieving cell performance of 350 Wh/Kg energy density for 1000 cycle life with a cost of ≤ $100/kWh.

Project Impact. Lithium dendrite growth during charge/discharge cycles limits the use of ASSBs. A criterion for lithium dendrite suppression that is developed through systematical investigation on thermodynamics and kinetics of lithium dendrite growth will guide the electrolyte design. Li_7N_2I-LiOH and Li_3YCl_6 SE with high ionic conductivity and low electronic conductivity will be used to validate the criterion for lithium dendrite suppression, to achieve the project objective.

Approach. The team will establish the relationship among interface energy, lithium plating/stripping overpotential, interface resistance, SE stability with lithium, and CCD. The dendrite suppression criterion will be developed based on the relationship. The dendrite suppression capability for the Li_7N_2I-LiOH pellet will be evaluated by testing the CCD.

Out-Year Goals. The project will study the thermodynamics and kinetics of lithium dendrite growth in SSEs and develop lithium dendrite suppression criterion in SSEs. The Li_7N_2I-LiOH electrolytes and Li_7N2I-LiOH/Li_3YCl_6 bi-layer electrolytes will used to validate the developed dendrite suppression criterion and support NCM cathodes.

Collaborations. There are no reported collaborations this quarter.

Milestones

1. Determine COP of Li_7N_2I-LiOH, LPS, and LLZO electrolytes. (Q1, FY 2021; Completed)
2. Develop lithium dendrite suppression criterion for SEs. (Q2, FY 2021; In progress)
3. Develop a kinetics model of SSEs. (Q3, FY 2021; In progress)
4. Critical current of Li_7N_2I-LiOH electrolytes should be > 4 mA/cm^2 at 3 mA/cm^2 of current. (Q4, FY 2021)

Progress Report

Develop Concept of Critical Overpotential (COP)

COP is a more representative criterion for the lithium dendrite suppression capability for an electrolyte. Figure 23 shows the 1D basic electrode charge-transfer kinetic model near lithium anode based on the Butler-Volmer equation and its corresponding spatially dependent potential distribution. Here, $x = 0$ means the Li|SSE interface, while $x > 0$ stands for inner SSE. At the distance to anode of x, the stress, concentration of species i, and interface energy against lithium metal are defined as $P(x)$, $C_i(x)$, and $E_{inter}(x)$, respectively. The stress, which is related to the density and modulus of the SSE, increases the overpotential for lithium whisker growth. The interface energy provides an energy penalty for lithium deposition in SSE. The SSE potential reduces near to lithium metal because of the compact double layer (Stern layer) and polarizing of the mobile charge carrier distributions. The thermodynamic equilibrium potential at lithium metal is defined to be E_{Li}^0, while SSE at the distance to lithium anode of x is $E_{SSE}^0(x)$. Thus, the potential difference between the SSE and lithium is $\varphi_{Li}^{SSE}(x) = E_{SSE}^0(x) - E_{Li}^0$. Generally, SSEs are electronic insulators that block the flow of electrons between SSE and Li-metal electrode, but they are ionic (Li^+) conductors. Hence, at thermodynamic equilibrium condition, electrochemical potential of Li^+ ($\tilde{\mu}_{Li^+}$), which equals to lithium atomic chemical potential (μ_{Li}) minus electron electrochemical potential (-eφ), reaches to 0, that is, $\tilde{\mu}_{Li^+} = \mu_{Li} - (-e\varphi) = 0$. The μ_{Li} in the SSE thus equals to $-e\varphi_{Li}^{SSE}(x)$. However, since most of the SSEs are not stable against lithium metal, SEI layer will form between the lithium and SSE, as shown in Figure 23b. If the SEI is electronic and ionic mix conductor layer, the μ_{Li} in the SSE should be equal to that in lithium metal, that is, 0 eV.

According to the Butler-Volmer model, the lithium plating current on lithium metal (Figure 23c, black lines) is related exponentially to the overpotential η. That is,

$$i_{Li} = FAk^0\left[C_{Li^+}(0,t)e^{-\alpha f\eta} - C_{Li}(0,t)e^{(1-\alpha)f\eta}\right]$$

where F, A, k^0, α, and f are the Faraday constant, frequency factor, standard rate constant, transfer coefficient and F/RT (R is gas constant and T is temperature), especially. The potential in SSE changes from E_{SSE}^0 to E_{SSE}, resulting in an overpotential $\eta_{SSE} = E_{SSE} - E_{SSE}^0 = \gamma \cdot \eta$ in SSE (Figure 23c, blue dashed lines), where γ is the overpotential transfer coefficient, which is related to the electronic conductivity of the SSE. Moreover, the stress P and interface energy E_{inter} in the SSE will raise an opposite overpotential for lithium deposit. The stress P is linearly with the overpotential by $\eta_{stress} = P \cdot V_m/F$, where V_m is the molar volume of lithium metal. Thus, the lithium plating current in SSE i_{SSE} is

$$i_{SSE} = FAk^0\left[C_{Li^+}(x,t)e^{-\alpha f(-\mu_{Li}^{SSE}(x)+\gamma\cdot\eta)} - C_{Li}(x,t)e^{[(1-\alpha)f(-\mu_{Li}^{SSE}(x)+\gamma\cdot\eta)+P_{Li}^{SSE}(x)\cdot V_m+E_{inter}]}\right]$$

Considering the dendrite free situation, the i_{SSE} should be infinitely close to 0; thus,

$$C_{Li}(x,t) = C_{Li^+}(x,t)e^{-[f(-\mu_{Li}^{SSE}(x)+\gamma\cdot\eta)+P_{Li}^{SSE}(x)\cdot V_m+c]}$$

Based on the equation, the summation of the overpotential should be as positive as possible to avoid dendrite formation, requiring low electronic conductivity, high density and mechanical strength, and interfacial energy.

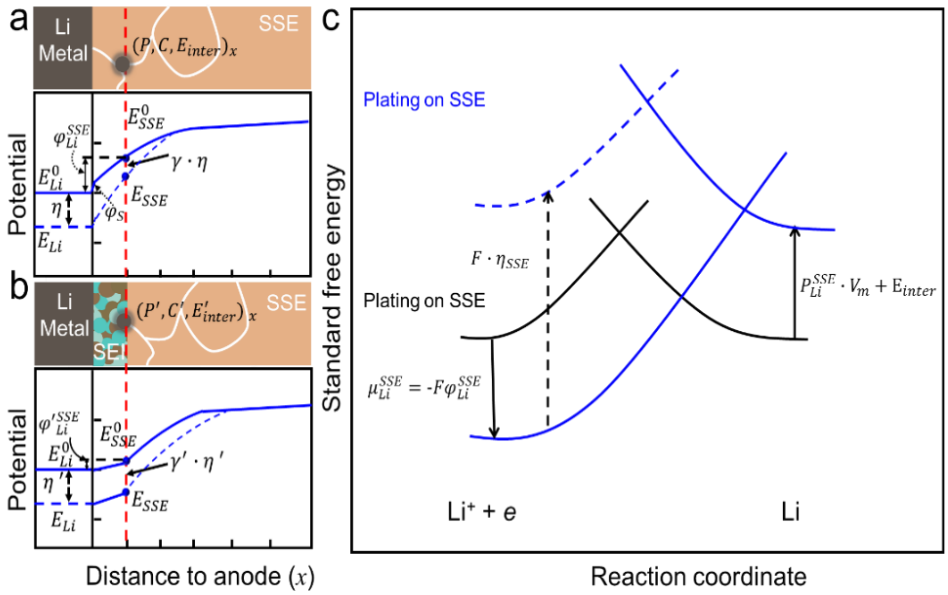

Figure 23. 1D battery model near anode and its corresponding spatially dependent potential distribution in (a) stable and (b) unstable solid-state electrolyte (SSE). (c) Effects of a potential change on the standard free energy of activation for oxidation and reduction on lithium metal (black lines) and SSE (blue lines).

Here, the μ_{Li}^{SSE}, P_{Li}^{SSE}, and P_{Li}^{SSE} are the intrinsic properties of SSEs. The applied η is considered as a disturbance that is required as small as possible. Since the team has concluded that the summation of the overpotential should be as positive as possible to avoid dendrite formation, it is critical to determine the η for the SE. By determining the COP, the dendrite intrinsic suppression capability of different SSEs can be evaluated. This quarter, the team shows that origin from the above model; the criterion can be further determined from electrochemical data of a certain cell in reality and can direct the team to find the more suitable SSE to resist the notorious lithium dendrite.

Determine COP of LLZO, LPS, and Li_7N_2I-LiOH

First, the team demonstrated COP with a commonly used oxide SE LLZTO ($Li_{6.5}La_3Zr_{1.5}Ta_{0.5}O_{12}$). Figure 24a shows the as-synthesized LLZTO electrolyte pellet has a total ionic conductivity ~ 6.04 x 10^{-4} S/cm with a relative density of 94%. The particle morphologies distribution of the ceramic particle size by scanning electron microscopy (SEM) is in Figure 24b, which demonstrates uniform distribution of grain size. Typically, to decrease interfacial resistance, different elements (A, B, C, and D) were added to molten lithium to increase the wettability between lithium and LLZTO pellets. The LiC-alloy|LLZTO interface is shown as an example for the well-contacted interface (Figure 24c). The EIS and Bode plots (Figure 24d-e) for a LiC| LLZTO |LiC cell also indicate a decent contact between lithium and LLZTO electrolyte. The optical picture of shorted LLZTO shows lithium dendrite penetrate a SSE (Figure 24f).

Four LiX|LLZTO|LiX cells with four types of different surface modifications were assembled. Here, the same batch of LLZTO pellets with the same thicknesses and diameters was used. As shown in Figure 25, the cells with surface modifications of A, B, C, and D deliver COPs as 0.18, 0.20, 0.16, and 0.15 V, respectively. The COP varies within a small region between 0.15-0.18 V. In contrast, the CCDs are much more discrete. The team believes the COP of an electrolyte should be a criterion for the lithium dendrite suppression capability for the following reasons: (1) it is an intrinsic parameter of the SE, as evidenced by a fixed number for SE; (2) the COP represents the largest overpotential that can be applied to the SSE without electrolyte decomposition and dendrite formation, which indicates the thermodynamic dendrite suppression capability of the SSE at a material level; and (3) it correlates to the parameters that control lithium dendrite growth, such as electronic conductivity, density, mechanical strength, and interfacial energy.

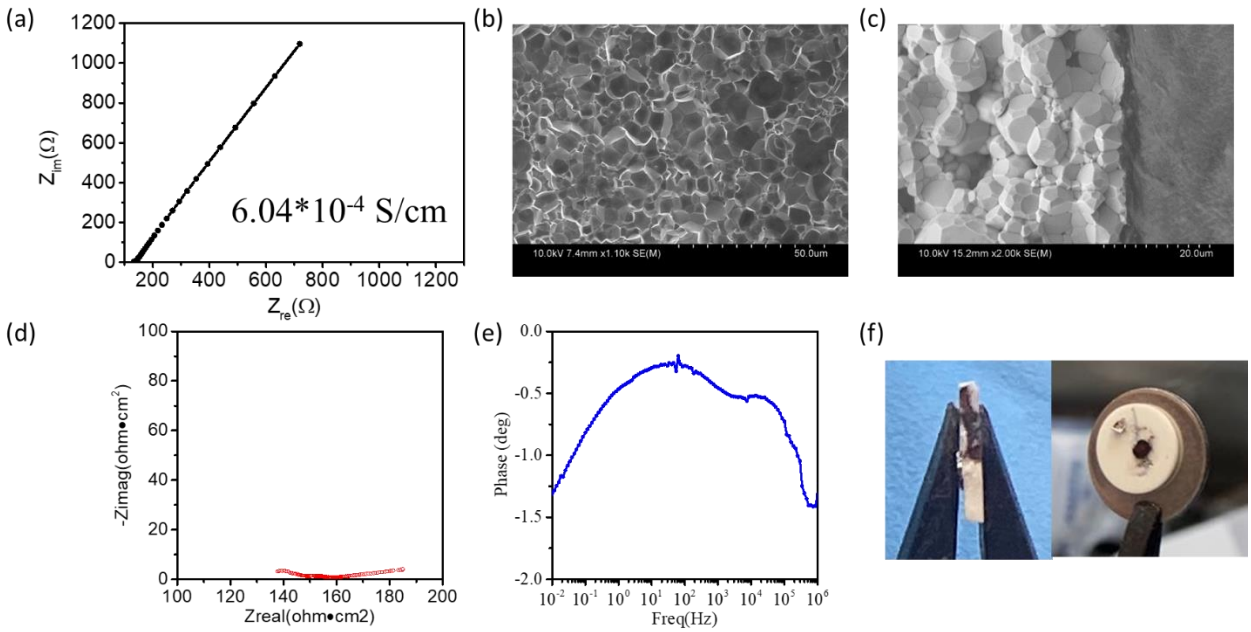

Figure 24. Electrochemical properties of LLZTO solid electrolyte pellet. (a) Electrochemical impedance spectroscopy (EIS) plot of Au|LLZTO|Au cell and calculated total ionic conductivity. (b) Particle morphologies distribution. (c) Scanning electron microscopy of Li-alloy|LLZTO interface. (d) EIS plot and (e) Bode plot for a LiC|LLZTO|LiC cell. (f) Optical picture of shorted LLZTO.

Moreover, the COPs of typical sulfide SSEs (Li_3PS_4 and Li_6PS_5Cl) have also been determined by the step-increase current plating and stripping process, which is also used for CCD (Figure 26). The determined CCD for Li_3PS_4 and Li_6PS_5Cl are 0.4 and 0.7 mA/cm^2, respectively. The determined CCD is similar to those reported values. The determined COPs are 0.065 V and 0.03 V for Li_3PS_4 and Li_6PS_5Cl SSEs. The COPs are much lower than those of LLZTO electrolytes, which can be related to the higher instability of the sulfide electrolytes. At small overpotential, the side reaction between lithium and sulfide electrolyte takes place and results in cracks and interphases with low interface energy against lithium metal.

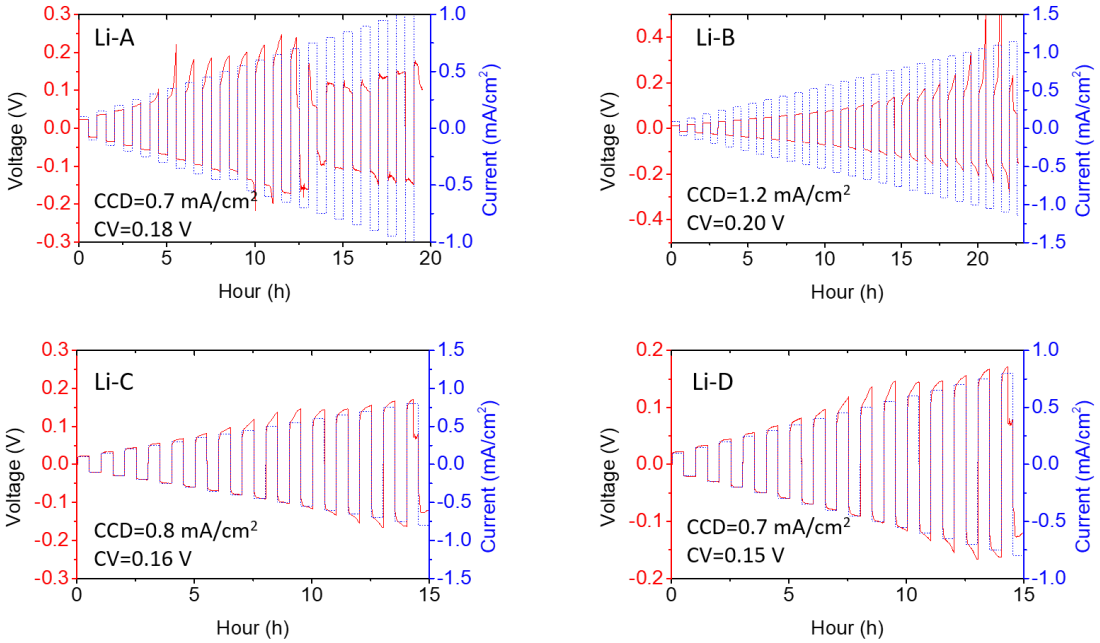

Figure 25. Lithium plating/stripping behaviors for the LiX|LLZTO|LiX cells at a step-increase current for 0.5 hours. Four cells with four different surface modifications of A, B, C, and D. The determined critical current density and critical overpotential are listed.

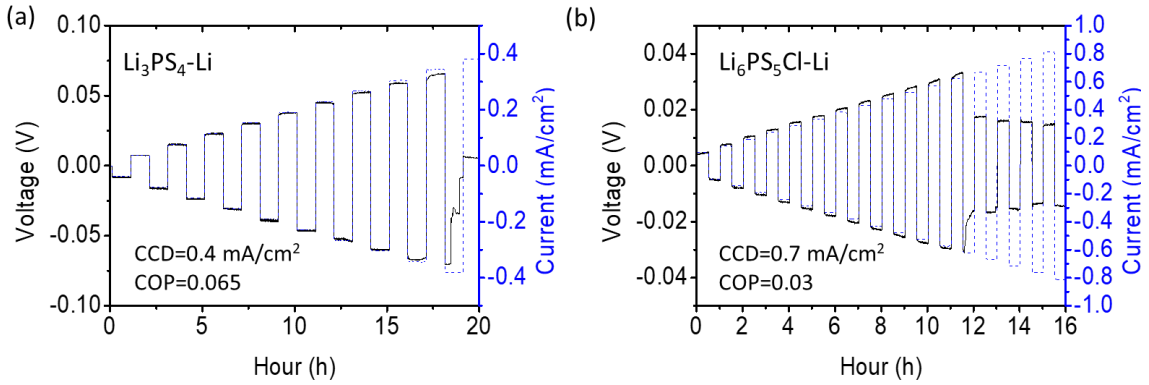

Figure 26. Lithium plating/stripping behaviors for the Li|Li_3PS_4|Li and Li|Li_6PS_5Cl|Li cells at a step-increase current for 0.5 hours. The determined critical current density and critical overpotential are listed.

The COP of Li_7N_2I-LiOH was further investigated. The size of the SSE pellet is the same as the above-tested oxides and sulfides. As shown in Figure 27, the COP is higher than 1.0 V, which is more than 10 times the COP of LLZTO. This may originate from its intrinsic stability with lithium metal. Figure 27b shows the box chart for the determined CCD and COP for different SSEs. The distribution of measured CCD of LLZO and LPS is more dispersed than that of COP, which indicates that COP is a more reliable indicator to reveal the intrinsic dendrite suppression capability of different SSEs at various situations.

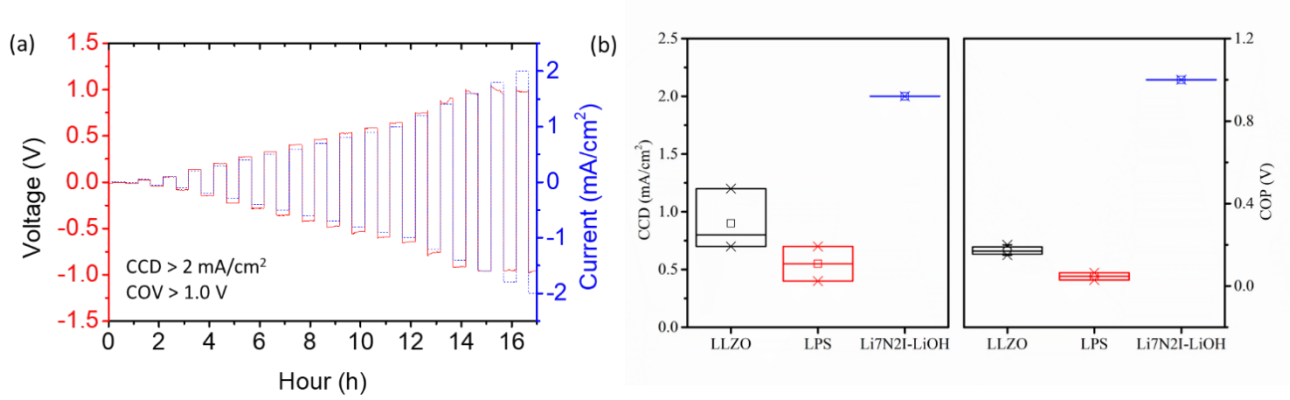

Figure 27. (a) Electrochemical behaviors of Li_7N_2I-LiOH measured with the Li|Li_7N_2I-LiOH|Li cells and Li|Li_5NI_2-LiOH|Li symmetric cell using a carbon-based intermediate layer. The critical current density (CCD) measurement for Li|Li_7N_2I-LiOH|Li cell at step-increase current with a constant charge/discharge time of 0.5 hours. (b) Box chart for the determined CCD and critical overpotential of different solid-state electrolytes.

Patents/Publications/Presentations

The project has no patents, publications, or presentations to report this quarter.

Task 1.9 – Low Impedance Cathode/Electrolyte Interfaces for High-Energy-Density Solid-State Batteries (Eric Wachsman and Yifei Mo, University of Maryland)

Project Objective. The project objective is to research, develop, and test Li-metal-based batteries that implement solid LICs equipped with NMC cathodes integrated into the Li-metal/LLZ tri-layer architecture. Specifically, the team will achieve the following: (1) identify and demonstrate interfacial layers to achieve low-impedance and stable NMC/LLZ interfaces; (2) develop novel processing techniques to fabricate NMC/LLZ composite cathodes with low interfacial resistance; and (3) enable high-performance ASSBs with an energy density of 450 Wh/kg and 1400 Wh/L and negligible degradation for 500 cycles.

Project Impact. Instability or high resistance at the interface of high-energy cathode materials with Li-garnet SEs limits the high-energy-density all-solid-state lithium battery. This project will lead to a fundamental understanding of solid-electrolyte/solid-cathode interfaces and a unique and transformative LLZ framework to enable high-energy-density, safe Li-metal batteries approaching ~ 400 Wh/kg.

Approach. In this new project, the team will build on their demonstrated expertise with garnet electrolytes and ASSB cells to accomplish the following: (1) engineer interfaces to overcome high NMC/LLZ interfacial impedance and interfacial degradation; (2) develop processing and fabrication techniques to achieve high-loading NMC/LLZ composite cathodes with low resistance and high cyclability; and (3) integrate the NMC/LLZ cathodes into all-solid-state Li-metal/LLZ cells to achieve high-energy-density batteries.

Out-Year Goals. The project will solve the current challenges of integrating garnet SE with a cathode to achieve a high-performance ASSB using a high-energy-density Li-metal anode. The resultant high energy density and stability using both high-energy-density Li-metal anodes and NMC cathodes will open new applications in portable electronics, EVs, and beyond.

Collaborations. This project funds work at UMD. The PI, E. Wachsman, will have management responsibility and will lead experimental efforts including garnet synthesis, interface processing, cell fabrication, and testing. The Co-PI, Y. Mo, will lead computational efforts on understanding stability between garnet and cathode and on identifying promising coating materials. No collaborations are reported this quarter.

Milestones

1. Computationally determine interfacial stability between LLZ SEs and NMC cathode. (Q2, FY 2020; Completed)
2. Determine thermochemical stability between LLZ and infiltrated NMC. (Q3, FY 2020; Completed)
3. Computationally determine the mechanism of interfacial stabilization between LLZ and NMC through coating layers. (Q3, FY 2020; Completed)
4. *Go/No-Go Decision*: Computationally determine appropriate compositions to stabilize the LLZ-NMC interface. Achieve design capable of meeting performance requirements. (Q4, FY 2020; Completed)

Progress Report

XRD experiments were further performed on composite pellets of Ta-doped LLZO (LLZTO) and the NMC-532 cathode material (1:1 in weight ratio) prepared by physical mixing, mold pressing, and co-sintering at 500-1000°C for 3 hours. Similar to other NMCs investigated previously, NMC-532 started to react with LLZTO at 600°C with formation of $La_2Zr_2O_7$ and $La_2Li_{0.5}M_{0.5}O_4$ (M= Ni or Co). The difference is that these new phases have lower intensity for NMC-532 compared to compositions with higher nickel contents, for example, NMC-811 and NMC-622 (Figure 28). This suggests a trend for increasing reactivity with LLZTO with increasing nickel content.

The reactivity of NMCs with LLZTO was further investigated by DSC of the powder mixture. All NMCs show an endotherm peak at 700°C (Figure 29), corresponding to a kinetically slow reaction with garnet. Most notably, the scan for NMC-811 shows a baseline that continues to increase after 700°C until another large endothermic peak beginning at 900°C emerges. This reaction above 900°C matches the XRD results, indicating there is a strong reaction between NMC-811 and LLZTO. Additionally, this large endothermic peak is similarly observable in the NMC-622 and NMC-532 samples, but has a higher onset temperature with decreasing nickel content. This feature is not observable in the measured temperature range for lower nickel content NMCs. This further supports the trend that NMC and LLZTO react more strongly with increasing nickel content. For this reason, future co-sintering experiments will not use NMC-811 and will limit the maximum co-sintering temperature to 900°C.

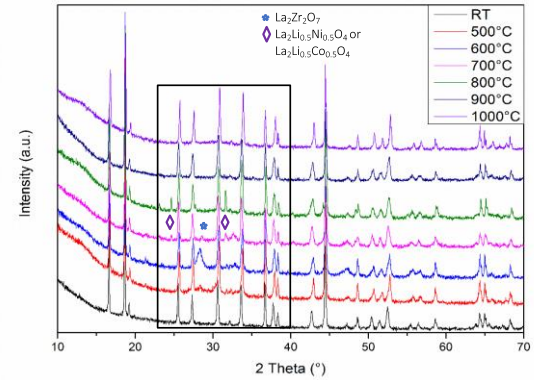

Figure 28. X-ray diffraction patterns of 50/50 w/w mixtures of LLZTO with NMC-532. The boxed region is where the new peaks are appearing.

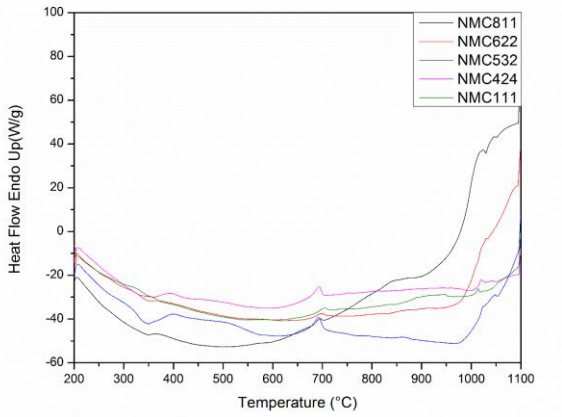

Figure 29. Differential scanning calorimetry curves of 50/50 w/w mixtures of LLZTO with NMCs of various compositions.

To investigate the effect of lithium content on the high-temperature stability of NMC against LLZTO, LLZTO was synthesized with 10% and 40% molar excess lithium and mixed with NMC-111 for XRD and DSC measurement. No new phases were detected by XRD in the mixtures with 40 mol% excess lithium, even after sintering to 900°C (Figure 30a), indicating the reaction between the two materials detected previously was mainly caused by lithium deficiency at high temperature. In the DSC curve (Figure 30b), a small endotherm peak at 400-500°C corresponding to the melting of LiOH (m.p. 462°C) can be detected for the mixture with higher lithium content. The endotherm peak detected at 700°C for the mixture with 10% excess lithium LLZTO is missing for the mixture with 40% excess lithium LLZTO, indicating the endotherm reaction is related to the loss of lithium at high temperature.

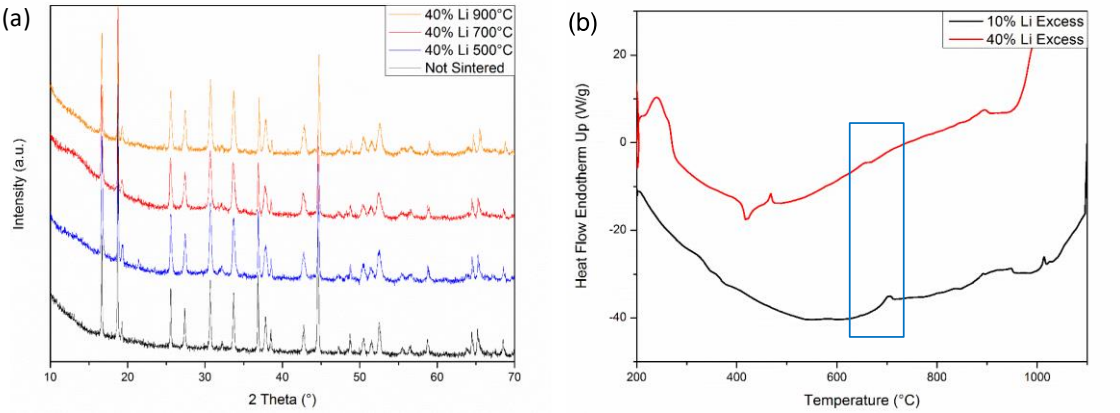

Figure 30. (a) X-ray diffraction and (b) differential scanning calorimetry curves of 50/50 w/w mixtures of LLZTO (with 10 mol% or 40 mol% excess lithium) with NMC-111.

Patents/Publications/Presentations

The project has no patents, publications, or presentations to report this quarter.

Task 1.10 – Developing an *In Situ* Formed Dynamic Protection Layer to Mitigate Lithium Interface Shifting: Preventing Dendrite Formation on Metallic Lithium Surface to Facilitate Long Cycle Life of Lithium Solid-State Batteries
(Deyang Qu, University of Wisconsin, Milwaukee)

Project Objective. The objective of this project is to research, develop, and test Li-metal-based batteries that implement solid LICs equipped with a formed dynamic protection layer. The proposed project aims to enable safe, long-cycle lithium anodes to achieve cell performance targets of 400 Wh/Kg, over 100 cycles, with 15-year shelf life and < $100/KWh cost.

Project Impact. Project efforts are to contribute an in-depth understanding of the lithium interface and dendrite growth prevention to the field of Li-metal batteries, which will pave the way for eventual development of high-energy-density, low-cost, and long-lasting lithium batteries. This advancement could be a crucial selling point for the greater adoption of EVs. This project will make possible the translation of fundamental research into practical implementation of high-energy lithium anodes, enabling eventual achievement of cell performance targets.

Approach. The novelty of this approach is that the team intends to mitigate the dendrite problem by creating a dynamic protection layer during the interface shift to prevent dendrite formation throughout battery operation.

Out-Year Goals. The project has three out-year goals: (1) *in situ* diagnostic tools are fully functional; (2) potential candidates for Li-anode modifications are identified; and (3) synthesis routes are designed.

Collaborations. The PI is the Johnson Control Endowed Chair Professor, who has close and frequent collaboration with Johnson Controls' scientists and engineers. The collaboration enables the team to validate the outcomes of fundamental research in pilot-scale cells. The PI also has been working closely with top scientists at Argonne National Laboratory (ANL), Brookhaven National Laboratory (BNL), LBNL, and Pacific Northwest National Laboratory (PNNL) and with U. S. industrial collaborators, for example, GM, Millipore Sigma, and Clarios. In addition, the team works with international collaborators in China, Japan, and South Korea. These collaborations will be strengthened and expanded to give this project a vision with both today's state-of-the-art technology and tomorrow's technology in development, while incorporating feed-back from the material designers and synthesizers upstream, as well as from the industrial end users downstream.

Milestones

1. Lithium anode electrochemical performance evaluation. Synthesis n-type polymer materials and evaluation of the electrochemical performance. (Q1, FY 2021; Completed)

2. Roll-press coating development. Complete the process development of roll-press coating. (Q2, FY 2021; In progress)

3. PAH derivative structure identified. Identification of the synergy of the parameters and their impact on dendrite growth. (Q3, FY 2021; In progress)

4. Synthesis and test of PE with PAHs. Synthesis of PE with various PAH functionality and test with lithium anode in a half cell. (Q4, FY 2021; In progress)

5. Dendrite suppression demonstrated / interim cell performance verified. Dendrite suppression on coated lithium anode demonstrated, and analysis indicates technical approach capable of achieving performance targets. (Q4, FY 2021; In progress)

Progress Report

This quarter, the team accomplished the following: (1) validated design of cell for long-term cell cycling tests; (2) finalized design of the *in situ* optical cell for real-time observation of dendrite growth at the SSE – lithium interface; (3) down selected SSE for long-term cell cycling; and (4) modified lithium anode for dendrite growth depression.

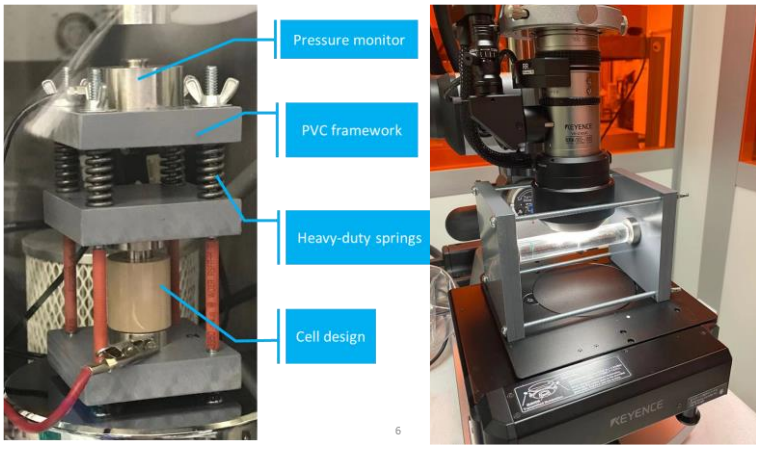

Figure 31. (left) Full cell for cycle testing. (right) *In situ* optical cell.

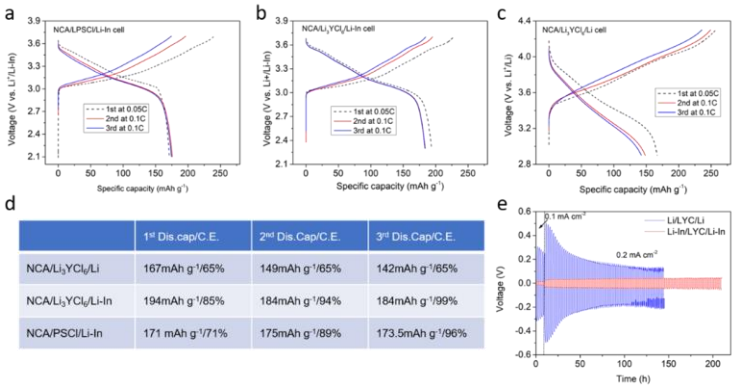

Figure 32. The first three charge/discharge profiles of (a) NCA/LPSCl/Li-In cell, (b) NCA/Li_3YCl_6/Li-In cell, and (c) NCA/Li_3YCl_6/Li cell. (d) A comparison of discharge capacity and Coulombic efficiency between different cell chemistries. (e) Plating/stripping profiles of symmetric cells.

Electrochemical Cells. Figure 31 shows the two validated cells for performance tests (right) and an *in situ* electrochemical optical cell for observing dendrite growth.

SEs and Lithium Anode. The most popular inorganic SEs are lithium thiophosphates, which are good ionic conductors. However, the inherent instability at high potentials limits their application in 4 V batteries. Halide SEs were reevaluated in 2018 by Asano et al. and considered as a potential SE due to their high ionic conductivity and high stability against oxidation. A typical halide SE, Li_3YCl_6, was synthesized and tested in a full cell containing a $LiNi_{0.8}Co_{0.1}Mn_{0.1}O_2$ (NCA) cathode and Li-metal anode. It was demonstrated that the halide/NCA interface is more stable compared to LPSCl/NCA interface, as manifested by the CE (Figure 32d). However, the halide / lithium metal interface is thermodynamically unstable, as confirmed by the NCA/halide/Li and Li/halide/Li cells. The formed SEI layer is a mixed-ionic conductor, which keeps growing and eventually leads to a high resistance. When in contact with lithium metal, Y^{3+} is reduced to Y^0, which can react further to form Y_2O_3 or $Y_2(CO_3)_3$. LiCl is the major component in SEI composite. Therefore, although Li_3YCl_6 superionic conductor is a good SE with oxide cathode (for example, NCA), it is not compatible with metallic lithium anode. The team has found that if Li-In alloy is used as an anode, not only can dendrite growth be suppressed, but Li_3YCl_6 SE also becomes stable.

Patents/Publications/Presentations

The project has no patents, publications, or presentations to report this quarter.

Task 1.11 – Molecular Ionic Composites: A New Class of Polymer Electrolytes to Enable All-Solid-State and High-Voltage Lithium Batteries (Louis Madsen, Virginia Polytechnic Institute and State University)

Project Objective. Based on a newly discovered class of solid PE materials, that is, molecular ionic composites (MICs), the overall objective is to develop solid-state lithium conductors targeted for use in transportation applications. MICs form a mechanically stiff, electrochemically stable, and thermally stable matrix. Specific objectives include the following: (1) development of robust MIC electrolyte thin films (~ 20 μm) to serve as simultaneous nonflammable separators and dendrite-blocking Li^+ conductors, (2) electrochemical quantification of key performance metrics including electrolyte stability, interfacial reactions, and suitability/compatibility with a range of electrode materials, and (3) comprehensive investigation of ion transport mechanisms and electrode-electrolyte interfacial reactivity under practical operating conditions using NMR and synchrotron X-ray analyses.

Project Impact. Commercialization of Li-metal SSBs is hampered by lack of a functional nonflammable SE that can provide high ionic conductivity, wide electrochemical window, favorable mechanical properties to inhibit lithium dendritic growth, and low interfacial resistance. The tunable MIC materials platform has potential to fulfill these requirements with relatively simple fabrication techniques, and thus shows promise for enabling nonflammable SSBs that can be optimized for low cost and high energy density.

Approach. MICs rely on a unique polymer that is similar to Kevlar® in its strength, stiffness, and thermal stability, but with densely spaced ionic groups that serve to form an electrostatic network that permeates mobile ions in the MIC. The team can tailor the ion concentrations and types to yield MIC electrolyte films that are electrochemically compatible with Li-metal anode as well as a range of high-voltage layered cathodes. They are searching the composition space of lithium salts, electrochemically compatible ionic liquids, and polymer (PBDT) molecular weight to determine best composition windows for MIC electrolytes. The team is also investigating best methods for casting thin films in terms of temperature, solvent/evaporation conditions, and control over the initial liquid crystalline gel formation point. Concurrently, they are testing MIC films in various electrochemical cells, quantifying transport and structural/morphology parameters with NMR and X-ray techniques, and measuring key mechanical (dynamic mechanical thermal analysis, stress-strain) and thermal [DSC, thermal gravimetric analysis (TGA)] properties.

Out-Year Goals. This year, the team will further optimize the film casting process to obtain thin MIC electrolyte films, but will focus primarily on detailed electrochemical quantification of key performance metrics including electrolyte stability, interfacial reactions, and suitability/compatibility with a range of electrode materials (with the focus on lithium metal and layered oxides). The team will understand and optimize the oxidative stability and interfacial impedance properties of MIC electrolytes. The team will develop and characterize working battery cells incorporating MIC electrolyte films with various cathode and anode materials, and will work to understand fundamental material compositions and interfacial compatibilities to choose favorable combinations for safe SSBs with high energy density.

Collaborations. The team is collaborating with T. J. Dingemans' group at University of North Carolina, Chapel Hill, in which they are forming composites based on PBDT polymer and carbon materials such as graphene oxide, and are beginning to develop charged rigid-rod polymers building on the PBDT structure. The team is exploring shear rheology and broadband dielectric spectroscopy collaboration with R. H. Colby at PSU. They are collaborating with D. Nordlund at SLAC National Accelerator Laboratory (SLAC) to conduct synchrotron X-ray studies on MIC films.

Milestones

1. Determine optimal synthetic conditions, Li-ion loading, and chemical composition. (Q4, FY 2020 / Q1, FY 2021; In progress)
2. Determine parameter spaces for film formation, and develop design capable of meeting performance requirements for film casting process. (Q2, FY 2021; In progress)
3. Optimize oxidative stability by using NMC/MIC/NMC and Li/MIC/NMC cell platforms to determine the upper limit of cycling voltage. (Q3, FY 2021; In progress)
4. Optimize electrolyte chemistry to achieve minimal interfacial impedance. (Q4, FY 2021)
5. Initial full cell integration and performance evaluation with Li/MIC/NMC and cycling under high current density (CD). (Q1, FY 2022)

Progress Report

This quarter, the team performed a systematic study of the long-term cycling stability of Li/MIC/$LiFePO_4$ cells at elevated temperatures. As shown in Figure 33, the cells can be successfully cycled at 60°C, 100°C, and 150°C with slow capacity decay during cycling. For example, when cycled at 150°C and 1C rate (Figure 33d), the cell shows a discharge capacity retention of 91% after 374 cycles. This clearly demonstrates that the SE used here, which is MIC material with only 10 wt% PBDT, is both mechanically and electrochemically stable at 150°C to enable successful cycling of $LiFePO_4$ batteries. Based on the literature, this MIC electrolyte appears to be the highest temperature polymer-based gel used as a SE for Li-metal battery cycling. Furthermore, this study also directly confirms the excellent cycling stability of $LiFePO_4$ as a cathode material at high temperature. This makes $LiFePO_4$ an ideal cathode material when constructing lithium batteries for wide temperature applications. The battery pack used for EVs usually contains a complex thermal management system to keep the temperature of the batteries within a safe range. Removing this unit by using wide temperature range batteries could be one option for improving energy density of the whole battery pack. This study shows promise for achieving that goal.

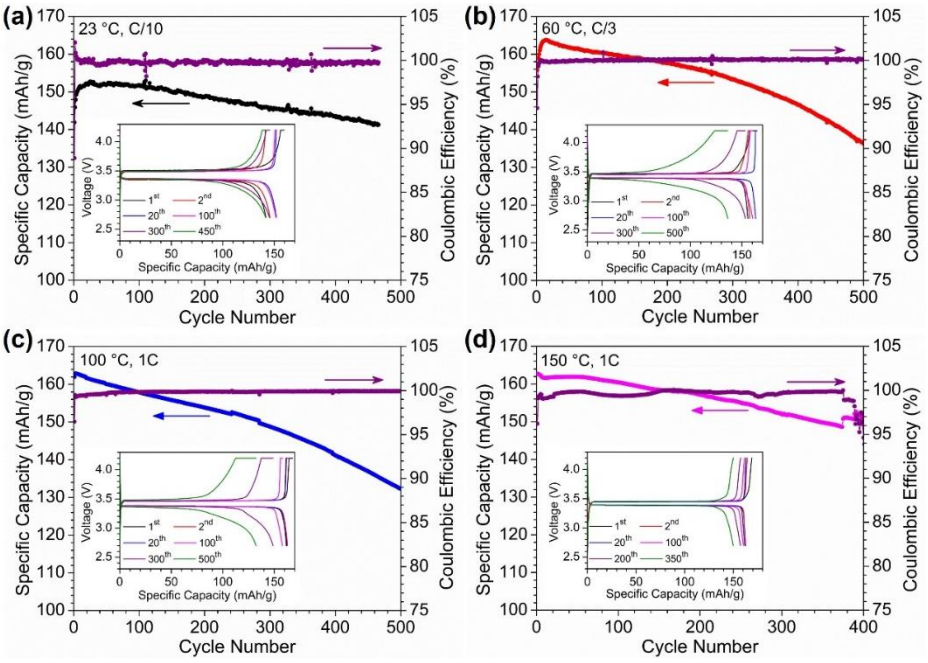

Figure 33. Li/MIC/$LiFePO_4$ coin cells demonstrate strong cycling stability over a temperature range from 23°C to 150°C. Li/MIC/$LiFePO_4$ cycled at (a) 23°C at C/10, (b) 60°C at C/3, (c) 100°C at 1C, and (d) 150°C at 1C. Inset figures are the voltage profile for selected cycles under each cycling condition.

Besides working on $LiFePO_4$ batteries, the team also explored the compatibility of MIC electrolyte with other high working potential cathode materials. Figure 34 shows the cycling performance of Li/MIC/NMC-622 cells at room temperature. The voltage cut-off for the charging process is 4.5 V. The specific discharge capacity and CE for the first cycle are 184 mAh/g and 83%, respectively. The CE is 99.8% for the following cycles, while the specific discharge capacity decays to 105 mAh/g after 200 cycles. This experiment demonstrates that MIC electrolytes are compatible with high working potential cathodes at least up to 4.5 V. Improving the capacity retention of Li/MIC/NMC-622 cells over long-term cycling represents the next major hurdle in this area.

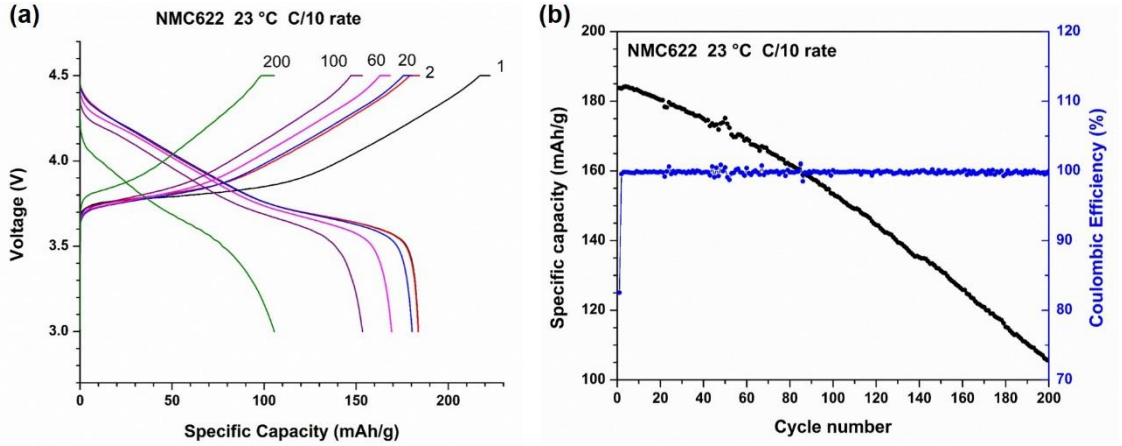

Figure 34. Cycling performance of Li/MIC/NMC-622 cells at 23°C and C/10 rate. (a) Voltage profiles for selected cycles. (b) Change of capacity and Coulombic efficiency during cycling.

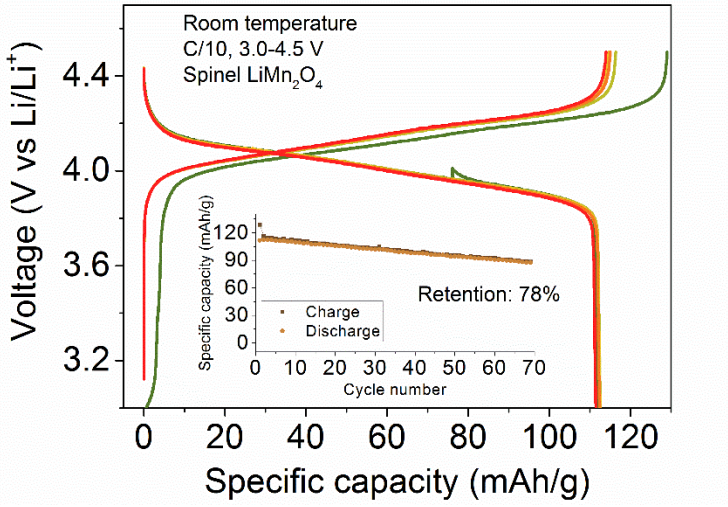

Figure 35. Charge/discharge profiles of the cell built with a spinel $LiMn_2O_4$ cathode, molecular ionic composite electrolyte, and Li-metal anode. The cell was cycled at C/10 in the range 3.0-4.5 V at room temperature. The inset shows specific capacity as a function of cycle number.

In addition, the team has utilized another promising cathode material, $LiMn_2O_4$, to explore its compatibility with the MIC electrolyte. The positive electrode was cast onto aluminum foil with a homogenous slurry containing $LiMn_2O_4$, carbon black, and PVDF in a mass ratio of 90:5:5. The cells were assembled with the positive electrode, MIC electrolyte, and Li-metal anode into CR2032 coin cells. The team first evaluated cell performance at room temperature (Figure 35). The discharge capacity of the cell can reach 112 mAh/g at C/10.

The charge and discharge profiles overlap well in the first several cycles. After 70 cycles, a capacity retention of 78% was achieved. These results indicate that the MIC electrolyte shows compatibility with the spinel $LiMn_2O_4$, which suggests the promise of integrating MICs into batteries with alternative cathode materials.

In summary, this period the team began construction and optimization of full battery cells based on Li-metal anodes and a range of different cathodes (three distinct classes so far). The team is assessing oxidative stability limits and continuing to understand electrochemical features of the MIC electrolytes when combined with different electrodes, including in working cells. Optimizing MIC electrolyte composition and synthetic/casting conditions is continuing in parallel with exploration of full-cell electrode chemistries and cycling parameters. One article is under final (minor) revision based on the results in Figure 33, and another article is under revision concerning development and understanding of the MIC film casting process.

Patents/Publications/Presentations

Presentation

- The Electrochemical Society (ECS) PRiME 2020 (Joint Meeting of the ECS, ECS of Japan, and Korean ECS), Virtual (October 4, 2020): "Room Temperature to 150°C Lithium Metal Batteries Enabled By a 'Molecular Ionic Composite' Solid Electrolyte"; D. Yu, X. Pan, C. J. Zanelotti, F. Lin, and L. A. Madsen.

Task 1.12 – All-Solid-State Batteries Enabled by Multifunctional Electrolyte Materials (Pu Zhang, Solid Power Inc.)

Project Objective. The project objective is to develop Li-metal SSBs enabled by multifunctional SSEs for EV application. The ultimate goal is scalable production of large-format ASSBs able to deliver ≥ 350 Wh/kg specific energy, ≥ 1000 cycle life, and ≤ $100/kWh cost.

Project Impact. The project impact is enabling scalable production of large format all-solid batteries required by the vehicle market and building domestic battery manufacturers as leaders in the global vehicle ASSB production. The proposed technology will address key limitations of state-of-the-art lithium batteries to meet DOE EV battery targets and accelerate their adoption as large-format EV batteries for sustainable transportation technology.

Approach. The project will develop a high-performance Li-metal solid-state cell enabled by a multifunctional SSE. The new SSE will: (1) have high conductivity (up to 10 mS/cm), (2) be stable against lithium metal and high-voltage cathode (0-4.5 V), (3) promote uniform lithium plating (enabling > 2C charge rate), and (4) be compatible with large-scale manufacturing processes. The specific cell chemistry to be demonstrated will be the SSE with Li-metal anode and high-nickel-content Li-metal oxide cathode. The solid-state cell will be assembled by scalable roll-to-roll processes developed by Solid Power.

Out-Year Goals. In Year 1, multifunctional SSE will be developed with lithium ionic conductivity of ≥ 3 x 10^{-3} S/cm. CCD of ≥ 6 mA/cm^2 will be achieved in a symmetric lithium cell. The SSE design concept will be proven by demonstrating cycle life of ≥ 200 in a full cell. In Year 2, SSE material will be optimized with lithium ionic conductivity of ≥ 5 x 10^{-3} S/cm. Scalable cell assembly processes will be developed. Cycle life of ≥ 500 will be demonstrated in a full cell. In Year 3, large-format solid-state cells (> 2Ah) will be assembled/tested to meet the final goal: ≥ 350 Wh/kg, ≥ 1000 cycles, and ≤ $100/kWh cost.

Collaborations. The proposed team consists of Solid Power and subcontractor UCSD. Solid Power (PI: P. Zhang) will develop the multifunctional SSE and other cell components, assemble cells, and conduct cell tests. UCSD (PI: Y. S. Meng) will carry out material characterization by using advanced techniques such as XPS, cryo – scanning transmission electron microscopy (cryo-STEM) imaging, cryo-STEM energy dispersive X-ray spectroscopy (EDX), electron energy loss spectroscopy (EELS), and cryo – focused ion beam (cryo-FIB) milling. The UCSD team seeks to quantify the kinetics and evolution of each contributing factor and its impact on battery performance.

Milestones

1. Charge rate ≥ 0.5C. (Q1, FY 2021; Completed)
2. Pouch cell capacity ≥ 200 mAh. (Q2, FY 2021; In progress)

Progress Report

SSE Separator Development

The SSE separator coating process has been developed at pilot scale. A separator slurry was prepared by mixing the SSE powder, a binder, and a solvent by using an industrial mixer. The slurry was cast on a carrier film on a slot-die coater. The separator was then laminated to an NMC cathode to form a separator-cathode bi-layer, which was assembled into a solid-state cell by coupling a stand-alone Li-foil anode.

Figure 36 shows a coated separator by a roll-to-roll process (left) and a SEM cross-section image of the separator on cathode (right). The separator thickness was 40 µm in this case.

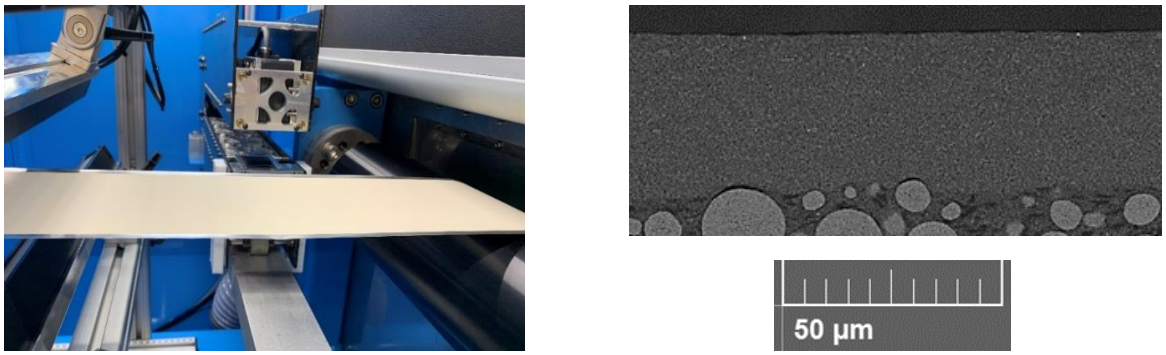

Figure 36. (left) Solid-state electrolyte separator coating on a slot die coater. (right) Cross-section of a 40-µm separator on NMC cathode under scanning electron microscopy.

Full Cell Demonstration

Lab-scale pouch cells were assembled and demonstrated > 300 cycles at 70°C last quarter. The cell contained a multifunctional SSE separator, an NMC-622 composite cathode (at 3 mAh/cm^2), and a Li-metal foil anode. The cell was designed to deliver a specific energy of 300 Wh/kg if scaled to 20 Ah.

This quarter, rate capability of the cell was evaluated by charging and discharging symmetrically from C/10 to 1C. As shown in Figure 37, the cell retained 95% capacity at C/2 and 90% at 1C, when compared to C/10. The high rate performance clearly indicates a low resistance cell built with the multifunctional SSE.

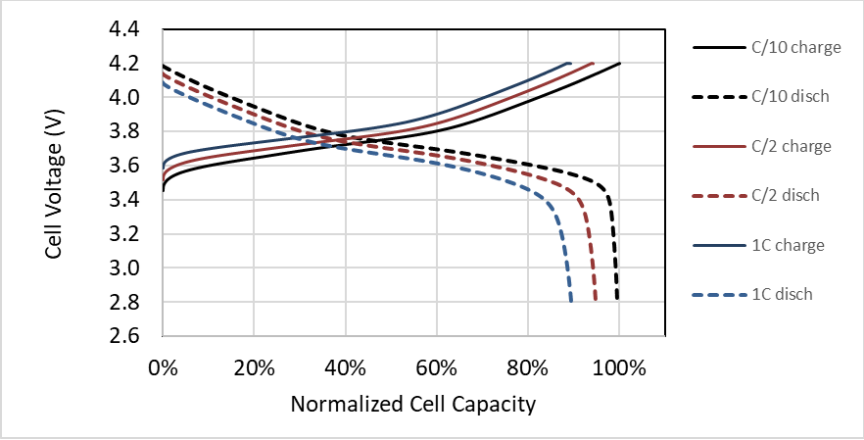

Figure 37. Rate capacity of an NMC/Li-metal solid-state pouch cell with the multifunctional solid-state electrolyte.

Cycle life of the cell at room temperature was also evaluated this quarter. When tested at 2.8-4.2 V, C/5 – C/5, and ambient temperature (~ 25°C), the pouch cell showed 93% capacity retention after 120 cycles up to date (Figure 38). More cycling data will be reported next quarter. It should be noted that the capacity fluctuation was due to the ambient temperature change.

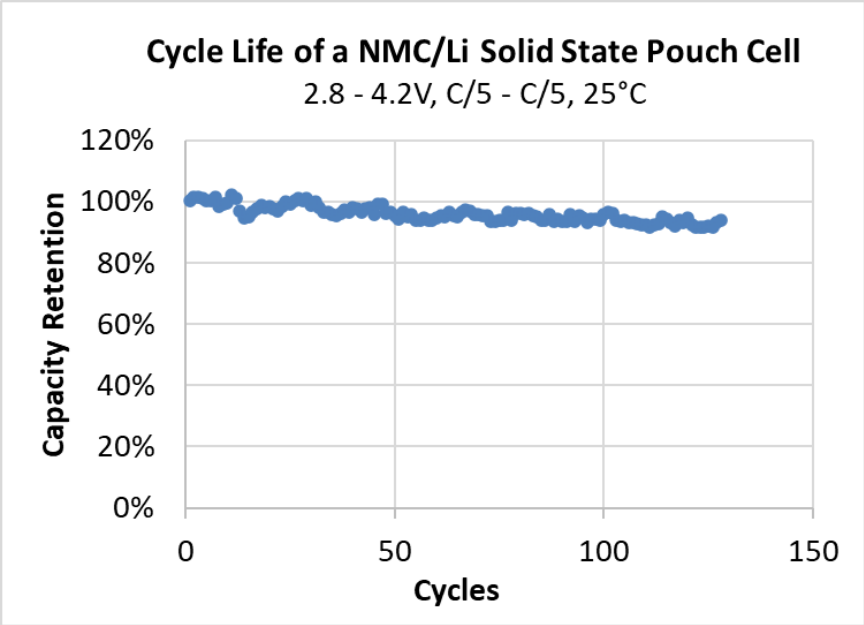

Figure 38. Cycle life of an NMC/Li-metal solid-state pouch cell with the multifunctional solid-state electrolyte at 25°C.

Patents/Publications/Presentations

The project has no patents, publications, or presentations to report this quarter.

Task 1.13 – Developing Materials for High-Energy-Density Solid-State Lithium-Sulfur Batteries (Donghai Wang, Pennsylvania State University)

Project Objective. The project objectives are to develop materials involving advanced S-C composite materials, solid additives, and sulfide-based SSEs, and to acquire knowledge for Li-S ASSBs. Li-S ASSBs with large areal sulfur loading (≥ 5 mg cm^{-2}) and high sulfur content (≥ 50 wt% in cathode), pairing with lithium or lithium alloy anode, will deliver a high initial specific capacity of over 1200 mAh g^{-1} at high charge/discharge rate (> 0.3 C) for 500 cycles with over 80% capacity retention.

Project Impact. This project aims to develop new materials to enable Li-S ASSBs with high energy density, excellent cycling stability, and good rate performance, and thus to build knowledge for fabrication of prototype Li-S ASSBs. Specifically, the developed new materials will greatly increase the specific capacity of sulfur and sulfur utilization at high areal sulfur loading, alleviate the interfacial problem between S-C composite and SSE within sulfur cathode, boost Li-ion conductivity, and improve moisture stability of glass and glass-ceramic sulfide-based SSE. Meeting the technical targets will potentially promote development of high-energy-density Li-S ASSBs and their practical application in EVs and plug-in hybrid EVs (PHEVs), and reduce petroleum consumption in the transportation sector by helping battery-powered vehicles become more accepted by consumers as a reliable source of transportation.

Approach. The project goal will be accomplished through developing new materials, together with in-depth characterization of sulfur cathode. Specifically, approaches to realize the project objectives include the following: (1) development of new carbon material with unique structure, high surface area, and large pore volume; (2) development of new S-C and S-C-M_xS_y materials (M = Li, Co, Ti, Mo, etc.) to facilitate electron/ion transport; (3) development of novel additives to tune interfacial behavior among components in the cathode; (4) development and optimization of new SSE through cation and anion doping with superior properties such as high ionic conductivity, good moisture, and stability; and (5) diagnostics, characterization, and cell tests on the developed new material or advanced sulfur cathode.

Out-Year Goals. The out-year goals are as follows: (1) develop new S-C-M_xS_y hybrid materials, new cathode additives, and anion-doped SEs (ionic conductivity above 3 mS cm^{-1} at room temperature), (2) conduct characterization and performance tests on both material and electrode levels. The *Go/No-Go Decision* will be demonstration of all-solid-state sulfur cathode with over 1000 mAh g^{-1} discharge capacity at 0.1 C discharge rate and 50 wt% sulfur content for 100 cycles at room temperature.

Collaborations. There are no active collaborations.

Milestones

1. Demonstrate sulfur cathode with above 1000 mAh g^{-1} capacity at 0.2 C at 60°C. (Q1, FY 2021; Completed)
2. Demonstrate new anion-doped electrolyte with ionic conductivity > 2 mS cm^{-1} at 25°C, and sulfur cathode with > 1000 mAh g^{-1} using additives (≤ 3 wt%) at 0.3 C for 50 cycles. (Q2, FY 2021; In progress)
3. Demonstrate sulfur cathode with > 1000 mAh g^{-1} at 0.3 C for 50 cycles at 60°C using hybrid conductive materials. (Q3, FY 2021)
4. Demonstrate sulfur cathode with >1000 mAh g^{-1} at 0.1 C for 100 cycles at room temperature, and anion-doped SEs with ionic conductivity > 3 mS cm^{-1} at 25°C. (Q4, FY 2021)

Progress Report

This quarter, the team has worked on new S-C-M_xS_y materials (M = Li, Co, Ti, Mo, etc.) for all-solid-state Li-sulfur batteries. Based on the knowledge accumulated from last year, they chose TiS_2 to prepare the hybrid composite cathode. TiS_2 is unique as it could be lithiated and serves as both electron carrier and Li-ion carrier in sulfur cathode. TiS_2 was incorporated into sulfur cathode and partially replaced the SE based on molar percentage (10%, 20%). The sulfur cathodes were prepared by ball-milling approach, and the final composition of the cathode is KB/S/SE+TiS_2 = 10/50/40. Li_6PS_5Cl was employed as the electrolyte membrane, and Li-In alloy was used as the anode. For the SE in the cathode, $70Li_2S$-$30P_2S_5$ glass was first used for study. The rate performance of the sulfur cathode with sulfur loading of 1.5 ~ 2 mg cm^{-2} was evaluated at 0.1 C, 0.2 C, 0.5 C, and 1 C. The voltage window is 0.5 ~ 2.5 V. The results are summarized in Figure 39a. It was found that by replacing 20% of SE with TiS_2, the initial discharge capacity would rise significantly from 1339.3 mAh g^{-1} to 1791.9 mAh g^{-1}. Such improvement is probably induced by the better electronic and ionic transport as well as the extra capacity contribution by TiS_2 lithiation. As shown in Figure 39b, a new plateau was observed at around 0.6 V when TiS_2 is incorporated. The generation of the new plateau probably is attributed to the lithiation of TiS_2. However, even though the discharge capacity improved significantly, the cycling stability for all cells was not good, and fast capacity decay was observed. The team thought it might be caused by the electrolyte degradation of $70Li_2S$-$30P_2S_5$ glass SE on cycling. Therefore, they replaced $70Li_2S$-$30P_2S_5$ glass SE with $75Li_2S$-$25P_2S_5$ glass SE in the cathode and performed similar testing.

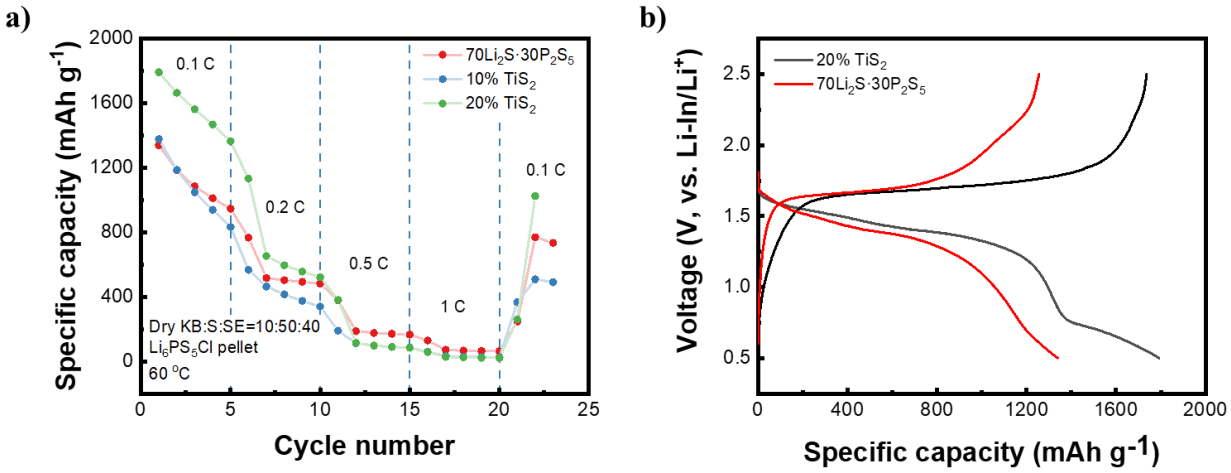

Figure 39. (a) Rate performance and (b) corresponding voltage profiles at 1st cycle. Electrolyte used is 70 Li_2S – 30 P_2S_5 in the cathode.

Testing results using $75Li_2S$-$25P_2S_5$ glass SE in the cathode are presented in Figure 40. It was observed that by using $75Li_2S$-$25P_2S_5$ glass SE in the cathode, cycling stability and rate capability at 0.2 C, 0.5 C, and 1 C were improved compared with the sulfur cathode using $70Li_2S$-$30P_2S_5$ glass SE. However, the discharge capacity at 0.1 C is lower at ~ 1000 mAh g^{-1} when using $75Li_2S$-$25P_2S_5$ glass SE. As for the sulfur cathode using 20 % TiS_2, even higher discharge specific capacity of 1857.2 mAh g^{-1} was observed at 1st cycle. Both cycling stability and rate capability improved compared with the cathode using $70Li_2S$-$30P_2S_5$ glass SE. At 0.2 C, discharge specific capacity > 1000 mAh g^{-1} was reached, which meets the targeted milestone for this quarter. However, cycling stability is still unsatisfactory, as discharge capacity faded below 1000 mAh g^{-1} in 3 cycles at 0.2 C. The voltage profiles of the cells were reviewed as well, as shown in Figure 40b. Similar to previous results, new plateau at 0.6 V was observed when TiS_2 was added, which contributed to cell capacity. Next quarter, the team will work on optimization of sulfur cathode compositions, electrochemical window, and other parameters to achieve stable cycling of the cell.

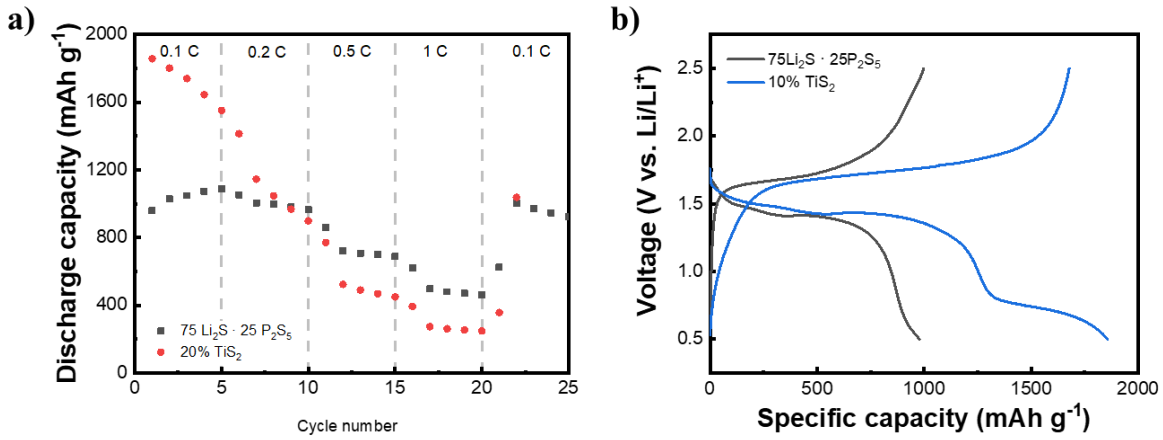

Figure 40. (a) Rate performance and (b) corresponding voltage profiles at 1st cycle. Electrolyte used is $75Li_2S – 25P_2S_5$ in the cathode.

In addition to developing new S-C-M_xS_y materials (M = Li, Co, Ti, Mo, etc.) for all-solid-state Li-sulfur batteries, the team also started to work on designing and synthesizing new anion-doped SEs. After screening different anions, they picked BH_4^- anion for their study. Li_3PS_4-3$LiBH_4$ SE was synthesized using solution approach by reacting Li_3PS_4-3THF with $LiBH_4$ in anhydrous THF (tetrahydrofuran) solution. Solution preparation was chosen because it is more suitable for industrial production compared with other techniques like ball-milling approach. The Li_3PS_4-3$LiBH_4$ SE powders were collected by evaporating the solvent under vacuum at 100°C and then further annealed at 160°C for several hours. The ionic conductivity of Li_3PS_4-3$LiBH_4$ was measured by EIS using Al/SE/Al cell. The calculated ionic conductivities at different temperatures and corresponding EIS spectra are summarized in Figure 41. A high ionic conductivity of 1.22 mS cm^{-1} was achieved at 25°C. In the future, the team plans to further optimize the composition, preparation approach and conditions, annealing temperatures, and many other parameters. At the same time, they will also adopt advanced characterization techniques to obtain structural and morphological information for the newly developed SEs.

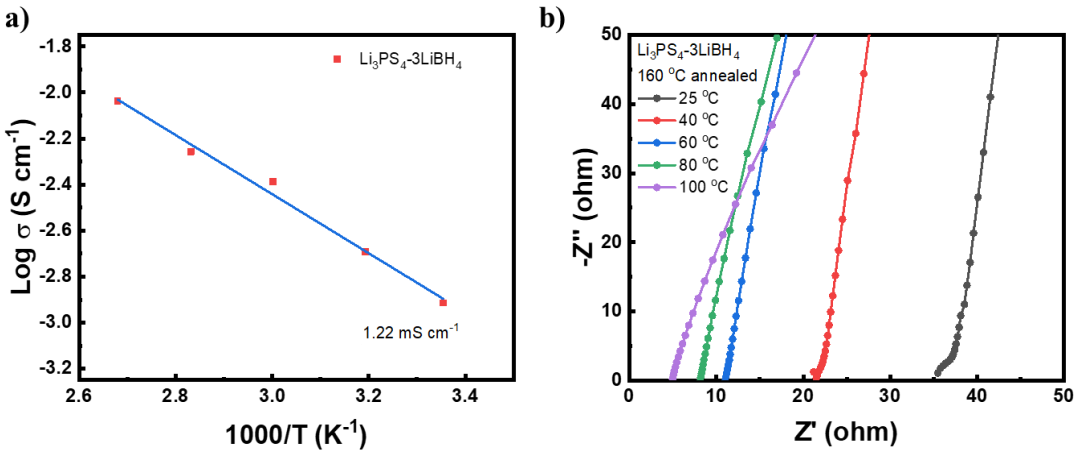

Figure 41. (a) Arrhenius plots and (b) corresponding electrochemical impedance spectra of Li_3PS_4-3$LiBH_4$ solid electrolytes.

Patents/Publications/Presentations

Presentation

- MRS Spring/Fall 2020 Meeting, Virtual (November 27 – December 4, 2020): "Mixed Ionic-Electronic Conductor for All-Solid-State Lithium-Sulfur Batteries."

TASK 2 – DIAGNOSTICS

Summary and Highlights

To meet the goals of the VTO programs on next-generation EVs, low-cost and abuse-tolerant batteries with higher energy density, higher power density, better safety, and longer lifetimes are needed. In pursuit of these goals, high cell operating voltages and demanding cycling conditions are used, which leads to unprecedented chemical and mechanical instabilities in cell components. Successful implementation of promising electrode materials (such as silicon anode and high-voltage cathodes) and new cell chemistry (such as high-energy Li-metal cells combined with SSEs) requires better understanding of fundamental processes, especially those at the interface/interphase of both anode and cathode. Identifying and understanding structure-property-electrochemical performance relationships in materials and various failure modes in cell chemistry are therefore more pressing than ever, not only in guiding battery development activities but also the scale-up efforts needed for commercialization.

Task 2 takes on these challenges by combining model systems, *ex situ*, *in situ*, and *operando* approaches, with an array of state-of-the-art analytical and computational tools. Numerous subtasks are tackling the chemical processes and reactions at the electrode/electrolyte interfaces in Li-metal batteries. Researchers at LBNL use surface- and bulk-sensitive techniques, including Fourier transform infrared (FTIR), attenuated total reflectance (ATR)-FTIR, near-field infrared (IR) and Raman spectroscopy/microscopy, and scanning probe microscopy (SPM) to characterize changes in materials and the physio-chemical phenomena occurring at the interface of Li-metal electrode. GM is developing *in situ* diagnostic techniques, including atomic force microscopy (AFM), nano-indentor, dilatometer, and stress-sensor, to be combined with atomic/continuum modeling schemes to investigate the coupled mechanical/chemical degradation of the SEI layer as well as the microstructural evolution at the interface/interphase of Li-metal anode. ANL aims to develop high-conductivity ceramic electrolytes through cation doping and to identify mechanistic barriers that limit chemical, mechanical, and electrochemical durability of solid/solid interfaces. University of Houston (UH) is developing multidimensional diagnostic tools, including FIB-SEM, time-of-flight secondary ion mass spectrometry (TOF-SIMS), and in-SEM nanoindentation, to probe structural, chemical, and mechanical evolution at the interfaces of SSLBs. At LBNL, model systems of electrode, SSE, and their interfaces with well-defined physical attributes are being developed and used for advanced diagnostic and mechanistic studies at both bulk and single-particle levels. These controlled studies remove the ambiguity in correlating a material's physical properties and reaction mechanisms to its performance and stability, which is critical for further optimization. Subtasks at BNL and PNNL focus on the understanding of fading mechanisms in electrode materials, with the help of synchrotron-based X-ray techniques (diffraction and hard/soft X-ray absorption) at BNL and high-resolution transmission electron microscopy (HRTEM) / STEM and related spectroscopy techniques at PNNL. The final subtask at Stanford/SLAC develops and utilizes an integrated X-ray characterization toolkit to investigate and generate insights on SSBs, by tracking the evolution of nanoscale chemistry as well as structure, microstructure, and transport properties. The diagnostics team not only produces a wealth of knowledge key to developing next-generation batteries, they also advance analytical techniques and instrumentation with a far-reaching effect on material and device development in various fields.

Highlights. The highlights for this quarter are as follows:

- The LBNL group (G. Chen) applied electrochemical analytical methods to investigate reactivities at the model interface of lithium metal and SSE. Compared to that of Li_3InCl_6/Li, much better stability was observed on Li_3YCl_6/Li interface, suggesting the critical role of metal center in halide SSEs.
- The GM team (X. Xiao) experimentally demonstrated the effect of external pressure on interfacial impedance of a symmetrical LLZO pouch cell. With increasing external pressure, the contact resistance between LLZO and lithium gradually reduced.
- The UH group (Y. Yao) successfully designed and fabricated an SSE nano-cell to investigate the evolution of interfacial structural and chemical properties with high spatial and chemical resolution.

Task 2.1 – Characterization and Modeling of Lithium-Metal Batteries: Model-System Synthesis and Advanced Characterization
(Guoying Chen, Lawrence Berkeley National Laboratory)

Project Objective. This project will use a rational, non-empirical approach to design and develop SSE materials and interfaces for next-generation Li-metal batteries. Combining a suite of advanced diagnostic techniques with carefully prepared model-system samples, the project will perform systematic studies to achieve the following goals: (1) obtain understanding on the role of SSE grain and grain boundaries (GBs) on ion conduction and dendrite formation, (2) obtain fundamental knowledge on rate- and stability-limiting properties and processes in SSEs when used in Li-metal batteries, (3) investigate the reactivities between SSE and electrodes, and gain insights on the dynamic evolution of the interfaces, and (4) design and synthesize improved SSE materials and interfaces for safer and more stable high-energy Li-metal batteries.

Impact. The project will focus on fundamental understanding of SSE and relevant interfaces to enable its use in Li-metal batteries. Knowledge gathered from model-system based studies will guide the design and engineering of advanced materials and interfaces. The use of the non-empirical, rational-design approach will develop high-energy battery systems with improved commercial viability.

Approach. The project will combine model-system synthesis and advanced diagnostic studies to investigate ion conduction and interfacial chemistry of SSE in Li-metal batteries. Single crystalline, polycrystalline, and amorphous model SSE samples with various grain and GB properties will be synthesized. Model interfaces between the SSE and electrodes with controlled properties will also be developed. Both bulk-level and single-grain level characterization will be performed. Global properties and performance of the samples will be established from the bulk analyses, while the single-grain-based studies will utilize time- and spatially-resolved analytical techniques to probe the intrinsic redox transformation processes and failure mechanisms under battery operating conditions.

Out-Year Goals. In the out-years, the project will deliver fundamental knowledge on the role of SSE microstructure in Li^+ conduction and lithium dendrite formation/propagation. Insights on performance-limiting physical properties and phase transition mechanisms as well as dynamic evolution of SSE/electrode interfaces will be obtained. Mitigating approaches, such as use of surface coating or "buffer layer" in stabilizing SSE/electrode interfaces, will be evaluated. Further, advanced SSE materials and interfaces for improved high-energy Li-metal batteries will be designed and synthesized.

Collaborations. This project collaborates with the following PIs: G. Ceder, K. Persson, M. Doeff, B. McCloskey, R. Kostecki, and R. Prasher (LBNL); W. Yang (Advanced Light Source, ALS); D. Nordlund and Y. Liu (Stanford Synchrotron Radiation Lightsource, SSRL); C. Wang (PNNL); and J. Nanda (Oak Ridge National Laboratory, ORNL).

`Milestones

1. Development of SSE/Li model interfaces for studying the reactivities and dendrite formation at the Li-metal anode interface. (Q1, FY 2021; Completed)
2. Synthesis of SSE model samples and model interfaces for studying reactivities and dendrite formation at Li-metal anode. (Q2, FY 2021; On schedule)
3. Advanced diagnostic studies of SSE/Li-metal anode interfaces. (Q3, FY 2021; On schedule)
4. Obtain mechanistic understanding and deliver design strategies to mitigate reactivities at SSE/Li anode interface. (Q4, FY 2021; On schedule)

Progress Report

This quarter, electrochemical analytical methods for probing the reactivities at the interfaces between SSE and Li-metal anode were evaluated. Two recently synthesized halide SSEs, Li_3InCl_6 (LIC) and Li_3YCl_6 (LYC), were used for the study. Figure 42a shows the voltage profiles of a Li|LIC|Li symmetrical cell when the CD gradually increased at a step size of 0.02 mA/cm^2. At a low CD (up to 0.04 mA/cm^2), the voltage response is largely constant, demonstrating a flat profile consistent with ohmic-dominating behavior. As the CD increases, cell polarization also increases, and the voltage profile becomes more slopy. Significant voltage fluctuation occurs when the CD is raised above 0.08 mA/cm^2. Assuming the cell remains in the ohmic regime, the evolution of cell resistance determined by the ratio between cell voltage and current is shown in Figure 42b. The overall resistance of LIC symmetrical cell is rather high, in the range of 10^3-10^4 Ohm. Cell hard-shorting was detected at a CD above 0.1 mA/cm^2, signaling extensive formation and propagation of electronically conducting species, likely Li-metal dendrites.

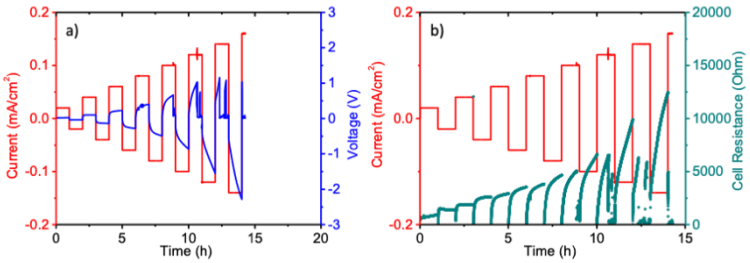

Figure 42. (a) Voltage profiles of Li|LIC|Li symmetrical cell during the step-increase of current density test and (b) corresponding cell resistance. The current density step size is 0.02 mA/cm^2, and the duration of each charge/discharge step is 1 hour.

The voltage profiles and cell resistance of a Li|LYC|Li symmetrical cell during a similar test are shown in Figure 43a-b, respectively. The deviation from the ohmic regime occurs when the CD is greater than 0.12 mA/cm^2, much higher than that in the LIC cell. The cell resistance is also significantly lower, in the range of 10^2 Ohm. At a CCD of 0.28 mA/cm^2, cell resistance begins to decrease, suggesting soft-shorting likely through the formation of electronically conducting "tunnels." Decrease in resistance continues with the further increase in CD; however, cell hard-shorting is not observed until the CD reaches a high value of 20 mA/cm^2. The results suggest that the LYC/Li interface is much more stable than that of LIC/Li, further confirming the critical role of metal center in halide SSE reactivity toward Li-metal anode.

EIS measurements were also carried out on the Li|LYC|Li cell after each DC cycling step. Figure 44 shows results collected on the cell at the as-assembled state as well as after DC testing at 1, 5, and 20 mA/cm^2. Before cycling, the Nyquist profile obtained on the symmetric cell shows the typical profile where the intercept at the real axis corresponds to the total bulk electronic/ionic conductivity, and the low-frequency region corresponds to charge transfer at the LYC/Li interface. Overall, DC cycling leads to a reduction in cell resistance. After cycling at 1 mA/cm^2, cell bulk resistance was reduced by more than half, from 80 to 30 ohm. Further decrease was observed after 5 mA/cm^2 cycling; however, significant changes on the EIS profile were only found after cycling at

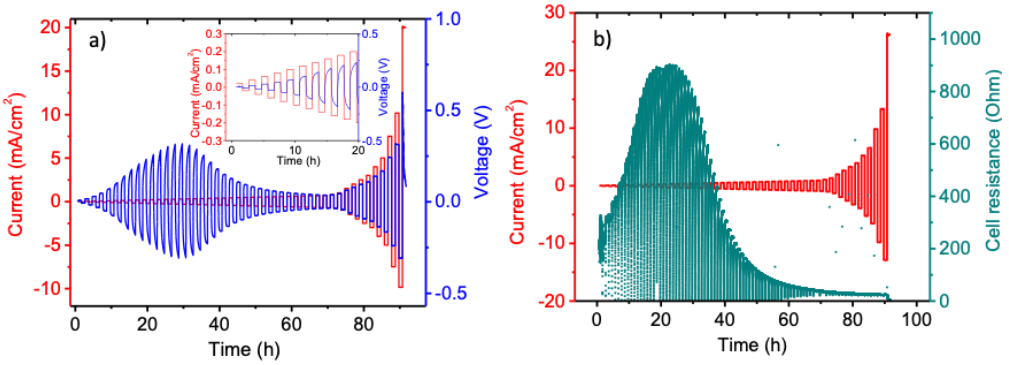

Figure 43. (a) Voltage profiles of a Li|LYC|Li symmetrical cell during the step-increase of current density and (b) corresponding cell resistance. Inset in (a) shows the voltage profile during the first 20 hours. The current density step size is 0.02 mA/cm^2, and the duration of each charge/discharge step is 1 hour.

20 mA/cm^2. Results are consistent with what was obtained from the symmetrical cell cycling, confirming that while low CD cycling leads to some minor reactions at the LYC/Li interface, electronic conduction pathways through the SSE were only established after cycling at a very high current density.

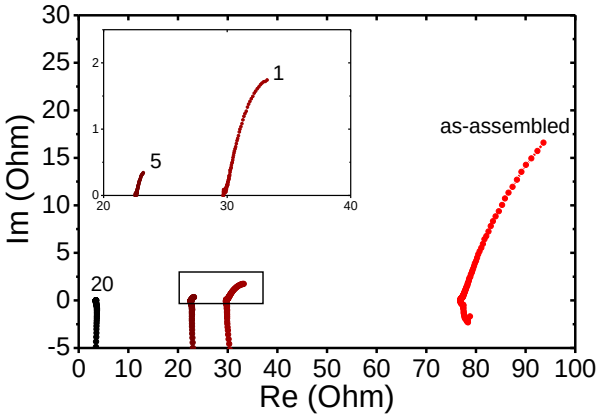

Figure 44. Nyquist plots of Li|LYC|Li symmetrical cells after various stages of DC cell testing at the indicated current density (mA/cm^2). AC amplitude was 10 mV, and frequency limit was 1 MHz to 0.1 Hz. Inset shows expanded view of the indicated area on the spectra.

Patents/Publications/Presentations

The project has no patents, publications, or presentations to report this quarter.

Task 2.2 – Interfacial Processes – Diagnostics
(Robert Kostecki, Lawrence Berkeley National Laboratory)

Project Objective. The objective of the proposed research is to establish specific design rules toward the next generation of low impedance Li-metal rechargeable batteries that are capable of performing 1000 deep discharge cycles at CE > 99.9% and suppressing lithium dendrite formation at high current densities (> 2 mA/cm^2). This project aims at the following: (1) establishing general rules between Li^+ transport properties in novel liquid/solid electrolytes, and (2) determining the mechanism of the SEI layer (re)formation. The other goal is development and application of far- and near-field optical probes and synchrotron-based advanced X-ray techniques to obtain insight into the mechanism of Li^+ transport and interfacial reactions in lithium/liquid model systems. Through an integrated synthesis, characterization, and electrochemistry effort, this project aims to develop a better understanding of lithium/LE interface so that rational decisions can be made as to their further development into commercially viable Li-metal cells.

Project Impact. Chemical instability and high impedance at the interface of Li-metal electrodes limits electrochemical performance of high-energy-density batteries. A better understanding of the underlying principles that govern these phenomena is inextricably linked with successful implementation of high-energy-density materials in Li-metal-based cells for PHEVs and EVs. New state-of-the-art techniques to identify, characterize, and monitor changes in materials structure and composition that take place during battery operation and/or storage will be developed and made available to the Program participants. The proposed work constitutes an integral part of the concerted effort within the BMR Program, and it supports development of new electrode materials for high-energy, Li-metal-based rechargeable cells.

Approach. The pristine and cycled composite electrode and model thin-film electrodes will be probed using various surface- and bulk-sensitive techniques, including FTIR, ATR-FTIR, near-field IR and Raman spectroscopy/microscopy, and SPM to identify and characterize changes in materials structure and composition. Novel *in situ / ex situ* far- and near-field optical multi-functional probes in combination with standard electrochemical and analytical techniques are developed to unveil the structure and reactivity at interfaces and interphases that determine materials electrochemical performance and failure modes.

Out-Year Goals. In the out-years, the project aims to achieve the following: (1) understand factors that control performance and degradation processes, (2) unveil structure and reactivity at hidden or buried interfaces and interphases that determine electrochemical performance and failure modes, and (3) propose effective remedies to address inadequate Li-metal-based battery calendar/cycle lifetimes for PHEV and EV applications.

Collaborations. The diagnostic studies will be carried out in sync with other diagnosticians (G. Chen, B. McCloskey, R. Prasher, and L-W. Wang) and theory and computational scientists (G. Ceder and K. Persson).

Milestones

1. Compete finite T phase diagram of L-P-S system. (Q1, FY 2021; Completed)
2. Quantify the conduction mechanisms in Li-neutralized polyanion solutions. (Q2, FY 2021; In progress)
3. Complete machine learning force field (ML-FF) theory/simulation for lithium transport in LE and LiS-polymer systems. (Q3, FY 2020; In progress)
4. Develop a valid model for amorphous structure as compared to experimental radial distribution function (RDF) data. (Q4, FY 2021; In progress)

Progress Report

This quarter, the team continued to characterize *in situ* interfaces in a model Li/LiTFSI-PEO/C (graphene) solid-state model battery cell during electrochemical cycling by near-field FTIR nano-spectroscopy (nano-FTIR) in a nitrogen-filled glovebox. A monolayer graphene sheet was used as a working electrode and optical window for nano-FTIR probe characterization. After the lithium plating process, morphological and chemical changes at the graphene/Li-electrolyte (SSE) interface were probed through the graphene window at nanoscale resolution. The dry nitrogen atmosphere prohibited any interference from oxygen and moisture, and allowed the team to obtain high-quality nano-FTIR spectra.

In this work, the team does just that (Figure 45a), utilizing a fully functional solid-state device comprised of graphene (Gr) as an infrared transparent model carbon anode, SSE of PEO/LiTFSI (EO:Li ratio 10:1), and a counter/reference electrode of lithium. The full-cell device is brought through one full electrochemical process (Figure 45b) in which lithium is galvanostatically (45 μA cm^{-2}) plated (stripped) to (from) the model carbon anode at an elevated temperature of 45ºC. The electrochemical process is stopped at four states (that is, pristine, heated, plated, and stripped) at which points AFM, scattering scanning near-field optical microscopy (s-SNOM), nano-FTIR, and ATR-FTIR are all conducted, at room temperature. Comparison of nano-FTIR and ATR-FTIR is particularly useful in delineating absorption signals that originate from the interface versus the bulk. This is because most spectral signals acquired in ATR-FTIR are attributable to absorption events occurring within tens of microns subsurface, while in nano-FTIR, tens of nanometers.

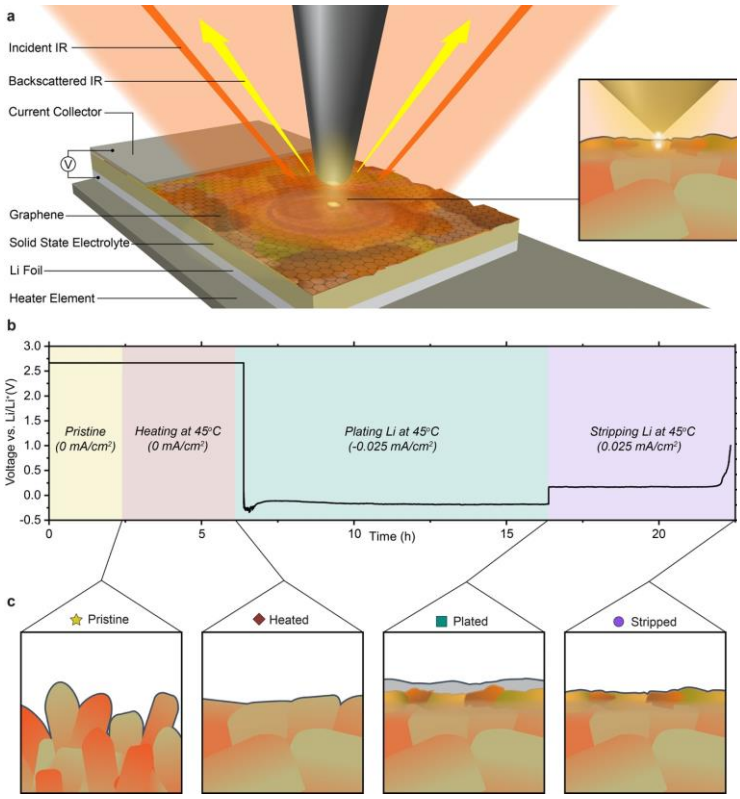

Figure 45. *In situ* characterization of the graphene (Gr) – solid-state electrolyte (SSE) interface and interphase as a function of heating and electrochemical state with scattering-type near-field infrared nanospectroscopy. (a) 3D schematic of experimental setup including metal-coated atomic force microscopy probe, incident and backscattered infrared light, and cross section of assembled anode-free Gr/SSE/Li cell atop heater element. Inset on the right is an artistic representation of the tip-sample near-field coupling that enables nanoscale Fourier transform infrared (FTIR). (b) Electrochemical voltage profile applied to full-cell device. Overlaid colored regions with descriptive text describe state of the device. Electrochemistry is suspended, and nano-FTIR measurements are conducted, at the four transition points between colored regions. (c) Cross-sectional illustrations of the device, near the Gr/SSE interface, for the four electrochemical states characterized.

Figure 45c conveys key findings. Pristine SSE has a rough surface in comparison to the heated surface and chemical inhomogeneity at the nanoscale (depicted by red-to-tan color gradients within grains). Heating improves these, but a flat and chemically homogeneous interface is not reached. After plating protocols, the team finds plating is non-uniform (both at the microscale and nanoscale), that an electrochemically induced SEI layer with a chemically diverse mosaic structure has grown, and that PEO within the SEI layer undergoes a phase transition from a crystalline state to an amorphous state, which increases ionic conductivity. This concludes efforts toward this quarter's milestone.

Patents/Publications/Presentations

The project has no patents, publications, or presentations to report this quarter.

Task 2.3 – Advanced *In Situ* Diagnostic Techniques for Battery Materials (Xiao-Qing Yang and Enyuan Hu, Brookhaven National Laboratory)

Project Objective. The primary objective of this project is to develop new advanced *in situ* material characterization techniques and to apply these techniques to support development of new cathode and anode materials with high energy and power density, low cost, good abuse tolerance, and long calendar and cycle life for beyond Li-ion battery systems to power PHEVs and battery electric vehicles (BEVs). The diagnostic studies will focus on issues relating to capacity retention, thermal stability, cycle life, and rate capability of beyond Li-ion battery systems.

Project Impact. The VTO Multi-Year Program Plan describes the goals for battery: "Specifically, lower-cost, abuse-tolerant batteries with higher energy density, higher power, better low-temperature operation, and longer lifetimes are needed for development of the next-generation of HEVs [hybrid electric vehicles], PHEVs, and EVs." The results of this project will be used for development of technologies that will significantly increase energy density and cycle life, and reduce cost. This will greatly accelerate deployment of EVs and reduce carbon emission associated with fossil fuel consumption.

Approach. This project will use a combination of synchrotron XRD and pair distribution function (x-PDF) and of neutron diffraction (ND) and pair distribution function (n-PDF); x-ray spectroscopies including hard/soft X-ray absorption spectroscopies (XAS), X-ray photon emission spectroscopy (PES); and imaging techniques including X-ray fluorescence (XRF) microscopy, transmission X-ray microscopy (TXM), and transmission electron microscopy (TEM).

Out-Year Goals. The out-year goals are to develop spectro-tomography, XRD, XAS, and PDF techniques and apply these techniques on Li-ion battery cathode, Na-ion battery cathode, and SSE.

Collaborations. The BNL team will work closely with material synthesis groups at ANL (Y. Shin and K. Amine) for the high-energy composite, at PNNL for the S-based cathode and Li-metal anode materials, and with ORNL on neutron scatterings. This project will also collaborate with industrial partners at GM and Johnson Controls, as well as with international collaborators.

Milestones

1. Complete 3D spectro-tomography studies of Li-rich layered material $Li_{1.2}Ni_{0.13}Mn_{0.54}Co_{0.13}O_2$ at various states of charge (SOC). (Q1, FY 2021; Completed)
2. Complete XRD, PDF analysis, XAS studies of single-crystal sodium cathode material $Na_xNi_{0.76}Mn_{0.14}Co_{0.1}O_2$. (Q2, FY 2021; In progress)
3. Complete XRD/x-PDF/XAS studies of O3-type Na-cathode material $Na_xLi_{1.2-y}Mn_{0.54}Ni_{0.13}Co_{0.13}O_2$. (Q3, FY 2021; In progress)
4. Complete sulfur and phosphorus XAS studies of SSE $Li_{10}GeP_2S_{12}$ from various SOCs during the 1st cycle. (Q4, FY 2021; In progress)

Progress Report

This quarter, the first milestone for FY 2021 was completed, and progress on other milestones was made. BNL focused on developing new diagnostic techniques to study and improve the performance of high-energy-density Li-ion batteries. In collaboration with Y. Liu at SLAC, the spectro-tomography technique has been applied to study the Li-rich NMC (LirNMC), which could spatially resolve the local valence state of the element of interest in 3D. Such capability is achieved by conducting tomographic scans at a number of different energy levels across the absorption edge of the targeted element of interest. This technique is first applied to manganese, the most abundant transition metal (TM) in LirNMC. Two particles at the pristine and the charged (to 4.8 V in the initial cycle, at the fully charged state) states are scanned. As shown in Figure 46a/d, the particle morphology is fairly similar, and their manganese K-edge spectroscopic fingerprints over different regions (see labeling in the virtual slices through the center of the particle) are shown in Figure 46b/e, respectively. The pristine particle appears to be relatively homogeneous in the manganese valence state, as indicated by the depth-dependent manganese X-ray absorption near-edge structure (XANES) plots in Figure 46b and the 3D rendering of the manganese K-edge energy distribution in Figure 46c. On the other hand, the charged particle clearly shows a depth-dependent manganese redox variation (see Figure 46e-g). The core and the surface layer of the charged LirNMC particle exhibit high manganese valence state at 4^{+}, while the manganese cations in the transition layers appear to be relatively reduced. These visual assessments of the pristine and charged particles are further confirmed by the depth profile of manganese K-edge energy shown in Figure 46. While the relative homogeneity of the manganese valence state distribution in the pristine particle is anticipated, the observed depth-dependent manganese valence in the charged LirNMC particle is somewhat of a surprise, specifically because of its non-monotonicity. This observation motivates a more systematic study of all the TM cations (manganese, cobalt, and nickel) in the LirNMC particle in a correlative manner.

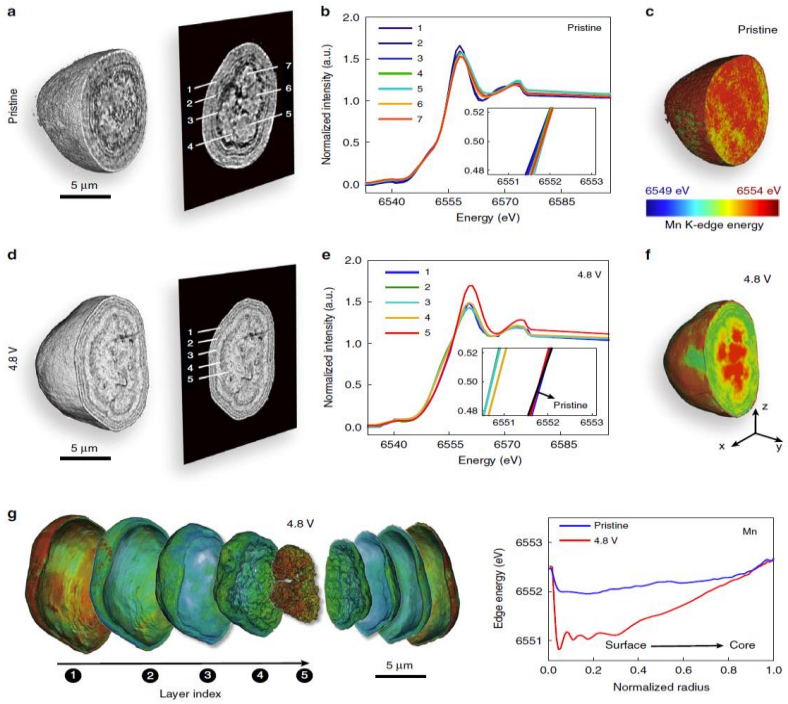

Figure 46. Spectro-microscopic investigation of Li-rich NMC particles. (a-c) On a pristine particle. (d-g) On a charged particle (at 4.8 V in the first charge). (a/d) 3D visualizations of pristine and charged particles, with labeling of different regions of interest on the respective central xz-slices. (b/e) Manganese K-edge X-ray absorption spectroscopic fingerprints over regions of interest shown in (a) and (c), respectively. (c/f) 3D renderings of manganese valence state distribution in pristine and charged particles. (g) Detailed layer-by-layer rendering of manganese valence state in the charged particle. (h) Comparison of depth profiles of particles in (c) and (f).

Patents/Publications/Presentations

Publications

- Lukatskaya, M. R.,* D. Feng, S-M. Bak, J. W. F. To, X-Q. Yang, Y. Cui, J. I. Feldblyum, and Z. Bao.* "Understanding the Mechanism of High Capacitance in Nickel Hexaaminobenzene Based Conductive Metal−Organic Frameworks in Aqueous Electrolytes." *ACS Nano* 14, No. 11 (2020): 15919–15925. doi: 10.1021/acsnano.0c07292; Publication Date (Web): November 9, 2020.
- Yang, S-Y., D-R. Shi, T. Wang, X-Y. Yue, L. Zheng, Q-H. Zhang, L. Gu, X-Q. Yang, Z. Shadike,* H. Li,* and Z-W. Fu.* "High-Rate Cathode CrSSe Based on Anion Reactions for Lithium Ion Batteries." *Journal of Materials Chemistry A* 8 (2020): 25739–25745. doi: 10.1039/D0TA08012H; Publication Date (Web): November 9, 2020.
- Cao, L., D. Li, E. Hu, J. Xu, T. Deng, L. Ma, Y. Wang, X-Q. Yang, and C. Wang.* "Solvation Structure Design for Aqueous Zn Metal Batteries." *Journal of the American Chemical Society* 142, No. 51 (2020): 21404–21409. doi: 10.1021/jacs.0c09794; Publication Date (Web): December 8, 2020.
- Bi, Y., J. Tao, Y. Wu, L. Li, Y. Xu, E. Hu, B. Wu, J. Hu, C. Wang, J. G. Zhang, and Y. Qi. "Reversible Planar Gliding and Microcracking in a Single-Crystalline Ni-Rich Cathode." *Science* 370, Issue 6522, (2020): 1313–1317. doi: 10.1126/science.abc3167; Publication Date (Web): December 11, 2020.
- Liu, X., T. Liu, R. Wang, Z. Cai, W. Wang, Y. Yuan, R. Shahbazian-Yassar, X. Li, S. Wang, E. Hu, X-Q. Yang, Y. Xiao, K. Amine, J. Lu,* and Y. Sun.* "Prelithiated Li-Enriched Gradient Interphase toward Practical High-Energy NMC–Silicon Full Cell." *ACS Energy Letter* 6 (2021): 320–328. doi: 10.1021/acsenergylett.0c02487, Publication Date: (Web): December 31, 2020.

Task 2.4 – Probing Interfacial Processes Controlled Electrode Stability in Rechargeable Batteries (Chongmin Wang, Pacific Northwest National Laboratory)

Project Objective. The main objective is to explore interfacial phenomena in rechargeable Li-ion batteries of both solid-state and LE configuration, to identify the critical parameters that control the stability of interface and electrodes as well as SE. The outcome will be establishing correlations between structural-chemical evolution of active components of batteries and their properties. These correlations will provide insight and guidance to battery materials development groups for developing high-performance battery materials.

Project Impact. The proposed characterization work focuses on atomic-level structural and chemical analysis and direct correlation with battery fading properties. The work can be directly used to guide design of electrode materials with tailored microstructure and chemistry for enhanced properties of increasing the energy density of Li-ion batteries and to accelerate market acceptance of EVs, especially for PHEVs as required by the EV Everywhere Grand Challenge.

Approach. The project will use integrated advanced microscopic and spectroscopic techniques, including *in situ* S/TEM and *ex situ* S/TEM, environmental S/TEM, cryo-electron microscopy, and *in situ* liquid SIMS to directly probe the structural and chemical information during lithium deposition and stripping. Cryo-S/TEM with analytical tools, such as EDX and EELS, will be used to gain chemical and electronic structural information at the interface between lithium metal and electrolyte of both solid-state and liquid configuration, which will allow direct correlation between the morphology and chemistry. STEM – high-angle annular dark-field (HAADF) atomic-level imaging and EDX/EELS will be used to probe the interface and bulk lattice stability of cathode and SE in SSB. The work will be in close collaboration with the battery development group within the BMR and U. S.–Germany Collaboration on Energy Storage.

Out-Year-Goals. This project has the following out-year goals:

- Atomic-level multi-scale *ex situ* / *in situ* and *operando* S/TEM and cryo-S/TEM investigation on the fading mechanisms of energy-storage materials and devices in the system of both LE and SE; develop a fundamental understanding of electrochemical energy-storage processes and kinetics of electrodes.
- Develop new *in situ* and *ex situ* S/TEM capability for probing challenging questions related to energy storage technology for both solid-state and LE energy storage system.

Collaborations. This project collaborates with G. Chen (LBNL); J. Nanda (ORNL); Y. Yao (UH); K. Amine (ANL); D. Wang (PSU); A. Manthiram (University of Texas, or UT, Austin); W. Tong (LBNL); Y. Cui (Stanford University); J. Zhang (PNNL); J. Liu (PNNL); W. Xu (PNNL); X. Jie (PNNL); D. Lu (PNNL); X. Xiao (GM); Y. S. Meng (UCSD); and M. S. Whittingham (State University of New York, Binghamton].

Milestones

1. Measure the electronic properties of SEI layer and identify their dependence on the electrolyte chemistry. (Q1, FY 2021; Completed)
2. Identify the structure and chemistry of surface layer formed on lithium metal when it contacts with LE. (Q2, FY 2021)
3. Reveal the nature of reaction product and the fading mechanism of NMC cathode when in contact with SE. (Q3, FY 2021)
4. Identify the structural and chemical difference of SEI on lithium dendrite and spherical particle to gain the correlation between SEI and lithium morphology. (Q4, FY 2021)

Progress Report

The aggressive dendritic growth of lithium metal during cycling could penetrate through the separator and result in internal short-circuit of the battery. Further, the high surface area of lithium dendrite will significantly elevate the side reactions between metallic lithium and electrolyte, thus consuming both lithium and electrolyte, forming more SEI compounds, increasing cell impedance, promoting generation of electrically isolated or "dead" lithium, and consequently contributing to the low CE of lithium deposition and stripping, essentially leading to fast capacity fading and short cycle life. Lithium growth is controlled by a range of factors, including electrolytes chemistry, electrode structure, and intrinsic properties of the SEI layer. Lithium morphology is closely correlated with the SEI structure and chemistry. However, it has never been clear how these factors couple and collectively control the lithium morphology. The team explores the structural, chemical, and electronic structure of electrochemically deposited lithium metal (EDLi) and SEI.

By applying high- resolution TEM (HRTEM), EDX and EELS techniques under cryogenic conditions, the team characterizes the detailed structure and chemical distribution of EDLi and SEI layers with systematic control of current density, to establish the correlation between electrochemical performance (interfacial impedance) and current density induced structure and chemical evolution in the electrolyte of 1.2 M $LiPF_6$/EC-EMC with vinylene carbonate (VC) additive under a systematically controlled variation of current density.

The team found that the microstructures and composition of SEI (Figure 47) strongly depend on the electrode material, the electrolyte (salts, solvents, and additives), and the working state of the cell. At a low current density (0.1 mA cm^{-2}), the SEI layer on the lithium whisker has a smooth surface, with a thickness of ~ 20 nm, as shown by the atomically resolved TEM image. The HRTEM image indicates the SEI layer is an amorphous structure. The interface between EDLi and SEI is atomically sharp. Under the current density of 2 mA cm^{-2}, the SEI layer is featured by the dispersion of Li_2O and Li_2CO_3 particles in an amorphous matrix. A Li_2O crystalline

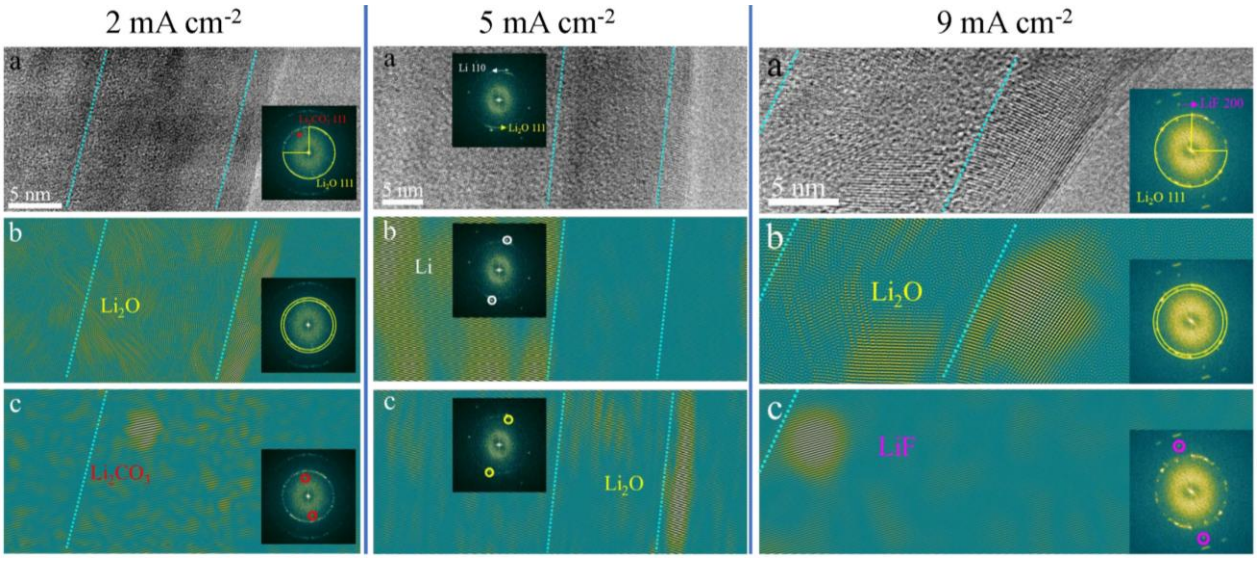

Figure 47. Structural evolution of SEI layer formed on lithium metal at different current densities, revealing dependence of SEI structure and chemistry on deposition condition. Left column: Current density 2 mA cm^{-2}. (a) High-resolution transmission electron microscopy (HRTEM) image of SEI layer formed on lithium at current density of 2 mA cm^{-2} for 5 minutes. (b) Invert fast Fourier transform (FFT) pattern shows spatial distribution of Li_2O, indicating Li_2O to form a thin layer on the surface of SEI. (c) Invert FFT pattern shows the distribution of Li_2CO_3 in the SEI. Middle column: Current density 5 mA cm^{-2}. (a) HRTEM image of SEI layer formed on lithium at current density of 5 mA cm^{-2} for 2 minutes. (b) Invert FFT pattern shows crystallinity of lithium deposit. (c) Invert FFT pattern illustrates the distribution of Li_2O, indicating a thin layer of Li_2O on the top surface of the SEI layer. Right column: Current density 9 mA cm^{-2}. (a) HRTEM image of SEI layer formed on lithium at current density of 9 mA cm^{-2} for 1.1 minutes. (c) Invert FFT pattern reveals distribution of Li_2O, demonstrating a layer of Li_2O on the SEI layer surface. (c) Invert FFT pattern shows the presence of LiF in the SEI.

layer 3 nm in thickness exists on the very surface. As the current density is increased to 5 mA cm^{-2}, a uniform SEI of a thickness of ~ 20 nm is formed on the lithium whisker. This SEI structure is similar to the SEI formed at the current density of 2 mA cm^{-2}, but without Li_2CO_3 particles embedded in amorphous matrix. The interface between the EDLi and the SEI is sharp, as similarly observed for the case of low current density (0.1 mA cm^{-2}). The SEI that is formed at very high current density (9 mA cm^{-2}) is different from those formed at lower current densities (0.1 to 5 mA cm^{-2}). Firstly, although the thickness of the amorphous matrix is similar, the surface Li_2O layer is thick, reaching 8 nm. The team found that besides the Li_2O particles, there are also LiF nanoparticles embedded in the amorphous matrix, which are not detected in SEI layers formed at lower current densities (0.1 to 5 mA cm^{-2}). LiF has a high energy barrier of 0.729 eV, which is much higher than that of Li_2O (0.152 eV) and Li_2CO_3 (0.227 eV). LiF particles also contribute to the increase of impedance due to the high energy barrier of Li-ion migration.

In terms of chemical composition, the EDLi and SEI layers are mainly comprised of oxygen and carbon at lower current densities (0.1 to 5 mA cm^{-2}). EDS mapping reveals the spatial distribution of oxygen, carbon, fluorine, and phosphorus. The carbon and oxygen maps demonstrate a core-shell structure, indicating that the SEI is mainly composed of carbon and oxygen. While at high current density (9 mA cm^{-2}), besides oxygen and carbon, high content of fluorine is distributed in lithium deposit and SEI, especially at the interface between lithium deposit and SEI.

Electron energy loss near-edge fine structure (ELNES) of lithium K-edge can be used to identify lithium related phase. Figure 48 shows the fine structures of the lithium K-edge acquired from the EDLi deposits, interfaces, SEIs, and surfaces formed at different current densities. All of the lithium K-edge spectra acquired from lithium deposited at different current densities show that the EDLi has a weak pre-peak centered at 56 eV and a main broad peak centered at 63 eV, which implies that the lithium deposits are indeed metallic. The slight peak shift (commercial Li-metal K-edge spectrum has a pre-peak centered at 55.5 eV and main broad peak centered at 62.5 eV) is attributed to the amorphous SEI covering on the EDLi. Lithium K-edge spectra acquired from the interface between EDLi and SEI, SEI layer, and SEI surface all exhibit strong Li_2O signals that are consistent with HRTEM and EDS results.

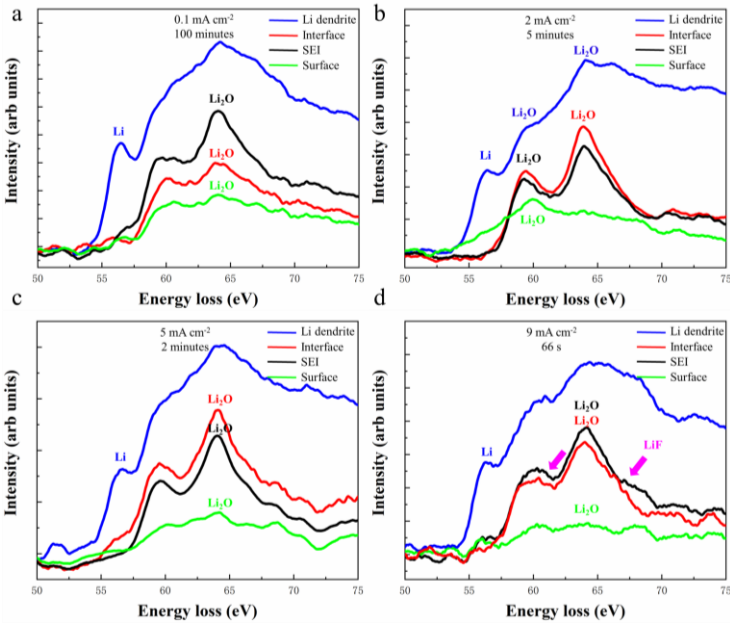

Figure 48. Comparison of electron energy loss spectroscopy (EELS) spectra of lithium metal and SEI to illustrate electronic structure evolution from lithium metal, interface to SEI at different current density. (a) 0.1 mA cm^{-2}; (b) 2 mA cm^{-2}; (c) 5 mA cm^{-2}; and (d) 9 mA cm^{-2}.

The results establish the correlation among deposition condition, lithium dendrite growth kinetics, and SEI formation mechanism. These results provide insights on the optimization of the lithium morphology and electrode-electrolyte interface by using proper deposition conditions.

Patents/Publications/Presentations

Publications

- Xu, Y., H. Wu, H. Jia, J-G. Zhang, W. Xu, and C. Wang. "Current Density Regulated Atomic to Nanoscale Process on Li Deposition and Solid Electrolyte Interphase Revealed by Cryogenic Transmission Electron Microscopy." *ACS Nano* 14 (2020): 8766−8775.
- Wu, H., H. Jia, C. Wang, J-G. Zhang, and W. Xu. "Recent Progress in Understanding Solid Electrolyte Interphase on Lithium Metal Anodes." *Advanced Energy Materials* 11 (2020): 2003092.
- Ryu, J., T. Bok, S. H. Joo, S. Yoo, G. Song, S. H. Kim, S. Choi, H. Y. Jeong, M. G. Kim, S. J. Kang, C. Wang, S. K. Kwak, and S. Park. "Electrochemical Scissoring of Disordered Silicon-Carbon Composites for High-Performance Lithium Storage." *Energy Storage Materials* 36 (2021): 139–146.

Presentation

- College of Engineering, University of Western Ontario, London, Ontario, Canada, Virtual Seminar (November 23, 2020): "Microscopy and Spectroscopy Diagnosis Guided Design of Materials for Better Batteries"; C. Wang. Invited.

Task 2.5 – Integrated Atomic-, Meso-, and Micro-Scale Diagnostics of Solid-State Batteries (Yi Cui, William Chueh, and Michael Toney; Stanford University / SLAC National Accelerator Laboratory)

Project Objective. By developing a characterization toolkit that tackles length scales (Å to mm), cell pressure (1-100 bars), and dynamics (during synthesis, fabrication, and cycling), the project aims to generate insights to engineer SSBs for deployment in EVs. This interdisciplinary team aims to achieve this objective by merging a broad range of characterization approaches as well as modeling to track the evolution of nanoscale chemistry and structure, microstructure, and transport.

Project Impact. The project will have an impact in several areas: (1) accelerate rational design of coatings and artificial SEIs in SSBs; (2) inhibit the root causes leading to cell shorting, and enable high current cycling; (3) accelerate design of cathode coating and composite electrode architectures; and (4) reduce degradation and variability during SSB manufacturing via composition and surface engineering.

Approach. The project has a multi-fold approach that will encompass the following: (1) resolve nanoscale structure and chemistry of SEIs via cryo-TEM; (2) track SE and lithium microstructure evolution in 3D via X-ray micro and diffraction tomography; (3) visualize nanoscale ionic and electronic transport at GBs via conducting AFM; (4) map current distribution in cathodes via scanning transmission X-ray microscopy (STXM); and (5) monitor nanoscale SE evolution with gas impurity via *in situ* environmental TEM (E-TEM).

Out-Year Goals. The project will develop an integrated characterization toolkit to characterize SSBs within a single cycle and over hundreds of cycles, spanning a wide range of relevant length scales.

Collaborations. Project collaborations include work with SSRL, ALS, and Advanced Photon Source (APS) synchrotron light sources.

Milestones

1. Demonstrate *operando* X-ray microscopy to track lithium reactivity with LPS SE at open circuit as a function of pressure. (Q1, FY 2021; Completed)
2. Achieve 20-nm resolution for electrochemical impedance AFM for recording ionic and electronic conductivity. (Q2, FY 2021)
3. Determine composition of reacted phase between LPS and NMC cathodes after 10 cycles using various microscopy methods. (Q3, FY 2021)
4. Demonstrate *operando* SEM and FIB to record sub-surface microstructure in LLZO during lithium plating. (Q4, FY 2021)

Progress Report

AFM is a powerful technique to probe microstructural, mechanical, and electrical properties at nanoscale. The application of AFM to investigate SSBs requires several special considerations. The most important aspect is atmosphere control, since both sulfide- and oxide-based SSBs are sensitive to air (water vapor and carbon dioxide). The team has developed and deployed a specially designed glovebox that houses an AFM. The glovebox is purged with argon continuously and is equipped with a heat exchanger to remove excess heat generated by the AFM to ensure a near-constant operation temperature for the SSB cells.

The team has developed and demonstrated several operation modes for the glovebox AFM using cells based on LLZO SEs. The first operation mode is conducting AFM, which probes the electronic conductivity within the SE. A second electrode is deposited using physical vapor deposition (PVD) method close to the region of interest. Electronic current between the probe and the second electrode is measured while scanning the probe. They have successfully demonstrated the measurement in both planar configuration and in cross-sectional configuration. Initial studies indicate GBs exhibit increased electronic conductivity; this implies that these more conductive sites provide an electrical path between the probe and the second electrode. This increased electronic conductivity is consistent with observation in standard cells.

A second operation mode is EIS AFM. Here, the electrical perturbation is applied between the probe and the second electrode. A low-magnitude AC voltage is applied as a function of frequency. Due to the extremely small electrode size on the probe, special care was taken to eliminate spurious signals, which could contribute to the capacitance and inductance. To test the setup, the team investigates a range of calibration samples including capacitive structure and metal-insulator patterns. The low-frequency impedance measures the electronic conductivity, whereas the high-frequency impedance measures the ionic conductivity. They demonstrate that the system correctly measures capacitance and conductivity variation at the nanoscale. Future work will involve measuring ionic and electronic conductivity in LLZO SSE.

A third operational mode is electrochemical AFM, where microstructure evolution is measured on thin-film current collector on top of the SE during cycling. In this mode, the SSB is cycled by applying a voltage between the thin-film current collector and the second electrode. To demonstrate the technique, the team monitored lithium nucleation on the thin-film current collector. Very small height change is detected, providing an *operando* diagnostic into the lithium plating and stripping kinetics in a so-called Li-free cell configuration.

Patents/Publications/Presentations

Presentations

- Panasonic Energy of North America, Virtual (December 4, 2020); W. C. Chueh.
- MRS Spring/Fall 2020 Meeting, Virtual (November 30, 2020); W. C. Chueh.
- Future of Electrochemistry, Max Planck Institute of Solid-State Research, Virtual (November 19, 2020); W. C. Chueh.
- Seoul National University, Department of Chemical & Biological Engineering, Virtual (November 17, 2020); W. C. Chueh.
- AABC Meeting, Virtual (November 4, 2020); W. C. Chueh.
- ALS Imaging Spectroscopy Forum, LBNL, Virtual (October 29, 2020); W. C. Chueh.
- ALS Innovations Forum, LBNL, Virtual (October 7, 2020); W. C. Chueh.

Task 2.6 – Investigating the Stability of Solid/Solid Interface (Zonghai Chen, Argonne National Laboratory)

Project Objective. The project objective is to characterize the physical/chemical properties of species at the solid/solid interfaces and to fundamentally understand the critical issues that limit the mechanical, chemical, and electrochemical stability of solid/solid interfaces at the cathode and the anode.

Project Impact. The project will lead to several areas of impact: (1) to generate knowledge that supports the rational design of materials and process development; (2) to establish structure-properties relationship of the interface; and (3) to understand the formation mechanism of lithium dendrite and to predict potential solutions.

Approach. The project approach is multi-fold: (1) understanding the physics behind the transformation between the low conductivity phase and the high conductivity phase; (2) investigating the bonding strength of the CEI using model systems; and (3) developing electrolytes with high ionic conductivity and good bonding to cathodes through cation doping.

Out-Year Goals. The project has the following out-year goals:

- Developing synchrotron-based diagnosis tools to investigate physical/chemical properties of solid/solid interface.
- Identifying mechanistic barriers that limit the chemical/mechanical/electrochemical durability of solid/solid interface.
- Developing model systems to validate the failure mechanism of solid/solid interface.

Collaborations. The project collaborates with A. Ngo (ANL), L. A. Curtiss (ANL), V. Srinivasan (ANL), Y. Ren (ANL), J. Libera (ANL), Y.Z. Liu (ANL), F. Wang (BNL), and X. H. Xiao (BNL).

Milestones

1. *In situ* electron microscopic characterization of the dendrite formation on LLZO. (Q1, FY 2021; In progress)
2. Investigation of electronic conducting path in LLZO pallet. (Q2, FY 2021; On schedule)
3. Investigation of the mechanical stability of cathode/LLZO interface using model system (Q3, FY 20201; On schedule)
4. Microscopic study of the mechanical stability of cathode/LLZO interface. (Q4, FY 2021; On schedule)

Progress Report

The compatibility between the lithium metal and the LLZO electrolyte was electrochemically investigated using Li/LLZO/Li symmetrical cells. When the current density exceeded 1 mA/cm^2, a sign of lithium dendrite formation was observed. The surface of LLZO electrolyte was surveyed using SEM. A rough surface on LLZO pallet was observed; most of the damages observed are pits that appear to be created by growth of lithium dendrite from lithium foil toward LLZO electrolyte. On the surveyed surface, there are several surficial cracks, at a special scale of sub-micrometers, on the LLZO pallet; this implies that the damage was made by growing some species inside out of the LLZO pallet.

To validate this observation, an *in situ* SEM experiment was conducted to visualize the growth mechanism of lithium dendrites. Figure 49a schematically shows the sample environment used for the *in situ* SEM experiment. Particularly, a tungsten needle was used as an electrochemical probe to supply negative potential to trigger the growth of lithium dendrite between the LLZO electrolyte and the tungsten probe. In most cases conducted, the team observed direct growth of lithium dendrite right below the tungsten probe. This observation is consistent with the prevailing belief that lithium dendrite grows from outside into the LLZO electrolyte. However, on a smaller number of cases (2 out of 12), they observed a dramatically different growth mechanism, as shown in Figure 49b-d. At the beginning of the experiment, the tungsten probe was placed at the center of one LLZO particle, which shows a smooth, clear, and continuous surface (Figure 49b). After applying negative potential for about 4 minutes, lithium dendrite growth appears from spots micrometers away from the tungsten probes (Figure 49c). The violent growth of lithium dendrite right beneath the tungsten probe was only observed after applying negative potential for about 8 minutes (Figure 49d). This observation implies that there is electronic conducting pathway inside the single LLZO particle so that electrons from the tungsten probe can be transported inside the LLZO particle, causing the growth of lithium at a location that is spatially away from the probe. This observation also implies that that such an electronic conducting pathway is not homogeneously distributed inside the LLZO particles; therefore, the new lithium growth pattern was not observed in all cases.

Due to the new working schedule under the COVID-19 pandemic, the detailed investigation on the electron conducting mechanism study will stretch into the next quarter.

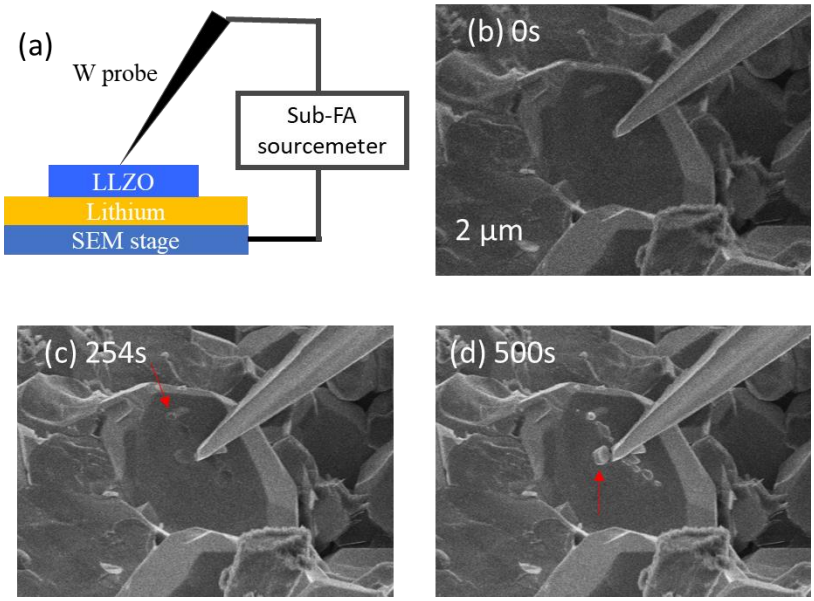

Figure 49. (a) Schematics of sample environment for *in situ* scanning electron microscopy study, and the morphology of LLZO particle during the *in situ* experiment at (b) 0 seconds, (c) 254 seconds, and (d) 500 seconds after applying a negative potential on the tungsten probe.

Patents/Publications/Presentations

The project has no patents, publications, or presentations to report this quarter.

Task 2.7 – Fundamental Understanding of Interfacial Phenomena in Solid-State Batteries (Xingcheng Xiao, General Motors)

Project Objective. The project objective is to develop a comprehensive set of *in situ* diagnostic techniques combined with atomic/continuum modeling schemes to investigate and understand the coupled mechanical/chemical degradation associated with dynamic interfacial phenomena in SSBs. Specifically, *in situ* observations and characterizations of lithium plating-stripping processes, lithium dendrite formation, interphase formation, and the induced interfacial stresses, as well as the mechanical and electrochemical properties of interfaces and interphases, are paramount. The study will provide useful guidelines for optimizing cell structure design and engineering interfaces and interphases to enable SSBs.

Project Impact. The project will provide fundamental understanding of the dynamic interfacial phenomena and the coupled mechanical and chemical degradation. In addition, it will establish a critical guideline to design safe and durable SSBs with energy density > 500 wh/kg for EV applications.

Approach. The multi-scale *in situ* diagnostic tools, including AFM, nanoindentation, dilatometer, stress sensors, and pressure cells, will be used to investigate mechanical behavior and microstructure evolution at interface/interphase during lithium plating and stripping. The information (along with Li-ion transport properties and microstructure evolution obtained using the advanced spectroscopic ellipsometry, and *in situ* TEM) will be correlated with electrochemical performance toward high cycle efficiency and dendrite-free SSBs. The goal of this understanding is to develop strategies for surface and interface engineering, apply them to commercially available SEs (including powder, pellets, and foils), and assemble SSBs for further validation and optimization, eventually extending cycle life for EV application.

Out-Year Goals. The project seeks to develop SSB model systems to capture critical mechanical properties and probe the coupled mechanical-chemical degradation by further developing comprehensive *in situ* diagnostic tools. All results obtained from these *in situ* studies, combined with advanced *postmortem* analysis and modeling, will be correlated with the cycling stability of SSBs. The *in situ* tools developed will be applied to the following two periods to deeply understand the coupled mechanical and chemical degradation of interface/interphase.

Collaborations. The co-PIs involved in experiments and simulation will be as follows: B. W. Sheldon (Brown University), Y-T. Cheng and A. Seo (University of Kentucky), Y. Qi (Michigan State University), and Q. Zhang (GM).

Milestones

1. Correlation between interfacial mechanical failure mechanisms and current density and pressure. (Q1, FY 2021; Completed)
2. Summary of the thickness, chemical bonding, and structural information of the interphases between anode and SE, and cathode and SE. (Q2, FY 2021)
3. Identified mechanisms of ionic transport through the interface/interphase. (Q3, FY 2021)
4. Multi-scale modeling framework to describe the coupled mechanical/chemical degradation. (Q4, FY 2021)

Progress Report

Incorporated Lithium Creep into the Kinetic Monte Carlo (KMC) Model to Study the Impact of Coating, Stress, and Delithiation Rate on Li-Surface Morphology

The project's previously developed multi-scale simulation framework has shown that interfacial properties (such as lithiophobic Li/LiF and lithiophilic Li/Li_2O) play an important role in maintaining smooth lithium surface during delithiation. The goal this quarter was to extend the KMC simulations to incorporate the impact of compressive stack stress on delithiation. The team considers that the mechanical stress creates a bias for lithium to hop toward the Li/SE interface. The elastic deformation has negligible impact on lithium hopping. The team's DFT calculations of lithium vacancy formation energy under a compressed strain (with the corresponding stress from 14 to 400 MPa) showed negligible differences. The elastic strain energy is on the order of 10-6 eV, which had little impact on lithium hopping barriers.

Under the stacking pressure, lithium creep cannot be neglected, given the low melting point of lithium (454 K). In the stripping process, creep effects will push the lithium atoms in the bulk toward the interface to fill the voids generated due to the stripped lithium atoms. Thus, the team converted the lithium-creep-induced lithium flux toward the interface as a bias energy for lithium hopping, and derived the formula for change in forward and backward hopping processes. Considering a lithium anode with a thickness L of 100 μm and a strain rate $\dot{\varepsilon}$ of 0.01 at 300 K, the bias energy is Ep = 0.55 eV. With the bias, all the forward rate constants are increased by at least a factor of 2, while the backward rate constants are decreased by more than 4 magnitudes. Figure 50 compares the simulated structures for Li/Li_2O (Figure 50a-b) and Li/LiF (Figure 50c-d) with (Ep = 0.55 eV) and without bias (Ep = 0 eV). In the Li/Li_2O interfaces, most vacancies are far away from the interface (deeply in the bulk) with a single vacancy in the bulk/interface transition region after imposing the bias (Figure 50a). In contrast, the systems without (Figure 50b) bias show several vacancies trapped near the interface and a few vacancies randomly distributed in the transition region. In the Li/LiF interfaces, the difference is more obvious. All the vacancies are localized in the bulk in the biased model (Figure 50c), but all are trapped in the model without bias (Figure 50d). Thus, the model can capture the impact of stack stress on lithium diffusion and filling the void generated during diffusion. More detailed studies will be performed next quarter.

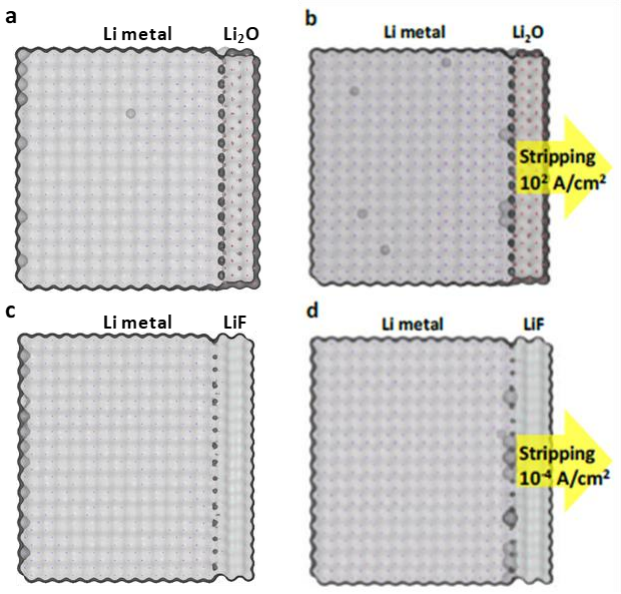

Figure 50. Kinetic Monte Carlo simulations of the stripping process. (a/c) Under stress bias (Ep = 0.55 eV, $\dot{\varepsilon}$ = 0.01), the lithium surface during delithiation is smooth at both interfaces. Without the stress, (b) the lithium surface is smooth with Li_2O layer, but (d) has trapped vacancies with LiF layer.

Investigated Effect of Pressure on Interface between LLZO and Li-Metal Electrodes

EIS was performed on a Li|LLZO|Li pouch cell under three different external pressure conditions: no pressure, low pressure, and high pressure. The lithium electrodes were first made by rolling 50-µm thick lithium foil onto copper foil, which served as the current collector. The electrodes were then punched, and nickel tabs welded to the copper. A piece of Ta-doped LLZO was first polished using isopropanol and 1200 grit paper, then allowed to dry. The LLZO pellet was placed between the lithium electrodes, and the stack was then inserted into a pouch cell. An EIS measurement was taken to determine the initial contact resistance between the lithium electrodes and the LLZO pellet before applying any external pressure. The cell was then placed in a pressure device shown in Figure 51b, and a 25-pound (11.34 kg) steel plate was placed on top of the cell, which served as the low-pressure condition. A second 25-pound steel plate was added, which served as the high-pressure condition. EIS measurements were taken immediately after pressure was applied.

Figure 51a shows the results of the EIS measurements for all three pressure conditions. Under no pressure, the EIS measurement was very noisy and followed the y-axis. This indicates a very large capacitance, and thus a very poor contact between the LLZO and lithium electrodes. Under both the low- and high-pressure conditions, the EIS measurements formed single semi-circles, similar to the case in Figure 51c. The semi-circles are indicative of the contact resistance. Overall, the contact resistance decreased with increasing pressure, showing that external pressure can improve the contact between LLZO and lithium. For future studies, a similar method will be used to study how pressure affects the contact resistance throughout cycling.

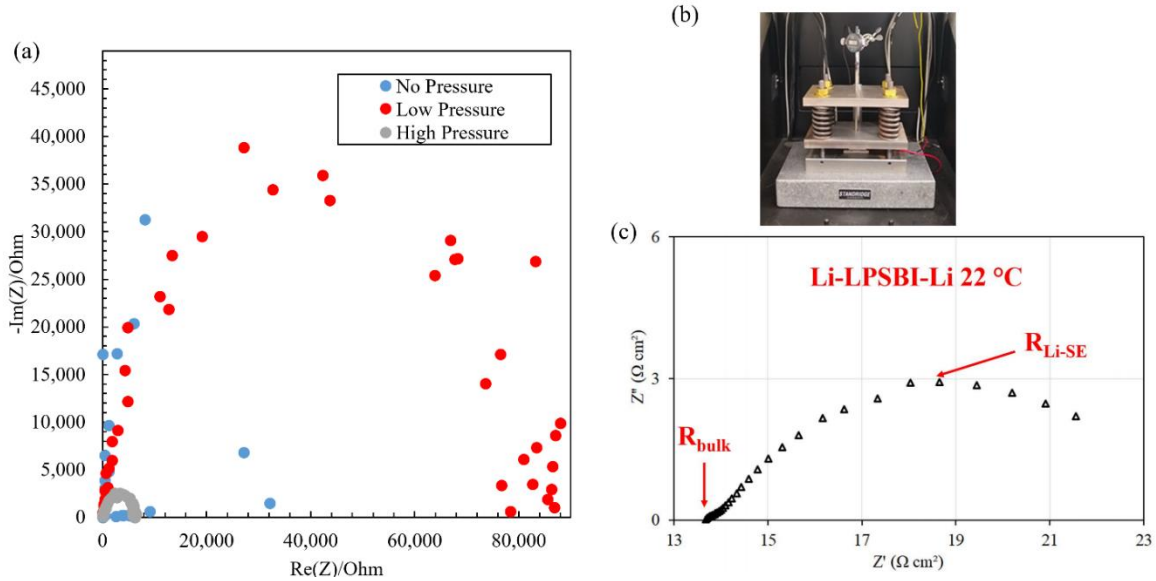

Figure 51. (a) Nyquist plot of a Li|LLZO|Li pouch cell under various external pressure conditions. (b) A pressure device used to apply and record the external pressure on the cell. (c) Image from literature distinguishing the interfacial resistance of lithium solid electrolyte versus resistance of bulk solid electrolyte.[1]

Reference

[1] Wang, Y., T. Liu, and J. Kumar. *ACS Applied Materials & Interfaces* 12 (2020): 34771–34776.

Patents/Publications/Presentations

Patent

- Xiao, X., M. Chen, Q. Zhang, and M. Cai. "A Solution-Based Approach to Protect Lithium Metal Electrode." P053352, U. S. patent application filed.

Task 2.8 – Multidimensional Diagnostics of the Interface Evolutions in Solid-State Lithium Batteries (Yan Yao, University of Houston)

Project Objective. The project objective is to develop a platform combining FIB-SEM tomography, TOF-SIMS, and in-SEM nanoindentation-based stiffness mapping for structural, chemical, and mechanical characterizations in SSLBs. Assessment of the influence of cell design and testing conditions (external pressure, current density, temperature) on the evolutions of interfaces will be performed.

Project Impact. The consolidated *in situ* structural–chemical–mechanical diagnostic platform established in this project will provide unprecedented insights into the failure mechanisms of SSLBs.

Approach. Space- and time-resolved structural, chemical, and mechanical characterizations of the cathode–electrolyte and anode–electrolyte interfaces will be performed on all-solid-state lithium batteries using FIB-SEM, TOF-SIMS, and in-SEM nanoindentation. Tasks include the following: (1) development of solid-state cell thin stacks and test-cell configurations that are suitable for *in situ* characterizations; (2) quantitative characterization and *in situ* tracking of interfacial voids formation within composite cathode and electrolyte layer; (3) identification and *in situ* tracking of the chemical composition, spatial distribution, and mechanical properties of electrolyte decomposition products at the lithium- and cathode-electrolyte interfaces; and (4) visualization, chemo-mechanical properties detection, and *in situ* tracking of lithium dendrites grown within the SE layer.

Out-Year Goals. In the out years, the project will develop thin-stack solid-state cells, micro-cells, in-SEM nanoindentation, and testing protocols. The correlation between structural evolution, electrolyte decomposition, and interfacial resistance increase will be investigated.

Collaborations. The UH team (Y. Yao, Z. Fan, and Y. Liang) works closely with the Rice University team (J. Lou and H. Guo).

Milestones

1. Nano-cell development. (Q4, FY 2021; In progress)
2. Cell optimization and electrochemical benchmarking. (Q2, FY 2021; In progress)

Progress Report

To understand the underlying capacity fading mechanism in SSBs, it is important to conduct *in operando* investigations with high spatial resolution during the charging-discharging process. To achieve this goal, the team designed and fabricated a nano-cell made from a ~ 300-µm-thick thin cell combined with Ar-beam polishing, as shown in Figure 52a. After polishing a cross-section, a 30-keV focused gallium ion beam was employed in a SEM/FIB system (the detailed fabrication process is described below) to lift out a lamella for nano-cell fabrication. The nano-cell comprising anode, electrolyte, and cathode is hundreds of nanometers in thickness and ~ 130 µm in length (see Figure 53d). Since electro-chemical reactions would occur at or near sample surface when the sample is at the length scale of a few hundred nanometers, such a design could enable direct observation of micro-structural change at high spatial resolution.

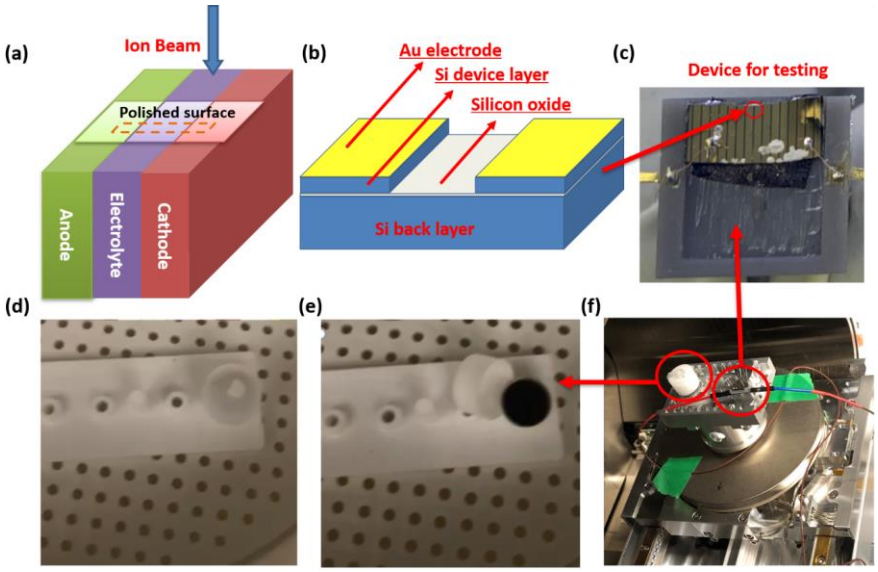

Figure 52. (a) Schematic illustration of nano-cell fabrication from polished thin-cell sample. (b) Schematic illustration of micro-fabricated device for nano-cell testing. (c) Optical image of micro-fabricated device for charging-discharging experiments. (d) Optical image of the closed pop-up scanning electron microscopy (SEM) stub. (e) Optical image of an opened pop-up SEM stub. (f) Complete *in operando* experimental configuration inside an SEM / focused ion beam (FIB) system.

Figure 52b shows a micro-fabricated chip for charging-discharging the nano-cell. Gold electrodes were deposited on an SOI wafer. The SiO_2 layer serves as the insulating layer under the 10-µm-thick silicon device layer. A 100-µm-wide gap between the electrodes was formed by the standard etching process. Since the nano-cell was suspended, both the top and bottom surfaces of the sample could be fine-polished by FIB. Figure 52c shows a picture of a nano-cell mounted on a 3D-printed chip carrier. Additionally, to protect the air-sensitive thin-cell sample, a pop-up SEM stub was machined for sample transfer between the glovebox and the SEM/FIB. Figure 52d shows a picture of the closed stub with argon sealed inside. The cap on the stub automatically pops up when the environment is pumped to vacuum, as shown in Figure 52e, simulating the scenario in a SEM/FIB chamber and demonstrating the effectiveness of the pop-up stub design. Figure 52f shows the experimental setup inside a SEM/FIB, including a thin-cell sample placed in a pop-up stub and the micro-fabricated chip carrier ready for charging-discharging experiments.

The nano-cell fabrication process is described in Figure 53. First, the as-prepared thin-cell was polished by Ar-ion beam polisher to expose a cross section. The NMC cathode / LPSCl SE / $Li_4Ti_5O_{12}$ anode can be clearly visualized in Figure 53a. A ~ 2-µm-thick lamella was cut out by FIB (30 keV, 21 nA) along the area outlined by the dashed line. An in-SEM Easylift™ manipulator was employed to lift out the lamella (~ 130 µm long, ~ 30 µm wide), as shown in Figure 53b; the lamella was then transferred onto the micro-fabricated chip. The connections between the nano-cell and the chip were formed by platinum deposition. Both surfaces of the lamella were polished to reduce the lamella thickness and remove the surface redeposition. Figure 53c reveals the morphologies. The nano-cell setup could serve as a platform for investigating the evolution of structural

and chemical properties with high spatial and chemical resolution. The team is optimizing the process to improve the yield. Detailed microstructural evolutions of the nano-cell during the electrochemical test will be reported next quarter.

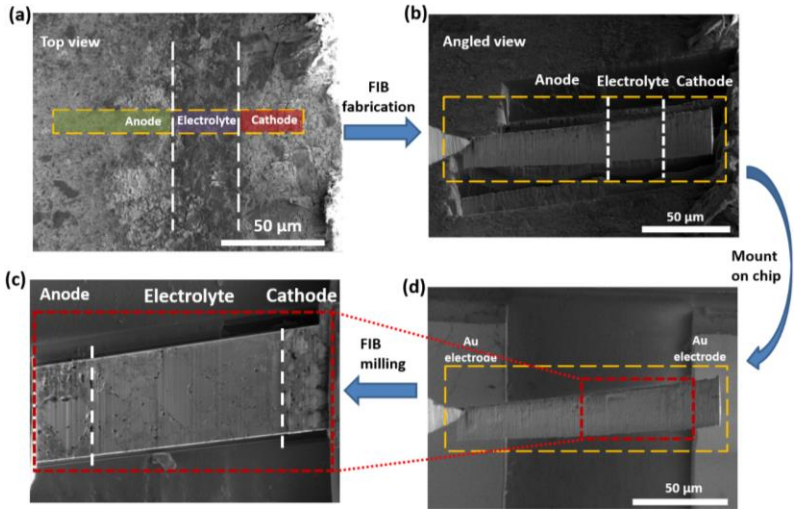

Figure 53. Nano-cell fabrication process. (a) Scanning electron microscopy (SEM) image of the polished surface of a thin-cell. (b) SEM image of a laminated thin layer prepared by focused ion beam. (c) SEM image of the nano-cell, clearly showing the anode/electrolyte/cathode configuration. (d) SEM image of the nano-cell bridging the gap of two gold electrodes for electrochemical tests.

Patents/Publications/Presentations

Publication

- Hao, F., Y. Liang, Y. Zhang, Z. Chen, J. Zhang, Q. Ai, H. Guo, Z. Fan, J. Lou, and Y. Yao. "High-Energy All-Solid-State Organic–Lithium Batteries Based on Ceramic Electrolytes." *ACS Energy Letters* 6 (2020): 201–207.

Presentations

- Mexican Energy Storage Network Webinar Series, Online (December 11, 2020): "Next-Generation Batteries for Electric Vehicles and Stationary Storage"; Y. Yan. Invited.
- UH Energy Webinar Series, Online (December 8, 2020): "Next-Generation Batteries for Electric Vehicles and Stationary Storage"; Y. Yao. Invited.
- MRS Spring/Fall 2020 Meeting, Virtual (December 1, 2020): "High-Energy All-Solid-State Organic-Lithium Batteries"; Y. Yao. Invited.
- MRS Spring/Fall 2020 Meeting, Virtual (December 1, 2020): "Charge Storage Mechanism of a Quinone Polymer Electrode for Aqueous Zinc-Ion Batteries"; Y. Yao. Invited.
- UH Department of Electrical and Computer Engineering (ECE) Luncheon, Online (October 14, 2020): "Next-Generation Batteries for Electric Vehicles and Stationary Storage"; Y. Yao. Invited.
- ECS PRiME 2020, Virtual (October 4, 2020): "Charge Storage Mechanism of a Quinone Polymer Electrode for Zinc-Ion Batteries"; Y. Zhang, Y. Liang, H. Dong, X. Wang, and Y. Yao. Contributed.
- ECS PRiME 2020, Virtual (October 4, 2020): "Solution-Processable All-Solid-State Batteries: Insights for Uniform Coatings"; B. Emley, J. Zhang, Y. Liang, C. Wu, Z. Chen, Z. Fan, and Y. Yao. Contributed.

TASK 3 – MODELING

Summary and Highlights

Achieving the performance, life, and cost targets outlined by VTO will require moving to next-generation chemistries, such as higher capacity Li-ion intercalation cathodes, silicon and other alloy-based anodes, Li-metal anode, and sulfur cathodes. However, numerous problems plague development of these systems, from material-level challenges in ensuring reversibility to electrode-level issues in accommodating volume changes, to cell-level challenges in preventing cross talk between the electrodes. In this task, a mathematical perspective is applied to these challenges to provide an understanding of the underlying phenomenon and to suggest solutions that can be implemented by the material synthesis and electrode architecture groups.

The effort spans multiple length scales, from *ab initio* methods to continuum-scale techniques. Models are combined with experiments, and extensive collaborations are established with experimental groups to ensure that the predictions match reality. Efforts also focus on obtaining parameters needed for the models, either from lower-length scale methods or from experiments. Projects also emphasize pushing the boundaries of the modeling techniques used to ensure that the task stays at the cutting edge.

A major focus of the effort is around Li-metal-based SSBs. While these chemistries hold promise, numerous challenges such as reactivity, conductivity, and mechanical stability prevent their commercialization. Mathematical models are ideal to provide the guidance and insights needed to solve these issues.

In the area of Li-metal anodes, the focus is on understanding how materials can be designed to prevent dendrite growth using continuum modeling approaches, combined with calculations on mobility in solid conductors. The results are used to guide materials development by providing the properties needed to prevent dendrites, while also achieving the energy and power goals. Models examine the role of the SEI on the morphology of the dendrite and describe the mechanical-electrochemical coupled effects that are critical for dendrite formation. Finally, efforts are focused on discovery of new solid ion conductors with properties that far exceed existing materials. The focus is on using these models as a guide before embarking on extensive experimentation.

Lithium metal with SEs will be paired with cathode materials, often intercalative in nature. Models are being developed to examine the solid-cathode interface in Li-metal based systems, where side reactions and interface debonding issues are known to limit cycling. These models are being used to understand how to prevent chemo-mechanical failure at the interface. Coatings, an effective strategy for high-voltage operation, are being explored with the aim of providing a rational design approach for new coating materials. In addition, focus is paid to porous electrodes with cathode particles to predict the impact of heterogeneities on electrode behavior.

Highlight. With growing evidence that the dissolution process of lithium metal during discharge is another bottleneck for uniform cycling in SSBs, the modeling efforts have moved to shed light on this process. V. Srinivasan and coworkers have used mesoscale models to study Li/LLZO interface and the dissolution of lithium. The model captures the impact of surface and bulk diffusion on void formation and performance. Depending on the operating conditions, delamination of the lithium from the SE represents a failure model for the system. The models provide insight into how best to operate the cell to avoid delamination.

Task 3.1 – Characterization and Modeling of Lithium-Metal Batteries: First-Principles Modeling and Machine Learning
(Kristin Persson, Lawrence Berkeley National Laboratory)

Project Objective. This project supports VTO programmatic goals by developing next-generation, high-energy cathode materials and enabling stable cathode operation at high voltages through target particle morphology design, functional coatings, and rational design of electrolytes. The end-of-project goals include the following: (1) understanding of the factors that govern charge transport in nonaqueous, superconcentrated LEs, (2) critical surface and coating design and optimization strategies that will improve cycling of Li-ion battery cathodes by reducing cathode degradation from oxygen loss, and (3) simulation and ML of the early formation of the SEI on Li-metal electrodes.

Project Impact. This project is aimed at providing fundamental insights into the atomistic mechanisms underlying surface reactivity and performance of Li-ion cathode materials and electrolytes with the ultimate goal to suggest improvement strategies, such as coatings, surface protection, novel electrolyte formulations, and particle morphology design. Transport modes as a function of solvent and salt concentrations will be clarified, and a data-driven reaction network framework will be designed and implemented to predict early SEI formation on lithium metal.

Approach. First-principles calculations, both static and dynamic approaches, are used to model SSE material thermodynamics and kinetics. LEs are modeled through coupled classical MD and first-principles methods to accurately capture solvation structure as well as reactivity of the liquid system. The reaction network is built on large-scale first-principles data, using graph theory and ML models.

Out-Year Goals. Electrolyte work will be aimed toward understanding the atomistic interactions underlying performance of lithium electrolytes, specifically elucidating conductivity (as a function of salt concentration) and impact on the charge transport mechanisms at play. Amorphous coatings will be evaluated based on ionic transport metrics and thermodynamic stability. The reaction network will be tested against known interfacial species forming on lithium metal in $LiPF_6$/EC electrolytes.

Collaborations. This project is highly collaborative between BMR PIs G. Chen (LBNL), G. Ceder (UCB), and R. Kostecki (ANL). Improved coating formulations will be examined by Chen and Ceder, and interfacial reactivity insights corroborated by Kostecki.

Milestones

1. Compete finite T phase diagram of L-P-S system (Ceder). (Q1, FY 2021; In Progress)

2. Quantify the conduction mechanisms in superconcentrated LiTFSI/EC (McCloskey). (Q2, FY 2021; In Progress)

3. Complete neural network – force field (NN-FF) theory/simulation for lithium transport in LE and combine it with classical force field (Wang). (Q3, FY 2021; In Progress)

4. *Go/No-Go Decision*: Develop a valid model for amorphous structure as compared to experimental RDF data (Persson). (Q4, FY 2021; In Progress)

Progress Report

One project goal is aimed toward modeling amorphous surface films using a series of large-scale *ab initio* molecular dynamics (AIMD) simulations.[1] The amorphous structure is generated by implementing a "liquid-quench" process, in which heating, equilibration, and quenching are done through an AIMD workflow. To generate a liquid phase of the amorphous structure, the structure is "heated" at a temperature that is higher than the material's melting point. At a sequence of 4 ps, AIMD simulations in the NVT ensemble are employed to equilibrate the external pressure, wherein the cell volume is rescaled according to the average external pressure before the next AIMD simulation until the averaged external pressure was below 5 kbar in a 2 ps duration. The energy equilibration is achieved when the difference between the averaged energy per atom in a 2 ps duration and the averaged energy per atom in a 4 ps duration is smaller than 1 meV/atom. Next, the liquid phases were simulated for an additional 10 ps, from which 10 independent configurations were selected and quenched to 0 K, via direct DFT structure optimization, to obtain the ground-state atomic positions in the amorphous structures. The entire framework can be seen in Figure 54.

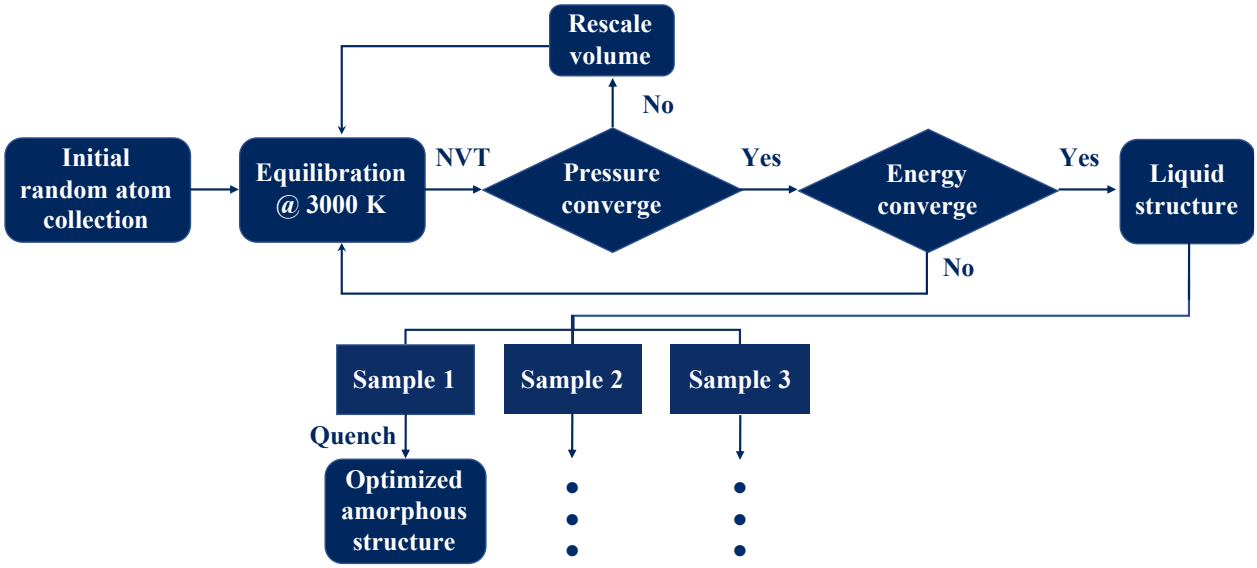

Figure 54. Framework for generation of amorphous structures.[1]

Unlike in crystalline materials, direct comparison to experimental structures is not possible; however, the team has compared the RDFs and local structure within the amorphous structures to experimental data and found reasonable agreement. The comparison of the RDF of amorphous Al_2O_3 generated through the project's liquid-quench process and experimental data obtained through X-ray and neutron diffraction is presented in Figure 55. The RDFs for each element pair agree well with the amorphous Al_2O_3 prepared by anodic oxidation of aluminum foils.

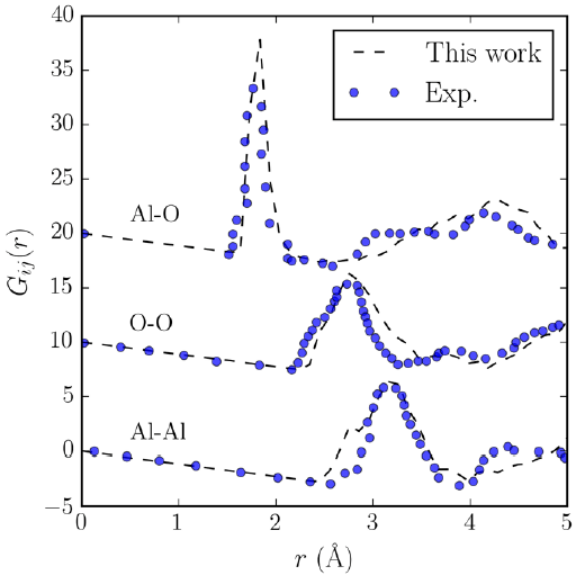

Figure 55. Radial distribution functions (RDFs) of amorphous configurations.[2] Comparison of the partial RDFs of *ab initio* molecular dynamics + density functional theory relaxation computed amorphous Al_2O_3 snapshots with experimental data from Lamparter and Kniep. $g_{ij}(r)$ is converted to the $G_{ij}(r) = 4r[g_{ii}(r) - 1]$ for comparison.

The team also investigated more in-depth the local structures within the Li-Si system, characteristic of the compositions of a when-lithiated silicon anode in a Li-ion battery. They compare the formation of silicon clusters/aggregates to those present during *in situ* NMR studies by Key et al.[3] They find that lithiation breaks up the networked silicon structure, quickly forming chains, rings, and dumbbells that contain 2-5 silicon atoms, in agreement with the NMR studies. At high lithium content (> Li_3Si), the presence of predominantly silicon dumbbells and isolated silicon is observed. Similarly, in their NMR studies, Key et al. find that $Li_{13}Si_4$ is the threshold for which clusters are observed, after which only dumbbells and isolated silicon are found.

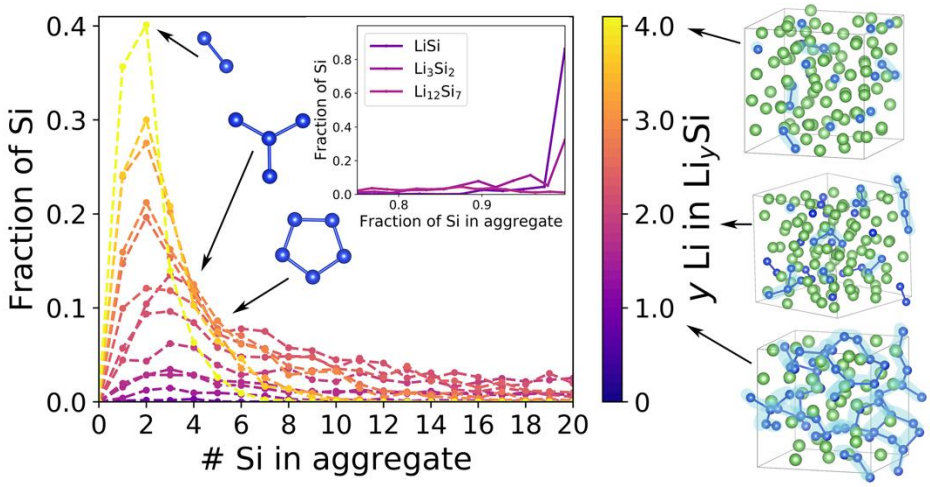

Figure 56. Aggregation of silicon in Li_ySi for 0 < y < 4.2, where the x-axis indicates the size of the silicon group and y-axis shows the fraction of silicon in each group size. Color indicates composition, as seen on the color scale. Inset shows the aggregation of silicon in networked regime, with x-axis indicating fraction of silicon in the simulation cell that composes the aggregate. Representative structural motifs are highlighted to the right, with silicon atoms shown in blue and lithium atoms in green.[4]

References

[1] Aykol, M., and K. A. Persson. "Oxidation Protection with Amorphous Surface Oxides: Thermodynamic Insights from *Ab Initio* Simulations on Aluminum." *ACS Applied Materials & Interfaces* 10, No. 3 (2018): 3039–3045.

[2] Aykol, M., S. S. Dwaraknath, W. Sun, and K. A. Persson. "Thermodynamic Limit for Synthesis of Metastable Inorganic Materials." *Science Advances* 4 (2018): eaaq0148.

[3] Key, B., et al. "Real-Time NMR Investigations of Structural Changes in Silicon Electrodes for Lithium-Ion Batteries." *Journal of the American Chemical Society* 131 (2009): 9239–9249.

[4] Sivonxay, E., M. Aykol, and K. A. Persson. "The Lithiation Process and Li Diffusion in Amorphous SiO_2 and Si from First-Principles." *Electrochimica Acta* 331 (2020): 135344.

Patents/Publications/Presentations

The project has no patents, publications, or presentations to report this quarter.

Task 3.2 – Electrode Materials Design and Failure Prediction (Venkat Srinivasan, Argonne National Laboratory)

Project Objective. The main project objective is to develop computational models for understanding the various degradation mechanisms for next-generation Li-ion batteries. This year's goal is to use the continuum-based mathematical model to investigate interfacial stability between Li-metal electrodes and SEs during deposition and dissolution of lithium under externally applied currents. Both soft polymer and hard ceramic type electrolytes will be investigated. The team also aims to develop a computational model for understanding the interdiffusion of ions and its impact on other degradation mechanisms at the CEI. Ceramic-based SEs are expected to enable high-energy-density and liquid-free, safe, next-generation Li-ion batteries. Li-metal anodes should be incorporated due to their substantially larger volumetric and specific capacity, as compared to present day graphite-based anodes. During charge, lithium dendrites are observed through the SEs, which are supposed to occur because of the non-uniform current distribution at the Li/electrolyte interface. Interfacial detachment between the lithium electrode and SE have been observed during electrochemical dissolution of lithium (or, the stripping process), which can lead to nonhomogeneous contact and substantially higher charge transfer resistance between the electrode and electrolytes. Similar issues have also been observed at the Li/polymer-electrolyte interface during lithium stripping, which will be investigated thoroughly. On the cathode side, diffusion of TMs into the SEs, along with delamination between cathode and SE, leads to increased interfacial resistance. The side reaction between cathodes and SEs is a bigger issue for the sulfides as compared to the oxide-based ceramics, whereas the delamination is supposed to be more dominant within the oxides. The developed computational model will be used to investigate the impact of physicochemical and transport properties of the SE on the overall interfacial degradation observed at both the cathode and anode sides. The main focus will be to elucidate interfacial issues and devise strategies to enable successful implementation of SE in next-generation Li-ion batteries.

Project Impact. Findings from this research will give a better understanding of the factors, at the electrode/SE interface, limiting the cycle life of SE-based Li-ion batteries. These results will help to enable all solid-state Li-ion batteries.

Project Approach. The approach used here is to develop mesoscale models based on governing principles at the continuum level to describe the critical processes occurring in the materials. Electrochemical, microscopic, and spectroscopic data from experiments are combined with theories for parameter estimation and model validation. The model is then used to provide insights and guidance for design of new materials.

Out-Year Goals. At the end of this project, a computational framework will be presented that is capable of estimating lithium stripping and interdiffusion of ions at electrode/electrolyte interface.

Collaborations. This project collaborates with L. A. Curtiss, A. T. Ngo, and C. M. Phatak at ANL.

Milestones

1. Develop a mesoscale model to capture the void formation at the Li/LLZO interface during dissolution. (Q1, FY 2021; Completed)

2. Understand current distribution around a dendritic protrusion during lithium dissolution. (Q3, FY 2021)

Progress Report

Develop a Mesoscale Model to Capture the Void Formation at the Li/LLZO Interface during Dissolution. It has been experimentally observed that voids evolve at the Li/LLZO interface during the electrochemical dissolution process. These voids are observed even if extremely good interfacial contact is developed between the electrode and the electrolyte prior to stripping. It is hypothesized that any form of surface heterogeneity, either pre-existing surface roughness, or heterogeneous reaction kinetics arising from grain/GB microstructure of the SEs, leads to non-uniform current distribution. This eventually results in excessive lithium stripping at certain places, and forms surface voids. Generation of voids brings in a new transport mechanism into picture, the "surface diffusion" of lithium, along with the conventional bulk diffusion process. This extra surface diffusion phenomena helps to understand the formation and evolution of pores at the Li/LLZO interface. In the present context, a computational model is developed that takes into consideration the surface diffusion of lithium and is capable of capturing the growth of surface voids and complete delamination of cathode and ceramic SEs. A Cahn-Hilliard type equation is solved with both bulk and surface diffusion phenomena. A sink term is incorporated at the electrode-electrolyte interface, which captures the non-uniformity in current distribution and drives void formation. Butler-Volmer reaction kinetics are adopted at the Li/SE interface. Figure 57a schematically demonstrates the computational domain along with the SE where nothing is being simulated. Figure 57b-c demonstrates the evolution of the void region for different magnitudes of the surface diffusivities, where the bulk diffusivities are kept constant. It is evident that increasing the surface diffusion coefficient helps to give the void a more circular shape. The team notes that all these simulations started with a small pre-existing pore at the Li/electrolyte interface, as shown in Figure 57a.

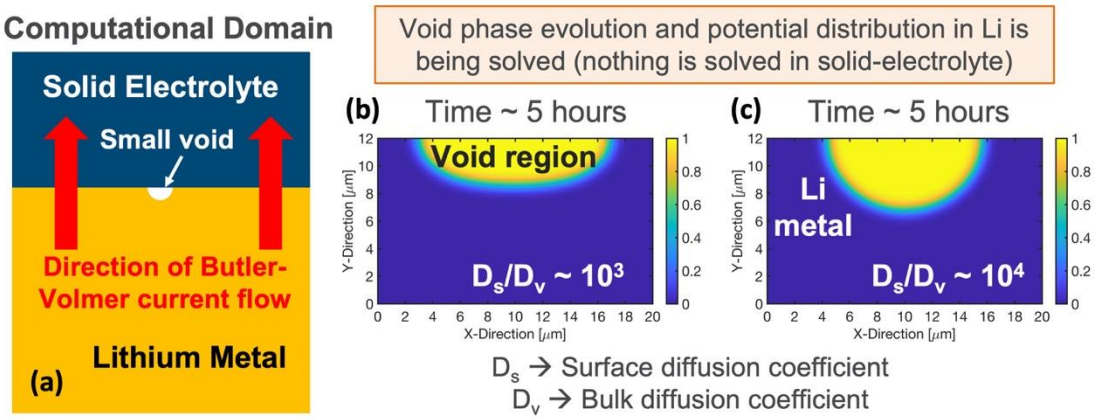

Figure 57. (a) Schematic of the computational domain where evolution of the surface void is being investigated. Flow of current and evolution of void space within lithium is studied. Nothing is being solved in the electrolyte. (b-c) Snapshot of a void after 5 hours of stripping, with ratio of surface over bulk diffusion coefficient being 10^3 and 10^4, respectively.

Influence of void formation on cell potential is plotted in Figure 58, which increases rapidly once the void starts to span across the entire domain. Increasing the current density aggravates the propagation of voids, and much earlier delamination is observed. Development of this mesoscale model, capable of capturing the formation and evolution of pores at Li/electrolyte interface, successfully completes the milestone for this quarter.

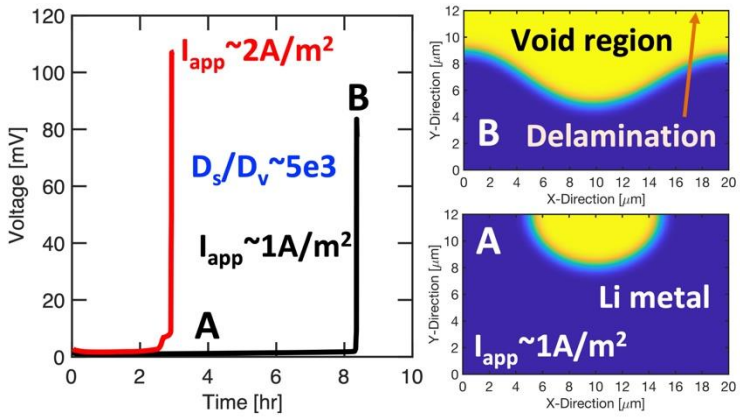

Figure 58. Voltage versus time response during the evolution of a void at the Li/electrolyte interface. Due to higher exchange current densities, the potential drop at interface is minimal. However, as the voids start to span the entire domain, the potential starts to increase rapidly. Partially and completely delaminated structures are pointed out by "A" and "B," which are obtained after lithium stripping for 4 and 8.5 hours, respectively. Increasing current density from 1 A/m² to 2 A/m² quickens the delamination process. Also, the surface diffusion coefficient is assumed to be 5 x 10³ times larger than the bulk diffusivity.

Patents/Publications/Presentations

The project has no patents, publications, or presentations to report this quarter.

Task 3.3 – Modeling of Amorphous Solid-State Conductors (Gerbrand Ceder, University of California, Berkeley)

Project Objective. SSBs are promising to achieve high energy density. The project objective is to determine the design principles needed to create SSEs with high Li-ion conductivity, while also achieving stability against common Li-ion cathodes and Li-metal anodes.

Project Impact. The project will lead to understanding the factors that control Li-ion motion in crystalline and amorphous solids and will develop strategies to create stable interfaces against lithium metal and high-voltage cathode materials. The understanding of such processes is necessary to determine design principles to develop reliable ASSBs.

Approach. HT computation is used to screen suitable SE with high electrochemical stability and high ionic conductivity, by incorporating nudged elastic band (NEB) and an AIMD method. Meanwhile, DFT is used to calculate bulk elastic constants of materials, surface energies, and interface decohesion energies of GBs. Thermodynamic interface stability is assessed from *ab initio* computed grand potential phase diagrams in which the lithium voltage can be controlled. Kinetic limits for SE decomposition are assessed by topotactic lithium insertion and removal from the SE.

Out-Year Goals. Future goals include the following: (1) gain insight into what creates high Li-ion conduction in sulfide and oxide solids, and (2) develop stable, processable solid-state conductors that can be applied in ASSBs.

Collaborations. There are no collaborative activities this quarter.

Milestones

1. Modeling of the Li_2S-P_2S_5 ground state phase diagram for SSEs: solid phases correctly modeled. (Q1, FY 2020; Completed)
2. Modeling of LPS lithium mobility in amorphous state with variations of PS_4 structural units. (Q2, FY 2020; Completed)
3. Development of model for the lithium conductivity in amorphous sulfide solids. (Q3, FY 2020; Completed)
4. Modeling of the full finite temperature L-S-P phase diagram to understand metastability of the highly conducting solids. (Q4, FY 2020; Completed)

Progress Report

Current Density Distributes Unevenly Inside Voids in the SE

Lithium metal can be deposited within voids inside the SE when both electronic current and ionic current can reach the location of the voids, and the plating potential is large enough for the lithium deposition reaction. Figure 59 plots the deposition current density at the surface of the void in the SE that is close to the anode. At the start of charging ($t = 0$), the part of the surface in yellow color, indicating the largest current, is oriented toward the anode. At time $t = 0$, lithium metal is plated on the surface of the void as the deposition is limited by the electronic current. However, the deposition current changes as more lithium metal is deposited ($t > 0$). This is because plating of metal on the inside of the void changes the electronic current, thereby modifying where the plating potential is largest.

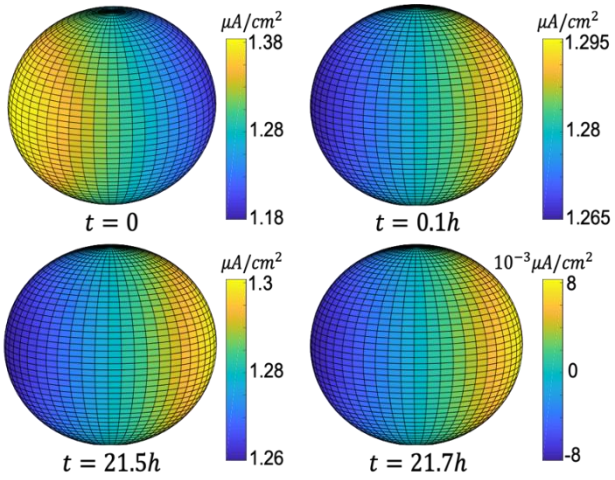

Figure 59. Current density distribution in the void.

Boundary of Void Evolves Unevenly as More Lithium Metal is Deposited

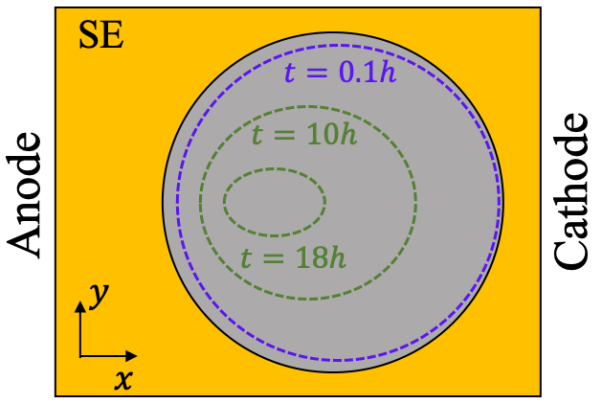

Figure 60. Evolution of the void boundary as lithium deposits inside the void.

Figure 60 shows the evolution of the metal boundary (dashed ellipses) in the void under the applied deposition current density described in Figure 59. After ≈ 0.1 hours, the total deposited thickness of lithium metal is ~ 1 nm, as indicated by the blue dashed ellipse. Meanwhile, the thickness of deposited metal on the left tip is larger than that on the right tip (blue dashed ellipses). This is because the deposition current on the left is larger than that on the right, as shown in Figure 59 before time $t = 0.1$ hours. After ≈ 10 hours of lithium deposition, the total deposited thickness of lithium metal reaches ~ 100 nm. Due to the larger current density at the cathode side ($t > 0.1$ hours in Figure 59), the thickness of lithium metal on the cathode side increased faster than that on the anode side, pushing the Li-metal boundary toward the anode side (two green ellipses).

Patents/Publications/Presentations

The project has no patents, publications, or presentations to report this quarter.

Task 3.4 – Characterization and Modeling of Li-Metal Batteries: Force Field Theory and Lithium-Sulfur Battery Simulations (Lin-Wang Wang, Lawrence Berkeley National Laboratory)

Project Objective. The project objective is to develop force field (FF) based on *ab initio* calculations to study Li-S cathode and lithium LE. It also includes designs for Li-S cathode systems for high gravimetric and volumetric capacities. Lithium diffusion in both LE in a confined space and in Li-S cathode systems is a main focus of this subtask. To enable calculation of large systems, ML-FF trained on *ab initio* calculation data will also be developed. The success of this new approach will greatly expand the capability of theoretical simulation for battery systems. ML-FF can also be used in combination with traditional classical FF to deal with the nonreactive parts of the system.

Project Impact. Making the Li-S battery a commercial reality will have a major impact on society and also help to realize the VTO goal of 500 km per charge for EV. However, the nature of chemical reaction makes it different from the traditional intercalation-based Li-ion battery. The molecular nature of Li_2S_n also allows solvation in the electrolyte. To address these problems, it is essential to have fundamental studies and understandings of the underlying mechanisms. Theoretical simulations can play an important role in discovering and designing new cathode materials. However, traditional *ab initio* calculations are limited by their computational size, while the classical FF simulations are limited by their accuracy and the lack of adequate FF. The development of ML-FF can overcome these problems by bridging the size gap between the *ab initio* simulation and the real systems that need to be studied.

Approach. ML-FF will be developed by first running *ab initio* simulations, which can generate hundreds of thousands of datasets. The project has a unique capability of decomposing the total energy of a DFT calculation into the energy of each atom. Compared to conventional DFT calculations, this increases the number of data by hundreds of times, an important requirement for ML model training. The dependence of the atomic energy to the local atomic bonding environment will be captured using ML methods. Three ML approaches will be: linear fitting, NN model, and Gaussian process regression (GPR) model. The team will compare the efficacies of these models. Meanwhile, they will also deal with the long-range Coulomb interactions existing in the electrolyte system and the ionic species in LE. The idea is to first fit the charge density of the system and also remove the long-range electrostatic energy before the fitting of the local energy on each atom. The team will design new Li-S and Na-S cathode materials. In particular, they will design an amorphous Li-S mixture, with other materials such as carbon nanotube (CNT), black carbon, or electric conductive 2D materials.

Out-Year Goals. In outgoing years, the project will further develop computational methods for more accurate entropy and interaction energy calculations for the electrolyte, as well as for Li-S cathode systems.

Collaborations. The project will collaborate with G. Liu and Y. Cui for cathode design. It has also collaborated with F. Pan of Beijing University for lithium battery research in general.

Milestones

1. Lithium charge density fitting in electrolyte, to fit the long-range Coulomb interaction. (Q1, FY 2021; Initiated)
2. Study of electrolyte behaviors, including their stability problems. (Q2, FY 2021; Initiated)
3. Incorporation of Coulomb interaction in the local energy calculation; ML-FF fitting. (Q3, FY 2021; In progress)
4. Further study of Li-S cathode with polymer, to study electric conductivity in such a system. (Q4, FY 2021; In progress)

Progress Report

The team has developed ML-FF for sulfur systems. This includes the S-S chain, and amorphous sulfur. This is to test how well the atomic descriptor (features) can be used to study such sulfur systems when there are chemical interactions for sulfur. They found it is particularly challenging to describe such an interaction due to the chain-like bonding structure in sulfur system, which implies some long-range chemical bond propagation effects might exist. They are testing new feature functions.

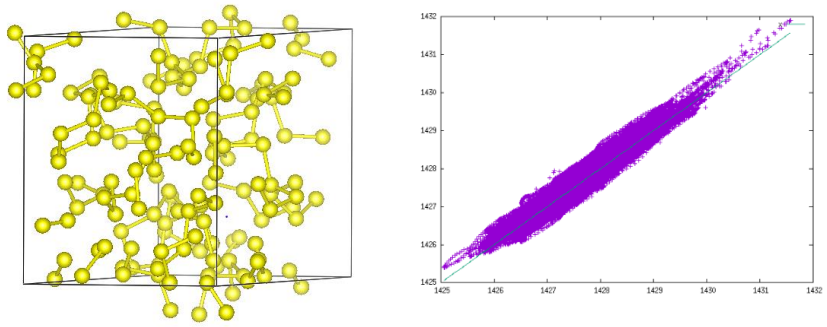

Figure 61. (left) Amorphous sulfur structures used for machine learning – force field (ML-FF) training. (right) Atomic sulfur energy fitting, the density functional theory results (vertical axis) versus the ML-FF predicted results (horizontal axis), in the unit of eV.

In another work, the team has used the fixed potential method to simulate the electrolyte EC molecule breakdown process before forming SEI. Potential governs the direction of electrochemical reactions. However, it is a challenge to simulate the effects of potential theoretically. Normally, DFT calculations are performed at a constant number of electrons, not a constant voltage. In this work, they apply a new fixed-potential method (grand canonical method) in the DFT simulation to mimic the electrochemical processes, in which the total number of electrons in the system was floated to match the 'applied voltage,' or the electrode Fermi energy at the atomic level.

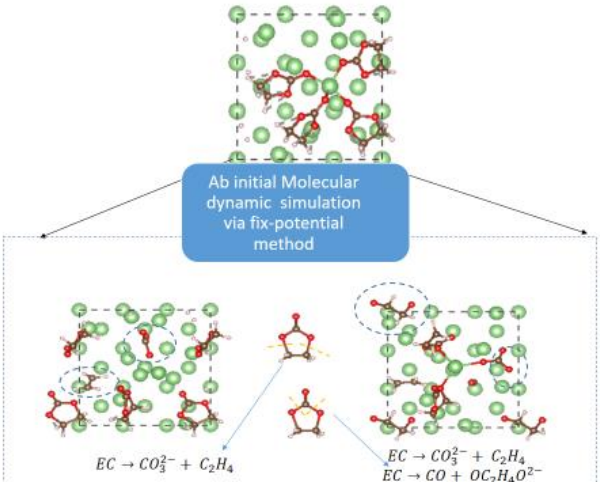

Figure 62. The possible composition of SEI obtained via *ab initio* molecular dynamics simulation under fixed potential method.

The team has investigated the decomposition of EC on the lithium anode via the fixed potential method. The goal is to understand the mechanism for formation of the SEI. With AIMD simulation via the fixed potential method, they obtained two possible composition pathways during the decomposition of EC: $EC \rightarrow CO_3^{2-} + C_2H_4$ and $EC \rightarrow CO + OC_2H_4O^{2-}$ (as shown in Figure 62). CO_3^{2-}, C_2H_4, CO, and $OC_2H_4O^{2-}$ are reported in the experimental literature. By analyzing these two decomposition pathways further next quarter, the team would like to find key factors, such as charge transfer and local atomic structures, that determine the decomposition. Based on such knowledge, they can provide suggestions for how to control the decomposition.

Patents/Publications/Presentations

The project has no patents, publications, or presentations to report this quarter.

Task 3.5 – *In Situ* and *Operando* Thermal Diagnostics of Buried Interfaces in Beyond Lithium-Ion Cells
(Ravi Prasher, Lawrence Berkeley National Laboratory)

Project Objective. Transport at various interfaces in *beyond lithium ion* cells will play a major role in electrochemical performance and reliability. It has not yet been possible to thermally profile a Li-metal cell during operation to provide a spatially resolved map of thermal transport properties throughout the cell. The objective of this research is to create a metrology capable of spatially resolved *in operando* thermal property profiling, and then to relate thermal property to the quality of electrodes and interfaces, and to use the developed thermal metrology to understand electrochemical processes in Li-metal batteries, such as dendrite growth, interface kinetics, and ionic transport.

Project Impact. Characterizing electrochemical processes in Li-metal cells such as lithium deposition and dendrite growth at interfaces is of great significance for understanding and enhancing their electrochemical performance and reliability. *In situ* and *operando* micro electrothermal sensors can provide significant information regarding the impact of buried interfaces as a function of time, material, voltage, current, temperature, etc. Therefore, it is important to develop *operando* micro electrothermal sensors and develop models relating those signals to electrochemical performance for *beyond lithium ion* cells. The physics-based model relating thermal and electrochemical properties based on these measurements can facilitate future design of Li-metal batteries.

Approach. To accomplish project goals, the team will utilize an in-house adapted 3-omega technique to probe thermal properties of a Li-metal cell while it is in operation, without affecting the operation of the cell. The 3-omega sensors will be deposited and fabricated on Li-metal cells based on previous learning on 3-omega sensor fabrication. The characteristic depth of the thermally probed region is defined by the wave's "thermal penetration depth," $\delta_p = \sqrt{D/2\omega}$, where D is the sample's thermal diffusivity, and 2ω is the heating frequency of the thermal wave. By depositing the project's 3ω sensors on the battery's outer surface and adjusting ω, the team controls δ_p to span the full range from the top to the bottom layer, thereby noninvasively probing the thermal transport in subsurface layers and interfaces within the bulk of the battery. Thermal transport can be related to quality of the interfaces. By doing concurrent thermal transport and electrochemical performance measurements, the team plans to relate thermal transport to electrochemical performance. As frequency based thermal measurement techniques provide excellent spatial resolution within the cell, the team also plans to study heat generation at the electrolyte – Li-metal interface and relate the thermal signals to the interface kinetics and ionic transport. The frequency dependence of heat generated due to transport resistance is different from that due to kinetic resistance. The team plans to utilize this difference to separate the contributions of kinetic and transport resistance at the interface, which will enable understanding of interface kinetics and transport at the Li-metal – SSE interface.

Out-Year Goals. The project will design, build, and implement the adapted 3-omega metrology to examine thermal properties and a general frequency-dependent thermal metrology to examine heat generation. This will involve developing and testing the metrology itself along with accompanying theory, designing compatible battery samples, and applying the technique to live cells. The team will measure thermal transport properties of battery materials provided by collaborators. Combined with the electrochemical performance measurement, this will provide significant information relating the thermal signal to the electrochemical process.

Collaborations. This project collaborates with two LBNL groups: V. Battaglia's for cell assembly for 3-omega studies, and R. Kostecki's for pristine battery active material growths for studies of thermal signals related to electrochemical process.

Milestones

1. Complete finite T phase diagram of L-P-S system. (Q1, FY 2021)
2. Quantify the conduction mechanisms in Li-neutralized polyanion solutions. (Q2, FY 2021)
3. Complete ML-FF theory/simulation for lithium transport in LE and LiS-polymer systems. (Q3, FY 2021)
4. Develop a valid model for amorphous structure as compared to experimental RDF data. (Q4, FY 2021)

Progress Report

Last quarter, the team described their approach of studying thermal signatures of the heat generated at multiple harmonics of the excitation current to extract the electrochemical properties of buried interfaces, which they named the multi-harmonic electrothermal spectroscopy (METS) method. They also presented a prototype design for a METS sensor and laid out an experimental plan for the verification of METS by comparing the electrochemical properties obtained from METS to those obtained from EIS on a Li-symmetric cell with Fc1N112-TFSI electrolyte.

This quarter, they worked on integrating the METS sensor on the Li-symmetric cell. They deposited the sensor on two substrates (glass slide and Kapton film) with e-beam deposition of platinum through a shadow-mask. The sensors on glass and Kapton are shown in Figure 63a-b. The team also quantified the maximum noise amplitude for 1ω, 2ω, and 4ω sensors. The noise amplitude for the signals at all three harmonics was obtained to be 1-2 μV, while the METS signal is expected to be > 20 μV, which makes the signal-to-noise ratio greater than 10.

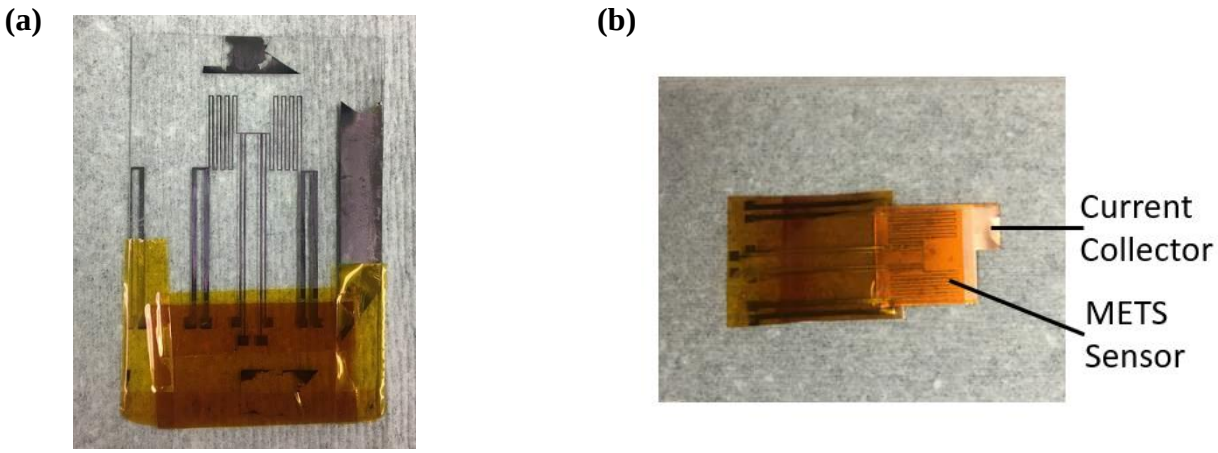

Figure 63. A multi-harmonic electrothermal spectroscopy (METS) sensor (a) deposited on glass and (b) deposited on Kapton and attached to a copper current collector.

Additionally, the team has assembled a Li-symmetric cell with a METS sensor integrated (Figure 64). Next quarter, they plan to make more cells with the METS sensors and carry out METS measurements on the cells to investigate the exchange current density, electrolyte conductivity, and SEI transport resistance.

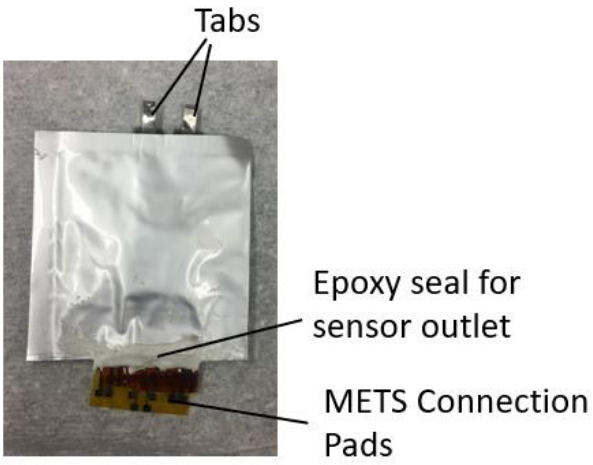

Figure 64. A multi-harmonic electrothermal spectroscopy (METS) sensor integrated on a Li-symmetric cell with Fc1N112-TFSI electrolyte.

Patents/Publications/Presentations

The project has no patents, publications, or presentations to report this quarter.

Task 3.6 – Multi-Scale Modeling of Solid-State Electrolytes for Next-Generation Lithium Batteries (Anh Ngo, Larry A. Curtiss, and Venkat Srinivasan, Argonne National Laboratory)

Project Objective. This project is part of a multi-scale modeling effort to obtain an in-depth understanding of the interaction of the electrode and the SE aimed at developing highly efficient SSE batteries for vehicle applications. Input parameters needed for mesoscale (continuum) level calculations are being obtained from atomistic calculations including DFT and classical MD simulations. This atomistic input will enable a multi-scale computational procedure for SSEs that is capable of successfully capturing the physicochemical aspects during charge and discharge process, including lithium transport mechanisms, interfacial phenomena during the insertion and extraction of lithium ions, and mechanical deformation of SSE.

Project Impact. A major safety concern experienced with commercially available Li-ion batteries under some scenarios is leakage of the LE, which can potentially catch fire. Replacement of the LE is necessary to decrease the fire hazard and improve safety associated with present-day Li-ion batteries. In addition, use of SEs provides a path to prevent dendrites in Li-metal anodes, thereby leading to batteries with significantly higher energy density. The impact of this project will be to help in development of good SSEs as a replacement for the commercially used organic LEs to improve safety and energy density in Li-ion batteries.

Approach. Parameters needed for mesoscale modeling of grain interior (GI), GB, and electrode-electrolyte interface will be calculated by DFT-based calculations along with Monte Carlo (MC) and MD simulations. The calculations will be used to determine properties of the electrode with the SE as well as in GB regions of the SE. This will include calculations of structure, stability, ionic conductivity, Young's modulus, fracture toughness, exchange current density, and other properties.

Out-Year Goals. The out-year goals of this work are to calculate other properties such as fracture toughness and include other SSEs and coatings in the multi-scale modeling.

Collaborations. This project collaborates with Y. Cui at Stanford University.

Milestones

1. Determine stable surface of the Li_6PS_5Cl SSE and the NMC-811/Li_6PS_5Cl interface. (Q1, FY 2021; Completed)
2. Conduct AIMD study of electrochemical interface between NMC-811/Li_6PS_5Cl. (Q2, FY 2021; Initiated)
3. Investigate Li-ion transport of the NMC-811/Li_6PS_5Cl interface, and calculate exchange current density. (Q3, FY 2021; Initiated)
4. Incorporate information obtained from the atomistic calculations into the mesoscale model, and predict the impact of performance. (Q4, FY 2021; Initiated)

Progress Report

SEs are expected to stabilize the Li-metal anodes due to higher stiffness than lithium, which can effectively suppress propagation of dendrites. Combination of SEs with Li-metal anodes can also improve the volumetric energy density of commercially used Li-ion batteries, as well as improve safety issues associated with them. Oxide SEs with garnet (LLZO) or NASICON (LATP) structure show extremely high elastic modulus (~ 150 GPa), which makes these solid ionic conductors non-conformable and decreases the electrochemically active surface area associated with the non-uniform Li-metal anode. On the other hand, sulfide-based SEs (LGPS, LPS) are mechanically softer (~ 20 GPa) and can potentially maintain better contact with the metal anode. These sulfide electrolytes also demonstrate better ionic conductivities (~ 1mS/cm or higher) than the oxides (~ 0.1 mS/cm). In the present research, the team will investigate the sulfide-based SE Li_6PS_5Cl, which has an argyrodite type crystal structure. Being a sulfide, it shows significantly enhanced ionic conductivities (~ 2.5 mS/cm) under room-temperature conditions, and the elastic modulus of this material is ~ 22 GPa. The inherent softness of Li_6PS_5Cl enables cold sintering of these materials with layered oxide cathodes, which effectively avoids many cathode/electrolyte side reactions. During processing, cathode/electrolyte side reactions at elevated temperatures are a major issue for several oxide-based SEs, such as NMC/LLZO.

In spite of these advantages, sulfide SEs demonstrate poor interfacial stability with both Li-metal anode as well as layered oxide cathodes, which leads to continuous capacity fade and performance decay with cycles. The major problems faced by the Li_6PS_5Cl electrolyte located adjacent to the cathode active materials are as follows:

- Interdiffusion of TM (nickel, cobalt, manganese), phosphorus, and sulfur ions and formation of a highly resistive CEI layer. Some experimental studies reveal the possible formation of phosphates (PO_4^{3-}) and sulfates (SO_4^{2-}), which can potentially increase interfacial resistance.
- Formation of space charge near the CEI due to strong attraction between lithium from electrolytes and oxygen from the cathode materials. Such a space charge layer can effectively increase interfacial resistance at the CEI.
- Oxidation and reduction of Li_6PS_5Cl itself during charge and discharge processes can substantially minimize effectiveness of the SE. For example, during charge, the SE can oxidize to LiCl, P_2S_5, and elemental sulfur. These side reactions can occur wherever there is a flow of electron.

$$2Li_6PS_5Cl \rightarrow 2LiCl + P_2S_5 + 5S + 10Li^+ + 10e^- \qquad (1)$$

Such side reactions are usually irreversible in nature because the conventional cathode cells are never operated at potentials where reduction of these side products occur (sulfur and phosphorus reduce at 2V and 1V, respectively). Such undesired side reactions may lead to very high first charge capacities with Li_6PS_5Cl SEs, but are never achieved later, not even the first discharge.

The first two phenomena mentioned above work to enhance the interfacial charge transfer resistance, which in turn aggravates the delamination-induced capacity fade. The third phenomena alters the bulk structure of the Li_6PS_5Cl electrolyte, which can substantially minimize bulk conductivity of the SE. The influence of these side reactions at the cathode/solid-electrolyte interface on the overall cell performance is investigated in this study. Strategies to mitigate these issues through application of interphase layers will also be studied using multi-scale modeling, which can provide insight into the mechanism for dendrite growth and other instabilities for guidance into how to prevent them. Mesoscale (continuum) modeling requires atomistic-level input from theory or experiment to accurately capture physicochemical aspects during charge and discharge processes.

The team has carried out *ab initio* DFT calculations on Li_6PS_5Cl (LPSCl) interfaces with NMC-811 cathode. They investigated the (10-14) surface of NMC-811, which is known to be the most stable surface and in previous literature was reported to provide apparent Li-ion conduction paths.

As an initial part of this study, the team investigated the four possible surfaces of Li_6PS_5Cl to determine which is most stable. Since the Li_6PS_5Cl surfaces can have different terminations, they also investigated four different terminations, that is, chlorine, lithium, phosphorus, and sulfur. The spin-polarized calculations were carried out with the Perdew-Burke-Ernzerhof (PBE) functional with a plane wave basis. A summary of the results for 16 possible surfaces is given in Figure 65. Six different index facets, including (100) surface with lithium and sulfur termination, (010) surface with chlorine and phosphorus termination, and (001) surface with lithium and sulfur termination, exhibit the lowest surface energy (1 meV/A^2).

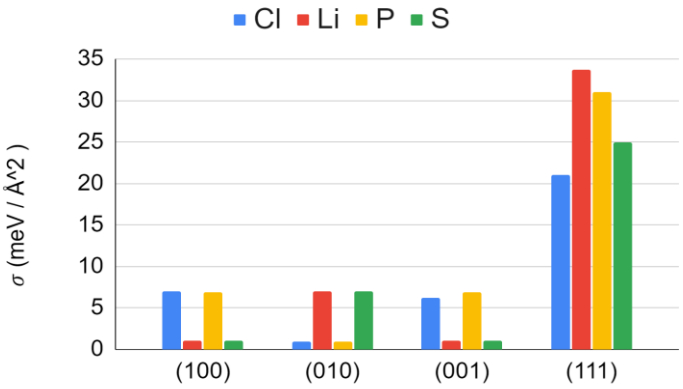

Figure 65. Surface energies from density functional theory calculations of different crystalline faces of Li_6PS_5Cl and different terminations.

The (111) surface with four terminations is generally quite high in surface energy. Based on the LPSCl surface studies, an interfacial supercell between NMC-811 cathode and LPSCl was built. The stability of the interface between the NMC-811 cathode and the lowest energy LPSCl surface [(100) lithium terminated] will be investigated with AIMD simulations as the second milestone. The calculated structure of the interface and the Li-ion migration barrier will be used for calculation of exchange current density for input into continuum-level modeling of the LPSCl/NMC-811 interface.

Patents/Publications/Presentations

The project has no patents, publications, or presentations to report this quarter.

Task 3.7 – Integrated Multi-Scale Modeling for Design of Robust 3D Solid-State Lithium Batteries (Brandon Wood, Lawence Livermore National Laboratory)

Project Objective. This project will develop a multi-scale, multi-physics modeling framework for probing the effects of materials microstructure and device architecture on ion transport within 3D ceramic SSB materials, with the goal of enhancing performance and reliability. The project has three primary objectives: (1) integrate multi-physics and multi-scale model components; (2) understand interface- and microstructure-derived limitations on ion transport; and (3) derive key structure-performance relations for enabling future optimization.

Project Impact. This project will lead to understanding interfacial losses and instabilities that impede performance and promote failure of SSBs. The multi-scale and multi-physics modeling framework developed in this work will address shortcomings of existing modeling strategies that either lack coupling of the multi-physics nature of various processes active in 3D batteries or fail to incorporate processes at different length scales to understand function. Ultimately, the tools and understanding generated by this project can be utilized to realize optimization of interface-dominated 3D batteries.

Approach. The project approach integrates simulations at three scales to predict ion transport limitations within the ceramic SSE LLZO, as well as across the interface between LLZO and $LiCoO_2$ (LCO) cathodes. A particular focus is on understanding the effects of microstructures and architectures resulting from processing of 3D SSBs as well as their mechanical and chemical evolution at different stages of cycling. First-principles and classical MD simulations are used to compute fundamental Li-ion diffusion within bulk SE and cathode materials, along/across GBs of the electrolyte, and along/across electrolyte/cathode interfaces. Next, phase-field simulations are used to generate digital representation of realistic microstructures of the materials, which are combined with the atomistic simulation results to parameterize mesoscale effective property calculations and to establish microstructure-property relationships for ion transport. Finally, these relationships inform a cell-level macroscopic electro-chemo-mechanical modeling framework, which can be used to optimize performance of ceramic 3D SSLBs based on LLZO SEs.

Out-Year Goals. Future activities will focus on applying potentials capable of scaling the atomistic interface diffusion models to longer timescales. The team will also work with collaboration partners to reconstruct microstructures of 3D-printed materials and apply them to determine effective stresses and ion transport through the polycrystalline materials. They will also further develop and validate the EIS models for connection to macroscale observables, including implementation of space-charge contributions near interfaces.

Collaborations. This project collaborates with N. Adelstein from San Francisco State University on atomistic diffusion modeling, and J. Ye from LLNL on 3D printing of SSB materials. They also partner with T. Danner and A. Latz from Deutsches Zentrum für Luft- und Raumfaurt (DLR) on impedance modeling and electrochemomechanical interface models, with P. Zapol from ANL on modeling of interfaces in LLZO, and with D. Fattakhova-Rohlfing from Forschungszentrum Jülich (FZJ) and E. Wachsman from UMD on properties of LLZO with varying densities and microstructures as part of the U. S.–Germany partnership on SSB research.

Milestones

1. Demonstrate microstructural model of stress effect on ion transport. (Q1, FY 2021; In progress)
2. Compute barriers for ion transport across LCO/LLZO interface. (Q2, FY 2021; On schedule)
3. Integrate polycrystalline diffusion model with EIS simulations. (Q3, FY 2021; On schedule)
4. Demonstrate full multi-scale EIS model using ion transport simulations of CEIs. (Q4, FY 2021; On schedule)

Progress Report

Atomistic Simulations of Li-Ion Diffusion across the LLZO/LCO Interface. This quarter, the team continued to sample the atomic structure of LLZO/LCO interface using high-temperature AIMD. Multiple snapshots were randomly chosen from the dynamics trajectories, and Li^+ diffusion pathways across the interfaces were identified. The corresponding activation energies E_a were then computed using the NEB method. The results are rendered as a histogram in Figure 66. The average E_a is found to be ~ 0.93 eV for forward diffusion (the direction for Li^+ to hop across the interface). Note that this is significantly higher than the values in both bulk LLZO and LCO (0.3 eV), implying orders-of-magnitude slower diffusion at the interface. The Li^+ diffusion pathways were also found to exhibit different values of E_a for forward and backward diffusion. As shown in Figure 66, the E_a values for backward diffusion along the diffusion channel across the LLZO/LCO interface are only ~ 0.32 eV on average. This implies that lithium ions reside predominantly near the surfaces of LLZO and LCO without moving into or across the interfacial region. Moreover, for Li^+ ions that do manage to cross the interface boundary, there is a high probability of back-hopping to the original sites, making continuous diffusion across the interface a challenge. This directly confirms the high interfacial impedance. Next quarter, the team will continue to explore the structural evolution of the LLZO/LCO interface and extract the correlation between Li^+ diffusion and local structure and chemistry. This can be used as a basis for future exploration of modifications to the interface and their effects on transport behavior.

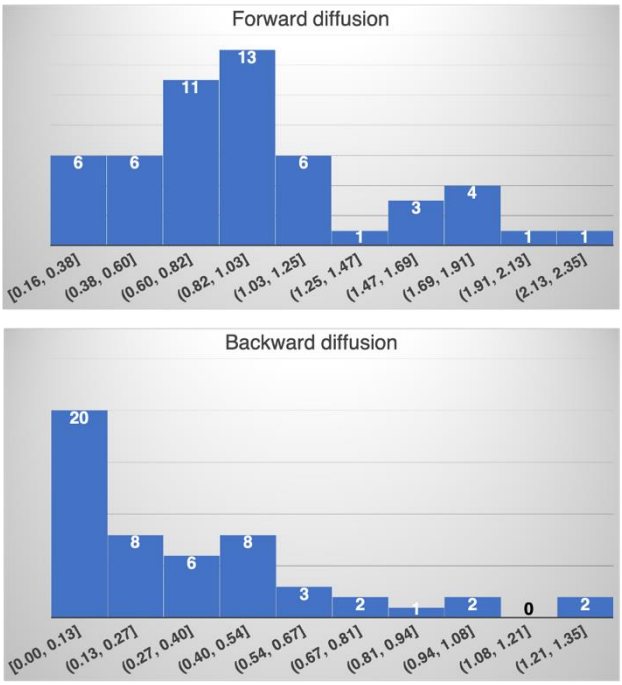

Figure 66. Histogram of calculated activation energies for lithium diffusion across the LLZO/LCO interface with ranges shown in eV.

Statistical Analysis of GB Conduction Mechanisms. In previous quarters, the team reported a "designability map" that illustrates the quantitative impact of key atomistic and mesoscale microstructural parameters on the role of GBs in the ion conduction mechanism in LLZO. These results were based on multi-scale modeling and simulations, but they did not directly account for the relative likelihood of each set of parameters in real devices. Accordingly, this quarter, the team extracted further practical information by combining the designability map with atomistically derived statistical distributions of GB diffusivity prefactor (D_0^{gb}) and activation energy (E_a^{gb}). Together, this combination can predict how likely GBs are to affect the conduction mechanism under a range of operating temperature conditions.

Specifically, the team estimated the statistical likelihood of the critical temperature T_c, which characterizes the mechanistic transition between grain-dominated and GB-dominated transport, by directly computing the joint probability $P(D_0^{gb}, E_a^{gb})$ for pairs of values of D_0^{gb} and E_a^{gb}. The statistical distributions of D_0^{gb} and E_a^{gb} were sampled from atomistic simulations of Li^+ ionic transport based on an approximate model of disordered high-angle GBs, and the joint probability was computed from the distributions as $P(D_0^{gb})P(E_a^{gb})$. Figure 67a shows the analyzed relative likelihood of T_c for different grain sizes (characterized by a unitless grain size $< \tilde{d} >$ dimension normalized by the GB width). The likelihood for T_c can provide guidance for identifying microstructural features with the best chance of controlling the dominant transport mechanisms within a relevant operating temperature window (for example, marked by the gray shaded region).

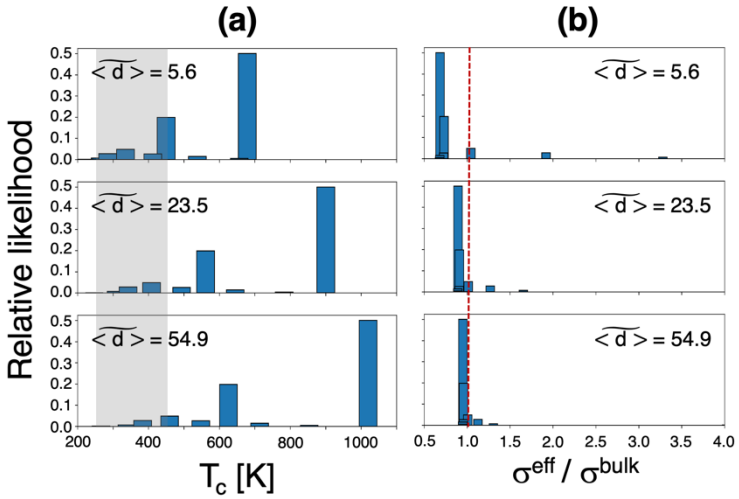

Figure 67. The computed relative likelihood for (a) the critical temperature T_c and (b) $\sigma^{eff}/\sigma^{bulk}$ at 298 K with different LLZO grain sizes.

A similar analysis was performed to compute the statistical likelihood of the ratio $\sigma^{eff}/\sigma^{bulk}$, where σ^{eff} is the overall effective ionic conductivity and σ^{bulk} is the reference bulk grain ionic conductivity at a given temperature. This quantifies the GB effect on the effective ionic conductivity at a given operating temperature: values less than unity represent GB blocking effects, whereas values greater than unity represent GB enhancement effects. The results at 298 K are shown in Figure 67b. It can be concluded that GBs are very probably blocking at 298 K for a small relative grain size of $< \tilde{d} >$ = 5.6 since the likelihood is highest for $\sigma^{eff}/\sigma^{bulk} < 1.0$ (to the left of the red dashed line). This blocking tendency clearly decreases for larger grains as the distribution of likelihood shifts toward higher values of $\sigma^{eff}/\sigma^{bulk}$. This new statistical analysis was prioritized above the stress-diffusion coupling that was the mesoscale modeling milestone for this quarter; nevertheless, the stress-diffusion coupling is in progress and will be completed next quarter.

Modeling of Microstructural Effects on EIS. Last quarter, the team reported a preliminary model to understand transport limitations in GB regions to increase the physical accuracy of the predicted EIS curve and better connect the simulations to macroscale experiments. This quarter, they extended this model to account for Li^+ GB segregation and corresponding space-charge effects, as well as their collective impacts on electrical potential distributions in polycrystalline SEs. A thermodynamically consistent model was developed with the phase-field method to predict these effects. The initial Li^+ concentrations considered are 0.5 and 0.75 M for the grain and GB, respectively, and Li^+ diffusivity (10^{-10} m^2/s) is twice in the grain than in the GB (0.5×10^{-10} m^2/s). Future iterations of the model will draw revised values directly from atomistic and mesoscale simulations. Figure 68a shows the segregation at the GB core and a shallow depletion region in a 1D domain that spans two grains separated by a GB. Figure 68b shows corresponding lithium concentration in a polycrystal and the space charge density distribution. Figure 68c shows the corresponding local electrical potential as a result of

Li^+ ion distribution across the GB. This phase-field model is now being coupled to the EIS model. This effort is being performed jointly with the U.S.-Germany CatSE partnership on SSB research, with planned incorporation into device-level models being devised at DLR.

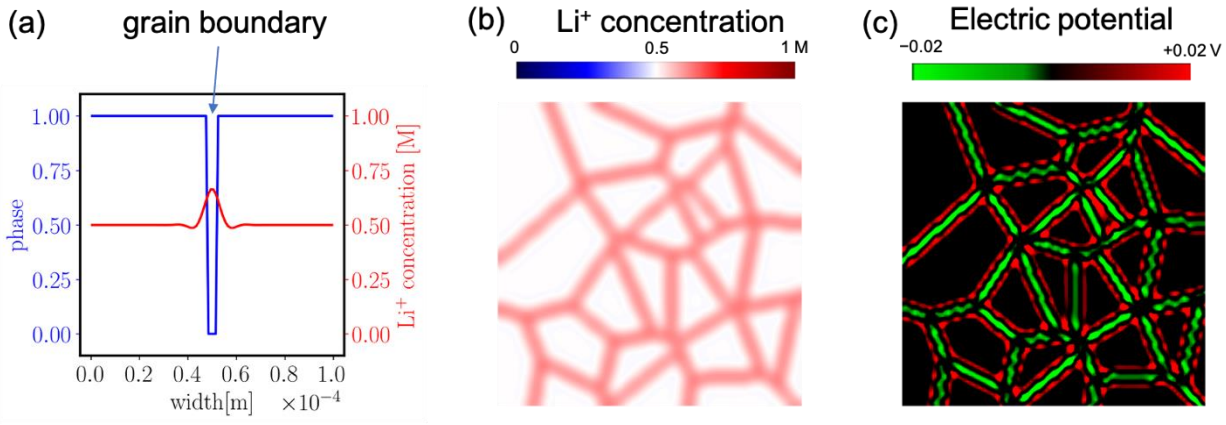

Figure 68. Grain boundary (GB) segregation of Li^+ ions using placeholder parameters. The "phase" in (a) varies between grain (= 1) and GB (= 0) regions. The steady-state concentration distribution in (b) shows GB segregation and nearby depletion of Li^+ ions, with the corresponding effect on electrical potential shown in (c).

Patents/Publications/Presentations

Presentations

- ECS PRiME 2020, Virtual (October 2020): "Understanding Kinetics of Complex Interfaces in Solid-State Batteries from Multiscale Simulations"; B. C. Wood.
- ECS PRiME 2020, Virtual (October 2020): "Integrated Modeling Framework for Investigating Multiscale Microstructural Impacts on the Ionic Conductivity of Garnet Solid Electrolytes"; T. W. Heo, A. Grieder, S. A. Akhade, L. F. Wan, N. Adelstein, and B. C. Wood.

Task 3.8 – First-Principles Modeling of Cluster-Based Solid Electrolytes (Puru Jena, Virginia Commonwealth University)

Project Objective. The objective of the project is to use cluster-ions, which are stable atomic clusters that mimic the chemistry of individual atoms, as the building blocks of new SEs for Li-ion batteries and the corresponding battery system. The advantages of using cluster-ions to replace elemental ions is that the size, shape, and composition of the former can be tailored to achieve higher superionic conductivity, electrochemical stability, and charge transfer across the solid-solid interfaces (SSIs) than the conventional materials. More specifically, the goal is to develop superior SEs based on cluster-ions and to model these SEs and their interfaces with electrodes, especially with the Li-metal anode, for successful integration into high-performance SSBs for EVs. The team will model and screen cluster-based SEs that, compared to conventional SEs, have low activation energies, practical room-temperature ionic conductivities, wide electrochemical stability windows, and desired mechanical properties that, for example, can inhibit the Li-metal anode dendrite growth. They will provide a fundamental understanding of the ionic conduction mechanism in the newly developed, cluster-based SEs and identify means to further improve property metrics via chemical and defect engineering. The team will model the interfacial properties, such as the structural, chemical, electrochemical, and ion/charge transfer properties, between the cluster-based SEs and electrodes at the atomic level, as well as find the interfacial coating materials with desired properties. Based on accumulated data from modeling, they will establish links between the basic parameters of the cluster-ions and the bulk/interface properties, which can directly guide experiments. Meanwhile, the team will work closely with experimentalists in the BMR Program to complement the project's theoretical efforts and to guide them in focused development of the predicted cluster-based SEs and the interfaces.

Project Impact. The proposed project will open a new avenue for guiding experiments in the synthesis of SSBs equipped with cluster-based SEs and capable of operating over a wide temperature range. Modeling and understanding of the ionic conduction of cluster-based electrolytes and their interfacial properties with electrodes, especially with Li-metal anode, will enrich current battery science and also train the future workforce in SSB development for next-generation EVs by supporting postdoctoral fellows.

Approach. This project will employ multi-scale theoretical methods and computational techniques.

Out-Year Goals. The out-year goals involve modeling development of new cluster-based SE materials and database.

Collaborations. The team is working with J. Nanda of ORNL on antiperovskite-based SSEs.

Milestones

1. Complete development of new cluster-based SE materials with a database. (Q4, FY 2021; Completed)
2. Structural studies of the chemically mixed systems containing both cluster-ions and elemental ions. (Q2, FY 2021; In progress)
3. Characterizations of the chemically mixed systems. (Q3, FY 2021)
4. Cation doping in the cluster-based SE systems. (Q4, FY 2021)

Progress Report

This quarter, the team has conducted MD and data analysis for ionic conductivities of the newly developed cluster-based SE materials. For each material, they studied the ionic diffusion coefficients and conductivities at different temperatures. To study the ionic conduction mechanism of these new SE materials, they established a physical model and wrote a program for analysis that allows them to answer the most basic questions regarding ion transport SEs, such as "What exactly makes these cluster-based materials have especially high ionic conductivity?" and "What are the key physical quantities that determine the ionic conductivity of the SE?"

Table 4. Cluster-ion based structures studied as candidates for electrolytes of lithium superionic conductors. A well-known typical argyrodite solid electrolyte, Li_6PS_5Cl, is listed for comparison. *Note*: EA – electron affinity of the cluster-ion; Z – number of formula units in unit cell; S – stable; INS – instable; C – electrically conducting; IC – calculated ionic conductivity at room temperature; E_a – activation energy; and band gaps – in eV.

Solid Electrolytes (SE) Type 1	Structure Identified	Z	Lattice Dynamics	Bandgap	IC (mS/cm)	E_a (eV)
Li_6PS_5Cl	○	4	S	3.4 (HSE)	0.25×10^{-3}	0.647
$Li_{6.25}PS_{5.25}Cl_{0.75}$	Nonstoichiometric Li_6PS_5Cl with Li-excess actually synthesized in the experiment				14	0.211
SE1	○	1	S	3.22 (HSE) 2.14 (mBJ)	0.23	0.342
SE2	●	1	S	4.34 (HSE) 3.18 (mBJ)	84	0.166
SE3	Nonstoichiometric configuration of SE2 with Li-excess				51	0.183
SE4	○	1	S	3.40 (HSE) 2.22 (mBJ)	1.8	0.206
SE5	Nonstoichiometric configuration of SE4 with Li-excess				14.4	0.185
SE6	○	1	S	3.34 (HSE) 2.25 (mBJ)	0.18	0.336
SE7	Nonstoichiometric configuration of SE6 with Li-excess				278	0.093
SE8	○	1	S	3.50 (HSE) 2.41 (mBJ)	0.30	0.299
SE9	○	1	S	4.39 (HSE) 3.21 (mBJ)	296	0.090
SE10	○	4	S	2.66 (mBJ)	268	0.108
SE11	●	4	S	2.32 (mBJ)	melting	
SE12	○	1	S	4.20 (HSE) 3.05 (mBJ)	78	--
SE13	●	1	S	C	13	0.242
SE14	○	1	INS	—	--	--
SE15	●	8	INS	—	--	--
SE15	○	8	INS	—	--	--
SE16	●	1	S	2.99 (HSE) 1.85 (mBJ)	103	0.101
SE17	○	2	S	3.96 (HSE) 2.87 (mBJ)	310	0.051

○The cluster-ion remains in the lowest-energy structure.
●The cluster-ion partially reacts in the structure.
—The cluster-ion is highly distorted or disintegrated in the lowest-energy structure.

The AIMD simulations are carried out for each material using a large supercell with its three sides well above 10 Å and containing hundreds of atoms. In each case, AIMD simulations are performed at 5 to 8 different temperatures. A typical AIMD simulation lasts over 120 ps with a 2 fs time step, where 20 ps is allowed for the system to reach thermal equilibrium before the data are collected to calculate the mean squared displacements (MSD) for all the atomic species in the system. The diffusivity at each temperature is then calculated by linear fitting to the MSD. Those data points of the diffusivity will be discarded if phase transitions or vibrational instabilities are spotted for elements other than lithium at high temperatures. Those remaining points are applied

to the Arrhenius relationship to extrapolate to room temperature and extract the activation energy. The team wrote a program (using Python and Fortran coding) to systematically analyze the simulated data and unravel the fast-ion transport mechanism.

Table 5. Cluster-ion based structures studied as candidates for electrolytes of lithium superionic conductors.
Note: EA – electron affinity of the cluster-ion; Z – number of formula units in unit cell; S – stable; INS – instable; C – electrically conducting; IC – calculated ionic (Li^+) conductivity at 300 K (room temperature); E_a – activation energy; and band gaps – in eV.

Solid Electrolytes (SE) Type 2	Tolerance Factor	Z	Lattice Dynamics	Bandgap	IC (mS/cm)	E_a (eV)
SE1 SE2	1.015 0.844	1	S	2.50 3.08	12 79	0.222 0.124
SE3 [a]	1.157	1	S	2.97	928 (800 K)	--
SE4	1.157	1	S	3.34	531 (600 K)	--
SE5	1.164	1	S	C	9.8	0.220
SE6	1.170	1	S	3.52	0.0	--
SE7 [a]	1.179	8	S	3.45	412 (500 K)	--
SE8 [a]	1.182	1	S	2.86	1185 (800 K)	--
SE9	1.197	1	S	C	36	0.136
SE10	1.202	8	S	1.40	0.37	0.357

[a] Calculations show that these materials exhibit little fast-ion conductivities at room temperature. In each of these cases, the Li^+ conductivity corresponds to the value at the simulated temperature specified in the parenthesis. The activation energy from the Arrhenius relationship is, therefore, unavailable.

Based on these studies, the *Go/No-Go Decision* (as set in Budget Period 1) to establish a database of new cluster-based SE materials is completely achieved. Tables 4 and 5 show key properties of the cluster-based SEs in the established database. For each material (entry) of the database, its crystalline structure, phonons, and electronic structures are also included, as demonstrated in Figure 69.

Most of the studied SEs exhibit high room-temperature ionic conductivities in the range of 10^{-4}-10^{-1} S/cm and low activation energies in the range of 0.05-0.35 eV. As shown in Table 5, a few materials are found to show fast-ion conductivities only at high simulation temperatures in the range of 500-800 K. The Li^+ conductivities at the high temperatures are in the range of 0.1-1.0 S/cm. Phase transitions, or partial melting, were observed in the superionic phases of these materials. Further chemical (for example, doping) and defect engineering may reduce the phase transition temperatures of these materials and improve the ionic conductivity at room temperature. It is also found that the boranes-based clusters in the studied materials show severe distortions from their gas-phase configurations, suggesting poor stabilities at high temperatures. However, such distortion can create large electric moments in these structures, which may enhance the ionic conductivity.

As mentioned, the team has established a model and created a program to systematically study the fast-ion transport mechanism of the new SEs. It is found that the key physical quantities that determine superionic conductivity can be categorized as (1) topological parameters, including total void space in the cell of a material, the volume of space available for the metal ions to transport, and the volume of the overlapping space between the neighboring metal ions; and (2) energy parameters, including the available energy states in the cell for the metal ions to transport and the energy states of the overlapping space between the neighboring metal ions.

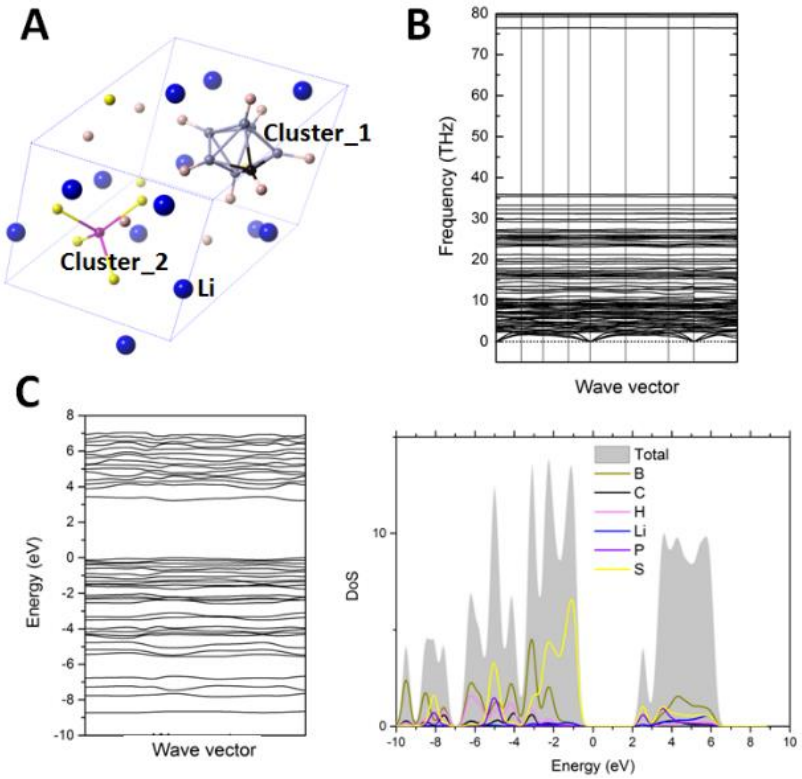

Figure 69. (a) Resulting unit cell of cluster-based solid electrolyte material that contains two types of cluster-ions with different compositions and shapes. (b) Calculated phonon spectrum of the material showing that it is lattice-dynamically stable. (c) Calculated electronic band structure showing the band gap, and density of states (DoS) showing elemental contributions.

The mechanism of a cluster-ion-based SE having high ionic conductivity is demonstrated in Figure 70. On thermal excitation, the cluster units with non-spherical shapes rotate in the structure of the material. The effect of this is that, although the total volume of the void space in the structure decreases, the volume of the space available for Li-ion to transport as well as the volume of the shared space between the neighboring lithium ion greatly increase, as shown in Figure 70a. Therefore, there are more topology states available for Li^+ to transport from one site to another. Indeed, the calculated maximum, minimum, and mean neighboring Li-Li distances, as shown in Figure 70b, suggest that lithium ions are taking advantage of these additional spaces. Meanwhile, as shown in Figure 70c, the disordered rotation of the cluster units enables more available energy states around the Li-sites toward the low energy side. These energy states become semi-continuous from around the zero energy to higher values, so that Li^+ can readily transport through these states on excitation, especially when many of these states appear at the shared space between the neighboring lithium ions. Thus, the combined topological and energetic advantages lead to the superior ionic conductivity of the cluster-based SE.

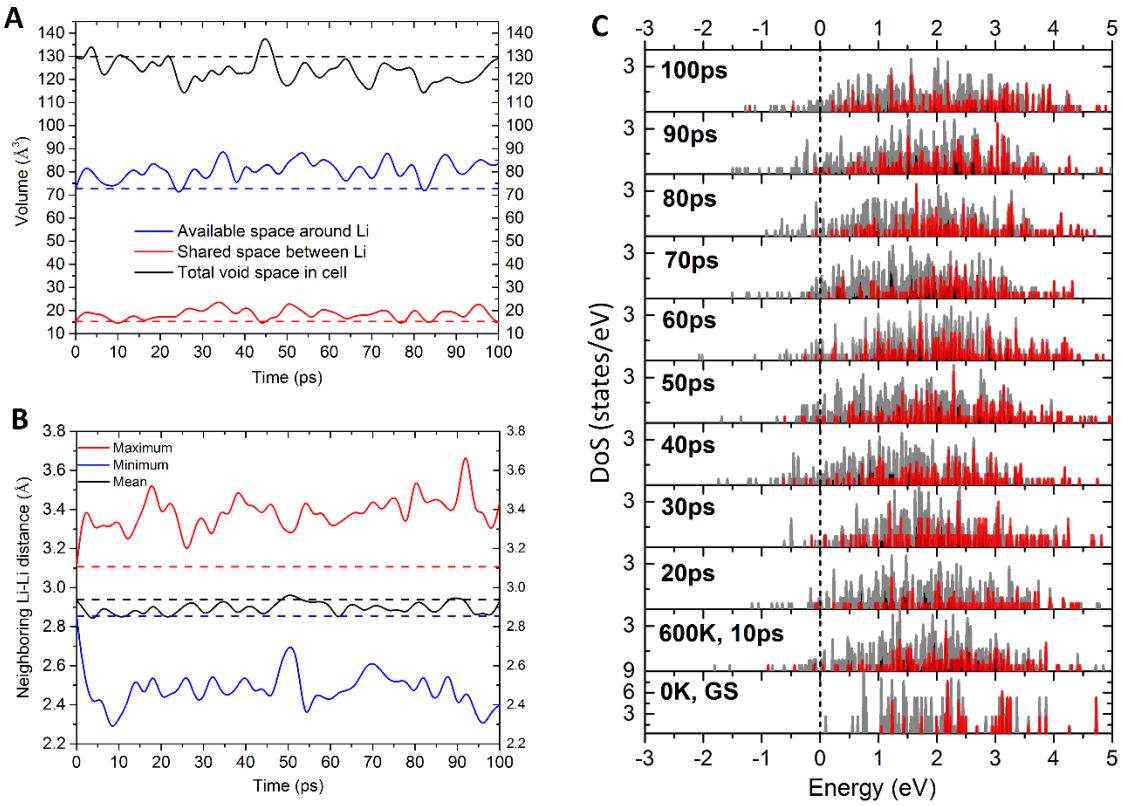

Figure 70. (a) Key topological parameters changing over the simulation time up to 100 ps for a typical cluster-based solid electrolyte. Dashed lines show values of parameters for the ground state structure at 0 K. On thermal excitation, the total volume of the void space in the cell almost always becomes smaller, while the space available for Li^+ to transport and the space shared by neighboring lithium ions become significantly greater. (b) Calculated maximum, minimum, and mean neighboring Li-Li distances throughout the simulation. Dashed lines are corresponding values for ground state structure at 0 K, for comparison. With thermal excitation, the maximum neighboring Li-Li distance becomes significantly larger, while the minimum distance becomes smaller, with the mean distance becoming larger. These suggest that the lithium ions are indeed using the available space and their shared space, as defined in (a), to transport in the cell. (c) The density of states (DoS) for the available energy states around each lithium ion (in grey) and for the energy states in the shared space between neighboring lithium ions (in red). The bottom panel shows these for the ground state structure (GS) at 0 K. Compared to the GS, on thermal excitation, the DoS disperses greatly to the low energy side. Note the big difference of the y-axis of the other panels compared to that of the bottom panel. The available energy states for Li^+ transport become semi-continuous, especially around 0 energy (where the lithium ion situates). A number of states with energy smaller than that of the lithium sites (energy states with negative values) also appear in each case. Energy states (in red) between neighboring lithium ions are across the energy band.

Patents/Publications/Presentations

Presentation

- Progress Update: Virtual EERE Meeting (January 5, 2021): "First-Principles Modeling of Cluster-Based Solid Electrolytes."

Task 3.9 – Predictive Engineering of Interfaces and Cathodes for High-Performance All-Solid-State Lithium-Sulfur Batteries
(Badri Narayanan, University of Louisville)

Project Objective. The primary goal of this project is to leverage data-driven methods and ML strategies to develop accurate multi-physics models for all-solid-state Li-S battery materials that can capture electrochemical and transport phenomena over atomic-to-mesoscopic length/timescales; these models will be rigorously validated by synthesis and advanced characterization experiments. The team will leverage the predictive power of these models, alongside synthesis/characterization experiments and battery fabrication to address longstanding issues at the electrode/electrolyte interfaces in all-solid-state Li-S batteries. The project's proposed technology involves the following: (1) halide-doped solid sulfide electrolytes that can concurrently provide high Li^+ ion conductivity and suppress dendrite growth; (2) novel mesoporous cathode composed of interconnected carbon nano-cages co-infiltrated with sulfur and sulfide electrolyte, which hold potential to allow high sulfur loading and optimal ion/electron pathways; and (3) functionalization of sulfide electrolyte with ionic liquids to improve physical contact and minimize impedance at the CEI.

Project Impact. All-solid-state Li-S batteries remain far from commercialization due to poor understanding of fundamental electrochemical/chemical and transport processes that occur at the interfaces, especially at atomic to mesoscopic scales. Successful development of proposed predictive models (at multiple scales) will bridge this knowledge gap and will advance fundamental understanding of reaction chemistry, kinetics, charge transfer, and dendrite growth at electrified SSIs. This will enable predictive design of effective strategies to mitigate interfacial problems in all-solid-state Li-S batteries, including poor interfacial contact, interfacial impedance to Li^+ ion transport, and poor electron/ion conduction within cathodes. Ultimately, the fundamental knowledge gained will lead to development of high-performance all-solid-state Li-S batteries that meet DOE targets of specific energy (350 Wh/kg @C/3), sulfur loading (> 6 mg/cm^2), and high cycle life (1000).

Approach. The project brings together innovative solutions in multi-scale materials modeling, electrolyte synthesis, fabrication of cathode architecture, and electrolyte functionalization to overcome the issues at electrode/electrolyte interfaces in all-solid-state Li-S batteries. The central idea is to employ a data-driven and ML-based approach to develop accurate multi-physics battery models at atomic-to-mesoscopic scales. This approach overcomes critical problems with existing model development methods by foregoing the need for pre-defined functional forms, introducing deep-learning technique to describe reactivity, and employing optimization methods that do not require human intuition. Multi-scale simulations based on the newly developed models will provide insights into electrochemical phenomena at electrode/electrolyte interfaces.

Out-Year Goals. In Year 1, the goal is to optimize electrolyte composition and to develop accurate reactive atomic-scale interaction models of representative SSE system and ionic liquids.

Collaborations. The team collaborates with the groups under A. Ngo and L. A. Curtiss at ANL for quantum simulations of battery systems; they plan to collaborate with J. Nanda at ORNL for advanced spectroscopic *in situ* characterization of interfaces.

Milestones

1. Extend reactive interatomic potential models to include interfaces. (Q1, FY 2021; Completed)
2. Advance characterization of CEIs to understand their reactivity, stability, and structure; validate predictions of reactive interatomic potentials. (Q2, FY 2021; In progress)
3. Utilize reactive MD to gain insights into interfacial processes, and predictively design stable interface with good ion transport. (Q3, FY 2021; In progress)
4. Fabricate batteries that meet interim performance metrics. (Q4, FY 2021; In progress)

Progress Report

This quarter, the team made good progress on (a) extending the reactive interatomic potential (Tersoff+Qeq) for Li-P-S ternary system (developed last fiscal year) to account for interfaces, (b) understanding the origin of stability of sulfide electrolyte $Li_6PS_5F_{0.5}Cl_{0.5}$ doped with two halogens using XPS, and (c) fabrication of baseline coin-cell batteries with improved CEIs by functionalizing with ionic liquids.

Extension of Reactive Interatomic Potential Models for Representative Sulfide Electrolyte (Li-P-S) System to Account for Interfaces. To improve the predictive power of the project's Tersoff+Qeq interatomic potential for electrode/electrolyte interfaces, the team refined the potential parameters by expanding their first-principles training data set to include atomic structures, energies, charges for numerous configurations of interfaces (such as Li/Li_7PS6, S_8/Li_7PS_6, Li_2S/Li_7PS_6, etc.). They are testing the performance of a newly developed set of parameters by performing preliminary MD simulations for three different interfaces containing Li_7PS_6 (LiPS) SE, namely: Li(001)/LiPS(001), S(001)/LiPS(001), and Li_2S(001)/LiPS(001). They model the anode using the most stable polymorph of lithium (body centered cubic), while the cathode is modeled at two extremes of charge state, namely: (a) fully charged: α-S_8 (cubic, *Fddd*), and (b) fully discharged: Li_2S (face-centered cubic).

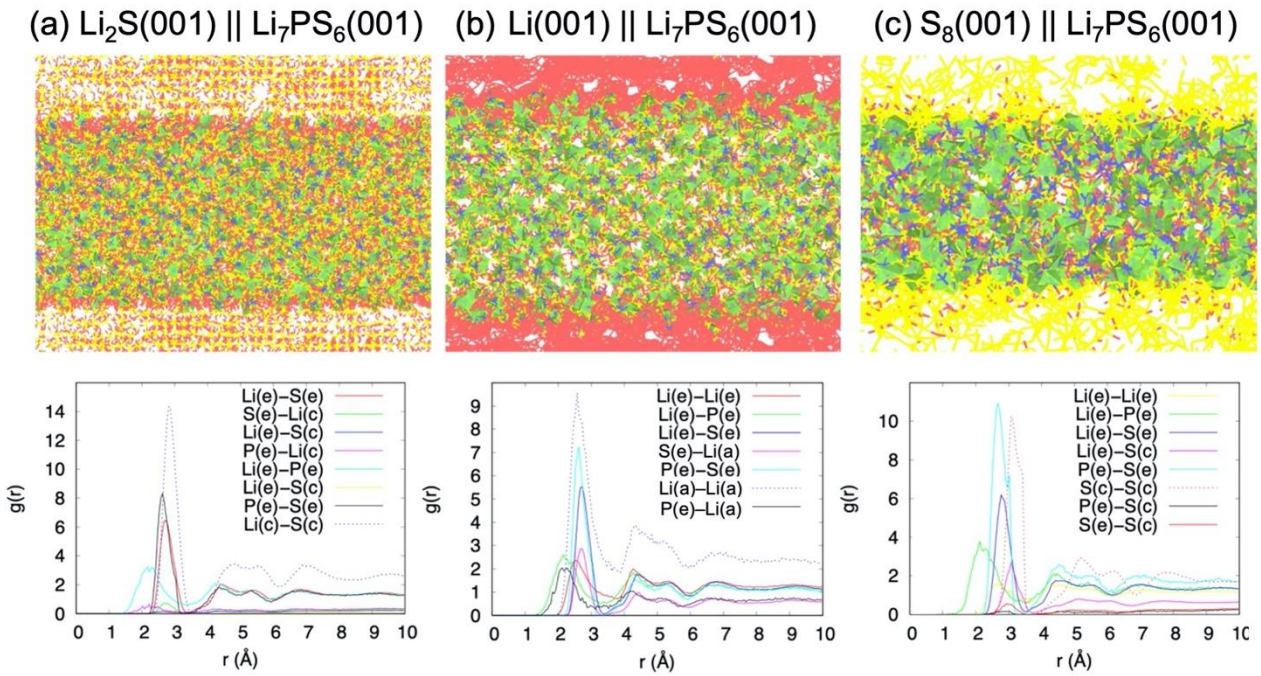

Figure 71. Equilibrated interface structures obtained from classical molecular dynamics simulations under ambient conditions. (a) Li_2S(001)/LiPS(001) Interface; (b) Li(001)/LiPS(001) Interface; and (c) S_8(001)/LiPS(001) interface. The lithium, sulfur, and phosphorus atoms are shown in red, yellow, and green colors. The PS_4^{3-} tetrahedra are shown in green. Radial distribution functions g(r) for selected atom pair types for each interface are shown in the bottom row. The labels (e), (c), and (a) identify the atoms that belong to electrolyte, cathode, and anode.

In the Li(001)/LiPS(001) interface, lithium electrode is composed of 8,880 atoms, and there are 56,448 atoms in the SSE. Similarly, for S_8(001)/LiPS(001), the S-electrode is composed of 18,432 atoms, and the SSE is built with 42,336 atoms. Finally, the Li_2S(001)/LiPS(001) consists of 25344 atoms in Li_2S electrode and 56448 atoms in SE. All the interfaces are constructed such that the epitaxial strain is < 2%. Before performing MD simulations, the interface structures are optimized using the conjugate gradient algorithm. After minimization, the team performed the equilibration run within a canonical ensemble (NVT) under ambient conditions for 0.2 ns with a timestep of 1 fs. Figure 71 shows the equilibrated structure of all three interfaces obtained from the MD simulations.

Careful analysis of the equilibrated structures shows dissociation of PS_4^{3-} tetrahedra in the SSE of all three structures due to interfacial reactions. In the $Li_2S(001)/LiPS(001)$ interface (Figure 71a), the team finds that a significant fraction of PS_4^{3-} tetrahedra break down to form PS_2, PS_3, and PS_5 clusters. New Li-P bonds also form between the lithium atom in the cathode (Li(c)) and the phosphorus (P(e)) in the electrolyte, as indicated by the first peak in the RDF for Li(c)-P(e) at ~ 2.4 Å. The RDF for the Li(c)-S(c) pairs shows characteristic peaks (albeit slightly broadened) corresponding to face-centered cubic structure, which indicates that the crystallinity of the cathode is largely retained. In the Li(001)/LiPS(001) interface (Figure 71b), the SE is composed of PS_2^+, PS_3^-, and PS_4^{3-} tetrahedra. Reactions between lithium and decomposed PS_4^{3-} yield new Li-P (first peak of Li(a)-P(e) RDF at ~ 2.1 Å), and Li-S bonds form (first peak of Li(a)-S(e) RDF at ~ 2.6 Å). These findings are consistent with previous AIMD studies reported in literature. The $S_8(001)/LiPS(001)$ interface exhibits an anomalous behavior, most of the S_8 rings in the cathode open, in stark contrast to previous AIMD reports, wherein S_8 structure remains largely unperturbed. This indicates that the Tersoff+Qeq parameters that govern the S-S interactions need to be refined further. The qualitative agreement (barring the S_8 cathode) between interface structures obtained from AIMD and classical MD simulations instills confidence in the predictive power of the newly developed Tersoff+Qeq interatomic potential. Efforts are in progress to perform experimental characterization of cathode/electrolyte and anode/electrolyte interfaces to rigorously validate the newly developed interatomic potential, and to refine the parameters for S-S interactions.

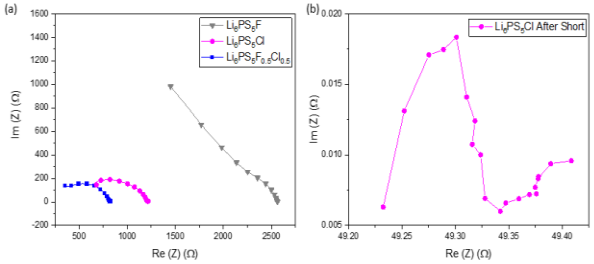

Figure 72. Impedance spectra of Li-symmetric cells with (a) Li_6PS_5F, Li_6PS_5Cl, and $Li_6PS_5F_{0.5}Cl_{0.5}$ solid electrolytes (SEs). (b) The resistance dramatically drops after a short occurs in a Li-symmetric cell with Li_6PS_5Cl as SE.

Electrochemical Characterization of Interface between Lithium Anode and Halide-Doped Argyrodite SSE. The team measured the electrochemical impedance of Li-symmetric cells with three SEs, namely, $Li_6PS_5F_{0.5}Cl_{0.5}$, Li_6PS_5F, and Li_6PS_5Cl. Before cycling, the cell with $Li_6PS_5F_{0.5}Cl_{0.5}$ as SE displays a resistance of 800 Ω, much lower than that for cells using Li_6PS_5Cl (1250 Ω) and Li_6PS_5F (2650 Ω). The resistance of Li-symmetric cells follows the trend: $Li_6PS_5F_{0.5}Cl_{0.5}$ < Li_6PS_5Cl < Li_6PS_5F, suggesting the best interface stability for $Li_6PS_5F_{0.5}Cl_{0.5}$ (Figure 72a). For the cell with Li_6PS_5Cl as SE, the resistance dramatically drops when the symmetric cells shorts on cycling (Figure 72b).

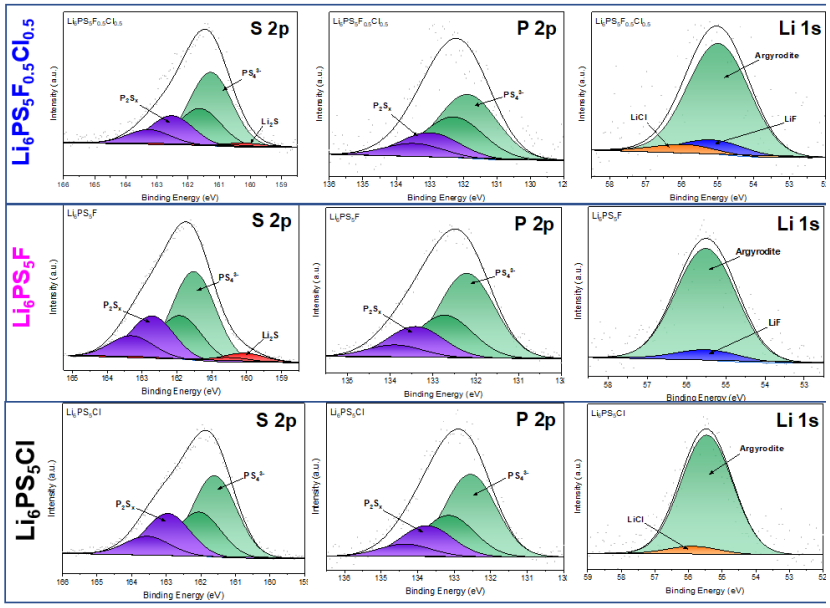

Figure 73. X-ray photoelectron spectra (S 2p, P 2p, Li 1s) of different solid electrolytes from cycled Li-symmetric cells: (a) $Li_6PS_5F_{0.5}Cl_{0.5}$, (b) Li_6PS_5F, and (c) Li_6PS_5Cl.

After cycling, Li-symmetric cells with different SEs were disassembled for interface studies via XPS. The XPS fitting results (Figure 73) show the presence of P_2S_x peak in S 2*p* and P 2*p* spectra for all three SEs, suggesting the interfacial reactions between SEs with lithium metal. However, the XPS spectra for $Li_6PS_5F_{0.5}Cl_{0.5}$ show an

area ratio of $(PS_4)^{3-}/P_2S_x$ of ~ 2.6, which is higher than that for Li_6PS_5Cl and Li_6PS_5F SEs (2.12). This indicates that the PS_4^{3-} tetrahedra are most preserved in $Li_6PS_5F_{0.5}Cl_{0.5}$, which underlies the highest stability of these electrolytes with respect to lithium anode. In addition, minor peaks of LiX (X = F, Cl) are observed from XPS spectra, further confirming interfacial reactions as follows: $Li_6PS_5F_{0.5}Cl_{0.5}$ + Li → > Li_2S + P_2S_x + Li_xP + LiCl + LiF.

Fabrication of Coin-Cell Batteries with Improved CEIs via Functionalization with Ionic Liquids. The team first prepared coin-cell batteries with a solid-state interface between $Li_6PS_5F_{0.5}Cl_{0.5}$ SE and a mesoporous cathode made up CNTs infused with sulfur (CNT-S); to improve interfacial bonding, the team subjected the C-S/SE interface to 10 flashes of intense pulse light (IPL) (2100 J/pulse with 2 ms duration) with 1 s delay time in argon atmosphere. The battery assembled with CNT-S cathode/SE interface subjected to IPL treatment against lithium shows a very small capacity (as shown in Figure 74a) and did not charge after 2 cycles. The XPS results taken from the SSE surface after discharge shown in Figure 74b consists of a single peak corresponding to Li_2S. Interestingly, it did not show any peak corresponding to bridging sulfur or sulfates/sulfites. The inability for further charging can also be attributed to the amorphization of the adjacent layers at the SSI as predicted by the theory. The team is planning to continue this study by adding SSE particles into the cathode material.

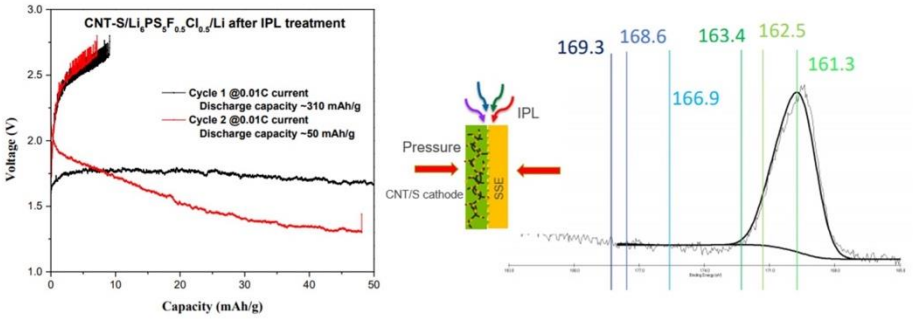

Figure 74. Coin-cell batteries with completely solid-state interface between mesoporous carbon nanotube – sulfur (CNT-S) cathode and $Li_6PS_5F_{0.5}Cl_{0.5}$ solid electrolyte (SE) treated with intense pulse light. (a) Charge/discharge curve for the battery-ray, and (b) S 2p peak of the X-ray photoelectron spectrum for the CNT-S/$Li_6PS_5F_{0.5}Cl_{0.5}$ SE interface after the battery failed to charge.

Next, to improve the CEI, the team assembled several cells with the cathode consisting of S-C (super P), lithium anode, and $Li_6PS_5F_{0.5}Cl_{0.5}$ as the SE with varying concentrations of LiTFSI in ionic liquid based on N-butyl-N-methyl pyrrolidinium (PYR-14). They systematically investigated the effect of salt concentration and volume of the ionic liquid used. Three salt concentrations (0.6 M, 0.8 M, and 1M) and three volumes (20μL, 30 μL, and 40 μL) were chosen, yielding 9 different coin cells.

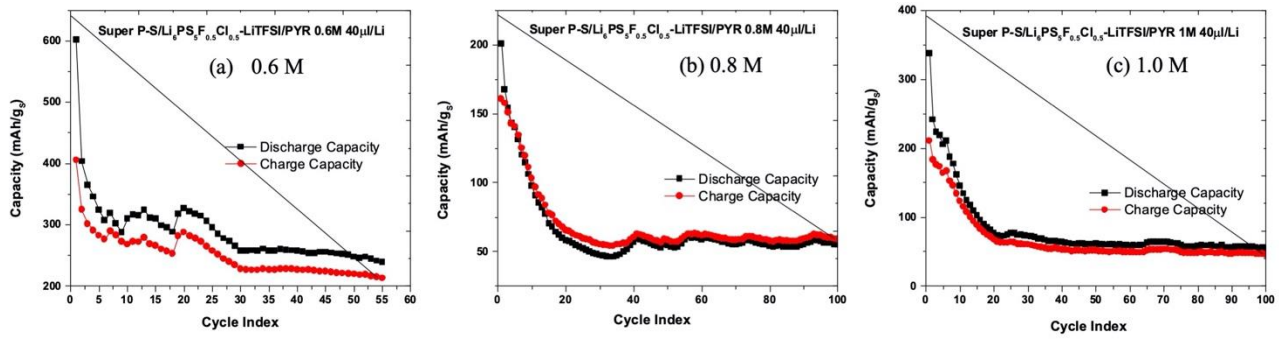

Figure 75. Capacity versus cycle number for batteries consisting of super P/C-S cathode, $Li_6PS_5F_{0.5}Cl_{0.5}$ solid-state electrolyte, and lithium anode, with the ionic liquid total volume of 40 mL and varying concentrations of LiTFSI in PYR (a) 0.6 M, (b) 0.8 M, and (c) 1.0 M.

At any given salt concentration, the team found that the volume of 40 μL yielded the best battery performance. Figure 75 shows the charge capacity versus cycle number for batteries consisting of super P/C-S cathode, $Li_6PS_5F_{0.5}Cl_{0.5}$ SSE and lithium anode with added ionic liquid of total volume of 40 μL with varying

concentrations of LiTFSI in PYR (a) 0.6 M, (b) 0.8 M, and (c) 1.0 M. Battery with 0.6 M ionic liquid concentration showed the highest capacity ~ 250 mAh/g_S after 55 cycles. XPS characterization of the CEIs are in progress to gain insights into the structure and electrochemical reactions at the cathode/SE interface.

Patents/Publications/Presentations

The project has no patents, publications, or presentations to report this quarter.

Task 3.10 – Predicting the Nucleation and Evolution of Interphases in All-Solid-State Lithium Batteries
(Sabrina (Liwen) Wan, Lawrence Livermore National Laboratory)

Project Objective. The goal of this project is to develop and apply a suite of new computational tools to predict early-stage formation of metastable interphases in SSBs. To achieve this goal, this project focuses on meeting three primary objectives corresponding to different regimes within the early-stage interphase formation: (1) identify chemical motifs for pre-nucleation; (2) predict possible interphase structures; and (3) model the kinetics of interphase formation.

Project Impact. Degradation of SSE and formation of undesired secondary interphases at the solid electrolyte / electrode interfaces are some of the key issues that limit SSB technology from practical applications. The computational tools developed in this project will allow modeling of nucleation and formation of interphases with quantum-level accuracy and significantly improved efficiency compared to currently available methods. Completion of this project will also provide valuable insights into the correlation between local chemistry and interphase formation, which can be used to inform the design of interfacial structures to lower interfacial resistance and to extend the cycling life of SSBs.

Approach. The project approach centers on close integration of *ab initio* simulations, ML, and stochastic methods to probe chemistry and nucleation across broad ranges of time and length scales. First, the team will identify chemical motif, which acts as chemical precursor for pre-nucleation based on ML and large-scale AIMD simulations. Second, they will predict possible interphase structures based on stochastic minimizations of population-weighted chemical motifs identified from the MD simulations. Third, they will model the kinetics of interphase formation and evolution using kinetic MC. To test the general applicability of the proposed computational methods, the team considers a variety of commercially viable SE and cathode materials, including cubic LLZO and LiPON SEs and $LiCoO_2$ (LCO) and $LiFePO_4$ (LFP) cathodes. These materials also represent a range of degrees of stability arising from their intrinsic properties—in particular, LiPON|LCO, LLZO|LCO, and LLZO|LFP are expected to form stable, less stable, and reactive interfaces, respectively.

Out-Year Goals. The future goal is to predict practical strategies either to facilitate the formation of desired interphase that allows for fast Li^+ diffusion and is stable on cycling or to suppress the formation of undesired interphase to reduce interfacial impedance of ASSBs.

Collaborations. There are no collaborative activities this quarter.

Milestones

1. Identify chemical precursors for interphase formation. (Q1 FY 2021; In progress)
2. Construct initial interphase structures. (Q2, FY 2021; Initiated)
3. Identify proper constraints for global optimization. (Q3, FY 2021; On schedule)
4. Obtain possible interphase structures and compositions. (Q4, FY 2021; On schedule)

Progress Report

Large-Scale *Ab Initio* Simulations of Interfaces. This quarter, the team continued efforts to sample the interfacial structures of LiPON|LCO, LLZO|LCO, and LLZO|LFP from high-temperature AIMD simulations. In addition to the large interfacial models (~ 800 atoms) that they used previously, smaller supercell models (~ 300 atoms) are constructed for a subset of the interfaces to speed up the sampling of interfacial structures. They analyzed this subset of interfacial models to identify chemical motifs/precursors formed at the interfaces that may lead to the nucleation and formation of secondary phases. Figure 76 represents example atomic configurations obtained from the AIMD trajectories for various LLZO|LCO interfaces. Significant degradation of bulk LCO associated with cobalt (Figure 76, blue) migration is observed. In addition, La-Co-O clusters are formed at the interface due to interdiffusion of lanthanum and cobalt, which may lead to formation of various $La_xCo_yO_z$ compounds at the LLZO|LCO interfaces, as has been observed in the experiments.

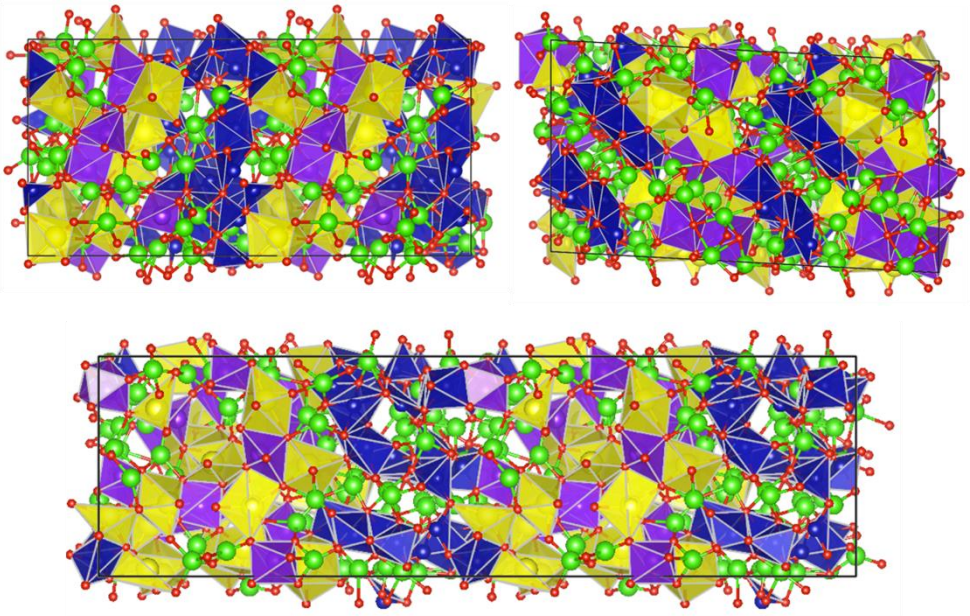

Figure 76. Snapshots of the LLZO|LCO interfacial structures obtained from *ab initio* molecular dynamics simulations. Two repeated simulation cells are rendered for each interfacial model for better visualization of the interfaces. The lithium, lanthanum, zirconium, cobalt, and oxygen atoms are represented as green, yellow, purple, blue, and red spheres, respectively; the La-O, Zr-O, and Co-O coordination are shown as yellow, purple, and blue polyhedra, respectively.

To identify various chemical motifs formed at the interfaces, the team considers cobalt atom as the reference and evaluates variations in the local coordination environment of cobalt within the LLZO|LCO interfacial structures. Figure 77 illustrates distribution of cobalt atoms with respect to other cations, including lanthanum, zirconium, and lithium. The relaxed interfaces show almost 80% of cobalt atoms possess six-fold coordination with lithium and cobalt (second nearest neighbors), which corresponds to the cobalt coordination environment in bulk LCO. During high-temperature AIMD, migration of cobalt and lanthanum from the respective bulk region to the interfacial region is observed, which leads to partial disintegration of bulk LCO. As shown in Figure 77, the six-fold coordination of cobalt with respect to lithium and cobalt is reduced during the AIMD run compared to its initial optimized geometries at 0 K. From these different local coordination environments of cobalt, the team identifies distinct chemical motifs comprising of La-Co-O, Co-O, Li-Co-O, Zr-Co-O, etc. at the interfaces. For La-Co-O clusters, ~ 80% show single coordination between cobalt and lanthanum, and the rest show two-fold coordination. Based on the combinations of these local chemical motifs identified, they have generated a number of atomic configurations with various compositions (see Figure 78 as an example) to study the potential nucleation and formation of new phases at the interfaces. They are working on energy minimizations of these atomic configurations.

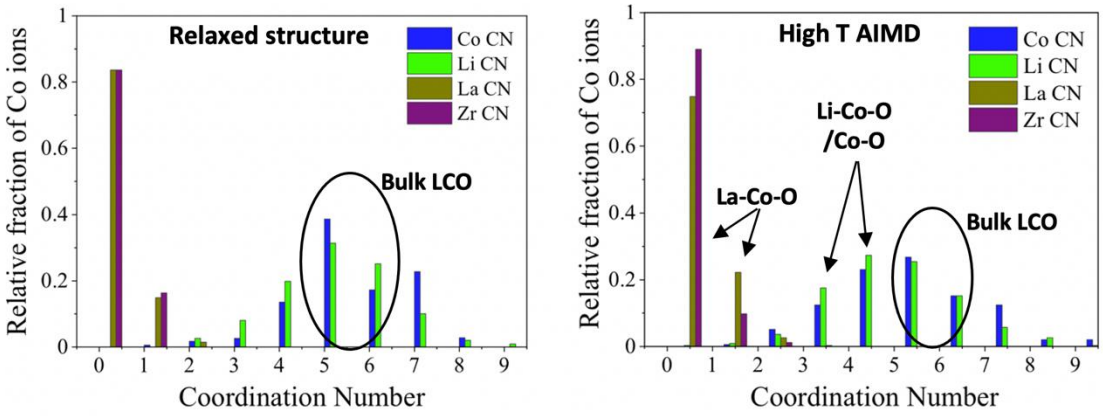

Figure 77. Distribution of local coordination environment of cobalt within the LLZO|LCO interfacial models for relaxed and post high-temperature *ab initio* molecular dynamics simulations.

Furthermore, the team has studied the LLZO|LFP interfaces using a similar approach as for LLZO|LCO interfaces. The LLZO|LFP interfaces are found to be highly reactive, and AIMD simulations reveal a higher degree of disintegration of bulk LLZO and LFP. Figure 79 shows a snapshot of the LLZO|LFP interfacial structure during the AIMD simulation, with generally observed migration of lanthanum, zirconium, iron, and phosphorus ions toward the interface. To facilitate identification of distinct chemical motifs formed at the interface, they search for unique atomic configurations around iron and phosphorus atoms. Figure 80 shows the distribution of local coordination of iron and phosphorus with respect to lanthanum, zirconium, and lithium atoms, in the LLZO|LFP supercell structures. It is found that only 10% of the Fe-La-O or P-La-O clusters have single coordination of lanthanum with iron or phosphorus, respectively. This implies that the bulk LFP is degraded significantly at the interface. The decrease in the local coordination environment of iron and phosphorus with respect to other cations effectively hints at the formation of numerous reaction or degradation products at the interface. The team is working on identification of local chemical motifs formed at the interface and the construction of seed clusters that may lead to the formation of secondary phases at the LLZO|LFP interfaces.

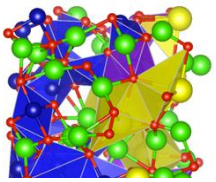

Figure 78. Example of a small seed cluster generated from La-Co-O, Li-Co-O, Co-O, and Li-La-Zr-O local units identified at the LLZO|LCO interfaces from high-temperature *ab initio* molecular dynamics simulations.

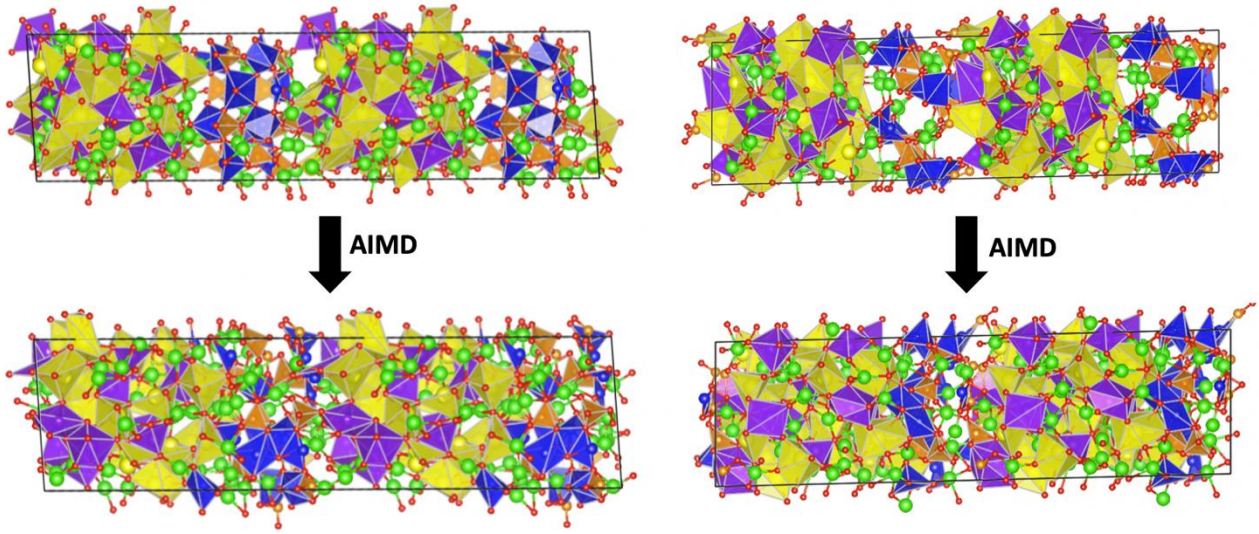

Figure 79. Example snapshots of the LLZO|LFP interfacial structures from *ab initio* molecular dynamics simulations. Again, two repeated simulation cells are shown in each structure representation. The lithium, lanthanum, zirconium, iron, phosphorus, and oxygen atoms are rendered as green, yellow, purple, blue, orange, and red spheres, respectively; the La-O, Zr-O, Fe-O, and P-O coordination are represented as yellow, purple, blue, and orange polyhedra, respectively.

The LiPON|LCO interface seems to be the most stable interface compared to LLZO|LCO and LLZO|LFP interfaces. This quarter, the team continued to perform high-temperature AIMD simulations on the LiPON|LCO interface; detailed analysis is in progress.

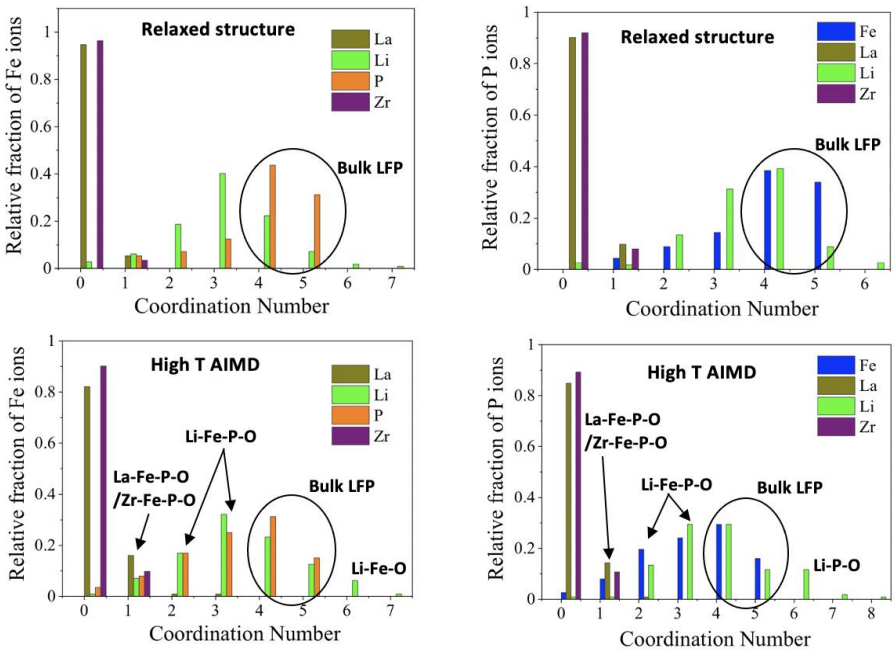

Figure 80. Distribution of local coordination environment of iron and phosphorus within the LLZO|LFP interfacial models for relaxed and post high-temperature *ab initio* molecular dynamics simulations.

Development of Machine-Learning Interatomic Potentials. This quarter, the team has been working on improving ML potential for LLZO crystalline-amorphous coexisting system, which could exist at the GBs of LLZO and at the interfaces between LLZO and the electrodes. Their refinement of the ML potentials relies on use of an iterative approach starting with an initial ML potential trained by a small dataset of near-equilibrium structures collected from *ab initio* simulations. The initial ML potential is used to perform MD simulations, from which relevant atomic structures are sampled, and the corresponding energies are computed from DFT. This new set of data is then added to the next training dataset if the ML potential poorly predicts their energies compared to DFT. Their initial training data are intended to teach the ML potential to learn the near-equilibrium potential energy surface, whereas the gradually added energies/structures sampled from AIMD simulations at elevated temperatures allow the ML potentials to learn the entire potential energy surface, in particular for regions further away from the equilibrium, which dictates the chemical reactivities of the atoms. The current ML model is based on artificial neural network (ANN) with a 20-20 architecture (two hidden layers with 20 nodes in each layer), and the Chebyshev polynomial representations of local atomic environment.

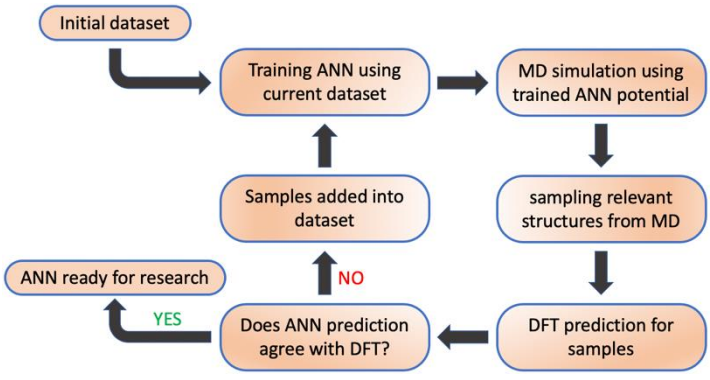

Figure 81. The iterative-refinement procedure to develop artificial neural network (ANN) potentials.

The team is validating training ML potentials by predicting and comparing Li-ion conductivities in bulk crystalline and amorphous LLZO, and the melting temperature of LLZO. They have started developing ML potentials for the LLZO|LCO interface and are collecting additional training datasets from *ab initio* simulations.

Patents/Publications/Presentations

The project has no patents, publications, or presentations to report this quarter.

Task 3.11 – Design of Strain Free Cathode – Solid-State Electrolyte Interfaces Using Chemistry-Informed Deep Learning
(Hakim Iddir, Argonne National Laboratory)

Project Objective. The main objective of this project is to use state-of-the-art ML techniques and high-performance computing (HPC) to model complex oxide materials that will allow the team to develop cathode – SE interfaces that exhibit minimal or no strain as well as provide chemical stability at the interface between the cathode material and the SSE. A deep understanding and control of the cathode/SSE interface (including its chemical and mechanical stability) is needed to develop an effective SSB. The active cathode material changes volume during cycling, particularly at high SOC.[1] This volume change leads to strained interfaces triggering loss of contact and delamination, and hence reduction/elimination of electron and ion transport pathways. The increased strain could also generate cracks within the SSE, creating new paths for lithium dendrite growth channels. These structural changes degrade the electrochemical performance of the battery. Several strategies have had limited success in alleviating these drawbacks, including mixed SSE, buffer layers between the cathode and the SSE, and dopants to improve chemical stability of the interface.[2] These approaches, although promising, could not solve both the chemical and mechanical stability of the interface. In this project, the team proposes a new approach that takes advantage of well-established ML techniques and HPC to screen for candidate dopants of high-Ni-content NMC cathodes that would both reduce the volume expansion and the chemical reactivity (mixing) at the interface, with minimum impact on electrochemical performance and energy density of the cathode.

Project Impact. Structure-property relationships are at the heart of most fundamental scientific approaches. However, the link between structure and property remains a challenge in the materials science of complex systems, such as the oxides that form battery components. In particular, the chemical and mechanical stability of the cathode-SSE interface presents a challenge to development of SSBs. High-performance DFT calculations provide the necessary framework to understand such systems. Unfortunately, given the limited number of atoms and time scales accessible by the method, along with the myriad calculations required to achieve satisfactory results, the computational cost of simulating all the possible configurations of a multicomponent oxide is prohibitive. In this work, the team augments the DFT data with ML—especially deep learning—techniques that allow them to access large system sizes and longer time scales necessary to build thermodynamic models. They focus on understanding the nature of benchmark $Li_{1-\alpha}Ni_{1-x-y-z}Mn_xCo_yM_zO_2$ structures (M dopant, $\alpha,x,y,z < 1$), their volume change with lithium content, the nature and concentration of the dopants, and chemical stability of the SSE-cathode interface. The DFT and ML approach will provide new cathode compositions that will reduce the strain of the SSE-cathode interface and hence improve its mechanical and chemical stabilities.

In this project, the team aims at developing a methodology that will allow them to explore and expand the configurational space using HPC approaches in a systematic and efficient way. The methodology will encompass DFT, AIMD, MD, and ML. The methodology will also take advantage of various software already developed at ANL and at other DOE laboratories (for example, Balsam) to automate, manage, and control the large number of calculations needed to achieve the project goal.

Approach. All calculations will be performed by spin-polarized DFT as implemented in the Vienna *ab initio* simulation package (VASP).[3-4] After geometry optimization within the DFT+U framework, electronic relaxation will be performed using a single-point calculation with the hybrid functional HSE06.[5] For production calculations, they will use the message-passing interface (MPI) parallelized version of VASP.

Exploration of the potential energy surface (PES) is needed to predict the structure of solid materials and interfaces. Such calculations are infeasible using MD or DFT calculations alone. Thankfully, the PES of a system can be represented by the sum of the energies of the local neighborhoods surrounding each atom. This enables the use of ML surrogate models trained with DFT calculations to capture the energies in local neighborhoods. The input to the ML surrogate must be a unique representation of the system under study.

Consequently, the local environment of each ion is described using a local environment descriptor that renders the atomic configuration invariant to rotations, translations, and permutations of the atoms. In recent years, several different descriptors have come to prominence with advantages and disadvantages. Once the ML surrogate is trained, the total energy and forces over all the ions of any structural configuration can be determined. Such information can be used for atomistic simulations, namely, MD and MC.

In this project, the team proposes to use the open-source DeepMDkit python/C++ package to construct the ML PES and FFs. The promise of DeepMDkit in this work is to provide near-DFT accuracy at orders-of-magnitude lower computational expense, comparable to traditional MD simulations. Efficiency in training is facilitated through integration with TensorFlow and MPI/GPU support.

One of the challenges of developing ML PES is achieving accurate predicted forces and energies across the entire configurational space, while minimizing the total number of calculations required for training. In recent years, active learning has been highlighted for its ability to target training examples most likely to improve the model quality or to achieve some other objective (that is, maximizing a predicted material property). DP-GEN, an open source python package based on DeepMDkit, implements a similar active learning scheme with HPC support, and has been employed to construct ML PES with accuracy approaching DFT and sometimes exceeding embedded atom potential for experimentally measured properties of interest.[6] In this work, the team proposes to leverage DeepMDkit and DP-GEN to efficiently generate ML-PESs for cathode-electrolyte systems including a variety of dopants.

Out-Year Goals. One out-year goal involves developing a DFT-trained ML model on NMC/LLZO interface, ready to use for large screening of new cathodes, SSE compositions, and cathodes/SSE interfaces. A second is to provide fundamental understanding on critical parameters limiting performance and stability of the cathode/SSE interface and hence of the SSB.

Collaborations. Project collaborators include J. Croy, C. Johnson, and E. Lee from ANL Chemical Sciences and Engineering Division for the synthesis phase of the project.

Milestones

1. DFT-trained ML model for delithiated $LiNiO_2$ and NMC-811. (Q3, FY 2020; In progress)
2. Complete ML model based on NMC/LLZO interfaces data. (Q4, FY 2020; In progress)
3. Determine volume changes and phase transformation during charging for $LiNiO_2$ using the developed DFT-trained ML model. (Q1, FY 2021; Completed)
4. Determine elemental segregation, volume changes, and phase transformation during charging of $Li(Ni_{0.8}Mn_{0.1}Co_{0.1})O_2$ using the developed DFT-trained ML model. (Q2, FY 2021; In progress)
5. Extend solid bulk models to include surfaces and dopants. (Q3, FY 2021; NMC-811 surfaces in progress)
6. Apply ML model to understand mechanical and chemical interactions on CEIs. (Q4, FY 2021)

Progress Report

One of the main challenges on Ni-rich cathode in SSE batteries is the mechanical strain produced at the CEI. In Ni-rich cathodes, the phase transformation at high state of charge is the main component of the total volume change. Hence, the atomistic models must be able to capture the key processes involved in the phase transformation. The team has set up a methodology to understand thermodynamics and lattice parameters of lithium nickel oxide (Li_xNiO_2) from ML and MD. They have explained in previous reports some of the controversies around the volume change of Ni-rich cathode at high state of charge. This quarter, they have successfully completed a model that describes the possible phases during the charge process.

The team used the ML interatomic potential framework DeepMDkit[1] to construct an interatomic potential for modeling the thermodynamic properties and lattice parameters at temperatures from room temperature up to 400 K, which is considered the maximum operating temperature for these Li-ion battery cathode materials. A bootstrapping scheme, where an ensemble of five potentials was fit with different re-samplings of the training datasets, was employed to obtain calibrated uncertainty estimates for the energies and forces. The potentials were fit using a cutoff radius of 9 Å for local atomic environment interactions and a training set comprising configurations from 20 fs AIMD trajectories of configurations of H2 and H3 phases of Li_xNiO_2 (x = 0.04, 0.08, 0.12, and 0.17). As shown in Figure 82, the predictions of the test set for the potential fall within 10 meV/f.u. of the DFT calculations, with one formula unit (f.u.) considered as 1 unit of NiO_2. The force predictions also show a high degree of correlation ($R^2 > 0.99$), indicating that MD provides a reliable model.

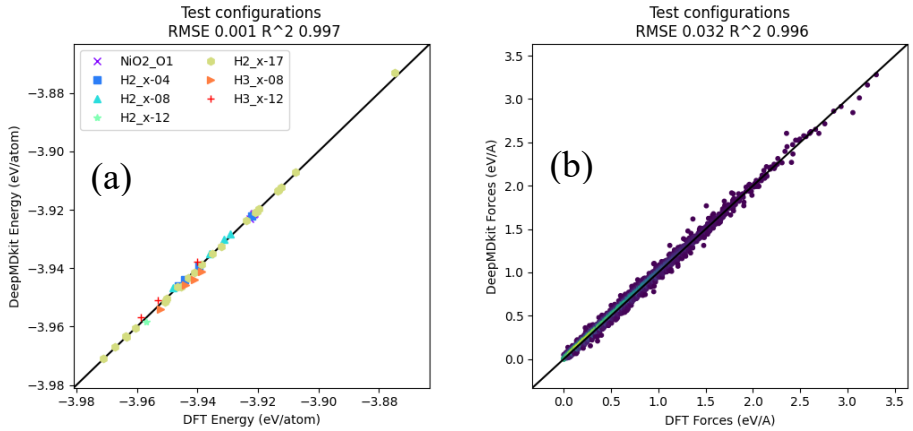

Figure 82. Predictive performance of the developed potential shown by parity plots on a test set, which was held out from the training set. A strong correlation ($R^2 > 0.99$) on (a) energy and (b) forces is observed. Strong degree of correlation is observed for each class of data (H2-rich and H3-rich phases of Li_xNiO_2 and *O1* stacked NiO_2).

Figure 83 provides an analytical means to evaluate the efficacy of the uncertainty estimates in the holdout test set for (a) energies, and (b) forces. In the figure, the DeepMDkit energies and forces are plotted against the errors versus DFT, respectively. The color scheme corresponds to the probability density of points in that area, with yellow being the densest and purple being the sparsest. It is desirable that most energies and forces fall below the 1-σ line, indicating that the prediction error is less than the predicted uncertainty. A lower portion should fall below the 2-σ and 3-σ boundaries, respectively. This is generally the case for both the energies and forces, with a minority of points exceeding the 3-σ boundary. The fractions of these points that fall within these boundaries are indicated in the title of the plot. Predicted energy and force uncertainties exceed the errors for 62.8% and 68.4% of the cases, respectively. The fact that these uncertainties are well calibrated gives confidence in their usefulness in improving the potential and identifying low energy structures via active learning. The quality of these predictive uncertainties could be further improved by adding to the bootstrap ensemble, but with commensurate computational expense.

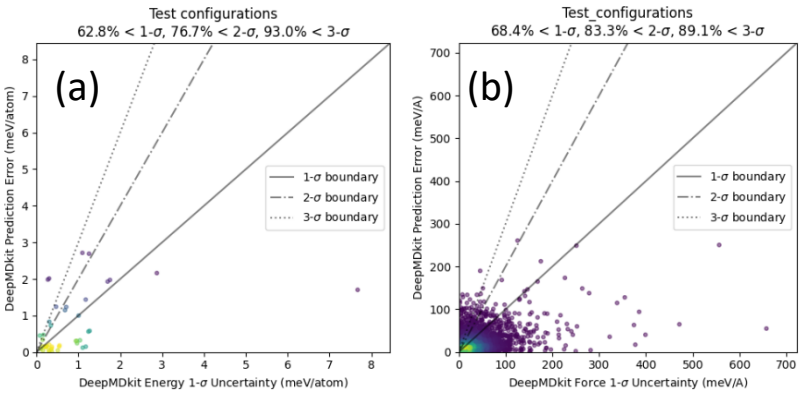

Figure 83. Efficacy of uncertainty estimates in holdout test set for (a) energies and (b) forces.

Using this potential, the team evaluated the phase stability of the H2-rich and H3-rich phases of Li_xNiO_2, to check if they can coexist over the operating temperature range (of 200 to 450 K) or lithium composition range. As a first step, they determine the enthalpy of each H2-rich and H3-rich phase obtained at 250, 298, 350, and 400 K from isobaric isothermal (*npt*) ensemble MD simulations in LAMMPS with the DeepMDkit potential. Shown in Figure 84a-d are the enthalpies for the H2-rich and H3-rich phases, across the lithium compositions of x = 0.04, 0.08, 0.12, and 0.17, and over the temperature range of 200 to 450 K. Applying a Bayesian automated weighting scheme,[2] they find that a linear model for the enthalpy is most supported by the data collected so far from MD simulations at the temperatures of 250, 298, 350, and 400 K. As shown in Figure 84, over the compositions x = 0.08, 0.12, and 0.17, the H2-rich and H3-rich phases differ in energy by about 25 meV/f.u. and within 95th confidence intervals of their respective linear enthalpy models. For x = 0.04, the difference in enthalpy is greater than 25 meV/f.u. and the 95th confidence interval of each model. This shows that the H2-rich and H3-rich phases may coexist over a temperature range of 200 to 450 K at the lithium compositions of x = 0.08, 0.12, and 0.17, while at x = 0.04 the H3-rich phase is lower in energy over the same temperature interval of 200 to 450 K. Free energy and entropy calculations are in progress to confirm this observation that, so far, is only based on enthalpy calculations.

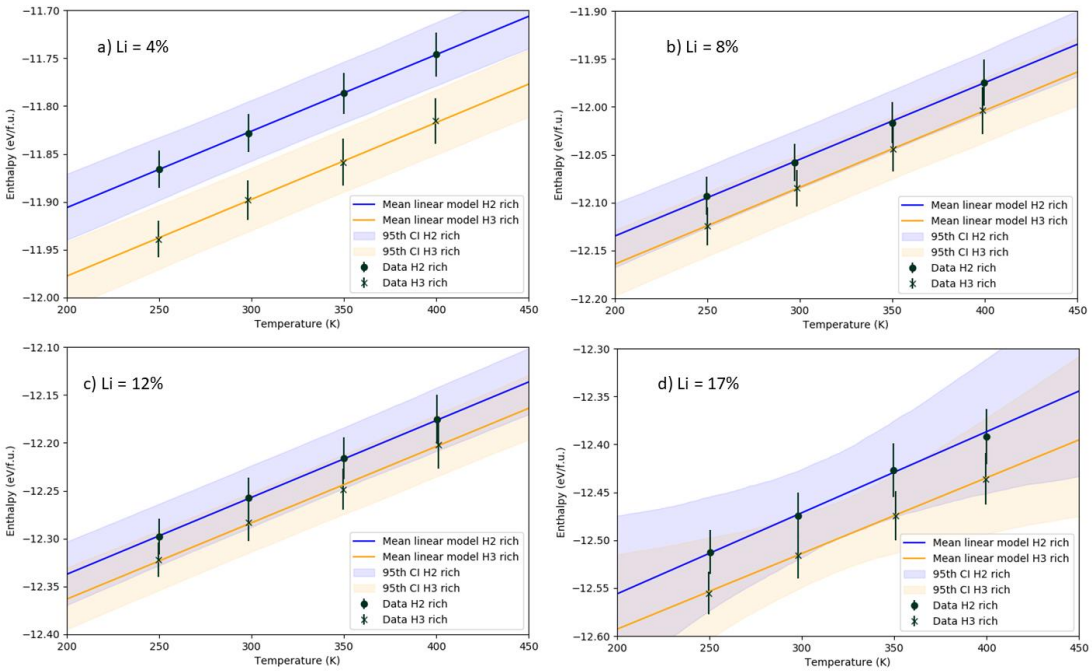

Figure 84. Enthalpies from molecular dynamics using the developed machine-learning interatomic potential for the H2-rich (blue) and H3-rich (orange) phases for lithium compositions (a) 4%, (b) 8%, (c) 12%, and (d) 17%, each over the temperature interval of 200 to 450 K.

Furthermore, it is known from experiments that the *c*-lattice constant collapses with decreasing lithium content. Figure 85 shows the calculated change in the *c*-lattice constant for the potential for four temperatures (250, 298, 350, and 400 K). The *c*-lattice constant decreases the most at Li = 0.08, irrespective of the temperature in the H2-rich phase, in agreement with the experimental observations.

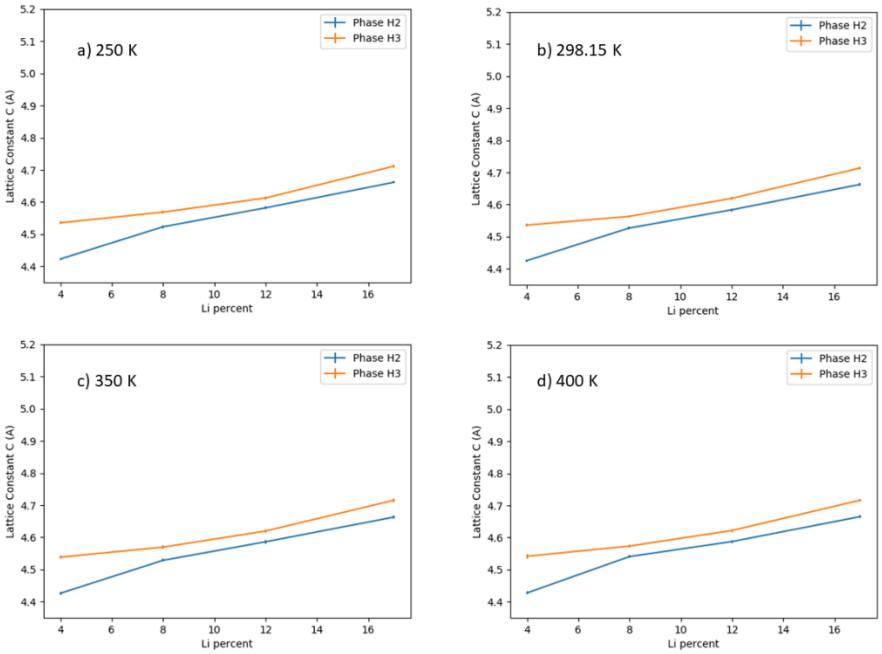

Figure 85. *c* – lattice constant predicted from molecular dynamics simulations at: (a) 250 K, (b) 298 K, (c) 350 K, and (d) 400 K.

As the team has reported last quarter, it is critical to include van der Waals (VDW) forces to model the collapse of Li_xNiO_2 as x approaches zero. The SCAN functional, which includes some VDW forces, has some binding energy between layers and significantly smaller c lattice constants. The SCAN+rVV10 functional includes a more complete description of the VDW forces and predicts a larger binding energy and c lattice constants close to experiment.

They have carried out a geometry optimization of NiO_2 with the Random Phase Approximation (RPA) to obtain a more accurate estimate of the relative energies for the O1 and O3 stacking for the NiO_2 layers. Their current lowest energy structures for both phases predict that the O1 phase is lower in energy than the O3 by 0.5 kJ/mol, while the energy difference predicted by the SCAN+rVV10 functional found O3 stacking 1 kJ/mol lower in energy than the O1 stacking, that is, essentially similar in energy.

Currently, the team is applying the same methodology for $Li(Ni_aMn_bCo_c)O_2$ NMC-abc cathodes. Given the final goal of understanding Ni-rich cathode, the initial chosen material is NMC-811. Since there are more cations in the system, and the team is interested in CEIs, TM segregation becomes a main issue to understand the properties of the material. As shown in previous reports, they collected DFT data for bulk NMC-811 and slabs representing several surface facet terminations. Based on the DFT results, a ML model is being fit to predict volume changes and segregation for larger length and time scales using MD.

References

[1] Wang, H., L. Zhang, J. Han, and W. E. "DeePMD-Kit: A Deep Learning Package for Many-Body Potential Energy Representation and Molecular Dynamics." *Computer Physics Communications* 228 (2018): 178–184.

[2] Paulson, N. H., S. Zomorodpoosh, I. Roslyakova, and M. Stan. "Comparison of Statistically-Based Methods for Automated Weighting of Experimental Data in CALPHAD-Type Assessment." *Calphad* 68 (2020): 101728.

Patents/Publications/Presentations

The project has no patents, publications, or presentations to report this quarter.

Task 3.12 – Tackling Solid-State Electrochemical Interfaces from Structure to Function Utilizing High-Performance Computing and Machine-Learning Tools

(Shinjae Yoo, Feng Wang, and Deyu Lu, Brookhaven National Laboratory; Nongnuch Artrith and Alexander Urban, Columbia University)

Project Objective. This project aims at elucidating the structural evolution and other dynamic properties of the interphases at the SSIs in SSBs under processing and electrochemical cycling conditions that strongly impact the cell performance. By leveraging synergies of first-principles theory, HPC, ML, and computational/experimental spectroscopy, this project involves a comprehensive investigation of SE systems and SSIs that may enable the practical use of lithium anodes and high-nickel NMC cathodes in SSBs. Specific project objectives are as follows: (1) develop realistic atomic-scale structure models of the heterostructural SSIs, (2) determine the impact of structural evolution on the stability and transport properties of the SSIs, and (3) identify the coating/doping chemistry that may stabilize SSIs during formation and electrochemical cycling.

Project Impact. Interfacial properties and the dynamical evolution of interphase structures are crucial for the stability and performance of SSBs. This project will lead to fundamental understanding of current materials limits and will identify key materials parameters for optimizing the performance of SSBs. By corroborating atomic-scale theory with experiment, the project will identify structure–property relationships of the heterostructural SSIs in SSB systems that are relevant for EVs. The outcomes of this project will therefore accelerate development of high-energy-density, safe SSBs for EVs.

Approach. Accurate ML potentials will be trained on an extensive database from DFT calculations to simulate the structure evolution and electrochemical properties of the SSIs. Using a second ML model, key physical descriptors will be extracted from EELS and XAS measurements. This spectral fingerprinting will enable the automated interpretation of spectroscopy measurements, thereby bridging between atomistic modeling and experiment. An experimental platform will be developed to integrate experimental/computational spectroscopy and modeling of SSIs. In combination, the two ML models and the spectroscopic data will facilitate the construction of a physics-based model to unravel the structure-property relationships of the SSIs.

Out-Year Goals. The project will progress toward establishing dynamic composition-structure-property relationships for interface stability and transport within and across the electrochemical SSIs in SSBs. The ML approach will be further developed to a general model for thermodynamic and transport properties of dynamic heterostructural electrochemical interfaces and will eventually be applied to the practical SSB systems.

Collaborations. The project is collaborating with Y. Du at BNL.

Milestones

1. Complete mapping of the phase diagram and structure-stability-conductivity relationships in the glass/ceramic (gc) Li_2S–P_2S_5 (LPS) system. (Q1, FY 2021; Completed)
2. Characterize initial stages of the interfacial reaction of gc-LPS with lithium metal using ML-augmented DFT and XAS spectroscopy. (Q2, FY 2021; In progress)
3. Correlate characteristic structural motifs of gc-LPS and the gc-LPS/Li interface with XAS spectral features using ML. (Q3, FY 2021; In progress).
4. Determine formation and evolution mechanisms of gc-LPS/Li interphases using XAS measurements and ML models. (Q4, FY 2021)

Progress Report

Last fiscal year, the team reported development of machine-learning potentials (MLPs) for large-scale modeling of NMC cathodes and doped LLZO electrolytes. This quarter, the developed MLP approach was adapted for modeling sulfide electrolyte system, Li_2S–P_2S_5 (LPS). The phase diagram of gc-LPS with varying compositions was mapped by combining DFT, ANN potentials, genetic-algorithm (GA) sampling, and AIMD simulations. The thermodynamic stability and ionic conductivity of glassy/ceramic phases were correlated with the local structural motifs in the known LPS crystal structures.

Exploration of the Compositional Space of LPS Compounds. Tackling the complexity of SSE interfaces requires a detailed understanding of the atomic structures of the electrode and electrolytes. Following previous studies on NMC cathode and LLZO electrolyte, the team extended the scope of their study to lithium thiophosphates (LPS) electrolytes with the composition of $(Li_2S)_x(P_2S_5)_{1-x}$, motivated by their superionic conductivity at room temperature (> 10^{-3} Scm^{-1}), soft mechanical properties, and low GB resistance.[1] To resolve the atomic structures of gc-LPS with varying compositions, they mapped the gc-LPS phase diagram by integrating DFT, ANN-GA sampling, and AIMD, as illustrated by the workflow in Figure 86.

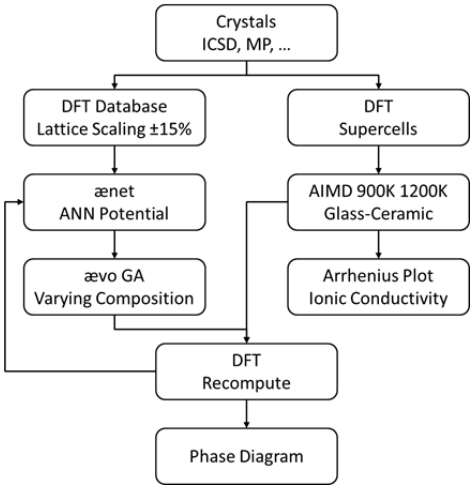

Figure 86. Flowchart for mapping of the glass/ceramic – LPS phase diagram by combination of density functional theory, artificial neural network – genetic algorithm, and *ab initio* molecular dynamics.

The team's calculations started with 10 crystal structures of LPS with the formula units $LiPS_3$, Li_2PS_3, $Li_4P_2S_7$, $Li_7P_3S_{11}$, α-Li_2PS_4, β-Li_3PS_4, γ-Li_3PS_4, $Li_{48}P_{16}S_{61}$, β-Li_4PS_4, and LT-Li_7PS_6 based on previous experimental characterizations and/or theoretical modeling. The crystal structures, which were obtained from the Inorganic Crystal Structure Database (ICSD)[4] and the Materials Project (MP)[6] database, are shown in Figure 87. As seen, the structures are composed of a variety of local motifs, which have previously been found to affect the ionic conductivity and the lithium transport

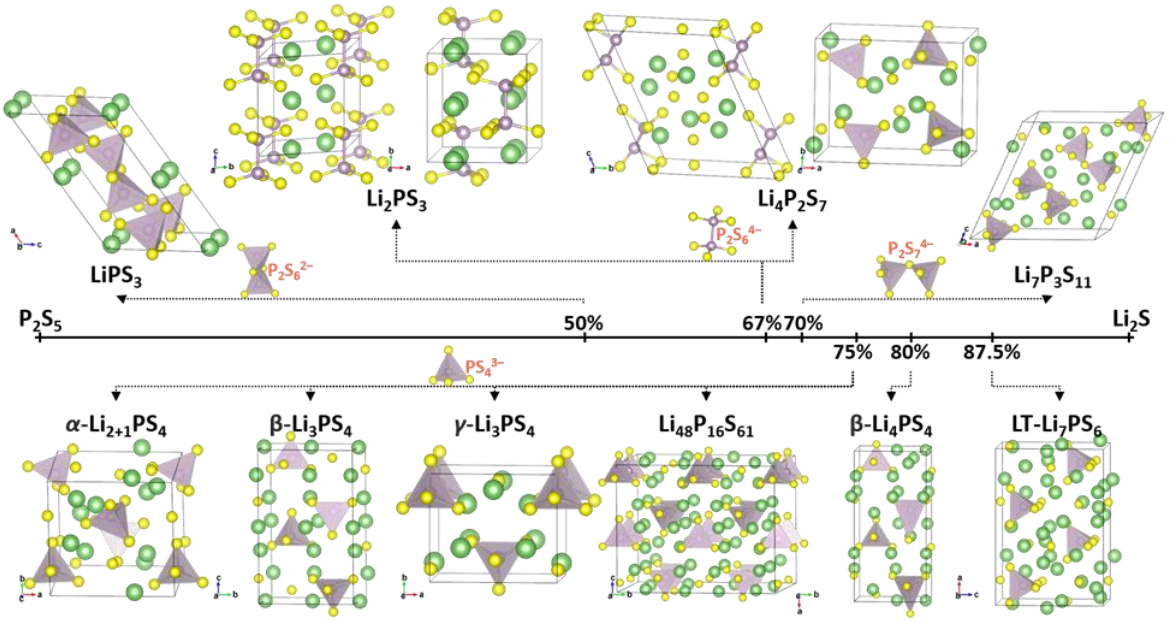

Figure 87. Crystal structures in Li_2S–P_2S_5 (lithium: green; sulfur: yellow; and phosphorus: purple).

mechanisms.[1] The isolated PS_4^{3-} tetrahedron is mostly observed in the gc-LPS compositions with high Li_2S content ($x \geq 0.75$), such as α-Li_3PS_4, β-Li_3PS_4, γ-Li_3PS_4, and Li_7PS_6. The $P_2S_7^{4-}$, constructed by two corner-sharing PS_4 tetrahedra, is the main building block of the $Li_7P_3S_{11}$ crystal structure as well as glassy LPS compositions with $x \leq 0.75$. The $P_2S_6^{4-}$, formed by two edge-sharing PS_4 tetrahedra, is observed in gc-LPS with $x \leq 0.6$ and is the only local motif in $LiPS_3$ crystals. The $P_2S_6^{2-}$ with direct P–P bonding is typically captured in gc-LPS with $0.6 \leq x \leq 0.7$. Note that only in the $P_2S_6^{2-}$ motif the oxidation state of phosphorus is +4, while it is +5 in all other local motifs. The $P_2S_6^{2-}$ motif also occurs in Li_2PS_3, which is a sulfur-deficient composition.

For accelerated sampling, an initial ANN potential was trained on a data set containing ~ 5,000 crystal structures with lattice parameters scaled by ± 15% and perturbed atomic positions from AIMD simulations using the atomic energy network package (ænet).[2] The initial ANN potential yields a root-mean-squared error of 1.412 meV/atom and a mean absolute error of 0.621 meV/atom, relative to the DFT reference energies on an independent validation set not included in the training. Note that this initial ANN potential cannot be expected to yield highly accurate results for glassy LPS phases, since the reference data set was derived from the ordered crystalline phases, but it can be used in conjunction with DFT for accelerated sampling.

With the initial ANN potential, the amorphous phases along the Li_2S–P_2S_5 composition line were sampled with a GA as implemented in the atomistic evolution (ævo) package.[3] Although the amorphous structures lack long-range ordering, the team expects that the local atomic motifs in each amorphous LPS phase resemble those of the known LPS crystalline phases. With this assumption, the phase diagram of all LPS compositions can be constructed by sampling the LPS composition space by varying the stoichiometry x in $(Li_2S)_x(P_2S_5)_{1-x}$ via removing Li_2S or P_2S_5 from the crystalline compositions, respectively. Starting from supercells of the ideal crystal structures of $LiPS_3$, $Li_7P_3S_{11}$, β-Li_3PS_4, γ-Li_3PS_4, and Li_7PS_6, either lithium and sulfur atoms were removed with the ratio of 1:2, or phosphorus and sulfur atoms were removed with the ratio of 2:5 with GA sampling. A population size of N = 32 trials and a mutation rate of 10% were employed. For each composition, at least 10 lowest energy structure models identified with the ANN-GA approach were selected and fully relaxed with DFT to obtain the first-principles phase diagram.

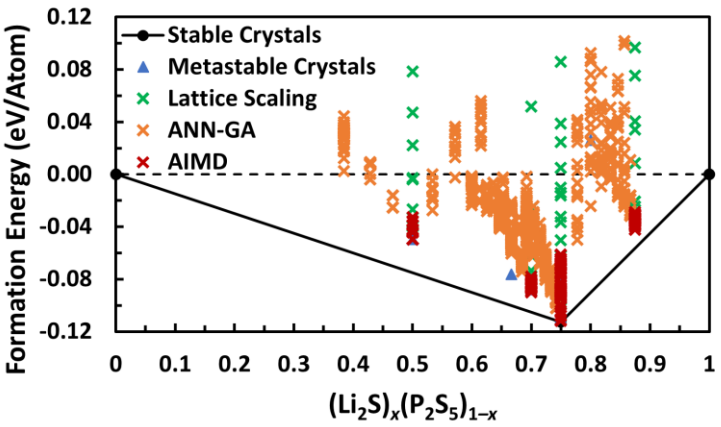

Figure 88. Phase diagram of glass/ceramic – LPS with varying compositions, including stable crystals, metastable crystals, lattice-distorted structures, amorphous phases generated either from artificial neural network – genetic algorithm or *ab initio* molecular dynamics simulations and recomputed with density functional theory.

On the basis of the DFT total energies of gc-LPS structures, the first-principles phase diagram referenced to Li_2S and P_2S_5 was constructed (Figure 88). As seen in the phase diagram, only one crystal structure (γ-Li_3PS_4) appears on the lower convex hull of the formation energies and is thus predicted to be thermodynamically stable at 0 K. The previously reported superionic conductors, β-Li_3PS_4 and $Li_7P_3S_{11}$, are above the convex hull, indicating that they are thermodynamically metastable at 0 K. However, the energy difference between β-Li_3PS_4 and γ-Li_3PS_4 is as small as 3.2 meV/atom compared to the thermal energy per degree of freedom at room temperature (~ 26 meV). Note that the crystal structures of $Li_4P_2S_7$ and $Li_{48}P_{16}S_{61}$ are theoretical predictions from the literature[5] and have not been synthesized yet, which is consistent with the phase diagram that both crystal structures are predicted to be highly unstable. The formation energies of the generated amorphous structures are also predicted to be thermodynamically unstable and can therefore be expected to form under certain conditions only (for example, under entropy control at high temperatures or via kinetic trapping).

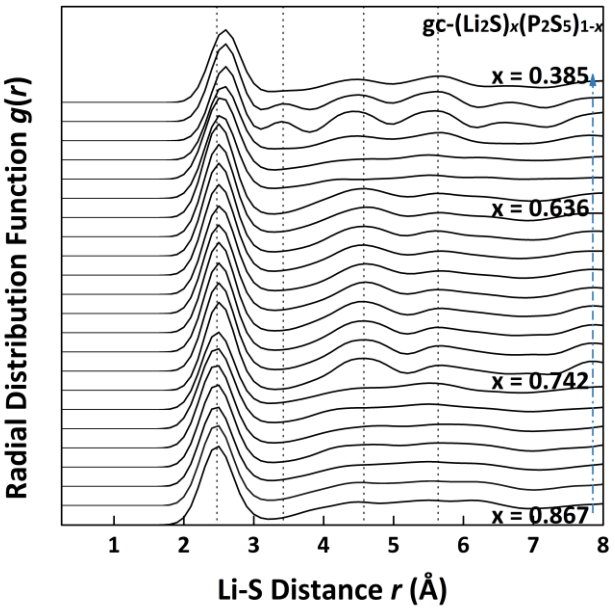

Figure 89. Calculated radial distribution functions of *gc*-LPS phases with different compositions.

To better understand the structures of the sampled gc-LPS phases, the team computed the radial pair distribution functions (RDFs) for Li-S in 23 gc-LPS compositions with $0.385 < x < 0.867$, as shown in Figure 89. As seen, the RDFs of the gc-LPS structures exhibit features of the crystal structure RDFs (indicated by thin dashed lines), but show broadened peaks and slight changes in the peak positions. With decreased amount of Li_2S in gc-LPS, the main Li-S peak shifts to greater distances, which is caused by formation of corner-sharing motifs, in agreement with previous reports.[8]

To determine the impact of local structural motifs and structural disorder on the ionic conductivity of gc-LPS, AIMD simulations were performed for select compositions at the temperatures of 700 K, 900 K, 1200 K, and 1500 K. The ionic conductivities at room temperature were obtained from Arrhenius extrapolation. Table 6 shows a comparison of the lithium conductivities in gc-LPS. As shown, the predicted ionic conductivity and activation energy in crystalline $Li_7P_3S_{11}$ are in good agreement with previously reported experimental measurements. Remarkably, the amorphous structure, gc-$Li_{42}P_{16}S_{61}$, with the composition located in the middle of $Li_7P_3S_{11}$ and γ-Li_3PS_4, processes an ionic conductivity of 6.60×10^{-3} S cm^{-1}, which is much greater than the conductivity of crystalline γ-Li_3PS_4, 3.0×10^{-7} S cm^{-1}.[4] This result further confirms the relationship between the structures and conductivity. Further simulations for other compositions and the correlation of conductivity with structural motifs are in progress.

A manuscript detailing the methodology and the first-principles LPS phase diagram is being prepared.

Table 6. Comparison of calculated activation energy and lithium conductivity in glass/ceramic – LPS with experimental measurements.

Formula	x	Moiety	Activation Energy (eV)		Ionic Cond. RT (S cm^{-1})	
			DFT	EXP	DFT	EXP
$Li_7P_3S_{11}$	0.700	$P_2S_7^{4-}$, PS_4^{3-}	0.18	0.18[5]	5.45×10^{-2}	1.16×10^{-2} [5]
gc-$Li_{42}P_{16}S_{61}$	0.724	PS_4^{3-}	0.27	N/A	6.60×10^{-3}	N/A

References

[1] Kudu, Ö. U., et al. *Journal of Power Sources* 407 (2018): 31.
[2] Artrith, N., et al. *Computational Materials Science* 114 (2016): 135.
[3] Artrith, N., et al. *Journal of Chemical Physics* 148 (2018): 241711.
[4] Homma, K., et al. *Solid State Ionics* 182 (2011): 53.
[5] Holzwarth, N. A. W., et al. *Journal of Power Sources* 196 (2011): 6870.
[6] Jain, A., et al. *APL Materials* 1 (2013): 011002.
[7] Chu, I-H., et al. *ACS Applied Materials & Interfaces* 8 (2016): 7843.
[8] Garcia-Mendez, R., et al. *Advanced Energy Materials* 10 (2020): 2000335.

Patents/Publications/Presentations

Presentations

- MRS Spring/Fall 2020 Meeting, Virtual (November 27 – December 4, 2020): "Structural Characterization of Solid-State Electrochemical Interfaces via Integrated Computation and Spectroscopy"; F. Wang, D. Lu, A. Urban, N. Artrith, and S. Yoo. F.EN04.27.01.
- MRS Spring/Fall 2020 Meeting, Virtual (November 27 – December 4, 2020): "Accurate Machine-Learning Models for the Atomic-Scale Simulation of Doped LLZO Solid Electrolytes"; Q. Wang, A. Urban, and N. Artrith. F.EN07.05.04.

TASK 4 – METALLIC LITHIUM

Summary and Highlights

The use of a metallic lithium anode is required for advanced battery chemistries like Li-ion, Li-air, and Li-S to realize dramatic improvements in energy density, vehicle range, cost requirements, and safety. However, use of metallic lithium with liquid and solid polymer or ceramic electrolytes has so far been limited due to parasitic SEI reactions and dendrite formation that eventually short circuit the battery. Adding excess lithium to compensate for such losses negates the high-energy-density advantage of a Li-metal anode and leads to further concern for battery safety. For a long lifetime and safe anode, it is essential that no lithium capacity is lost either (1) to physical isolation by roughening, dendrites, or delamination processes, or (2) to chemical isolation from side reactions. The key risk, and current limitation, for this technology is the gradual loss of lithium over the cycle life of the battery.

BMR, Battery500, and other DOE programs are addressing this challenge with many innovative and diverse approaches. Key to all is the need for a much deeper analysis of the degradation processes and new strategies to maintain a dense, fully connected lithium and a dendrite-free electrolyte so that materials can be engineered to fulfill the target performance metrics for EV application, namely 1000 cycles and a 15-year lifetime, with adequate pulse power. Projecting the performance required in terms of just the lithium anode, this requires a high rate of lithium deposition and stripping reactions, specifically about 30 μm of lithium per cycle, with pulse rates up to 10 and 20 nm/s (15 mA/cm^2) charge and discharge, respectively, with little or no excess lithium inventory. This is daunting in the total mass and rate of material transport that must be achieved without failures.

The efficient and safe use of metallic lithium for rechargeable batteries is then a great challenge, and one that has eluded R&D efforts for years. This project takes a broad look at this challenge for both SSBs and batteries continuing to use LEs. Electrolytes reported here include nonflammable liquid solutions, gel type polymer-in-a-salt, composites of ceramic polymer phases, common and novel PEs, and both oxide and sulfide ceramic electrolytes. In most studies, the electrolyte phases were modified by addition of plasticizers or interface coatings to improve transport, stability, and ease of manufacturing. Researchers are typically working toward cycling of full cells with relevant and balanced capacities for the lithium anode and cathode using measures of CE, interface resistance, and post-cycling observation of the disassembled cell components to assess stability of the Li-metal anode and chosen electrolyte.

Highlights

The group at PNNL led by W. Xu continues their investigation of lithium metal with a variety of high concentration electrolytes (HCEs). The focus this quarter was to evaluate a nonflammable polymer gel containing trimethyl phosphate (TMPa) and a comparable LiFSI-TMPa liquid with a nonflammable polymer matrix. Results indicate that neither are compatible with Li//NMC-622 chemistry for extended cycling at 60°C. The ongoing effort will expand to test composites with localized high concentration electrolytes (LHCEs). AIMD models are being used to understand the coordination of Li^+ and FSI^- ions in ionic-liquid-plasticized polymer-in-salt electrolytes (PISEs), which are promising for stable Li//NMC-622 cells.

At ORNL, X. Chen is leading efforts to use powders of the garnet LLZO SE supplied by the ANL Mobile Examination and Remediation Facility (MERF) facility to prepare thin composite electrolytes. Baseline studies of processing and Li/Li cycling were completed using the as-received powder that was pressed or tape cast and sintered to a porous LLZO body. This was subsequently filled with a thermally crosslinked PEO-based PE. Also, composites of dispersed LLZO particles in the crosslinked PEO polymer were prepared and characterized. This work forms the base for comparison of alternative synthesis and processing approaches that are now underway with ORNL and MERF. In addition, the team is advancing models of the ion polarization within composites of single-ion conducting particles in a binary PE matrix to compare with the laminated structures addressed earlier.

S. Tepavcevic and L. A. Curtiss lead the group at ANL evaluating the chemical stability of Li-metal contacts to doped LLZO. XPS has proven a useful technique to follow the partial reduction of Zr^{+4}, indicating conditions resulting in lithium reaction and formation of an oxygen-deficient interface (ODI). This quarter, the ANL team collaborated to investigate the effect of different vacuum processing to form a lithium coating on clean polished LLZO surfaces. Interestingly, the ODI varied as lithium was grown via e-beam evaporation, sputtering, and electrochemically under electron bombardment. Results, published in *Chemistry of Materials*, suggest that energetic deposition can overcome the kinetic passivation energy barrier to give rise to an ODI reaction.

At LLNL, J. Ye is leading efforts to demonstrate 3D-printing processes for SEs and cathodes. This quarter, five sources of LLZTO powder were compared by XRD, SEM, and inductively coupled plasma – optical emission spectrometry (ICP-OES) characterizations of the composition and morphology. The sintering behavior was then compared for each powder under identical conditions of pressing and heating. Results varied significantly, leading to wide difference in the density and the presence of impurity phases. Addition of SiO_2 may serve as a sintering aid, potentially due to reaction with Li_2CO_3 at the LLZTO surface.

Sulfide-based electrolytes and cathodes are being investigated at ORNL, as led by J. Nanda. The team shows how the conductivity of β-Li_3PS_4 (LPS) electrolyte improves to 0.3 mS/cm at room temperature with refined processes to remove residual solvent from the LPS powder and to heat the material during pressing. Interestingly, the LPS density did not vary. This electrolyte was used with a solid-state composite cathode of LPS, NMC, and carbon. Capacity loss and increasing resistance during cycling in a lithium battery suggest an irreversible oxidation forming a resistive NMC-LPS interface. A lower-voltage cathode of FeS_2 shows a more stable cycling performance.

The Stanford University team, led by Y. Cui, is working toward a different goal of prelithiated anodes, such as silicon. This quarter, reduced graphene oxide (rGO) sheets were calendered to achieve a range of thicknesses. Contacting the rGO with molten lithium loads lithium inside the channels. This lithium loading in the rGO is comparable to a lithium foil of 0.5- to 20-μm thickness. It is exceedingly difficult to achieve such thicknesses by extruding lithium metal as free-standing ultra-thin ribbons. Using Li-rGO is a promising approach to prelithiate the silicon and other Li-free anode materials to compensate for initial loss of active lithium in the cell.

Task 4.1 – Lithium Dendrite Prevention for Lithium Batteries (Wu Xu and Ji-Guang Zhang, Pacific Northwest National Laboratory)

Project Objective. The objective of this project is to enable lithium metal to be used as an effective anode in rechargeable Li-metal batteries with good stability and high safety. The investigation this fiscal year will focus on two aspects. First, develop nonflammable polymer composite electrolytes (NPCEs) and investigate effects of various flame-retardant solvents and polymers on ionic conductivity, lithium CE, Li-anode morphology, flammability, and battery performances in terms of long-term cycling stability and rate capability at various temperatures. Second, establish correlation of morphologies of SEI layer and deposited lithium with electrolyte formulation, current density, and lithium deposition/stripping cycling.

Project Impact. Lithium metal is an ideal anode material for high-energy-density rechargeable batteries; however, the application of Li-metal anode is hindered by safety concerns and short cycle life. The safety concerns of Li-metal batteries mainly arise from lithium dendrite growth and electrolyte flammability, while the short cycle life is related to low lithium CE. Although much progress has been achieved in suppressing lithium dendrites and increasing lithium CE in LEs, most LEs are flammable and may pose safety hazards in case of extreme conditions. Therefore, development of electrolytes with improved safety for advanced battery chemistry is imperative. An ideal electrolyte for Li-metal anode should not only suppress lithium dendrite growth and have high CE, but also be intrinsically nonflammable. This fiscal year, the team will develop NPCEs that have high lithium CE, suppress lithium dendrites, and are stable with high-voltage cathodes. The success of this project will increase safety of Li-metal and Li-ion batteries and accelerate market acceptance of EVs, as required by the EV Everywhere Grand Challenge.

Approach. The approach will encompass several areas: (1) develop NPCEs that can enable long-term cycling with significantly improved safety features of Li-metal batteries, (2) develop current collectors with 3D structure for Li-metal anode to suppress lithium dendrite growth, increase lithium utilization, and extend cycle life of Li-metal batteries, and (3) conduct mechanistic studies on lithium deposition behavior to lay groundwork for future improvement of electrolytes (salts, solvents, and additives) for Li-metal batteries.

Out-Year Goals. The long-term goal of the proposed work is to enable Li-metal and Li-ion batteries with a specific energy of > 350 Wh/kg (in cell level), 1000 deep-discharge cycles, 15-year calendar life, and less than 20% capacity fade over a 10-year span to meet the goal of EV Everywhere Grand Challenge.

Collaborations. This project collaborates with C. Wang of PNNL on characterization by TEM/SEM; K. Xu and M. Ding of U. S. Army Research Laboratory (ARL) on DSC measurements; and B. Polzin at ANL on coated electrode sampling.

Milestones

1. Evaluate properties of NPCEs and cycling performance of Li||NMC cells using the NPCE. (Q1, FY 2021; Completed, December 31, 2020)
2. Elucidate influencing factors on lithium deposition behavior by *in situ* AFM. (Q2, FY 2021)
3. Fabricate 3D-structured current collectors and characterize their physical properties. (Q3, FY 2021)
4. Evaluate influence of 3D-structured current collector on Li-metal deposition behavior and cycling performance of Li||NMC cells. (Q4, FY 2021)

Progress Report

Evaluation of Nonflammable Composite Gel Polymer Electrolyte (GPE)

To improve the mechanical strength of the nonflammable GPE based on a nonflammable HCE of LiFSI-TMPa (1:1.4 by mol.) and a nonflammable polymer matrix developed last quarter, the nonflammable GPE was combined with a separator before being applied to Li-metal batteries. Due to the relatively low ionic conductivity of the HCE-based GPE at room temperature, cycling performance tests of the Li||NMC-622 cells were carried out at 60°C. Figure 90 shows that the cells using the GPE-separator composite exhibit a continuous capacity decay after ca. 30 charge/discharge cycles (black square symbol). To understand the reason behind the fast capacity decay, the Li||NMC-622 cells using the liquid TMPa-based HCE and separator were assembled and tested, exhibiting even faster capacity decay (red dot symbol). These results indicate that the TMPa-based HCE is not compatible with the Li||NMC-622 cell chemistry at high temperatures. The GPE / separator composite electrolyte with a TMPa-based LHCE was prepared and is under evaluation in Li||NMC-622 cells at room temperature because the LHCE has a relatively higher ionic conductivity than the HCE. The results will be reported next quarter.

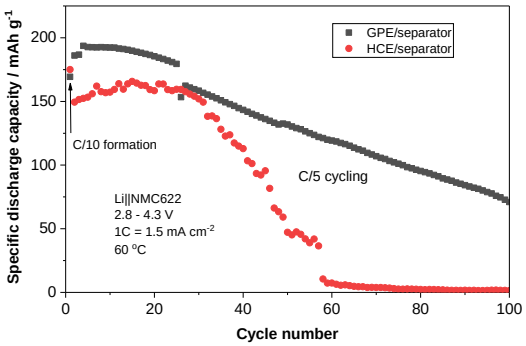

Figure 90. Cycling performance of Li||NMC-622 cells using gel polymer electrolyte / separator composite electrolyte and high-concentration electrolyte (liquid) / separator.

Influence of Separator on Lithium Deposition Behavior

In a separate effort, the influence of polyolefin separator on lithium deposition behavior was investigated. Figure 91 shows the lithium morphologies deposited on copper substrates in a conventional electrolyte in the coin cell with a polyolefin separator and the electrochemical cell without separator. As shown in Figure 91a/c, the lithium deposited in the conventional coin cells exhibits a highly irregular morphology. Whisker-like and flake-like lithium deposits can be observed. In the absence of the polyolefin separator, the deposited lithium exhibits a rod-array morphology (Figure 91b/d), being much more regular than that in coin cell. The reason behind such a phenomenon is still not completely understood. The difference could be possibly assigned to either the uneven Li^+ flux induced by the polyolefin separator or the mechanical pressure in the coin cell. More investigations are being performed to understand how the separators influence the lithium deposition morphology.

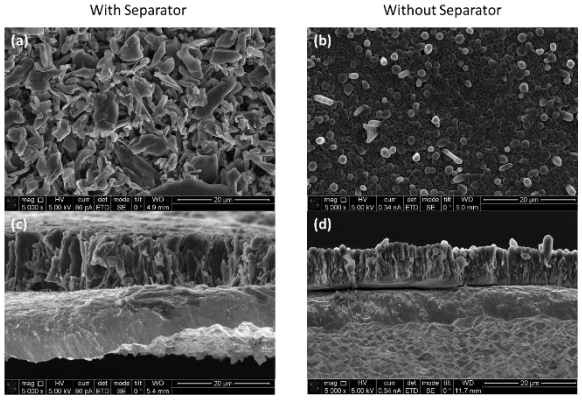

Figure 91. Morphologies of deposited lithium in 1.2 M $LiPF_6$/EC-EMC (3:7 by wt.) in the presence (a/c) and absence (b/d) of polyolefin separator: (a/b) top view, and (c/d) cross-section.

PISE for Li-Metal Batteries

This quarter, the PISEs based on LiFSI and PEO were further studied. AIMD simulations indicate that the coordination number (CN) of oxygen atoms to each lithium ion is about 4 when the ethylene oxide (EO) / lithium molar ratio is 4 or less. Decreasing the EO/Li ratio increases the CN of oxygen in FSI anion, while it reduces the CN of oxygen in PEO. The lowest HOMO (highest occupied molecular orbital) energy is located at the PISE with EO/Li = 1, which is in agreement with the LSV test results. The *postmortem* analyses demonstrate the good protection of the ionic liquid-plasticized PISE on lithium metal and NMC-622 when charged to 4.3 V. The manuscript is being prepared.

Patents/Publications/Presentations

Publication

- Wu, H., H. Jia, C. Wang, J-G. Zhang, and W. Xu. "Recent Progress in Understanding Solid Electrolyte Interphase on Lithium Metal Anodes." *Advanced Energy Materials* 11, No. 5 (2020): 2003092. doi: 10.1002/aenm.202003092.

Task 4.2 – Composite Electrolytes to Stabilize Metallic Lithium Anodes (Nancy Dudney and X. Chelsea Chen, Oak Ridge National Laboratory)

Project Objective. The project has several objectives: (1) prepare novel polymer and ceramic electrolyte materials that can work together to achieve thin membranes that have the unique combination of electrochemical and mechanical properties required for practical manufacturing and to stabilize the metallic lithium anode for good power performance and long cycle life, (2) identify key features of the composite composition, architecture, and fabrication that optimize performance, and (3) fabricate thin electrolyte membranes to use with a thin metallic lithium anode that provides good power performance and long cycle life.

Project Impact. A stable lithium anode is critical to achieve high energy density with excellent safety, lifetime, and cycling efficiency. This study will identify key design strategies that should be used to prepare composite electrolytes to meet the challenging combination of physical, chemical, and manufacturing requirements to protect and stabilize the Li-metal anode for advanced batteries. By utilizing well characterized and controlled component phases, design rules developed for composite structures will be generally applicable toward substitution of alternative and improved SE component phases as they become available. Success will enable DOE technical targets: 500-700 Wh/kg, 3000-5000 deep discharge cycles, and robust operation.

Approach. This project seeks to develop practical SEs to provide stable, long-lived protection for Li-metal anode. Current electrolytes have serious challenges when used alone: oxide ceramics are brittle, sulfide ceramics are air sensitive, polymers are too resistive and soft, and many electrolytes react with lithium. Composites provide a clear route to address these issues. While work continues to emphasize study of ceramic electrolyte / PE interfaces, this effort has expanded to address the following: (1) practical processing routes to fabricate full batteries using better composite electrolytes with a composite cathode and thin Li-metal anode, and (2) introduction of alternative polymer and ceramic phases to replace well-known model materials and develop improved composite electrolytes. In addition to solid-state devices, hybrid batteries are investigated using a fluid or gel catholyte within the porous cathode. Coatings have also been employed to stabilize electrode interfaces. These directions increase complexity of the studies, but are needed to improve cycling stability and rate performance and to advance practical implementation of the SE and Li-anode technology.

Out-Year Goal. The goal is to use advanced manufacturing processes where the architecture of the composite membrane can be developed and tailored to maximize performance and cost-effective manufacturing.

Collaborations. Work is conducted by Y. Zhang and X. Chen. Ceramic electrolyte powders (LICGC™) are obtained from Ohara Corporation. ORNL internal collaborators include B. Armstrong and S. Kalnaus. For the single-ion conducting polymers, the team partnered with J. L. Schaefer at University of Notre Dame. Joseph Libera from ANL provided large quantity of LLZO powders.

Milestones

1. Sinter and characterize porous LLZO network by different processes. (Q1, FY 2021; Partially completed; waiting on LZO)
2. Compare polymer-LLZO ceramic composites with four different ceramic loadings. (Q2, FY 2021; Initiated)
3. Elucidate the Li-ion path through at least two distinct polymer-ceramic composites. (Q3, FY 2021, Initiated)
4. Measure Li^+ transference number with at least two different anion receptors. (Q4, FY 2021)

Progress Report

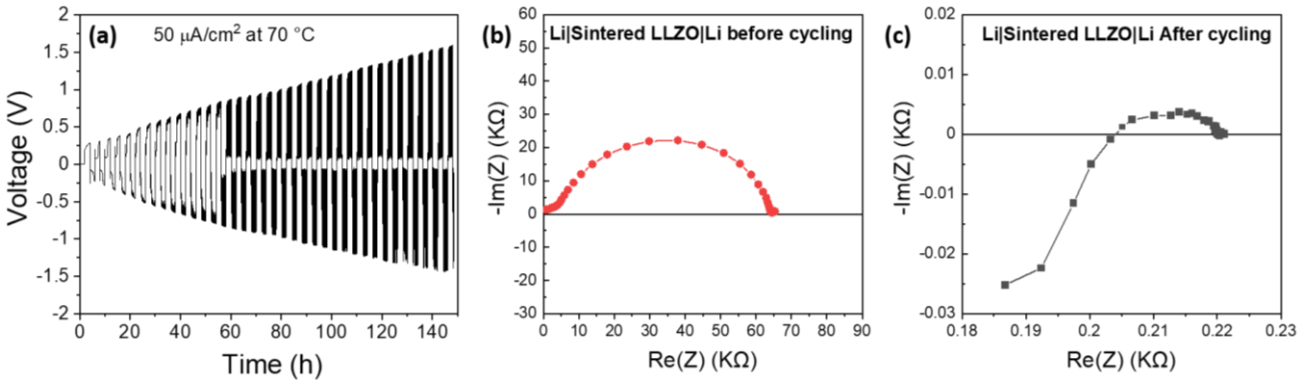

Figure 92. Cycling of Li|sintered LLZO|Li. (a) Li-symmetrical cell cycling performance using partially sintered LLZO. Cycling was performed at 70°C with a current density of 50 μA/cm². (b) Nyquist plot of the Li-symmetrical cell *before* cycling, at room temperature. (c) Nyquist plot of the Li-symmetrical cell *after* cycling, at room temperature.

LLZO powders obtained from the MERF facility at ANL (J. Libera) were partially sintered at 900°C in dry air for 3 hours (protocol reported last quarter). Li-symmetrical cell was assembled using partially sintered LLZO pellet and thick lithium foil. Lithium foil was brushed to remove the surface layer and rolled out thin in a polypropylene bag in a glovebox. Sintered LLZO pellet, without further treatment, was placed in between two lithium electrodes with a half-inch diameter. The cell was assembled on a hot plate at 180°C with two stainless-steel rods (also half-inch diameter) as the current collector. The cell was sealed in two layers of heat shrink tubing and tested in AA battery holder at 70°C with a current density of 50 μA/cm^2. Cycling results are shown in Figure 92a. The overpotential rapidly increased with cycling, and the cell exhibited soft shorts after ~ 10 cycles. The Nyquist plots before and after cycling are shown in Figure 92b-c. Before cycling, large resistance (~ 70 kΩ) was observed. After cycling, the Nyquist plot showed characteristics of a short circuit with a relatively large lead resistance (~ 200 Ω).

Postmortem analysis of the sintered LLZO symmetrical cell is shown in Figure 93. Black colored regions were observed throughout the cross-section of the LLZO pellet (Figure 93, top row). The zoomed-in image of the black region showed that some voids were covered by a dark-grey-colored soft material. In contrast, the white region remained the same morphology as before cycling (Figure 93, middle row). EDS analysis could not identify this soft material. The team suspects that this material is lithium, since the lithium signature peak is out of the EDS energy range. The black region penetrated the whole cross-section of the LLZO pellet; therefore, lithium dendrite growth is likely the cause of the cell shorting.

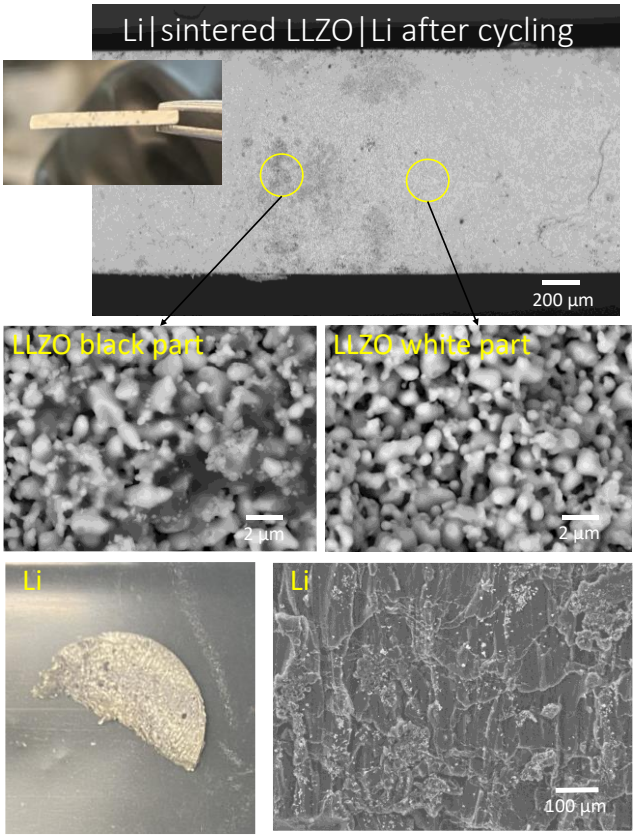

Figure 93. *Postmortem* analysis of Li|sintered LLZO|Li. (Top row) Cross-sectional scanning electron microscopy (SEM) image of the sintered LLZO pellet after cycling. Inset: digital photograph of pellet. (Middle row) Zoomed-in SEM images of the LLZO pellet, showing two distinct regions. (Bottom row) Digital photograph of lithium and SEM image of the surface of lithium that was in contact with the LLZO pellet.

The surface of cycled lithium significantly roughened (Figure 93, bottom row). On the other hand, the surface of cycled lithium remained silver and shiny, indicating that LLZO is chemically stable with lithium. The team also tested Li-symmetrical cell cycling using partially sintered LICGC™ pellet, and this cell could not cycle at all as lithium was quickly consumed by the reaction with LICGC™.

In addition to pressing thick pellets, the team also began working on fabricating LLZO electrolyte tapes using a tape-casting process. Initial work focused on building a baseline process in laboratory air to have a direct comparison to electrolyte fabricated in controlled atmospheres. Control of the reactivity of LLZO starting powder was an issue during this initial work; a quick study to evaluate which step in the fabrication process was the root cause of the reactivity was completed. Characterization of these results is incomplete, but efforts have been initiated to address potential causes. These efforts include replacing constituents in the tape-casting process and/or starting with an LZO powder and reacting the lithium in post-processing. LZO powders are being synthesized by J. Libera from MERF.

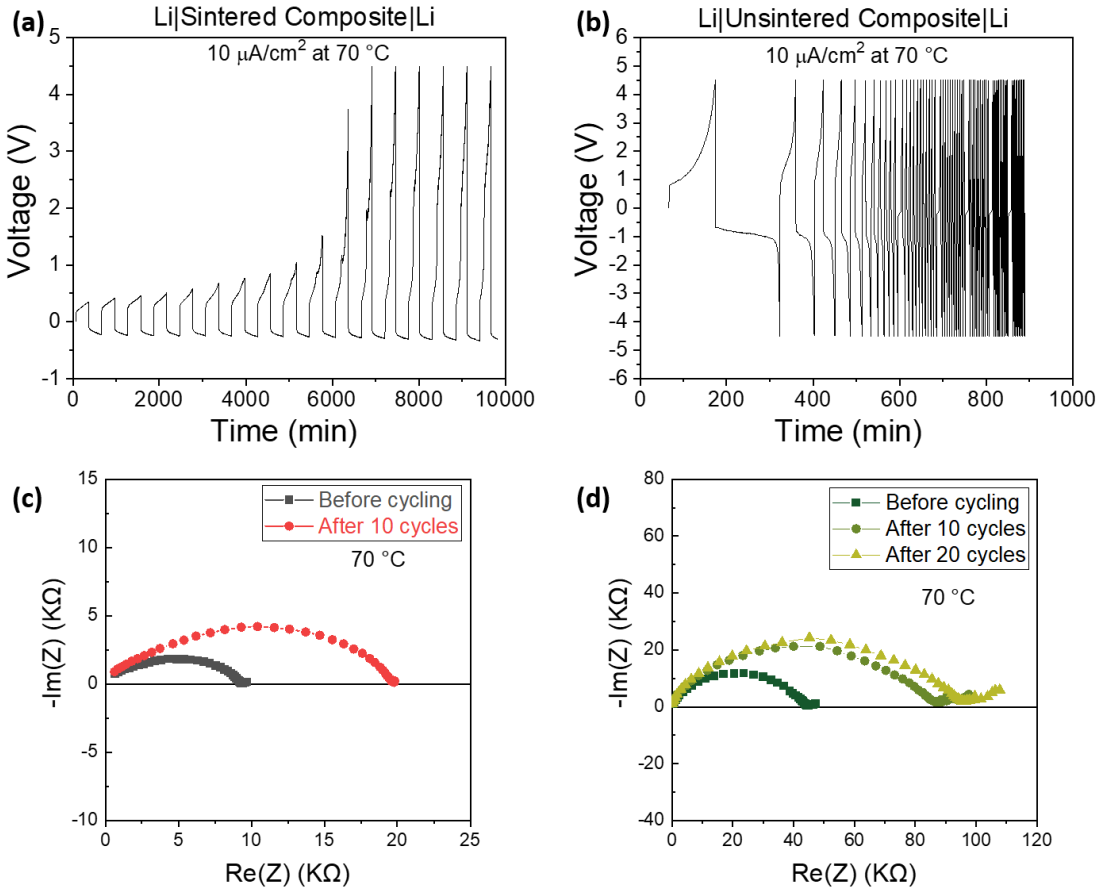

Figure 94. Li-symmetrical cell cycling using LLZO/xPEO composites. (a) Cycling results of sintered LLZO/xPEO composite. (b) Cycling results of unsintered LLZO/xPEO composite. (c) Nyquist plots of cell in (a), at different cycling stages. (d) Nyquist plots of cell in (b), at different cycling stages.

While waiting for the LZO powders, the team began addressing next quarter's milestones. Two types of LLZO composite electrolytes were made for comparison. The first composite was a sintered LLZO/xPEO composite made by filling the partially sintered LLZO pellet with xPEO precursors [mixture of Jeffamine, poly(ethylene glycol) diglycidyl ether (PEGDGE), and LiTFSI) and curing at 100°C for overnight. The composite electrolyte was dried in the glovebox antechamber for 24 hours and then soaked in dried tetraethylene glycol dimethyl ether (TEGDME) in a sealed vial in the glovebox for 1 hour. For comparison with this composite, the team cold-pressed a pellet using LLZO powders and filled the pellet with xPEO without sintering. The filling and

drying procedure was the same as for the sintered pellet. The sintered and unsintered composite electrolytes were made into a Li-symmetrical cell with AA-battery geometry, similar to the Li|sintered LLZO|Li cell described earlier. Cycling results are shown in Figure 94. The sintered composite was able to cycle at very low current density (10 μA/cm^2) for a few cycles at 70°C. The overpotential on one side started increasing rapidly after 5 cycles (Figure 94a). Correspondingly, cell impedance doubled after 10 cycles (Figure 94c). *Postmortem* of this cell shows severe reaction on the backside of lithium (in contact with stainless steel), and the composite pellet changed from a white color to a yellowish off-white color. The increase in cell resistance and overpotential could be due to reaction between the gel polymer xPEO/TEGDME and lithium. This hypothesis can be verified by filling the LLZO pellet with a different PE.

Compared to the sintered composite, initial impedance of the unsintered composite was nearly five times larger (~ 50 kΩ versus ~ 10 kΩ). This cell could not cycle well at all, as the overpotential reached the cutoff value of 5 V in cycle 1. Cell impedance almost doubled after 10 cycles, similar to the sintered composite.

These results are summarized as follows: (1) although chemically stable with lithium, the partially sintered LLZO is too resistive compared to LICGC™, with a similar morphology; (2) without the polymer filling, lithium dendrite easily penetrated the porous LLZO network; (3) with the polymer filling, the cell failure mechanism is not soft shorts, but instead increased cell resistance and overpotential. The GPE used to fill the ceramic network may be too reactive with lithium. These results show that both the ceramic and the polymer need to be improved or modified. Next quarter, the team will work on improving both the polymer and the ceramic. For the ceramic, they will examine the first-sinter-then-lithiate approach by using LZO as the starting material. For the polymer, they will examine linear PEO as a comparison.

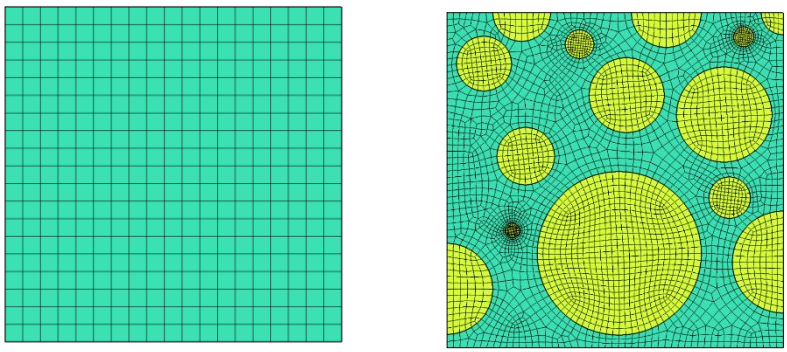

Figure 95. Simulation domains and meshes showing (a) homogenous binary electrolyte and (b) composite electrolyte with single-ion conducting particles added to binary electrolyte matrix.

The numerical modeling efforts continued toward understanding of how addition of SIC to a binary PE changes the cation concentration gradients in a composite. Initial studies were performed in the third quarter of FY 2020, and the team simulated 1D concentration gradients in a thick sandwich structure with the SIC middle layer. Here, they report on a 2D model for a particulate composite with explicitly resolved two phases: LICGC™ particles (SIC) and binary PE. The small (5 × 5 μm) area was seeded with discs representing single-ion conducting particles. The particle size follows Bi-Weibull distribution used to simulate the particles size distribution measured from LICGC™ sample by laser diffraction particle size analyzer (LDPSA). Such a 2D-composite was compared to a homogenous binary electrolyte sample of the same area (Figure 95). In both cases, the sample was sandwiched between lithium electrodes, and a 10-mV potential was applied to the sample edge.

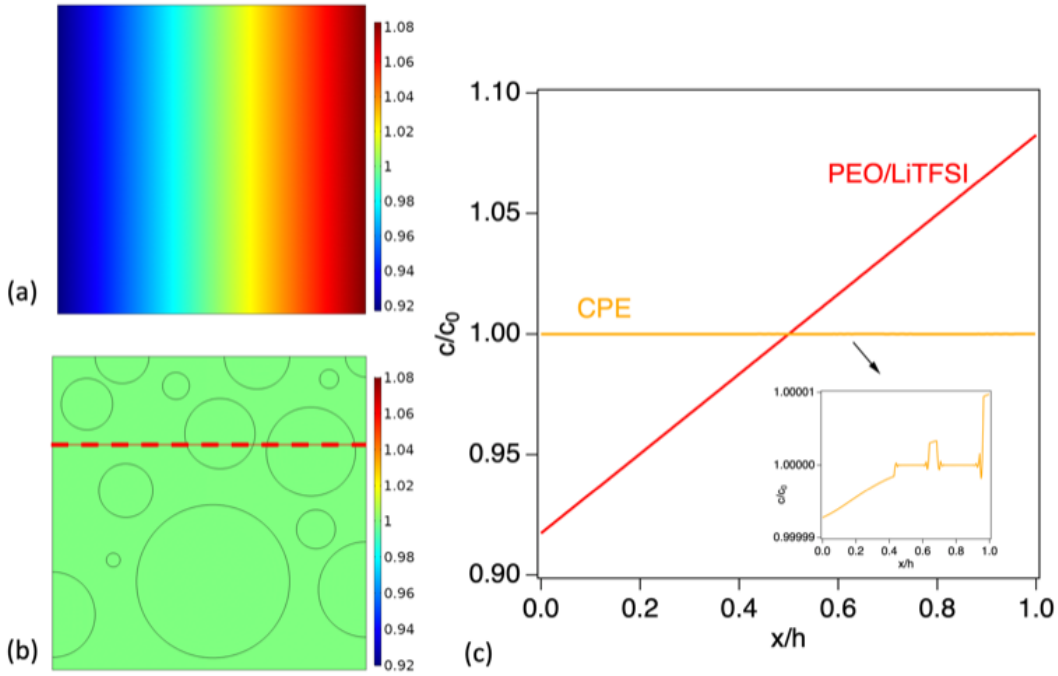

Figure 96. Lithium cation concentration maps in (a) PEO/LiTFSI binary electrolyte and (b) composite electrolyte of PEO/LiTFSI and LICGC™ particles. (c) Comparison of the two scenarios along the cross-section (b, red line). Normalized concentrations and distances are shown. Significant reduction in gradients can be seen with addition of LICGC™. When plotted on a separate scale, the Li^+ concentration shows some variation (c, inset); cross-sections of the two LICGC™ particles can be clearly identified where the concentration remains constant.

The model is based on Nernst-Planck equations for ionic transport in both phases. The equations describe diffusion and migration of charged species and therefore require component diffusivities for cations and anions. The binary electrolyte was modeled as a PEO/LiTFSI system, and individual diffusivities of Li^+ and $TFSI^-$ ions were taken from pulse-field gradient nuclear magnetic resonance (PFG NMR) measurements in literature.[1] In SIC with ionic transport based on vacancy hopping, the diffusivity of negative charge was fixed as zero, leading to constant concentration of lithium ions within the particles. Results show that addition of single-ion conducting particles reduces the concentration gradient of ionic species across the sample (Figure 96). This indicates effective increase in transport number for Li^+ by adding the second phase to the PE. While for simplicity the team considers 2D geometry here, they expect this conclusion to hold in 3D as well.

To their knowledge, the concentration gradient of a composite electrolyte has not been modeled in a 2D geometry. Many studies report the "transference number" of composite PEs using the Bruce-Vincent method. However, the validity of the Bruce-Vincent method is limited to the extremely dilute concentration regimes and cannot be applied to more practical electrolyte systems. This modeling result, while only adopting a small domain, reveals the benefit of adding single-ion conducting ceramic particles into a binary electrolyte. In this model, the initial Li-ion concentration, C_0, is assumed to be 10 M in both the polymer phase and the ceramic phase. This restriction will be removed in future efforts.

Reference

[1] Choo, Y., D. M. Halat, et al. *Progress in Polymer Science* 102 (2020).

Patents/Publications/Presentations

Presentations

1. Seton Hall University, South Orange, New Jersey (October 2020): "Ion Transport in Soft-Hard Hybrid Materials"; X. C. Chen. Invited lecture.
2. MRS Spring/Fall 2020 Meeting, Virtual (December 2020): "Challenges in Enabling Li Metal Anode – A Composite Electrolyte Approach"; X. C. Chen. Invited.

Task 4.3 – Enabling Solid-State Batteries through Characterization and Modeling (Sanja Tepavcevic and Larry A. Curtiss, Argonne National Laboratory)

Project Objective. The project objectives are multi-faceted, including development of a new mechanically and chemically stable and Li-ion conductive ($\geq 2 \times 10^{-4}$ S/cm at 298 K) crystalline/amorphous SE for SSB. The anode and cathode are composed of lithium metal and a Li-based oxide, respectively, allowing operation at cathode potentials > 5 V (denoted as a S_{Li}-S_{EL}-S_C system).

Project Impact. Protective organic and inorganic compounds can enhance stability of the interface, improve Li-ion interfacial transport, minimize dendrite formation, and increase safety in Li-ion batteries.

Approach. The project proposes to develop and use interdisciplinary, atomic-/molecular-level insight obtained from integrating both experimental- and computational- based methodologies to define the landscape of parameters that control interfacial properties for a new generation of the Li-ion solid-solid battery systems. The strategy will involve transferring knowledge gained from well-characterized thin-film materials to real-world materials. This strategy forms a closed loop wherein the knowledge gained from model systems is used to design more complex, real-world materials, and vice versa. The work will focus on utilizing existing in-house synthesis and characterization methods to enable rapid transition from fundamental science to realistic cells.

Out-Year Goals. The out-year goals are to use and develop the physical and chemical synthesis methods for design of SSI with unique chemical/mechanical/conductivity properties. The proposed work will develop and exploit a variety of *ex situ* and *in situ* experimental optical and surface sensitive techniques and electrochemical methods to explore and explain bulk and interfacial properties of the selected materials. The results will serve to unravel many puzzling bulk and interfacial properties of S_{Li}-S_{EL}-S_C systems, including various types of ceramic and glass materials.

Collaborations. This project funds work at ANL and collaboration with J. Sakamoto at UM.

Milestones

1. Evaluating chemical stability and correlating with interfacial reactivity for vacuum-deposited Li/Al- doped LLZO interfaces. (Q1, FY 2021; Completed)
2. Understanding impact of different dopants in LLZO (aluminum versus gallium) on chemical and electrochemical reactivity with metallic lithium by surface and bulk sensitive techniques and computational tools. (Q2, FY 2021)
3. Modifying energy barrier for Li^+ transport in Al-doped LLZO by controlling the chemistry of the GBs via additives. (Q3, FY 2021)
4. Optimizing nanoLLZO+PEO composite and characterizing chemical and electrochemical reactivity with metallic lithium by surface and bulk sensitive techniques. (Q4, FY 2021)

Progress Report

LLZO garnet-based oxides are a promising class of SEs used as the separator in ASSBs. While LLZO is considered to have a wide electrochemical stability window, its intrinsic stability in contact with lithium metal is not sufficiently well understood, and there is still a debate on the key question of whether LLZO forms passivation layers before and during cycling. The question of reaction kinetics remains largely unaddressed, as many measurements and theoretical insights rely on analysis of the thermodynamic ground state of the system to determine stability. As the team's previous work indicates, some of the discrepancies that exist in the literature likely derive from differences in surface cleanliness (that is, presence or absence of surface Li_2CO_3 and LiOH layers), with even relatively thin reaction layers modifying the interfacial reactivity of LLZO with lithium metal. Furthermore, the specific dopant used to stabilize the cubic phase clearly impacts the nature and extent of reactivity between LLZO and lithium, with Ta-doped LLZO exhibiting very little reactivity as compared to Nb-doped LLZO, whose reactivity with lithium propagates into the bulk via the likely formation of a mixed conducting interphase (MCI). However, these results still do not directly address the kinetics of the reactivity of lithium metal with LLZO, as no time-dependent evolution of the ODI layer discovered in this work was resolved for either Ta- or Al- doped LLZO. This indicates that more precise knowledge of interfacial stability is needed to advance the understanding of Li-metal electrode kinetics and dendrite growth in LLZO-based SSBs. Indeed, determining the critical link between chemical reactivity and electrochemical performance is essential to enable inorganic SEs for next-generation ASSBs.

To develop such insights, the team has utilized a variety of *in situ* and *operando* XPS techniques, coupled with electrochemical measurements, to investigate in detail the factors impacting the interfacial stability of Al-doped LLZO in contact with lithium metal (Figure 97). It is shown that lithium metal deposited onto the LLZO surface via different techniques (that is, magnetron sputtering, electron-beam evaporation, and electrochemical deposition) results in different reactivities that depend sensitively on the energetics of arriving lithium species.

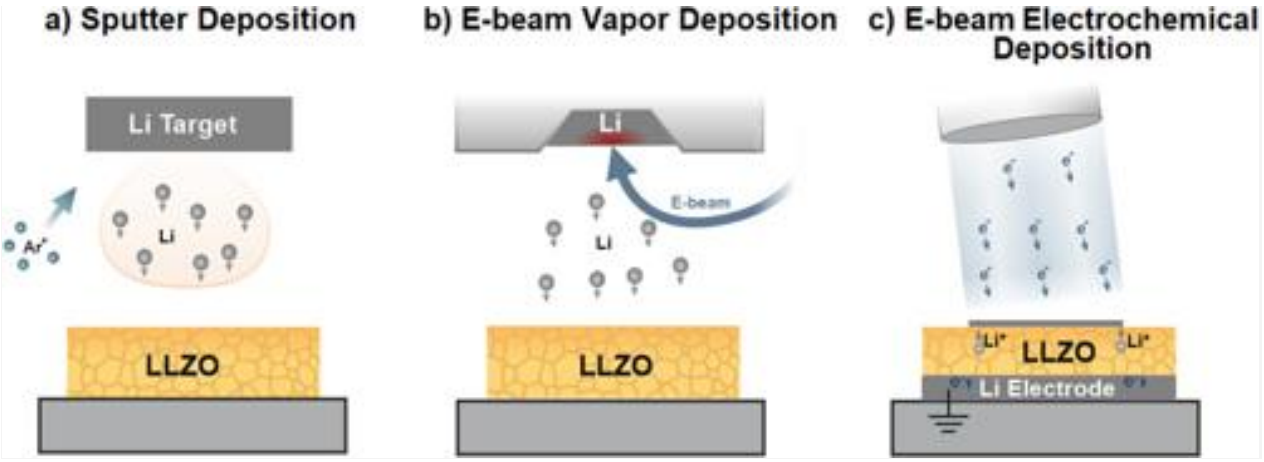

Figure 97. Schematics of the different lithium deposition processes that were utilized in this work. (a) Sputter deposition of lithium and transfer under ultra-high vacuum (UHV) conditions for X-ray photoelectron spectroscopy (XPS) measurements. (b) Electron-beam vapor deposition with UHV transfer for the XPS measurements. (c) *Operando* electrochemical deposition inside the XPS chamber via the electron-beam electrode method.

Through the use of both *in situ* and *operando* XPS methodologies, the team demonstrates the presence of a kinetic barrier to the reduction of LLZO by lithium metal. The extent of ODI formation is found to depend sensitively on the energetics of lithium metal as it arrives at the LLZO surface, with electrochemical and sputter deposition intrinsically leading to reduction of Zr^{4+} and resulting in ODI layer formation (Figure 98a). Lower energy e-beam evaporation does not result in any reduction of Zr^{4+}, even when lithium is deposited at elevated temperatures; however, subsequent irradiation of e-beam-deposited lithium by energetic Ar^+ species is able to reproduce the extent of ODI formation observed from electrochemical and sputter deposition. The

electrochemical deposition of lithium metal does indeed result in reduction of the LLZO surface, resulting in ODI formation that is consistent with previous results by sputter deposition (Figure 98b). Furthermore, these results support the hypothesis that there is a kinetic barrier to LLZO reduction by lithium, as the application of sufficient overpotential to electrochemically nucleate and grow lithium metal provides sufficient energy to drive Zr^{4+} reduction at the Li|LLZO interface. Indeed, the only case in which no reduction is observed is in the case of very low incident lithium deposition energies during e-beam evaporation. The presence of a kinetic barrier further explains the similar lack of reduction observed after simple physical contact of lithium metal with LLZO surfaces, even at temperatures above the melting point. Therefore, it can be concluded that the formation of an ODI is dependent on the lithium energy during the deposition process, and that under further electrochemical cycling conditions, ODI formation is expected to occur. Despite the presence of a kinetic barrier to reduction, EIS measurements of Li|LLZO|Li coin cells reveal an identical response whether or not the ODI is present, indicating that interphase formation does not impede the charge transfer kinetics of lithium ions across the Li|LLZO interface and likely explaining the favorable electrochemical performance of LLZO-based ASSBs. However, a possible link between formation of the ODI layer in LLZO and dendrite nucleation should be considered in future work. Overall, these results highlight the additional complexities governing the reactivity of solid-state interfaces in ASSBs and underscore the importance of *operando* characterization of interfacial stability to design more robust, high-performance protection strategies for SEs in contact with reactive electrodes.

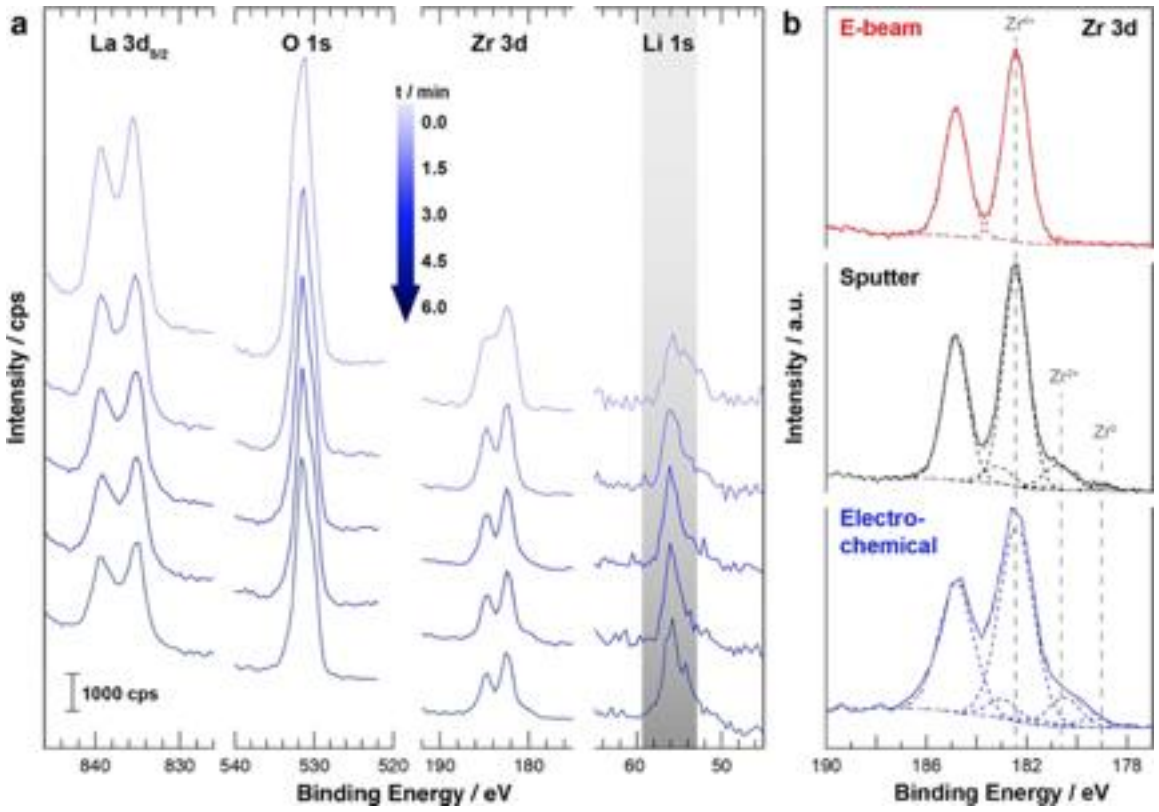

Figure 98. (a) *Operando* X-ray photoelectron spectroscopy measurements of individual core-level spectra during electrochemical deposition of lithium showing their evolution with increasing lithium deposition time. All core-level spectra are plotted on the same absolute scale in counts per second, except Li 1s spectra, which are magnified by 10× for clarity. (b) Zirconium 3d core-level spectra comparing the extent of Zr^{4+} reduction as a function of the deposition technique.

Patents/Publications/Presentations

Publication

- Connell, J., T. Fuchs, H. Hartmann, T. Krauskopf, Y. Zhu, J. Sann, R. Garcia-Mendez, J. Sakamoto, S. Tepavcevic, and J. Janek. "Kinetic Versus Thermodynamic Stability of LLZO in Contact with Lithium Metal." *Chemistry of Materials* 32, No. 23 (2020): 10207–10215.

Task 4.4 – 3D Printing of All-Solid-State Lithium Batteries (Jianchao Ye, Lawrence Livermore National Laboratory)

Project Objective. This project has three objectives: (1) tuning microstructures of 3D-printed SSE separators, (2) determining material and processing compatibilities with cathode printing, and (3) 3D printing of sintering-free SSE separators.

Project Impact. All-solid-state lithium batteries are difficult to process due to the brittleness of ceramic materials, poor solid-solid contact, and electrolyte-electrode stability issues. As a result, the energy and power density and also cycling stability are far from satisfying. This project will address fabrication difficulties by using state-of-the-art 3D-printing techniques that can introduce 3D interfaces and architectures to enhance solid-solid contact and reduce charge transfer resistance. Success will benefit the DOE by establishing the best manufacturing methods for ASSBs to achieve VTO goals on the performance of beyond Li-ion batteries.

Approach. The project employs 3D-printing techniques to manufacture SSEs and related components for ASSBs. The team starts with direct ink writing (DIW) to develop ink recipes with desired rheological properties and explore post-sintering approaches to achieve high densification. In parallel with DIW 3D printing, the team also explores other 3D printing options, such as projection microstereolithography (PuSL). Both sintering and sintering-free approaches can gain benefit from 3D printing and therefore will be investigated.

Out-Year Goals. The team will determine the co-sintering stability of printed NMC/LLZTO films and compare with that of hydraulic pressed NMC/LLZTO pellets. They will print SSE/cathode bilayer structures with controlled interfaces and determine their electrochemical performance with or without post sintering process.

Collaborations. Microstructures, ionic conductivities, and mechanical properties will be provided to the LLNL simulation team, led by the PI, B. Wood, for establishing and validating phase-field modeling methods.

Milestones

1. Evaluate new commercial LLZTO powder sources. (Q1, FY 2021; Completed)
2. Determine performance of ASSBs based on 3D-architected LLZTO structure. (Q2, FY 2021; In progress)
3. Determine performance of ASSBs based on composite PE. (Q3, FY 2021; In progress)
4. Evaluate ASSBs based on co-sintering approach. (Q4, FY 2021; In progress)

Progress Report

Due to the discontinuation of the $Li_{6.4}La_3Zr_{1.4}Ta_{0.6}O_{12}$ (LLZTO) powder product from the previous vendor (vendor 1), the project switched to new providers. This quarter, new LLZTO powders from four manufacturers were received and evaluated. SEM, XRD, ICP-OES, and density measurements were conducted, and the results were compared with previous powders.

Figure 99 shows the XRD analysis and SEM imaging of the as-received LLZTO powders from the previous vendor and three new vendors. All powders exhibit cubic phase with no detectable or little impurities. 5.05 wt% of $La_2Zr_2O_7$ phase was detected in vendor 4 powders. The particle sizes of vendor 2 and vendor 3 are smaller than that of vendor 4 and vendor 1 powders, which explains the lower tapped density of the former two. The grain sizes from XRD analysis may also be different (Table 7). ICP-OES analysis revealed some compositional difference compared with the nominal composition of $Li_{6.4}La_3Zr_{1.4}Ta_{0.6}O_{12}$. For example, vendor 3 powders have 0.5Ta instead of 0.6Ta. Vendor 4 powders show less lithium and lanthanum contents. Both vendor 1 and vendor 2 powders have extra lithium added. Those compositional differences together with morphological differences may explain the discrete sintering behaviors.

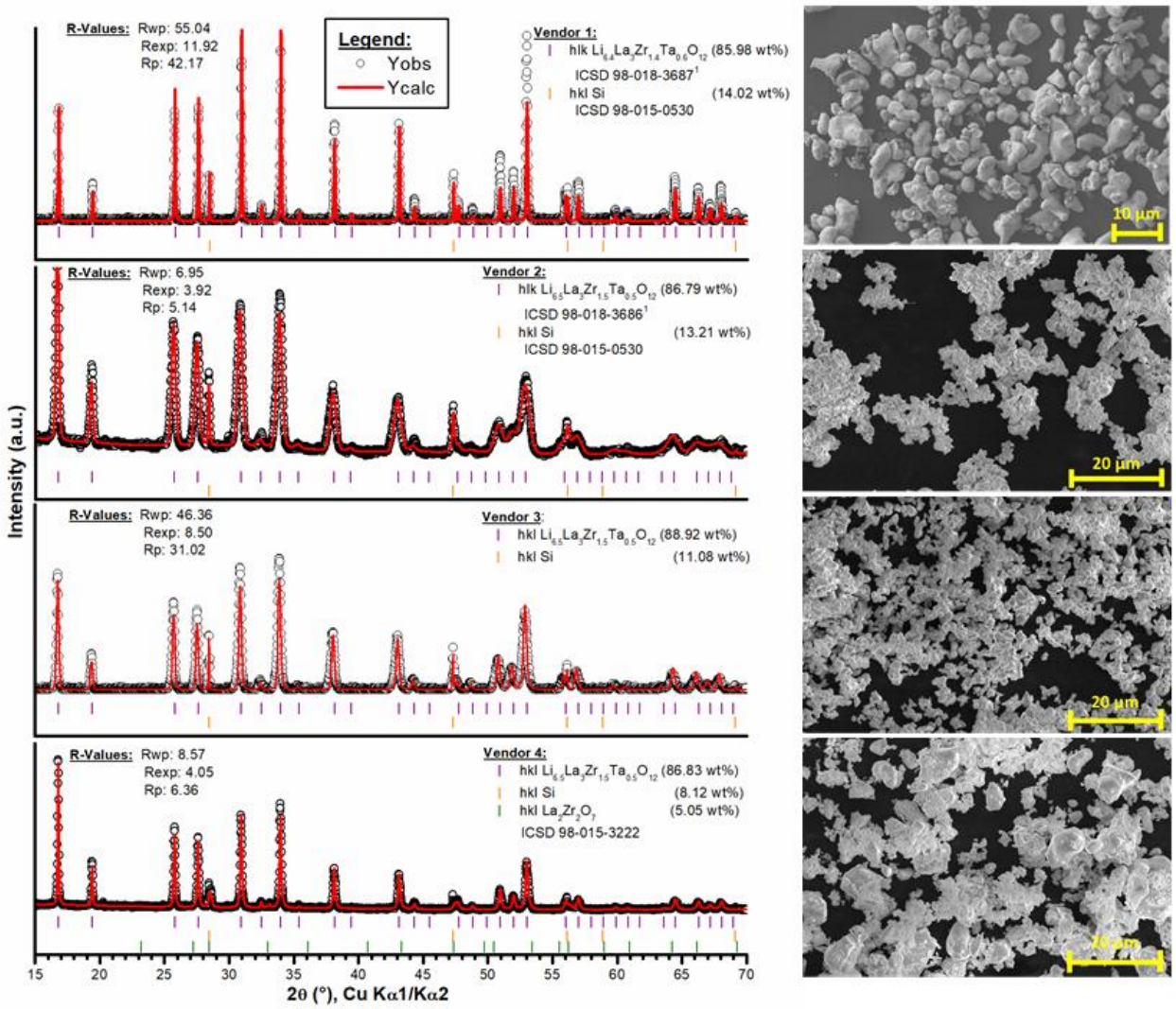

Figure 99. (left) Rietveld refinement fits of LLZTO raw powders mixed with 8-12 wt% of silicon, which was used as an internal standard. (right) Scanning electron microscopy images of the LLZTO raw powders.

To evaluate their sintering capability, all powders were pressed under the same pressure and sintered at 1100°C in argon for 6 hours. It was found that only vendor 2 powder can be densified well, with 92% relative density, close to the original powder from vendor 1 that achieved 93%. The other two and a fifth international supplier (results not included here) showed very little shrinkage and very low final density.

Table 7. Composition, grain size, relative density, and shrinkage of LLZTO pellets sintered at 1100°C for 6 hours.

Manufacturer	ICP-OES analysis	Grain size (nm)	Shrinkage (%) and Relative density (%) of sintered pellets @ 1100°C
Vendor 1	$Li_{7.10}La_{3.00}Zr_{1.39}Ta_{0.61}O_x$	----	~13% and 93%
Vendor 2	$Li_{6.84}La_{3.00}Zr_{1.38}Ta_{0.60}O_x$	149.9	31.02% and 92%
Vendor 3	$Li_{6.53}La_{3.00}Zr_{1.46}Ta_{0.50}O_x$	----	1.42% and 60%
Vendor 4	$Li_{6.26}La_{3.00}Zr_{1.53}Ta_{0.67}O_x$	346.9	2.49% and 75%

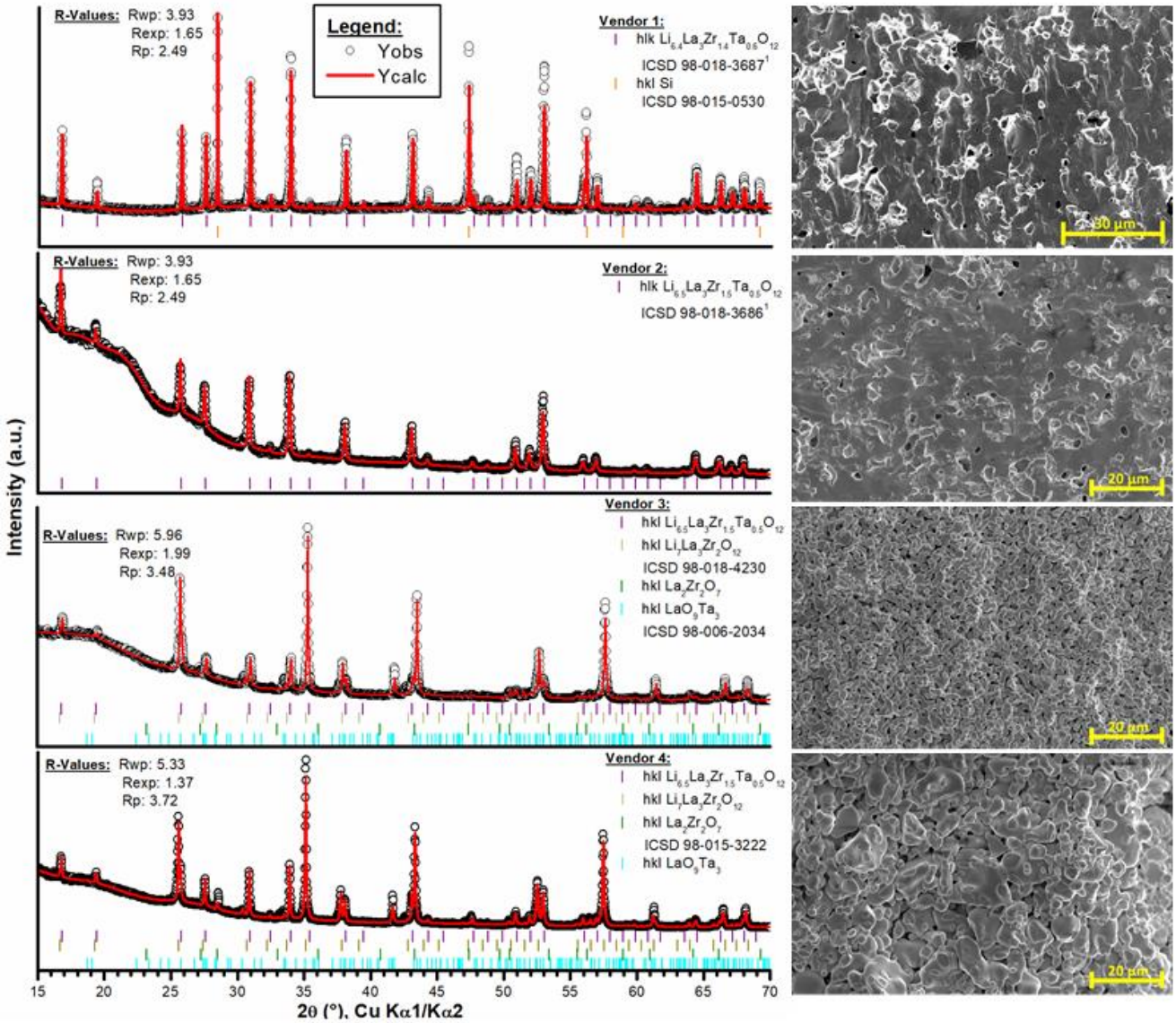

Figure 100. (left) Rietveld refinement fits of LLZTO powders sintered at 1100°C for 6 hours. (right) Scanning electron microscopy images of the LLZTO pellets.

XRD (Figure 100) reveals clean cubic LLZTO phase in sintered vendor 2 pellets, while a significant amount of $La_2Zr_2O_7$ and LaO_9Ta_3 impurity phases were found in sintered vendor 3 and 4 pellets. It is likely the decomposition of the cubic LLZTO phase at 1100°C impeded the densification. The decomposition of the cubic LLZTO phase is due to either low tantalum doping level (0.5 versus 0.6) in vendor 3, or further lithium loss in the initially low-Li-content vendor 4 powders.

Although the vendor 3 powder itself with low tantalum doping cannot be sintered well, the team found that adding a few percent of SiO_2 as a sintering agent can stabilize cubic LLZTO phase and accelerate the densification process (Figure 101). The added SiO_2 likely reacts with the insulating Li_2CO_3, which forms on the surface of LLZTO on exposure to air, forming ion-conductive Li_4SiO_4 phase (1.16×10^{-4} S cm^{-1} @ 100°C). The lower melting point of the silicon phase will enhance the mass transport and therefore promote sintering of LLZTO. Silicon may also incorporate into the LLZO lattice and therefore stabilize the cubic phase.

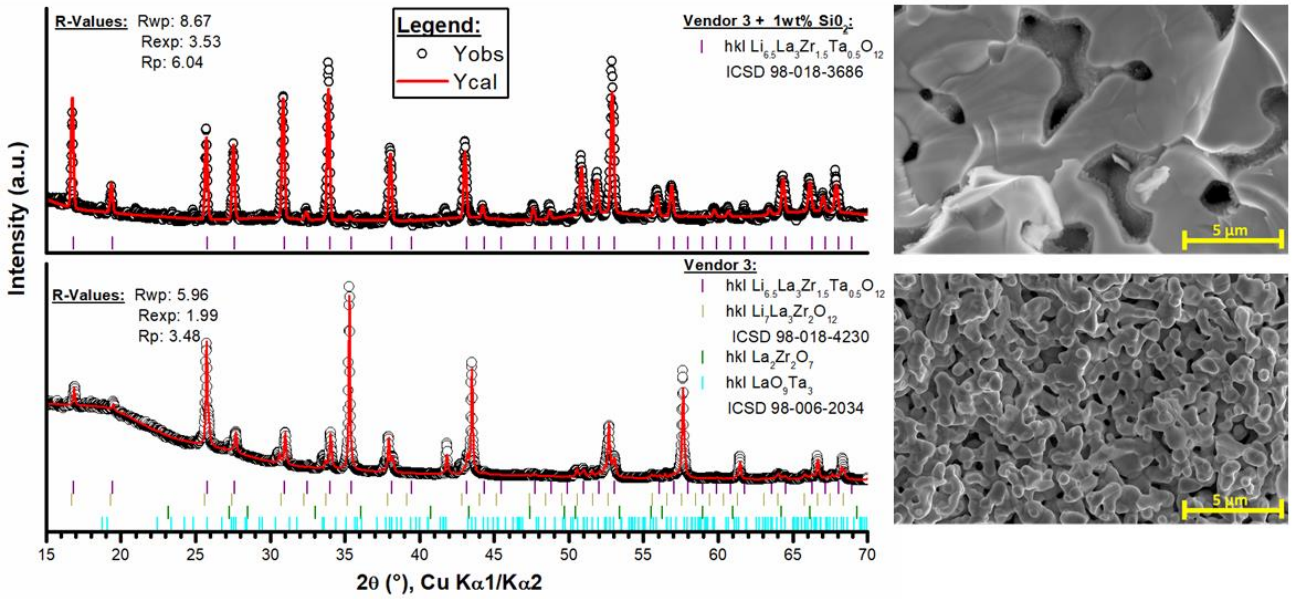

Figure 101. (left) Rietveld refinement fits of LLZTO powders sintered at 1100°C (vendor 3) and 1120°C (vendor 3 + 1 wt% SiO_2) for 6 hours. (right) Scanning electron microscopy images of the LLZTO raw powders.

In summary, four additional vendors for LLZTO powders were evaluated. Vendor 2 powders behave similarly to the one from the original provider and will be used for future studies. Another powder from vendor 3 can be modified by adding a few percent of SiO_2 sintering agent to stabilize cubic phase and accelerate densification.

Patents/Publications/Presentations

Publication

- Wood, M., X. Gao, R. Shi, T. W. Heo, J. A. Espitia, E. B. Duoss, B. C. Wood, and J. Ye. "Exploring the Relationship between Solvent-Assisted Ball Milling, Particle Size, and Sintering Temperature in Garnet-Type Solid Electrolytes." *Journal of Power Sources* 484 (2021): 229252

Task 4.5 – Interfacial Studies on Lithium Thiophosphate Based Solid Electrolytes and Cathodes (Jagjit Nanda, Oak Ridge National Laboratory)

Project Objective. Capacity fading and the underlying interfacial side reactions between thiophosphate SEs and cathode active materials are not well understood. A key project deliverable is to combine EIS measurements with complementary *in situ* and *ex situ* spectroscopy and microscopy to identify decomposition reaction products at the CEI. Ultimately, this work will enable a mechanistic understanding of factors that limit the rate performance and capacity loss of SSBs. The goal here is to combine the information from these techniques to provide a unified overview of the interfacial layer's composition, structure, and morphology. In this multi-year work, the team will investigate a number of SEs [Li_3PS_4 (LPS), $Li_{10}GeP_2S_{12}$ (LGPS), and $Li_{9.54}Si_{1.74}P_{1.44}S_{11.7}Cl_{0.3}$ (LSiPCl)] and cathode compositions belonging to different structural families [$LiFePO_4$ (olivine), FeS_2 (sulfide-based conversion cathode), and $LiNi_{0.6}Mn_{0.2}Co_{0.2}O_2$ (NMC-622, layered oxide)].

Project Impact. SSBs are poised to be the next-generation battery technology for meeting EV goals in terms of energy density, cycle life, and safety. Among other technical barriers, the success of this technology relies on design of stable electrode/electrolyte interfaces. Sulfide-based SEs have high ionic conductivity ($> 10^{-4}$ S/cm) and are mechanically soft, which simplifies processing compared to their oxide counterparts. Furthermore, sulfide SEs are comprised of earth abundant materials (for example, sulfur and phosphorus) and can be easily synthesized using scalable, low-temperature solution-based routes.

Approach. A low-temperature (< 350°C) solution-based synthesis method will be used to synthesize the LPS family of SEs. The structure of these materials is characterized using XRD, Raman spectroscopy, and neutron scattering. Standard AC/DC electrochemical methods are used to characterize ionic conductivity, electrochemical stability, and CCD. The work scope includes using various *in situ* and *ex situ* electrochemical, microscopic, and spectroscopic tools for characterizing the structure, morphology, and kinetics of the interfacial reaction layer formed between thiophosphate SEs and cathodes.

Out-Year Goals. Develop thiophosphate SEs – sulfide cathode interfaces with low area specific resistance (ASR) for ASSBs.

Collaborations. This project will collaborate with G. Ceder (UCB) and P. Jena (Virginia Commonwealth University) on modeling and synthesis guideline, as well as with S. Greenbaum on solid-state NMR to measure ion-diffusivity and local bonding.

Milestones

1. Demonstrate and test hot-sintering method to fabricate composite thiophosphate SE-NMC cathodes. (Q1, FY 2021; Completed, December 31, 2020)
2. Optimize synthesis and processing conditions (for example, interfacial coatings and stack pressure) to minimize the ASR between argyrodite SEs and NMC cathodes. (Q2, FY 2021)
3. Perform Raman microscopy, NMR, and electron microscopy to characterize bulk argyrodite SE and cathode SE-interfaces to investigate capacity loss and degradation mechanisms. (Q3, FY 2021)
4. Select and optimize a few solid-state cathode compositions to demonstrate room-temperature cycling with LPS and/or argyrodite SEs. Stretch Goal: 50 cycles with < 20% capacity fade. (Q4, FY 2021)

Progress Report

This quarter, research activities focused on investigating: (1) how various processing steps impact the Li^+ conductivity of ß-Li_3PS_4, and (2) electrochemical properties of ASSBs containing ß-Li_3PS_4 SE and either NMC-811 or FeS_2-based cathodes. As part of this effort, the team established a hot-pressing system inside an argon glovebox for fabricating Li_3PS_4 and other lithium thiophosphate SE pellets at elevated temperatures (25-250°C, see Figure 102). Controlling pressing temperature can be used to optimize SE conductivity and surface morphology, which may improve interfacial compatibility with lithium metal and cathodes. Table 8 summarizes the measured Li^+ conductivity (σ_{Li+}) and activation energy (E_A) for various ß-Li_3PS_4 samples prepared through a solvent-mediated route. In these experiments, two key processing variables were investigated, including: (1) rinsing 0-4 times with THF to remove soluble species prior to thermal annealing (the composition of these soluble species is unknown at this time), and (2) pellet pressing temperature. As shown in Table 8, rinsing twice with THF increased the room-temperature conductivity by a factor of 2, but additional rinses had no measurable impact on the conductivity. Similarly, a hot-pressed pellet exhibited a two-fold higher conductivity compared to the same sample pressed at room temperature. These findings are a bit surprising since all pellets had the same density within experimental error (ca. 1.70 ± 0.05 g/cm^3). Overall, the results in Table 8 highlight how minor differences in processing conditions can have a significant impact on the properties of SE powders.

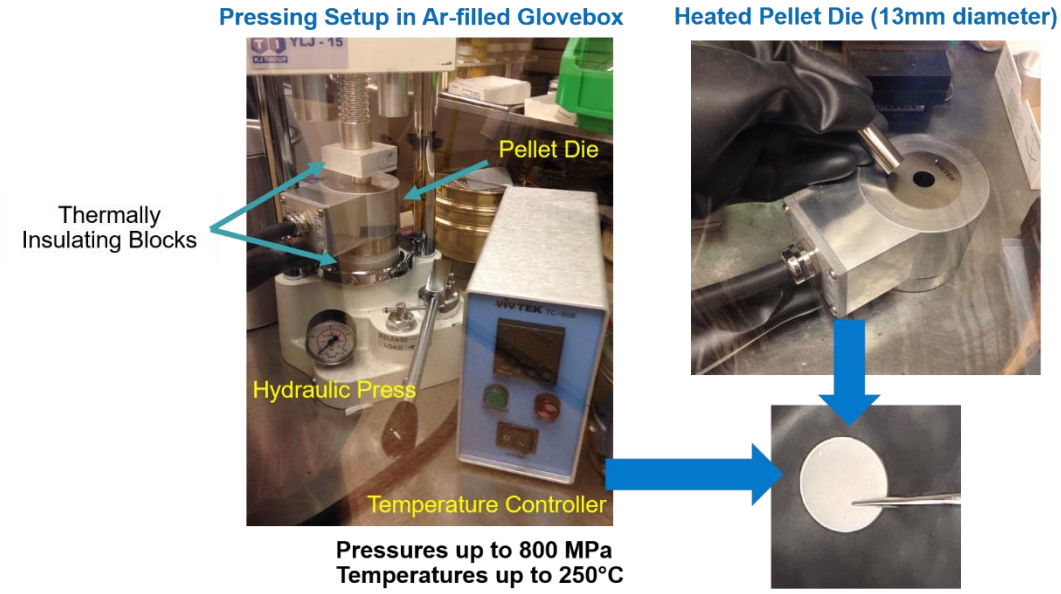

Figure 102. Hot-press setup inside an argon glove box for processing sulfide-based solid electrolyte pellets and solid-state cells.

Table 8. Li^+ conductivity (σ_{Li+}) and activation energies (E_A) of ß-Li_3PS_4 prepared through solvent-mediated synthesis routes. Samples were pressed at either room temperature or 240°C. Dried samples (still containing coordinated solvent) were rinsed with THF 0-4 times prior to thermal annealing at 140°C.

Sample Description	Pressing Temperature (°C)	σ_{Li+} at RT (S/cm)	E_A (eV)
0 rinse, cold press	25	8.5×10^{-5}	0.37
2 rinse, cold press	25	1.5×10^{-4}	0.33
4 rinse, cold press	25	1.5×10^{-4}	0.38
4 rinse, hot press	240	3.0×10^{-4}	0.38

The team also investigated the electrochemical properties of SSBs containing either NMC-811 or FeS_2-based cathodes. The composite cathodes were prepared by dry mixing active material, carbon powder, and ß-Li_3PS_4 in a mortar and pestle, and cells were constructed by cold-pressing tri-layer Li|ß-Li_3PS_4|cathode pellets (diameter, .5-inch; thickness, ~ 1 mm) in a PEEK mold. The SSBs were tested at room temperature using a stack pressure of 5 MPa. Figure 103a shows galvanostatic charge/discharge curves for the NMC-811 cathode. While the cell exhibited a high charge capacity (200 mAh/g) during the first cycle, the initial Coulombic efficiency (ICE) was only 54%, which corresponds to a reversible capacity of 110 mAh/g. The cathode exhibited gradual capacity fade with increasing voltage hysteresis during subsequent cycles. This poor performance is attributed to irreversible oxidation of the ß-Li_3PS_4 SE and formation of a resistive cathode/SE interface at potentials > 3 V versus Li/Li^+. Notably, this decomposition process was exacerbated by the high surface area carbon in the composite cathode. To mitigate ß-Li_3PS_4 oxidation, the team also prepared and tested a FeS_2-based cathode that has an operating voltage of 1-3 V versus Li/Li^+. As shown in Figure 103b, the FeS_2 showed a sloping voltage profile during the first lithiation step followed by two pseudo-plateaus ~ 2.0 and 2.5 V versus Li/Li^+ during subsequent charging. When cycled between 1.5-3.0 V versus Li/Li^+, the FeS_2 cathode exhibited a high CE (average of 99.8% over cycles 2-10 compared to 98.2% for NMC-811) and a stable capacity ~ 100 mAh/g. Ongoing experiments will investigate how different depths of discharge (for example, $FeS_2 + 4\ Li^+ + 4e^- \leftrightarrow Fe^0 + 2Li_2S$, 894 mAh/g) impact the cathode's reversible capacity and cyclability.

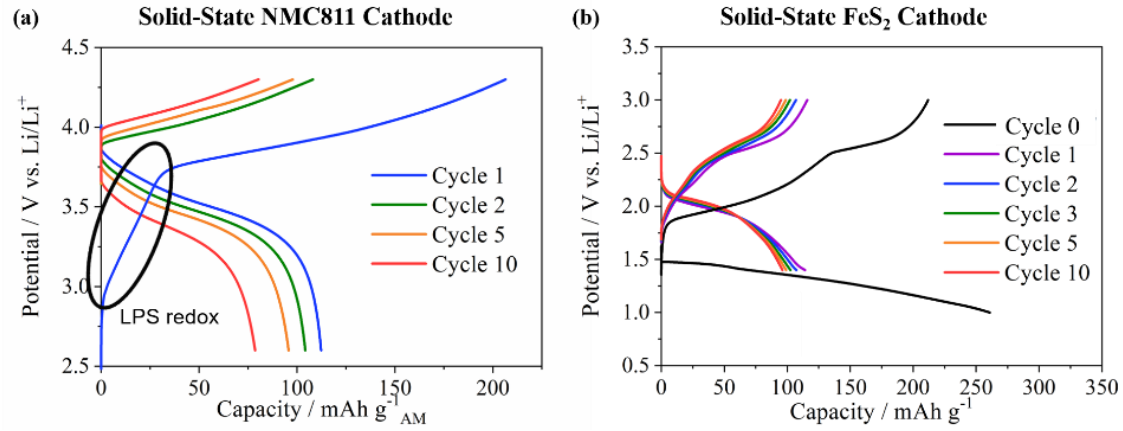

Figure 103. Voltage profiles of all-solid-state batteries (Li|ß-Li_3PS_4|cathode) containing either (a) NMC-811 or (b) FeS_2-based cathodes. Composite cathodes contained 60 wt% active material, 30 wt% ß-Li_3PS_4, and 10 wt% carbon with an active material loading of 6.6 mg/cm². Cells were cycled at room temperature with a current density of 66 µA/cm² (10 mA/$g_{active\ material}$) and stack pressure of 5 MPa.

Patents/Publications/Presentations

Publications

- Delnick, F. M., G. Yang, E. C. Self, H. Meyer III, and J. Nanda. "Investigation of Complex Intermediates in Solvent Mediated Synthesis of Thiophosphate Solid-State Electrolytes." *The Journal of Physical Chemistry C* 124 (2020): 27396–27402.
- Yang, G., M. L. Lehmann, S. Zhao, B. Li, S. Ge, P-F. Cao, F. M. Delnick, A. P. Sokolov, T. Saito, and J. Nanda. "Anomalously High Elastic Modulus of a Poly(ethylene oxide)-Based Composite Electrolyte." *Energy Storage Materials* 35 (2020): 431–442.

Presentation

- MRS Spring/Fall 2020 Meeting, Virtual (November 27 – December 4, 2020): "Solvent-Mediated Synthesis of Amorphous Li_3PS_4/PEO Composite Solid Electrolytes with High Li^+ Conductivity"; E. C. Self.

Task 4.6 – Prelithiation of Silicon Anode for High-Energy Lithium-Ion Batteries (Yi Cui, Stanford University)

Project Objective. Prelithiation of high-capacity electrode materials is an important means to enable those materials in high-energy batteries. This study pursues three main directions: (1) developing facile and practical methods to increase 1st cycle CE of anodes, (2) synthesizing fully lithiated anode to pair with high-capacity Li-free cathode materials, and (3) prelithiation from the cathode side.

Project Impact. Prelithiation of high-capacity electrode materials will enable those materials in the next generation of high-energy-density Li-ion batteries. This project's success will make high-energy-density Li-ion batteries for EVs.

Approach. Silicon electrode film will be prepared by coating the slurry of silicon nanoparticles, carbon black, and binder mixture on copper foil through a doctor-blading method. The silicon electrode film will be prelithiated by pressing a Li-metal foil on top of it and heating it in an argon glovebox for a certain time. Then, Li_xSi electrode film can be obtained by removing the redundant lithium foil through a peeling-off approach. The redundant lithium foil is reusable for the next prelithiation. The structure, morphology, and other properties can be analyzed by SEM, TEM, XPS, Raman spectroscopy, XRD, etc. In the first year, the team aims to fabricate Li_xSi freestanding electrode film and improve its air stability. In the second year, the team aims to improve the electrochemical stability in full cells.

Out-Year Goals. Materials containing a large quantity of lithium will be synthesized for pre-storing lithium ions inside batteries. Materials and process will be developed to be compatible with battery electrode and cell fabrication. First-cycle CE of anodes will be improved and optimized by prelithiation materials. Develop materials for prelithiation from the cathode side.

Collaborations. This project engages in collaboration with the following: BMR PIs; SLAC: M. Toney *(in situ* X-ray); and Stanford: W. Nix (mechanics).

Milestones

1. Produce ultra-thin lithium foil as a new dry prelithiation reagent. Produce lithium foil of different thickness to match the varied anode capacity. (Q1, FY 2021; Completed)
2. Demonstrate controllable ICE improvement by prelithiation with ultra-thin lithium foil of different thickness. (Q2, FY 2021; In progress)
3. Demonstrate the microstructural and chemical evolution of silicon anode during ultra-thin lithium foil prelithiation. (Q3, FY 2021)
4. Demonstrate the role of ultra-thin lithium foil prelithiation to improve good cycle capacity retention in full battery. (Q4, FY 2021)

Progress Report

Substantial improvements on energy density of Li-ion batteries require development of high-capacity electrodes. Silicon anodes, which have high theoretical capacities (3579 mAh/g) ten times higher than conventional graphite anodes (372 mAh/g), hold great potential for application in high-energy Li-ion batteries. However, silicon anodes exhibit a low ICE of 50-80%, which means 20-50% of active lithium ions will be lost after the first cycle due to side reactions and also indicates inefficient usage of active materials and battery energy density degradation. Therefore, a strategy to compensate the initial active lithium loss and improve ICE is urgently needed to prevent battery energy density degradation.

In the last quarterly report, the team presented a novel one-step controllable prelithiation approach by electrochemical shorting between silicon anode and a layer of lithium mask. Prelithiation capacity can be decently controlled by varying the lithium mask porosity. However, the thickness of commercially available lithium foil (~ 25 μm) and the technical difficulties in increasing porosity limit the range of available prelithiation capacity (1-5 mAh/cm^2). To further broaden the lower limit to widen the prelithiation application, here, the team produces ultra-thin lithium foil as another dry prelithiation reagent promising for facile and controllable prelithiation.

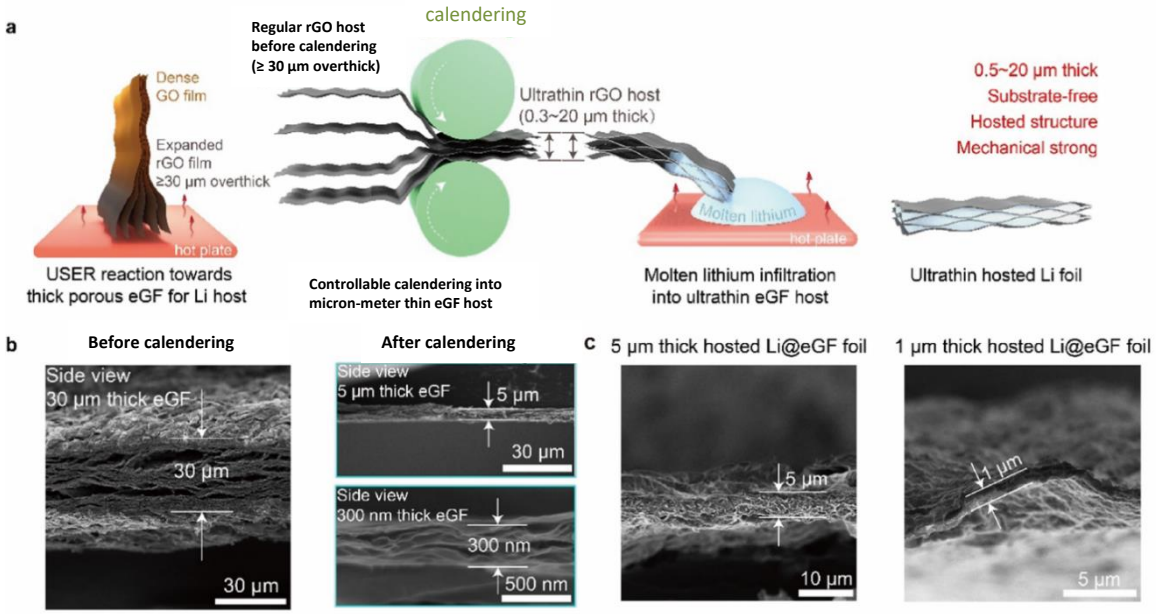

Figure 104. (a) Schematic of fabrication of ultra-thin lithium foil. (b) Cross-sectional scanning electron microscopy (SEM) images comparing the common thick host before calendering and the submicron-scale ultra-thin host after controllable calendering. (c) Cross-sectional SEM images of fabricated ultra-thin 1-μm-thick and 5-μm-thick hosted lithium films after preliminary calendering process.

Current industrial extrusion-based fabrication technologies are only capable of producing Li-metal foil with thicknesses of 20 to several hundreds of microns. Extruding free-standing Li-metal foil with a thickness less than 20 microns presents the challenge of mechanical fragility. Here, the team develops a process that generates a microns-thin, free-standing, and hosted Li-metal foil down to sub-micron thickness. First, they use a tunable calendering process to decrease the thickness of a porous rGO host to a thickness of 0.3 to 20 μm (Figure-104a-b). GO film is chosen because it makes the process scalable and has good mechanical strength. Edge-contacting molten lithium to the ultra-thin rGO host loads metallic lithium inside its internal channels, while retaining similar micron-scale thickness. As a result, the team has fabricated a robust, free-standing, scalable, and flexible Li-metal film with thicknesses ranging from 0.5 to 20 μm (corresponding to ultra-low areal capacities of 1-4 mAh cm^{-2}), as seen in Figure 104c. This procedure fabricates a micron-scale-

thin lithium foil that overcomes thinness limitations of available lithium films (20-750-μm thick, 4-150 mAh cm^{-2} capacity). In addition, the embedded graphene host provides strong mechanical support to the free-standing ultra-thin Li-metal foil. The tunable and ultralow capacity of this Li-metal film makes it promising for prelithiation for a wide range of anode choices with different amounts of initial active lithium loss.

Patents/Publications/Presentations

The project has no patents, publications, or presentations to report this quarter.

TASK 5 – SULFUR ELECTRODES

Summary

The collected work of the projects in this Task encompasses the following areas:

- Conducting focused fundamental research on the mechanism of "shuttle effect" inhibition for rechargeable Li-S batteries.
- Developing electrode and electrolyte systems that can mitigate the "shuttle effect" so the low self-discharge and long cycle life can be achieved.
- Synthesizing sulfur composite materials with an emphasis on polymer sulfur composite materials.
- Developing creative electrode-making processes to improve processability and aerial capacity; for example, polymeric sulfur composites may not be suitable for the traditional slurry casting process.
- Developing a novel S_xSe_y cathode material for rechargeable lithium batteries with high energy density and long life, as well as low cost and high safety.
- Delivering an electrochemically responsive self-formed hybrid LIC as a protective layer for Li-metal anodes, enabling Li-metal anodes to cycle with a high efficiency.
- Developing high-energy, low-cost Li-S batteries with long lifespan.

Highlights. The highlights for this quarter are reported below.

- K. Amine's group at ANL focused on using their in-house Li-S and Li-Se/S pouch cell assembly capability to fabricate and test utilizing their previously developed Se-doped sulfur (core – shell structure) cathodes with fluorinated ether-based (HFE) electrolytes at different electrolyte (E)/Se-S ratios. The team has shown the ability to fabricate and assemble 100 mg Se/S loaded Li-Se/S pouch cells with an E/Se-S ratio of 10, delivering an initial specific capacity of 1312 mAh/g at a current density of 200 mA/g. The cell still retained a reversible capacity of 1103 mAh/g, corresponding to a high capacity retention of 84.1%. These results are claimed by the team to be the first report of such high capacity retention in Li/Se-S pouch cells. The team attributes this electrochemical response to the prevention of loss of soluble LiPSs/LiPSes due to the use of HFE-based electrolyte forming a robust SEI *in situ* on the surface of the Se/S cathode, serving as a protective layer between the electrode and electrolyte and thus preventing the attack of solvent molecules on the Se/S cathode. However, when the Li/Se-S pouch cell was tested at a lower E/Se-S ratio of 5, employing a reduced Se/S loading of 50 mg, the cell expectedly showed a lower capacity of 800 mAh/g, although maintaining a relatively stable cycle life. This was attributed to reduced reaction kinetics due to reduced electrolyte amounts. The results nevertheless demonstrate the benefits of using HFE-based electrolytes in Li-Se/S batteries.
- D. Lu and J. Liu's group at PNNL studied the effects of particle size of the sulfur cathode. They studied large particle size > 90 μm (LPC) and small particle size < 20 μm (SPC) electrodes at E/S ratios of 10 μL/mg S and 4 μL/mg S, respectively, at electrode porosities of ~ 62%, ~ 53%, and ~ 45%. At the larger E/S ratio, LPC electrodes show slightly improved cycling stability from 62% to 53% porosity, while maintaining similar performance even at very low porosity of 45%. After 30 cycles, LPC electrodes with porosities of 62%, 53%, and 45% deliver reversible capacities of 932, 937, and 917 mAh/g, corresponding to 87.9%, 88.1%, and 88.7% capacity retention, respectively. These were much higher than the SPC electrodes, which show capacities of 793, 742, and 728 mAh/g at similar porosities. Under lean electrolyte conditions, capacity decay improved for both, with LPC at 45% porosity still exhibiting a promising initial specific capacity of 1001 mAh/g and 90.8% capacity retention after 30 cycles. Results thus show the efficacy of controlling the particle size of sulfur and porosity on the electrode performance.

- Y. Cui's group at Stanford University reports on a homemade *in situ* optical cell fabricated using Li_2S or TiS_2 coated on Li_2S (TiS_2@Li_2S) as the working electrode, lithium metal as the counter electrode, and PEO/LiTFSI as the electrolyte to study the dissolution behavior of the intermediate polysulfides (Li_2S_x, $3 \leq x \leq 8$) in solid polymer based all-solid-state Li-S batteries. They show that using the optical cell, with base Li_2S electrodes, within the first charge process itself, the color of the PEO/LiTFSI electrolyte gradually changes from pale yellow to reddish brown starting from the interface between the working electrode and the electrolyte. The reddish brown color spreads over the entire electrolyte area within two cycles, reflecting the polysulfide dissolution prevalent for bare Li_2S. However, the TiS_2@Li_2S cell reflected no change in color, indicating the beneficial influence of the TiS_2 coating. The work reflects use of this optical electrochemical cell for studying visible wavelength related changes occurring during battery operation.
- E. Hu and D. Qu's group (BNL and UWM) screened and attempted to identify the best polymeric sulfur cathode. The team investigated three types of polymeric sulfur cathode materials, named as SP1, SP5, and SP7. They compared the performance to that of the control, which was elemental S_8 sulfur. They compared SP1 and SP7, which indicated similar ability to retain sulfur within the electrodes after leaching of the soluble polysulfides. SP1 retained 78.2% of its initial capacity after 50 cycles, while only 49% was retained by the SP7 sulfur cathode. Using high-performance liquid chromatography (HPLC), the team determined that the separators collected from cycling of SP1 sulfur cathode contained more fragments of short-chain polysulfide species of S_3^{2-}, S_4^{2-}, and S_5^{2-} compared to the separators collected from cycling of cells containing the other two polymers. Thus, SP1 electrodes retained a larger fraction of more soluble long-chain polysulfides in the electrode, demonstrating better capacity retention ability. The results show the efficacy of HPLC to garner fundamental understanding of polysulfide dissolution in Li-S batteries.
- G. Liu's group at UCB studied the transference number for Li-ion migration in the micelle-based electrolyte that they reported earlier, which comprises dissolving LiTFSI salt in F_4EO_2 fluorinated ether molecules blended in 1,1,2,2-Tetrafluoroethyl 2,2,2-Trifluoroethyl Ether, TTE solvent. They used the Bruce-Vincent method to determine the Li-ion transference number (t_{Li^+}) using three electrolyte concentrations ranging from 0.5 M to 2.0 M. They first ran a Li-Li symmetrical cell in which the electrolyte is sandwiched between two identical lithium electrodes, with the cell allowed to complete two cycles of plating and stripping at 0.4 mA/cm^2 for 1 hour per cycle to form a stable SEI, following which initial impedance is determined. An initial current is then measured with a small DC polarization followed by measuring the steady-state current after 40 hours of polarization, culminated by measurement of cell impedance. They determined the transference number, t_{Li^+}, to be ~ 0.8 for all the electrolyte concentrations studied, which is higher than typical LEs, which demonstrates the promise of the micelle-based electrolyte.

Task 5.1 – Novel Chemistry: Lithium Selenium and Selenium Sulfur Couple (Khalil Amine, Argonne National Laboratory)

Project Objective. The project objective is to develop a novel S_xSe_y cathode material for rechargeable lithium batteries with high energy density and long life, as well as low cost and high safety.

Project Impact. Development of a new battery chemistry is promising to support the goal of PHEV and EV applications.

Approach. The dissolution of lithium polysulfides in nonaqueous electrolytes has been the major contribution to the low energy efficiency and short life of Li-S batteries. In addition, insulating characteristics of both end members during charge/discharge (sulfur and Li_2S) limit their rate capacity. To overcome this problem, sulfur or Li_2S is generally impregnated in a carbon-conducting matrix for better electronic conductivity. However, this makes it difficult to increase the loading density of practical electrodes. It is proposed to solve these barriers using the following approaches: (1) partially replace sulfur with selenium, (2) nano-confine the S_xSe_y in a nanoporous conductive matrix, and (3) explore advanced electrolytes with suppressed shuttle effect.

Out-Year Goals. This new cathode will be optimized with the following goals:

- A cell with nominal voltage of 2 V and energy density of 600 Wh/kg.
- A battery capable of operating for 500 cycles with low capacity fade.

Collaborations. This project engages in collaboration with the following: Y. Ren and C. Sun of APS at ANL, and L. A. Curtiss and L. Cheng at ANL.

Milestones

1. Build in-house Li-S pouch cell fabrication line, and demonstrate > 100 mAh pouch cell performance using Se-doped sulfur cathode and fluorinated ether-based electrolytes. (Q1, FY 2021; Completed)
2. Design and characterize novel cathode host for Li-S and Li-Se/S batteries. (Q2, FY 2021; In progress)
3. Validate electrochemical performance of new cathode host. (Q3, FY 2021; In progress)
4. Conduct *operando* and *ex situ* characterization on developed cathodes during charge/discharge. (Q4, FY 2021; In progress)

Progress Report

Li-S batteries are attractive alternatives to Li-ion batteries because of their high theoretical specific energy and the natural abundance of sulfur. In the past decade, with the application of advanced nanotechnology in rational cathode design to suppress the shuttling effect in Li-S batteries, the electrochemical performance of sulfur cathodes has been greatly improved in terms of cycle life and fast charging performance. However, most of these cathodes were evaluated in coin-cell configurations with a thin sulfur cathode, thick Li-metal anode, and flooded electrolytes, whereas tests in practical pouch cells showed disappointingly lower specific energy and shorter cycle life. This quarter, the team mainly focused on building in-house Li-S and Li-Se/S pouch cell assembly and testing line using their previously developed Se-doped sulfur (core-shell structure) cathodes and fluorinated ether-based (HFE) electrolytes under different E/Se-S ratios.

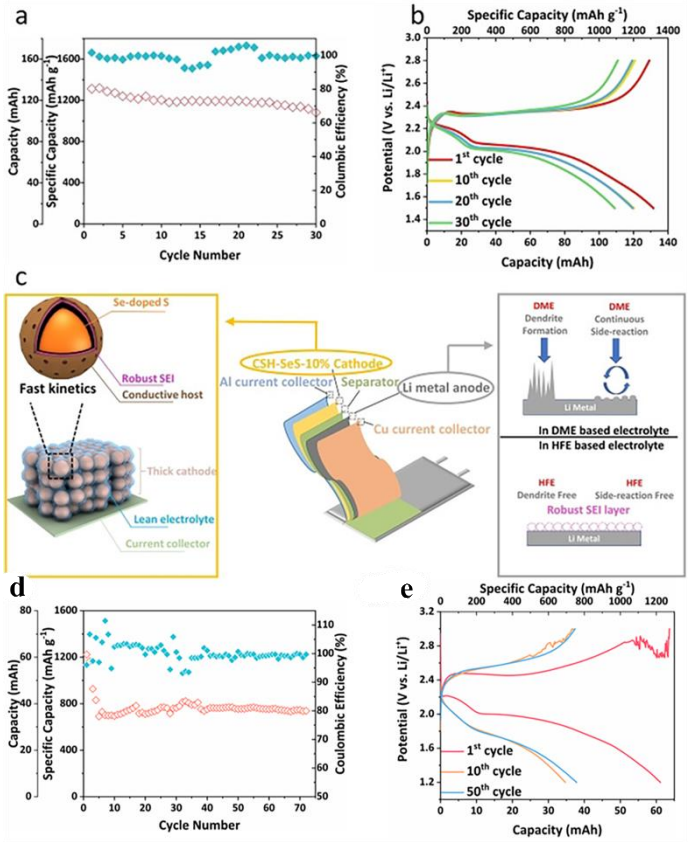

Figure 105. Validation of potential practical application. (a) Cycling performance and (b) charge/discharge curves of Li-Se/S pouch cell with 100 mg Se/S loading at 200 mA g^{-1} with E/S ratio of 10. (c) The effectiveness of the combination of cathode design, selenium doping, and fluorinated electrolyte in achieving a shuttle- and dendrite-free Li-S pouch cell under thick-cathode and low-E/S ratio conditions. (d) Cycling performance and (e) charge/discharge curves of Li-Se/S pouch cell with 50 mg Se/S loading at 200 mA g^{-1} with E/S ratio of 5.

Figure 105a-b presents the cycling performance and voltage profiles of the as-assembled Li-Se/S pouch cell with 100 mg Se/S loading in the HFE-based electrolyte. As shown, with an E/Se-S ratio of 10, this cell delivered initial specific capacity of 1312 mAh g^{-1} at a current density of 200 mA g^{-1}. After 30 cycles, it maintained reversible capacity of 1103 mAh g^{-1}, corresponding to a high capacity retention rate of 84.07%. To the best of the team's knowledge, this is the first report of such high capacity retention for Li/Se-S pouch cells. The excellent cycle performance together with the high CE (> 98.5%) of the pouch cell in HFE-based electrolyte serves as a good validation of the concept.

Figure 105c presents a schematic of the mechanism behind the excellent stability of the Li-Se/S system in the HFE-based electrolyte. In the conventional DME-based electrolyte, the severe loss of active material caused by the shuttling of highly soluble LiPS/LiPSe leads to the fast capacity decay. However, in the case of HFE-based electrolyte, a layer of robust SEI forms *in situ* on the surface of the Se/S cathode, which can act as a protective layer between the electrode and electrolyte, thus preventing the attack of solvent molecules on the Se/S. As a result, the polysulfide dissolution issue is well addressed. Meanwhile, as shown in Figure 105c, in the DME-based electrolyte, the parasitic reactions between lithium metal and electrolyte molecules lead to dendrite formation and low CE, resulting in poor cycling stability and severe safety concerns. In contrast, with the HFE-based electrolyte, a robust SEI layer is uniformly formed on the Li-metal surface to effectively eliminate the parasitic reactions between lithium metal and electrolyte molecules, significantly improving the cycling stability and CE.

To further increase the specific energy, the team additionally tested the Li/Se-S pouch cell under a lower E/Se-S ratio to 5. The corresponding cycling performance and charge/discharge curves are shown in Figure 105d-e, respectively. Despite using a lower E/Se-S ratio, the pouch cell can still maintain a relatively stable cycle life, albeit specific capacity is decreased to ~ 800 mAh g^{-1}. Meanwhile, the voltage curves shown in Figure 105e reflect a larger voltage polarization than that observed under a higher E/Se-S ratio. This is because of the reduced reaction kinetics due to the low E/Se-S ratio. To mitigate this issue, future efforts will focus on development of more rational cathode materials and electrolyte modulation to realize high-specific-energy Li-S and Li-Se/S pouch cells.

Patents/Publications/Presentations

Publication

- Zhao, C., G. L. Xu,* Z. Yu, L. Zhang, I. Hwang, Y-X. Mo, Y. Ren, L. Cheng, C-J. Sun, Y. Ren, X. Zuo, J-T. Li, S-G. Sun, K. Amine,* and T. Zhao.* "A High-Energy and Long-Cycling Lithium-Sulfur Pouch Cell via a Macroporous Catalytic Cathode with Double-End Binding Sites." *Nature Nanotechnology* 16 (2021): 166–173. doi: 10.1038/s41565-020-00797-w.

Task 5.2 – Development of High-Energy Lithium-Sulfur Batteries (Dongping Lu and Jun Liu, Pacific Northwest National Laboratory)

Project Objective. The project objective is to develop high-energy, low-cost Li-S batteries with long lifespan. All proposed work will employ thick sulfur cathode (≥ 4 mg/cm^2 of sulfur) at a relevant scale for practical applications. The diffusion process of soluble polysulfide out of thick cathode will be revisited to investigate cell failure mechanism at different cycling. The fundamental reaction mechanism of polysulfide under the electrical field will be explored by applying advanced characterization techniques to accelerate development of Li-S battery technology.

Project Impact. The theoretical specific energy of Li-S batteries is ~ 2300 Wh/kg, which is almost three times higher than that of state-of-the-art Li-ion batteries. The proposed work will design novel approaches to enable Li-S battery technology and accelerate market acceptance of long-range EVs required by the EV Everywhere Grand Challenge.

Approach. The project proposes to (1) identify and address key issues of applying high-energy sulfur cathodes including materials, binders, electrode architectures, and functional electrode additives, (2) advance the mechanism study of sulfur cathode and electrolyte by using *in situ* / *ex situ* techniques and custom-designed hybrid cell setup, and (3) verify effectiveness of the new approaches with coin/pouch cells by using high-loading electrodes (> 4 mg/cm^2), limited lithium (< 200% lithium excess), and lean electrolyte (E/S < 4 μL/mg).

Out-Year Goals. This project has the following out-year goals:

- Fabricate Li-S pouch cells with thick electrodes to understand sulfur chemistry/electrochemistry in environments similar to real application.
- Leverage the Li-metal protection project funded by the DOE and PNNL advanced characterization facilities to accelerate development of Li-S battery technology.
- Develop Li-S batteries with a specific energy of 400 Wh/kg at cell level, 1000 deep-discharge cycles, improved abuse tolerance, and less than 20% capacity fade over a 10-year period to accelerate commercialization of EVs.

Collaborations. This project engages in collaboration with the following: X-Q. Yang (BNL), J. Bao (PNNL), P. Khalifah (BNL), and J. Tao (PNNL).

Milestones

1. Optimize electrode architecture to realize sulfur utilization of > 1000 mAh/g in high loading sulfur electrode (> 4 mg S/cm^2) at very low porosity (< 40%). (Q1, FY 2021; Completed)
2. Build an electrode model to understand the effects of electrode porosity and tortuosity on the electrolyte transport and sulfur reaction kinetics. (Q2, FY 2021; In progress)
3. Enable a quasi-solid electrolyte network by introducing polymer and/or solid electrolytes into the low porosity electrodes, and realize cell operation at an extremely low E/S. (Q3, FY 2021; In progress)
4. Identify compatible binder and solvent combinations to enable the scale-up preparation of the quasi-solid electrodes. (Q4, FY 2021; In progress)

Progress Report

This quarter, a high sulfur utilization rate (> 1000 mAh g^{-1}) was realized in dense electrodes with porosities as low as ~ 40%. Effects of cathode particle size on sulfur reactions were studied at various porosities and electrolyte conditions by using SPC (< 20 µm) and LPC (> 90 µm) as example materials. Under flooded electrolyte conditions, electrode wetting problems associated with dense electrodes can be minimized to some extent, making it easier to understand the impact of particle size on cell performance. Figure 106a-f compares the capacity retentions of SPC and LPC at an E/S ratio of 10 µL mg^{-1} S. Reducing porosity has different impacts on sulfur electrodes composed of large or small particles. Compared with SPCs, at each level of porosity, the LPCs have a very similar capacity for the 1st discharge, but much higher capacity and better capacity retention for the subsequent cycles. The LPC electrode shows slightly improved cycling stability from 62% to 53% porosity and maintains similar performance even at very low porosity of 45%. After 30 cycles, LPC electrodes with porosities of 62%, 53%, and 45% deliver reversible capacities of 932, 937, and 917 mAh g^{-1}, corresponding to capacity retentions of 87.9%, 88.1%, and 88.7%, respectively. It is important to notice that for LPC, most of the capacity loss occurs in the second discharge process, and then it becomes very stable in the following cycles (Figure 106d-f). Apparently, at each porosity, the 30th discharge curve is well overlapped with that in the 2nd cycle, showing a similar capacity and cell polarization for LPC. On the contrary, clear detrimental effects are detected in SPCs as the porosity decreases. After 30 cycles, reversible capacities / capacity retentions of SPCs at 62%, 53%, and 45% porosity are 793 (76.1%), 742 (68.8%), and 728 mAh g^{-1} (71.1%), respectively. Also, capacity loss of SPC in the 1st five cycles drastically increases when the porosity is reduced from 62% to 45%. Another important observation is that particle size has a direct impact on CE. As shown in Figure 106d-f, at each porosity, the LPC electrode always shows higher CE in the 1st and subsequent cycles if compared with SPC electrodes. This is consistent with capacity retention observed in SPC and LPC and could be ascribed to the longer diffusion path of the larger particles. Under lean electrolyte conditions (E/S = 4 µL mg^{-1}), capacity decay related to polysulfide shuttling was improved for both SPC and LPC electrodes (Figure 106g-i). At a relatively high porosity of 62%, the SPC electrodes have almost identical reversible capacity and capacity retention with those of LPC electrodes, although polarization is slightly higher. Performance difference between the SPC and LPC becomes more obvious with reduction of electrode porosity. At 53% porosity, deteriorated polarization

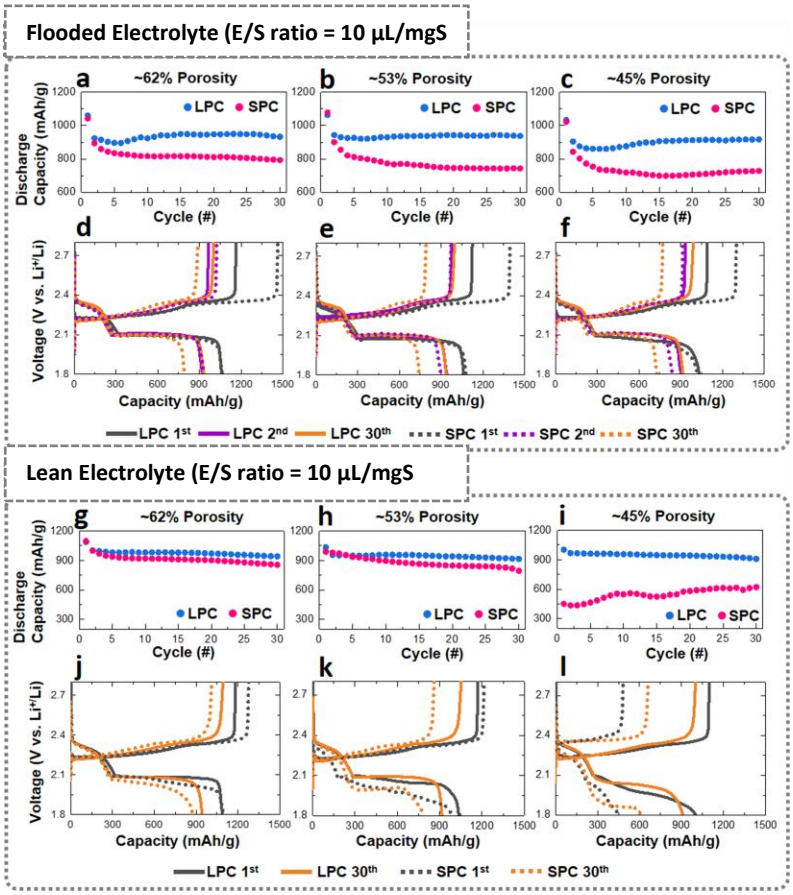

Figure 106. Electrochemical performances of small particle cathode (SPC) and large particle cathode (LPC) electrodes (4 mgS/cm²) under flooded (E/S ratio = 10 µL mg^{-1}S) and lean (E/S ratio = 4 µL mg^{-1}S) electrolyte conditions. Capacity retention (a-c) and corresponding discharge/charge curves (d-f) of SPC and LPC under flooded electrolyte conditions at 0.1 C (1 C = 1000 mA/g). Capacity retention (g-i) and corresponding discharge/charge curves (j-l) of SPC and LPC under lean electrolyte conditions.

and capacity decay are observed in SPC. At a very low porosity of 45%, the 1st discharge capacity drops to only 451 mAh g^{-1}. On the other hand, LPC at 45% porosity can still deliver a promising specific capacity of 1001 mAh g^{-1} and 90.8% capacity retention after 30 cycles. The team is studying sulfur reaction pathways in SPC and LPS under practical conditions.

Patents/Publications/Presentations

The project has no patents, publications, or presentations to report this quarter.

Task 5.3 – Nanostructured Design of Sulfur Cathodes for High-Energy Lithium-Sulfur Batteries (Yi Cui, Stanford University)

Project Objective. The charge capacity limitations of conventional TM oxide cathodes are overcome by designing optimized nano-architectured sulfur cathodes. This study aims to enable sulfur cathodes with high capacity and long cycle life by developing sulfur cathodes from the perspective of nanostructured materials design, which will be used to combine with Li-metal anodes to generate high-energy Li-S batteries. Novel sulfur nanostructures as well as multi-functional coatings will be designed and fabricated to overcome issues related to volume expansion, polysulfide dissolution, and the insulating nature of sulfur.

Project Impact. The capacity and cycling stability of sulfur cathode will be dramatically increased. This project's success will make Li-S batteries to power EVs and decrease the high cost of batteries.

Approach. The approach involves three main efforts:

- Advanced nanostructured sulfur cathodes design and synthesis, including (1) engineer empty space into sulfur cathode to solve problem of electrode volume expansion, (2) develop novel sulfur nanostructures with multi-functional coatings for confinement of S/Li polysulfides to address issues of active materials loss and low conductivity, (3) develop/discover optimal nanostructured materials that can capture the polysulfide dissolved in the electrolyte, (4) develop space-efficiently-packed nanostructured sulfur cathode to increase volumetric energy density and rate capability, and (5) identify interaction mechanism between sulfur species and different types of oxides/sulfides, and find optimal material to improve capacity and cycling of sulfur cathode.
- Structure and property characterization, including *ex situ* SEM, XPS analysis, and *in operando* XRD and optical microscopy (OM).
- Electrochemical testing including coin cells and pouch cells as well as a set of electrochemical techniques.

Out-Year Goals. The cycle life, capacity retention, and capacity loading of sulfur cathodes will be greatly improved (200 cycles with 80% capacity retention, > 0.3 mAh/cm^2 capacity loading) by optimizing material design, synthesis, and electrode assembly.

Collaborations. This project collaborates with the following: BMR PIs; SLAC: M. Toney *(in situ* X-ray); and Stanford: W. Nix (mechanics) and Z. Bao (materials).

Milestones

1. Understanding polysulfides dissolution behavior in polymer-based all-solid-state Li-S batteries. (Q1, FY 2021; Completed)
2. Demonstrating nanoscale encapsulation concept from liquid to all-solid-state Li-S batteries. (Q2, FY 2021; Ongoing)
3. Exploring mechanism of nanoscale encapsulation in improving all-solid-state Li-S batteries experimentally and theoretically. (Q3, FY 2021; Ongoing)
4. Enabling all-solid-state Li-S batteries with high energy density, long-term cycling stability, and high safety. (Q4, FY 2021; Ongoing)

Progress Report

This quarter, the team fabricated a homemade *in situ* optical cell (Figure 107a) by using lithium sulfide (Li_2S) or TiS_2-coated Li_2S (TiS_2@Li_2S) as the working electrode, lithium metal as the counter electrode, and polyethylene oxide/lithium bis(trifluoromethanesulfonyl)imide (PEO/LiTFSI) as the electrolytes to study the dissolution behavior of intermediate polysulfides (Li_2S_x, $3 \leq x \leq 8$) in solid-polymer-based all-solid-state Li-S batteries. All components are sealed between a glass substrate and a piece of transparent cover glass slide to enable *in situ* optical observation and heated at 60°C (Figure 107b).

Figure 107c-d shows the evolution of the interface between the working electrode and the solid-state PEO/LiTFSI electrolyte during the cycling process. Before charging, the interface can be clearly observed, and the pure PEO/LiTFSI electrolyte part shows pale yellow color by OM imaging at OCV. For optical cells with bare Li_2S electrodes, only after the first charging process, the color of PEO/LiTFSI electrolyte gradually changes from a pale-yellow color to reddish brown, starting from the interface between the working electrode and the electrolyte. The red-brown coloration fully spreads over the whole PEO/LiTFSI electrolyte after only two cycles, suggesting that polysulfides are dissolving into the PEO/LiTFSI electrolyte (Figure 107c). In contrast, no obvious color change of the PEO/LiTFSI electrolyte is observed in optical cells with Li_2S@TiS_2 electrodes after three cycles (Figure 107d).

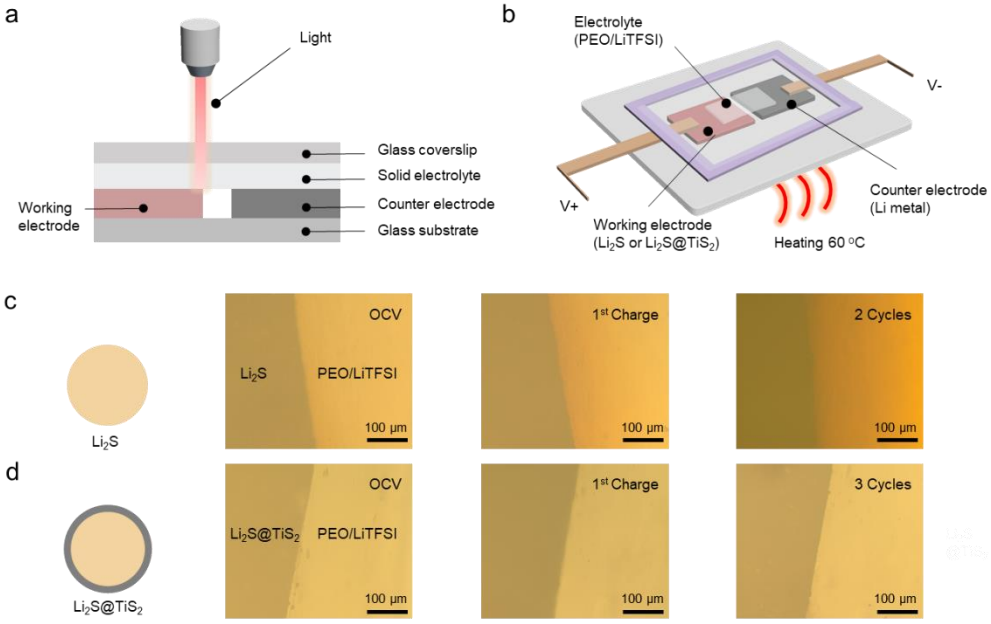

Figure 107. Polysulfides entrapment in Li_2S@TiS_2 cathodes. (a) Schematic of the setup for *in situ* optical observation of electrochemical processes. A thin gap (1-2 mm) between the working electrode and the counter electrode is designed to avoid any occurrence of short circuits. (b) Illustration of the electrochemical cell assembled with bare Li_2S working electrode or Li_2S@TiS_2 working electrode, PEO/LiTFSI electrolyte, and Li-metal counter electrode. The entire cell is heated to 60°C. The open circuit voltage of the as-prepared cell is 2.5 V. The cell is first charged to 3.8 V at a constant current of 5 μA and then discharged to 1.6 V at a current of -2 μA. The *in situ* optical microscopy imaging shows the working electrode/electrolyte interface for (c) bare Li_2S electrode and (d) Li_2S@TiS_2 electrode.

Patents/Publications/Presentations

The project has no patents, publications, or presentations to report this quarter.

Task 5.4 –Investigation of Sulfur Reaction Mechanisms (Enyuan Hu, Brookhaven National Laboratory; Deyang Qu, University of Wisconsin, Milwaukee)

Project Objective. The primary objectives are as follows:

- To continue conducting fundamental research on the mechanism of the sulfur redox reaction, especially those on the interplay of the dissolved polysulfides in electrolyte and those in the solid phase in cathode during charging.
- To continue developing the polymeric sulfur electrode, adequate anode, and corresponding electrolyte to achieve high-energy-density, long-cycle-life Li-S batteries. The team will focus on the overall dissolution of polysulfide in an electrolyte and the effectiveness of polymeric sulfur electrodes.
- To develop the alternative anode materials having low reactivity with dissolved polysulfide ions.
- To continue to develop and optimize creative electrode making processes to improve processability and aerial capacity (for example, dry process and thick electrodes).

Project Impact. Further understanding of the mechanisms of all reactions in a Li-S cell will lead to mitigation of the "shuttle effect." The project results will thus guide development of sulfur cathode and Li-S designs with significant increase of energy density and of cycle life and with reduction of cost. This will greatly accelerate deployment of EVs and reduce carbon emission associated with fossil fuel consumption.

Approach. This collaborative project involves the following: (1) continue to synthesize cross-linked polymerized sulfur compounds, in which a sulfur is attached to the conductive backbone with covalent bonds; therefore the polysulfides can be immobilized within the matrix, (2) investigate the sulfur redox reaction mechanism in the solid phase, (3) continue exploring the alternative anode materials that can cycle well and do not react with dissolved polysulfide and sulfur in the electrolyte to mitigate the "shuttle effect," and (4) develop an engineering process for high sulfur loading electrodes.

One-Year Goals. In FY 2021, the interim goal is to develop a Li-sulfur battery with sulfur containing cathode of 600-800 mAh/g capacity with mitigation of the "shuttle effect."

Collaborations. The PI works closely with beamline scientists at synchrotron facilities to develop novel Li-S characterization tools. The PI and co-PI collaborate closely with top scientists at ANL, LBNL, and PNNL, as well as U. S. industrial collaborators at GM, Duracell, Clarios, etc. The PI and co-PI also collaborate with scientists in China, Japan, and South Korea. These collaborations will be strengthened and expanded to give this project a vision on both today's state-of-the-art technology and tomorrow's technology in development, with feedback from the material designer and synthesizers upstream and from industrial end users downstream.

Milestones

1. Synthesize new polymeric sulfur compounds. Conduct preliminary electrochemical, optical, and synchrotron based testing of sulfur redox reaction in the solid phase (in cathode). (Q1, FY 2021; Completed)
2. Test alternative anode materials with both sulfur and polymeric sulfur electrodes and determine their interaction with dissolved polysulfide ions and overall electrochemical performance. (Q2, FY 2021; In progress)
3. Investigate sulfur redox reaction in the solid phase in cathode. Test the newly synthesized polymeric sulfur materials. (Q3, FY 2021; In progress)
4. Test full cell in either coin or pouch cell format with polymeric sulfur cathode and alternative anode. (Q4, FY 2021; In progress)

5. Conduct preliminary investigations of sulfur redox reaction mechanism in the solid phase in cathode and the interplay between dissolved polysulfide ions in electrolyte and sulfide compounds in the solid. Complete and continue testing of polymeric sulfur cathode and alternative anode in full cell format. (Annual Milestone; In progress)

Progress Report

This quarter, the team screened and attempted to identify the best polymeric sulfur cathode. They investigated three kinds of polymeric sulfur materials, as shown in Table 9. The organic monomer substrates for those three polymeric sulfur materials were different. Cell performances of the polymeric sulfur materials are shown in Table 9.

Table 9. Summary of electrochemical and analytical data for Li-S batteries with different sulfur cathodes.

Sample	Contents	Ratio	1st discharge (mAh/g)	50th Discharge (mAh/g)	50-cycle capacity Retention (%)	Sulfur in DME (mM)
SP1	S/DCDP/Limonene	50/25/25	673	526	78.2	1.858
SP5	S/DCDP/EGDMA	50/5/45	449	219	48.7	4.005
SP7	S/DCDP/EGDMA	50/25/25	381	187	49.1	1.683
S_8(control)	50%		1094	404	36.9	About 10

To understand the influence of chemical composition of the three polymeric sulfur materials on cell performance, the team first studied dissolution of elemental sulfur in the electrolyte for each of the polymeric sulfur materials by the HPLC method they developed. As shown in the last column in Table 9, the SP5 polymeric sulfur materials exhibited the highest concentration of elemental sulfur after being soaked in DME solution. This indicates that the SP5 electrode had the least ability to retain sulfur within the electrode. Correspondingly, the battery made with SP5 cathode showed the lowest performance among the three polymeric sulfur compounds. Only 48.7% initial capacity left, which was similar to the controlled S_8 cathode (elemental sulfur physically loaded on carbon matrix). However, although the SP1 and SP7 polymeric sulfur materials have a similar capability to retain sulfur within the electrodes, cell performances of those two were quite different. The battery with SP1 polymeric sulfur cathode retained 78.2% of its initial capacity after 50 cycles, while only 49% capacity retention was achieved for the battery with SP7 polymeric sulfur cathode. To understand the underlying differences between SP1 and SP7, the team studied the dissolved polysulfide distributions in the separator. They observed that the dissolved polysulfide ions produced from the better performing polymeric sulfur electrode (SP1) were short-chain polysulfide ions, mainly S_3^{2-}, S_4^{2-}, and S_5^{2-}. As reported in FY 2020, the short-chain polysulfide ions outperform the long-chain polysulfide ions in the electrolyte. Therefore, the polymeric structure that has the capability to retain the very soluble long-chain polysulfides, such as S_6^{2-} and S_7^{2-}, within the electrodes performs better. Figure 108 shows the distribution of polysulfides in the separator at different stages of discharge on different sulfur cathodes. SP1 polymeric sulfur cathode demonstrated relatively higher distributions of middle-chain (S_5^{2-}) and short-chain (S_4^{2-} and S_3^{2-}) compared to the other two polymeric sulfur cathodes. These results indicate that the SP1 polymeric structure has better ability to retain both

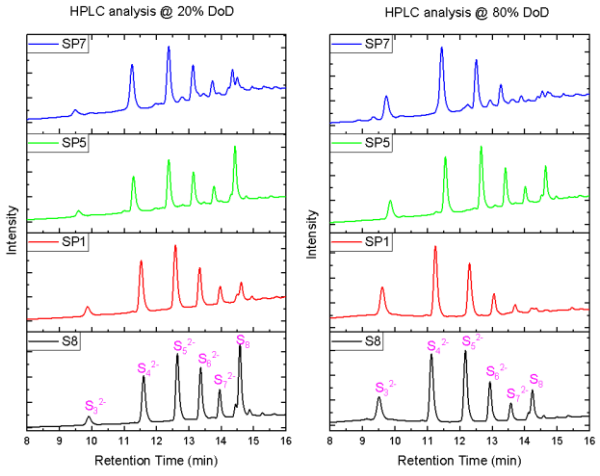

Figure 108. High-performance liquid chromatography (HPLC) chromatograms of Li-S batteries with different sulfur cathodes at different depths of discharge.

elemental sulfur and long-chain polysulfides within the cathode than that for the other polymeric sulfur materials. Thus, the Li-S battery involving SP1 polymeric sulfur materials as the cathode has the best capacity retention ability.

Patents/Publications/Presentations

Publications

- Shadike, Z., S. Tan, Q-C. Wang, R. Lin, E. Hu, D. Qu, and X-Q. Yang. "Review on Organosulfur Materials for Rechargeable Lithium Batteries." *Materials Horizons* 8 (2021): 471-500. doi: 10.1039/D0MH01364A.
- Xu, Y., D. Zheng, W. Ji, N. Abu-Zahra, and D. Qu. "A Molecular Dynamics Study of the Binding Effectiveness between Undoped Conjugated Polymer Binders and Tetra-Sulfides in Li–S Batteries." *Composite Part B: Engineering* 206 (2021): 108531.

Task 5.5 – New Electrolytes for Lithium-Sulfur Battery (Gao Liu, Lawrence Berkeley National Laboratory)

Project Objective. The project objective is to develop new electrolytes, additives, and electrode compositions for Li-S battery with high ion-conductivity, stable toward polysulfide and promoting the polysulfide affiliation with the electrode substrate to prevent polysulfide dissolution.

Project Impact. This work will address the high cost and low energy density of Li-ion rechargeable batteries. The emerging Li-S batteries could feature both high energy density and low cost. This project enables applications of the low-cost, abundant sulfur element as a major chemical component for electrical energy storage. This project will develop new approaches for electrolytes and electrode compositions of Li-S rechargeable batteries.

Approach. This project aims to develop new electrolytes and additives for Li-S battery. The properties of the ideal electrolyte for sulfur electrode would be high ion conductivity, stable toward polysulfide, and promoting the polysulfide affiliation with the electrode substrate to prevent polysulfide dissolution. The project is designed to first understand the electrode substrate interaction with the polysulfides in different electrolytes. This will lead to better understandings of the polysulfide nucleation and precipitation mechanisms in common electrolytes. The second stage of the project will focus on chemically modifying the structures of the solvent and salt electrolyte molecules to increase electrolyte stability and ionic conductivity, to prevent polysulfide dissolution, and to promote polysulfides precipitation.

Out-Year Goals. The team will also investigate the contribution of Li-metal electrodes to overall Li-S battery performance and will develop methods to stabilize Li-metal surface.

Collaborations. This project collaborates with J. Guo and W. Yang (ALS/LBNL), A. Minor (National Center for Electron Microscopy at LBNL/UCB), L-W. Wang (LBNL), and P. B. Balbuena, Texas A&M University.

Milestones

1. Measure polysulfide dissolution in the new amphiphilic electrolytes. (Q1, FY 2021; Completed)
2. Map out the Li-ion diffusion path in sulfur materials. (Q2, FY 2021; In progress)
3. Develop optimized sulfur electrodes according to the electrolyte properties and Li-ion transport in sulfur materials. (Q3, FY 2021; Not yet initiated)
4. Investigate the Li-metal electrode properties in the Li-S cell. (Q4, FY 2021; In progress)

Progress Report

The micelle-based electrolyte was made by dissolving LiTFSI salt in F_4EO_2 fluorinated ether molecules blended with solvent TTE. This study is focused on 0.5 M and 1.0 M LiTFSI concentration electrolytes, which were made by using 1:5 and 1:2.5 F_4EO_2/TTE volume ratio, respectively. A key property of the electrolyte system is transference number, aside from ionic conductivity. The Bruce-Vincent method is a convenient electrochemical approach to investigate the transference number, an important electrolyte transport property. The measurement was conducted on Li-Li symmetrical cell in which the analyte, electrolyte was sandwiched by two identical pieces of lithium electrodes. The cell was first run to complete two cycles of lithium plating/stripping at 0.4 mA/cm^2 for 1 hour per cycle to form the stable SEI. Next, impedance of the cell was measured with the frequency range of 300 kHz-100 mHz. The initial current i_T was then measured once a small DC polarization (ΔV =10mV) was applied. After 40 hours of polarization, the steady current i_0 was reached and immediately recorded. Finally, the impedance of the cell was measured again with the same frequency range. The transference number of t_{Li^+} can then be expressed by the following equation:

$$t_{Li^+} = \frac{i_0(\Delta V - i_T R_T)}{i_T(\Delta V - i_0 R_0)}$$

where R_T and R_0 are the initial and steady-state resistance of passive layers (R_{SEI}), which can be extracted from the impedance measurement data. Figure109a-b shows the *i-t* curve of polarization process and Nyquist plot of impedance measurement prior and post polarization for 0.5 M LiTFSi in F_4EO_2/TTE (v/v, 1:5) electrolyte. These two plots demonstrate the selection of important data points of i_0, i_T and R_0, R_T. Figure 109c reveals transference number as a function of LiTFSI electrolyte with 0.5 M - 2.0 M concentrations. The number plotted is the average of three repeated tests, with error bars included on the plot. As can be seen, the transference number of Li^+ was ~ 0.8 through all the concentrations, which is higher than that of conventional LE systems.

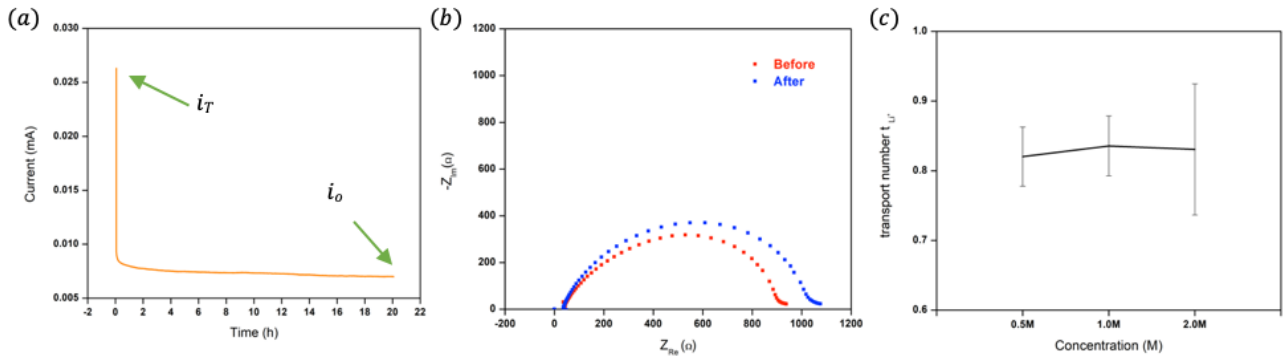

Figure 109. 0.5 M LiTFSI in F_4EO_2/TTE (v/v, 1:5) electrolyte: (a) i_T curve for the DC polarization process; (b) impedance of the cell before and after polarization. (C) Transference number of LiTFSI in F_4EO_2/TTE electrolyte as a function of concentration with error bars depicting results of multiple tests.

Patents/Publications/Presentations

The project has no patents, publications, or presentations to report this quarter.

TASK 6 – AIR ELECTRODES / ELECTROLYTES

Summary and Highlights

High-density energy storage systems are critical for EVs required by the EV Everywhere Grand Challenge. Conventional Li-ion batteries still cannot fully satisfy the ever-increasing needs because of their limited energy density, high cost, and safety concerns. As an alternative, the rechargeable lithium-oxygen (Li-O_2) battery has potential to be used for long-range EVs. The practical energy density of a Li-O_2 battery is expected to be ~ 800 Wh kg^{-1}. The advantages of Li-O_2 batteries come from their open structure; that is, they can absorb the active cathode material (oxygen) from the surrounding environment instead of carrying it within the batteries. However, the open structure of Li-O_2 batteries also leads to several disadvantages. The energy density of Li-O_2 batteries will be much lower if oxygen must be provided by an onboard container. Although significant progress has been made in recent years on fundamental properties of Li-O_2 batteries, research in this field is still in an early stage, with many barriers to be overcome before practical applications. These barriers include:

- Instability of electrolytes—The superoxide species generated during discharge or O_2 reduction process is highly reactive with electrolyte and other components in the battery. Electrolyte decomposition during charge or O_2 evolution process is also significant due to high over-potentials.
- Instability of air electrode (dominated by carbonaceous materials) and other battery components (such as separators and binders) during charge/discharge processes in an O-rich environment.
- Corrosion of Li-metal anode in an electrolyte saturated with oxygen.
- Low energy efficiency associated with large over-potential and poor cyclability of Li-O_2 batteries.
- Low power rate capability due to electrode blocking by the reaction products.
- Absence of a low-cost, high-efficiency oxygen supply system (such as oxygen selective membrane).

The main goal of this Task is to provide a better understanding on the fundamental reaction mechanisms of Li-O_2 batteries and identify the required components (especially electrolytes and electrodes) for stable operation of Li-O_2 batteries. This task will investigate several new approaches to improve stability of Li-metal anode in Li-O_2 batteries:

- Li-metal anodes will be protected using two approaches: (1) *in situ* formation of a stable SEI layer before Li-O_2 cell operation through various electrolyte formulations and treatment protocols, and (2) *ex situ* formation of stable inorganic/polymeric hybrid electrolyte layers through dip-coating or tape-casting method to coat the inorganic/polymeric hybrid electrolyte layer on Li-metal surface.
- A joint theoretical/experimental approach for design and discovery of new cathode and electrolyte materials will act synergistically to reduce charge overpotentials and increase cycle life. Synthesis methods, in combination with design principles developed from computations, will be used to make new cathode architectures. Computational studies will be used to help understand decomposition mechanisms of electrolytes and how to design electrolytes with improved stability.
- A new cathode will be developed based on high-efficiency catalyst such as 2D TM dichalcogenides (TMDs). These cathode materials will be combined with new electrolyte blends and additives that work in synergy to reduce charge potentials and increase stability of the Li-air system.

State-of-the-art characterization techniques and computational methodologies will be used to understand charge and discharge chemistries. Success of this Task will establish a solid foundation for further development of Li-O_2 batteries toward practical applications for long-range EVs. The fundamental understanding and breakthrough in Li-O_2 batteries may also provide insight on improving performance of Li-S batteries and other energy storage systems based on chemical conversion process.

Highlights. The Task highlights for this quarter are as follows:

- The ANL group (K. Amine, L. A. Curtiss, and J. Lu) explored a series of nanocarbon materials with unique pore structures via a low cost, facile, and nanoscale controllable method (lignin, xylan, cellulose, and pomelo peel derived products). Li-O_2 batteries using these materials have demonstrated improved cyclability.
- The ANL and University of Illinois at Chicago (UIC) group (L. A. Curtis, A. Ngo, and A. Salehi-Khojin) found that a conductive metal organic framework (MOF) in combination with a redox mediator (RM) results in formation of a conductive amorphous Li_2O_2 that facilitates the growth and decomposition of the discharge product in a Li-O_2 battery. The battery with this configuration exhibits sustainable and efficient operation with a low charge potential and extended lifetime of 300 cycles at a capacity of 1000 mAh/g under a current density of 1 A/g.
- The PNNL group (J-G. Zhang and W. Xu) found that a uniform polymer-supported SEI layer leads to smaller impedance and two times longer cycle life of Li-O_2 batteries. The salt and concentration of RM used in these batteries are optimized.

Task 6.1 – Rechargeable Lithium-Air Batteries (Ji-Guang Zhang and Wu Xu, Pacific Northwest National Laboratory)

Project Objective. The objective of this project is to develop rechargeable Li-O_2 batteries with long-term cycling stability through in-depth research on more stable electrolytes and highly efficient catalysts for air electrodes, protection of Li-metal anodes, and deeper understanding on the oxygen reduction reaction (ORR) and oxygen evolution reaction (OER) mechanisms behind the electrochemical performance of Li-O_2 cells. In FY 2021, the team will further improve the cycle life and safety of Li-O_2 batteries using novel polymeric colloidal localized high concentration electrolytes (PC-LHCEs), binder-free catalysts with a robust artificial SEI layer, and synthesis of stable solvents. The fundamental mechanism behind the enhanced stability of Li-O_2 batteries using these new materials will also be investigated.

Project Impact. The project will develop rechargeable Li-O_2 batteries with long-term cycling stability through in-depth research on more stable electrolytes and highly efficient catalysts for air electrodes and protection of Li-metal anodes. This fiscal year, the team will further investigate stability of electrodes with different types of catalysts to keep the reversible reactions during the Li-O_2 battery operation and electrolytes to build more stable Li-O_2 batteries with long-term cycling capability.

Approach. Develop highly stable electrolytes, including novel PC-LHCEs with an optimization of Li-metal surface protection and effective catalysts to prevent the irreversible parasitic reactions at the electrodes (cathode and anode). The electrochemical test of Li||Li symmetric cell containing above stable electrolyte will be first measured comparatively with typical ether (TEGDME) based electrolytes to evaluate the stability of the electrolyte itself and the artificial SEI layer. Then, the stability of proposed electrolytes at the cathode side with reactive oxygen species during ORR/OER will be further characterized in the Li-O_2 cells. In addition, with new synthesis of solvents to stabilize the electrolyte system, the team will find the key parameters for suitable electrolyte in Li-O_2 batteries.

Out-Year-Goals. The long-term goal of the proposed work is to enable rechargeable Li-air batteries with a specific energy of 800 Wh/kg at cell level, 1000 deep-discharge cycles, improved abuse tolerance, and less than 20% capacity fade over a 10-year period to accelerate commercialization of long-range EVs.

Collaborations. This project collaborates with C. Wang of PNNL on characterization of cycled air electrodes by TEM/SEM, with P. Gao of PNNL on computational calculations and simulations, and with J. Read of ARL on oxygen solubility tests.

Milestones

1. Develop binder-free electrocatalysts on the surface of air electrode with polymer-supported SEI and redox mediators. (Q1, FY 2021; Completed, December 31, 2020)
2. Develop PC-LHCEs using osmosis effect. (Q2, FY 2021)
3. Understand the interphase properties of PC-LHCE/electrode. (Q3, FY 2021)
4. Develop new solvents that are stable against oxidation and singlet oxygen species for reversible Li-O_2 battery systems. (Q4, FY 2021)

Progress Report

This quarter, the effect of polymer-supported solid electrolyte interface (PS-SEI) layer generated on Li-metal surface on the cycling stability of Li-O_2 cells was investigated. The suitable lithium salt in tetraglyme solvent (G4) with the PS-SEI layer and the effect of concentration RM on the cell resistance were studied to achieve long-term Li-O_2 battery operation. SEM, EDX, and EIS measurement revealed that the cell resistance greatly related to the properties of the type of SEI layer (see Figure 110). The cell resistance with the uniform and robust PS-SEI layer was much smaller (Figure 110b; 117 Ω) than that of the non-uniform SEI layer (Figure 110a; 278 Ω) without a polymer support after 50 cycles at 25°C. This result strongly supports that much better (2x) cycle number in the cells with the uniform and robust PS-SEI layer can be attributed to the stabilized SEI layer on lithium metal, as reported last quarter.

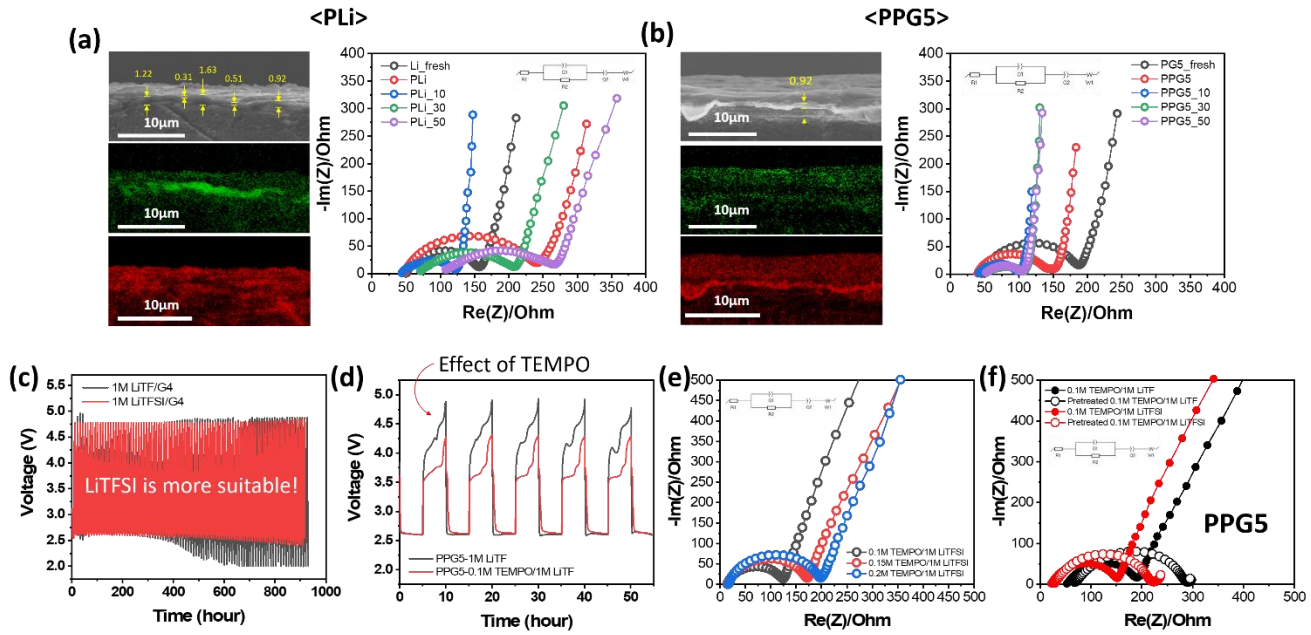

Figure 110. (a-b) Cross-sectional images (top), oxygen (middle), and carbon (bottom) energy dispersive X-ray maps of Li-metal surface with PPG5 [PEO-based gel polymer (PG) coating, and electrochemical pretreatment under O_2) and with PLi (without PG coating, and electrochemical pretreatment under argon). Electrochemical impedance spectroscopy (EIS) of Li-O_2 batteries with PPG5 and PLi after pretreatment; 10th, 30th, and 50th cycles at a current density of 0.2 mA cm^{-2} under a capacity limited protocol of 1.0 mAh cm^{-2} in the operation voltage range of 2-5 V operated at 25°C. (c) Charge/discharge curves of Li-O_2 batteries with different lithium salts and (d) with and without 0.1 M TEMPO. (e) EIS of fresh Li-O_2 batteries with different concentration of TEMPO in the LiTFSI-based electrolytes. (f) EIS of Li-O_2 battery cells with different lithium salts and PPG5 layer before and after pretreatment step.

It is also found that LiTFSI is more suitable than lithium trifluoromethanesulfonate (LiTf) for G4 in Li-ion batteries (Figure 110c). Since the cell overpotential significantly deceases with 0.1 M TEMPO in 1 M LiTf/G4 electrolyte, and the cell can be operated in a narrow cut-off voltage range (2-4.5 V) (Figure 110d), EIS analysis was carried out with different concentrations of TEMPO in 1 M LiTFSI/G4 electrolytes. The LiTFSI-based electrolytes have much lower solution resistance (R_s, Figure 110e) than LiTf-based electrolyte (Figure 110b), and cell resistance increases as the concentration of TEMPO in the electrolytes increases (Figure 110e). Since the RM molecules cause more side reactions on Li-metal surface, the team optimized TEMPO concentration in 1 M LiTFSI/G4 electrolyte with the PS-SEI as a protection layer generated by electrochemical pretreatment. Even after the pre-charging step to generate the PS-SEI layer, the cell with LiTFSI-based electrolyte keeps lower solution resistance (28 Ω) than the LiTf-based electrolyte (67 Ω) with PPG5 layer (Figure 110f). The optimization in this study could be a critical key to extend the lifespan of Li-O_2 batteries much longer than the 130 cycles achieved last quarter.

Patents/Publications/Presentations

The project has no patents, publications, or presentations to report this quarter.

Task 6.2 – Lithium-Air Batteries
(Khalil Amine, Larry A. Curtiss, and Jun Lu; Argonne National Laboratory)

Project Objective. This project will develop new cathode materials and electrolytes for Li-air batteries for long cycle life, high capacity, and high efficiency. The goal is to obtain critical insight that will provide information on the charge and discharge processes in Li-air batteries to enable new advances to be made in their performance. This will be done using state-of-the-art characterization techniques combined with state-of-the-art computational methodologies to understand and design new materials and electrolytes for Li-air batteries.

Project Impact. The instability of current nonaqueous electrolytes and degradation of cathode materials limits performance of Li-air batteries. The project impact will be to develop new electrolytes and cathode materials that are stable and can increase energy density of electrical energy storage systems based on lithium.

Approach. The project is using a joint theoretical/experimental approach for design and discovery of new cathode and electrolyte materials that act synergistically to reduce charge overpotentials and increase cycle life. Synthesis methods, in combination with design principles developed from computations, are used to make new cathode architectures. Computational studies are used to help understand decomposition mechanisms of electrolytes and how to design electrolytes with improved stability. The new cathodes and electrolytes are tested in Li-O_2 cells. Characterization, along with theory, is used to understand the performance of materials used in the cell and to make improved materials.

Out-Year Goals. The out-year goals are to find catalysts that promote discharge product morphologies that reduce charge potentials and to find electrolytes for long cycle life through testing and design.

Collaborations. This project engages in collaboration with K. C. Lau (UC at Norridge), Y. Wu (Ohio State University), D. Zhai (China), and R. Shahbazian-Yassar (UIC).

Milestones

1. Design functionalized cathodes to achieve high electrochemical performance of Li-O_2 batteries. (Q1, FY 2021; Completed)
2. Characterize cathode materials and investigate electrochemical behaviors. (Q2, FY 2021)
3. Gain understanding of the processes of ORR and OER of these materials, and reveal the possible parasitic reactions. (Q3, FY 2021)
4. By understanding the effects, engineer new catalysts with improved catalytic performance and suppressed side reactions. (Q4, FY 2021)

Progress Report

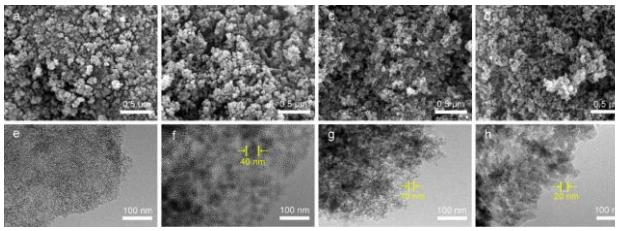

Figure 111. (a-d) Scanning electron microscopy images of C_L, C_X, C_C, and C_P. (e-h) Corresponding transmission electron microscopy images.

Li-O_2 batteries have attracted extensive research interest due to their high energy density. Unfortunately, although electrolyte stability and basic cathode reactions in nonaqueous Li-O_2 battery have been extensively studied, the current system is plagued by porous cathode materials that are easily blocked by the solid discharge product Li_2O_2 during discharge process, which degrades the reaction kinetics with shortened cycle life. A reasonable pore architectonic design and good catalytic capacity of the cathode are considered to be the key to solve this problem. Biomass carbon materials with unique nanostructures have been employed as porous cathode materials with certain catalytic properties. However, the current synthesis methods of carbon materials are always limited to a specific biomass raw material that is not conducive to its large-scale practical application. Even worse, because carbon materials synthesized so far are mostly concave cylindrical-like pore structures that are easily blocked by the discharge products, the internal micro- and mesoporous structures and the active reaction sites are not all effectively involved in the electrode reaction, and thus result in the termination of discharge.

Herein, a series of nanocarbon materials with unique pore structures was prepared via a low-cost, facile, and nanoscale controllable method (lignin, xylan, cellulose, and pomelo peel derived products are defined as C_L, C_X, C_C, and C_P, respectively). SEM images (Figure 111a-d) show that all samples consist of loosely stacked carbon nanospheres, except for that CL contains micron-sized particles, which have abundant open and mesoporous macropores in the cracks among carbon clusters. C_X, C_C, and C_P have a nano-scale uniform structure that no longer maintains the integrity and microscopic morphology of the original biomass, and the diameter of carbon microspheres made from different biomass raw materials is diverse. Further research with TEM reveals that the diameters of C_X, C_C, and C_P with homogeneous distribution are about 40 nm, 10 nm, and 20 nm, respectively, whereas C_L possesses a solid micron-scale structure (Figure 111e-h).

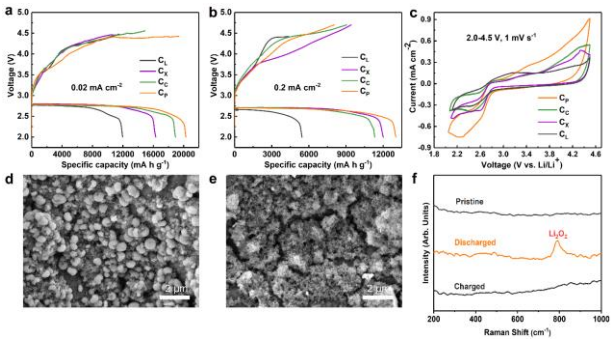

Figure 112. Initial full discharge-charge voltage profiles of C_L, C_X, C_C, and C_P cathode at current density of (a) 0.02 mA cm^{-2} and (b) 0.2 mA cm^{-2}. (c) Cyclic voltammetry curves of C_L, C_X, C_C, and C_P electrodes within a voltage window of 2-4.5 V at a scanning rate of 1 mV s^{-1}. (d-e) Scanning electron microscopy images of C_P cathode after first discharge (d) and charge steps (e) at current density of 0.02 mA cm^{-2}. (f) Raman spectra of C_P cathode at different stages: pristine, and after first discharge and charge steps.

The electrochemical properties of four carbon materials are tested (Figure 112a-c). At current density of 0.02 mA cm^{-2}, C_X, C_C, and C_P deliver excellent specific capacity of 16320, 18931, and 20300 mA h g^{-1}, respectively, which is higher than 11985 mA h g^{-1} of C_L. When current density is increased to 0.2 mA cm^{-2}, four carbon materials, except C_L, still keep a specific capacity exceeding 11300 mA h g^{-1} with a decreased discharge voltage platform of ~ 70 mV only; particularly, the specific discharge capacity of C_P is still as high as 13030 mA h g^{-1}. The remarkable specific capacity of C_P is beyond almost all the cathode materials in nonaqueous system that have been reported according to the results of the literature search. The CV curves demonstrate that C_P has the highest ORR onset potential and the lowest OER onset potential, and also the highest ORR and OER peak currents, indicating good catalytic performance of C_P for both ORR and OER processes.

The electrochemical reaction process was preliminary investigated. SEM images of C_P cathode after first discharge and charge steps indicate an excellent reversibility of the cathode reaction (Figure 112e), and Raman result has verified the formation and complete decomposition of Li_2O_2 (Figure 112f). Considering the best performance of C_p, the correlation between electrochemical reaciton and unique pore structure requires further study.

Patents/Publications/Presentations

Publications

- Bi, X., M. Li, C. Liu, Y. Yuan, H. Wang, B. Key, R. Wang, R. Shahbazian-Yassar, L. A Curtiss, J. Lu, and K. Amine. "Cation Additive Enabled Rechargeable LiOH Based Lithium-Oxygen Batteries." *Angewandte Chemie International Edition* 59 (2020): 22978–22982. doi: 10.1002/anie.202010745. (Designed cover)
- Plunkett, S. T., H-H. Wang, S. H. Park, Y. J. Lee, J. Cabana, K. Amine, S. Al-Hallaj, B. P. Chaplin, and L. A. Curtiss. "Charge Transport Properties of Lithium Superoxide in Li–O_2 Batteries." *ACS Applied Energy Materials* 3, No. 12 (2020): 12575–12583. doi: 10.1021/acsaem.0c02495.

Task 6.3 – Lithium Oxygen Battery Design and Predictions
(Larry A. Curtiss/Anh Ngo, Argonne National Laboratory; Amin Salehi-Khojin, University of Illinois, Chicago)

Project Objective. The objective of this work is to develop new materials for Li-O_2 batteries that give longer cycle life and improved efficiencies in an air environment. New electrolyte blends and additives will be investigated that can reduce clogging and at the same time promote the cathode functionality needed to reduce charge overpotentials. New cathode and anode materials will be investigated that can work in conjunction with the electrolytes to improve cycle life in the presence of air components.

Project Impact. Li-air batteries are considered as a potential alternative to Li-ion batteries for transportation applications due to their high theoretical specific energy. The major issues with the existing Li-O_2 systems include degradation of the anode electrode, reactions with air components, clogging of the cathode, and electrolyte instability. Thus, this project is using a comprehensive approach to improve cycle life and efficiency through developing new materials for electrodes, anodes, and electrolytes that work in synergy.

Approach. The experimental strategy is to use cathode materials based on 2D TMDs that the team has found to be among the best oxygen reduction and evolution catalysts. These cathode materials will be combined with new electrolyte blends and additives that work in synergy to reduce charge potentials and increase stability of the Li-air system. DFT and AIMD simulations are used to gain insight at the electronic structure level of theory of the electrolyte structure, and function both in bulk and at interfaces with the cathode, anode, and discharge product. Classical MD is used to obtain understanding at longer length and time scales of processes occurring in the electrolyte and growth mechanisms of discharge products. The team will also utilize a HT screening strategy based on experiment and theory to develop a large database of properties and outcomes of electrolyte combinations that can be analyzed using ML to predict electrolytes and additives with the best performance.

Out-Year Goals. The out-year goals are to find electrolytes that give high capacities and long cycle life in an air atmosphere using HT screening.

Collaborations. This project engages in collaboration with R. Assary and J. G. Wen of ANL, B. Narayanan of University of Louisville, T. Li of Northern Illinois University, and F. Khalili-Araghi and R. Klie of UIC.

Milestones

1. Use a conductive MOF for Li-O_2 battery to increase the number of active sites in cathode materials based on MOFs as well as localize them in pores. (Q1, FY 2020; Completed)
2. Perform computational studies of lithium peroxide formation in a conductive MOF for Li-O_2 batteries. (Q2, FY 2021; Initiated)
3. Utilize new TMD alloy catalyst for Li-O_2 batteries to increase charge/discharging rates. (Q2, FY 2021; Initiated)
4. Investigate new concepts in electrolyte additives that work with the new alloy catalyst to give both effective anode protection and lowering charge potentials. (Q4, FY 2021)

Progress Report

$Li-O_2$ batteries are considered as an advanced energy storage system that could provide a much higher specific energy than Li-ion batteries for electrical transportation. However, there are major issues with existing $Li-O_2$ systems, including degradation of anode electrode, poor volumetric energy density, electrolyte instability, low charge/discharge rates, and high charge overpotential. The team is focused on finding a combination of electrolytes, additives, and cathode catalysts to enable a $Li-O_2$ battery that can overcome these challenges as well as operate in an air atmosphere. This quarter, the team has investigated the effect of adding conductivity directly to the MOF instead of combining the MOFs with carbons to make them conductive. This has the advantage of providing active sites situated within the pores as opposed to being located away from the pores in the carbon part of the composite. MOFs have been used in $Li-O_2$ batteries because of their high surface area. Including conductivity in the framework has enabled the team to achieve high charge rates for extended cycles and low charge potentials.

A bulk conductive copper tetrahydroxyquinone (Cu-THQ) MOF with the electrical conductivity of $\sim 1.5 \times 10^{-7}$ S cm^{-1} was exfoliated into 2D nanoflakes via a liquid-phase exfoliation technique. This prepared Cu-THQ cathode was used in combination with an electrolyte combination comprised of a lithium nitrate ($LiNO_3$) salt and a bifunctional indium bromide ($InBr_3$) RM in TEGDME solvent. To evaluate the battery performance of this system, a constant current density of 1 A/g was applied within a potential range of 2.5-4 V versus Li/Li^+ under two limiting capacities of 1000 mAh/g and 2000 mAh/g. Figure 113(left) shows the obtained charge-discharge profiles for the battery with the increased capacity of 2000 mAh/g and current density of 1 A/g. A potential gap of 0.92 V was observed at the first cycle, which remained stable, with only a slight increase reaching 1.0 V at the end of cycling. Figure 113(right) shows the results obtained under 2000 mAh/g limiting capacity and doubled current density of 2 A/g. The battery operates for 100 cycles before reaching the discharge cut-off potential. Under this condition, the potential gap increased from 1 V at the 1st cycle to 1.31 V at the 100th cycle. Considering the significantly high current density rates and extended capacity values, the charge profile remains stable throughout the cycling of these batteries with a low potential of < 3.69 V. In addition, the results show efficient battery operation, with a low charge potential of 3.64 V and an extended lifetime of 300 cycles with the capacity of 1000 mAh/g, under the current density of 1 A/g (not shown).

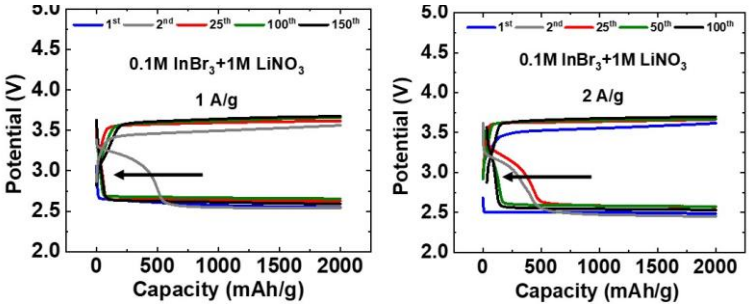

Figure 113. $Li-O_2$ battery voltage profiles for cathode based on copper tetra-hydroxyquinone (Cu-THQ) metal organic framework with current densities of 1 A/g (left) and 2 A/g (right).

The nature of the discharge product on the cathode after the 10th discharge was analyzed using TEM. The TEM images obtained from a cathode flake (Figure 114) suspended over a holey region of grid show a crystalline Cu-THQ with an amorphous Li_2O_2 on it. The diffraction spots in the inset of Figure 114 confirm the crystalline nature of Cu-THQ and are superimposed over the diffuse halo from the Li_2O_2 region, which exhibits an amorphous nature. To further complement the TEM observation on Li_2O_2, XRD patterns of the cathode after the 10th discharge were obtained. No diffraction peaks are observed for crystalline Li_2O_2 after the 10th discharge, confirming the amorphous feature of this product. Previously, it was shown that the amorphous Li_2O_2 exhibits high electrical conductivity. Thus, the amorphous Li_2O_2 in close contact with the Cu-THQ cathode can serve as new active sites for the product growth. This amorphous Li_2O_2 along with a relatively high concentration of RM seems to facilitate the high rate for the charge and discharge processes found for this $Li-O_2$ battery.

In summary, the team has found that the conductive MOF and the $InBr_3$ RM produces conductive amorphous Li_2O_2 rather than insulator crystalline structure, which facilitates the growth and decomposition of discharge products. These results show an efficient battery operation with a low charge potential of 3.64 V and an extended lifetime of 300 cycles with the capacity of 1000 mAh/g, under current density of 1 A/g. Furthermore, this system exhibits a very stable and reduced charge potential of ≤ 3.69 V and cycle life of 150 and 100 with the specific capacity of 2000 mAh/g and current density values of 1 A/g and 2 A/g, respectively. The performance of this Li-O_2 battery with a conductive MOF framework is much improved over previous studies that used MOF composites with carbons added to provide a conductivity to the cathode.

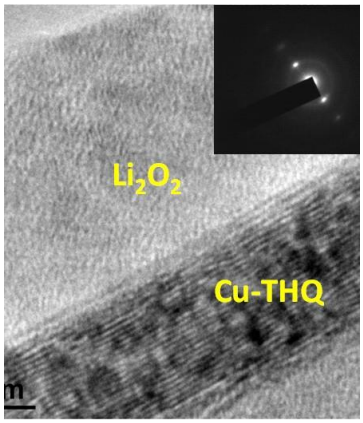

Figure 114. Transmission electron microscopy results of the copper tetrahydroxyquinone (Cu-THQ) metal organic framework cathode after the 10th discharge of the Li-O_2 battery.

Patents/Publications/Presentations

The project has no patents, publications, or presentations to report this quarter.

TASK 7 – SODIUM-ION BATTERIES

Summary

The Na-ion battery will require investigations to identify optimal electrode materials, electrolytes, separators, and binders to reach full potential. The BMR program will therefore have a limited effort directed toward identifying Na-ion battery materials that have potential value for vehicle applications. During FY 2019, the BMR added several new projects in the area of Na-ion batteries, four of which have been continuously funded. Progress on these projects is described in this report.

Highlights. The highlights for this quarter are as follows:

- The ANL team reported development of a hierarchical micro/nanostructured antimony (Sb)-doped RP/carbon anode (RP = red phosphorus, carbon type = Ketjenblack/MWCNTs), which demonstrates extraordinary electrochemical performance with high ICE of ~ 90% and high areal capacity together with good cycle stability and rate capability.
- The BNL team carried out synchrotron-based spectroscopy studies on two new P2 type layered cathode materials for Na-ion batteries: $Na_{0.67}[Mn_{0.66}Ni_{0.33}]O_2$ (MN) and Sb-substituted MN, $Na_{0.67}[Mn_{0.61}Ni_{0.28}Sb_{0.11}]O_2$ (MNS). The 2D XANES obtained from TXM shows that $Mn^{3.7+}$ and Ni^{2+} are uniformly distributed throughout the bulk of pristine MN and Sb-substituted MNS samples.
- The LBNL team studied the effects of drying temperature on the electrochemical properties and structure of the lepidocrocite titanate anodes. Heating to 600°C degrees induces a structural change to a related phase and removes water. The new phase must be activated by discharging to a lower voltage initially, and excellent cycling is obtained when the low voltage limit is raised to 0.1 V from 0.05 V versus Na^+/Na after the first cycle, with 185 mAh/g obtained.
- The PNNL team has developed a novel carbon anode with a record specific capacity by chemical vapor deposition (CVD) coating of soft carbon on porous carbon precursors. The anode exhibits a 1st discharge capacity of 489 mAh/g and initial efficiency of 88%. After 400 cycles, a full cell using this anode still retains a capacity of 70%.

Task 7.1 – Exploratory Studies of Novel Sodium-Ion Battery Systems (Xiao-Qing Yang and Zulipiya Shadike, Brookhaven National Laboratory)

Project Objective. To meet the challenges of powering PHEVs and BEVs, new rechargeable battery systems with high energy and power density, low cost, good abuse tolerance, and long calendar and cycle life need to be developed. The primary objective of this project is to develop new advanced synchrotron-based material characterization techniques and apply these techniques to study the new rechargeable battery systems beyond the Li-ion batteries, namely the Na-ion battery systems for electrified vehicles.

Project Impact. The results of this project will be used for developing technologies that will significantly increase the energy density and cycle life and reduce the cost of beyond Li-ion battery systems. This will greatly accelerate deployment of EVs and reduce carbon emission associated with fossil fuel consumption and will help in the direction of building U. S. based energy storage manufacture chains.

Approach. This project will use the synchrotron-based *in situ* x-ray diagnostic such as *in situ* XRD and *in situ* XAS tools, combined with TEM, STEM, and TXM imaging techniques developed at BNL to evaluate the new materials and redox couples to obtain in-depth understanding of the reaction mechanisms of these materials, aiming to improve existing materials and to provide guidance for new materials and new technology development for Na-ion battery systems.

Out-Year Goals. The out-year goal is to complete the synchrotron-based XRD, XAS, and XANES mapping studies of new cathode materials P2-$Na_{0.66}[Mn_{0.61}Ni_{0.28}Sb_{0.11}]O_2$ and P2-$Na_{0.7}Mg_{0.2}[Mn_{0.6}Fe_{0.2}\square_{0.2}]O_2$ (□ here representing TM vacancy) and a high-capacity, high-C rate, multi-component cathode material.

Collaborations. The BNL team has been closely working with top scientists on new material synthesis at ANL, LBNL, and PNNL, with U. S. industrial collaborators at GM and Johnson Controls, and with international collaborators.

Milestones

1. Complete XAS (including XANES and EXAFS) and 2D XANES mapping of the pristine P2-$Na_{0.66}[Mn_{0.61}Ni_{0.28}Sb_{0.11}]O_2$ cathode material at nickel and manganese K-edge. (Q1, FY 2021; Completed)
2. Complete nickel and manganese K-edge XAS (including XANES and EXAFS) of P2-$Na_{0.66}[Mn_{0.61}Ni_{0.28}Sb_{0.11}]O_2$ cathode material at different SOCs. (Q2, FY 2021; In progress)
3. Complete *ex situ* TEM, XRD study, and 2D XANES mapping of a high-capacity high-C rate multi-component sodium cathode material with P2 type at different SOCs. (Q3, FY 2021; In progress)
4. Complete iron and manganese K-edge XAS of P2-$Na_{0.7}Mg_{0.2}[Mn_{0.6}Fe_{0.2}\square_{0.2}]O_2$ cathode material at different SOCs. (Q4, FY 2021; In progress)

Progress Report

This quarter, the 1st milestone for FY 2021 was completed, and the project progressed on other milestones. BNL focused on developing new diagnostic techniques to study and improve performance of Na-ion batteries. These techniques have been applied to study two new P2-type layered cathode materials for Na-ion batteries: $Na_{0.67}[Mn_{0.66}Ni_{0.33}]O_2$ (MN) and Sb-substituted MN, $Na_{0.67}[Mn_{0.61}Ni_{0.28}Sb_{0.11}]O_2$ (MNS). To verify the element and valence distribution in MNS, TXM combined with XANES spectroscopy was collected by using synchrotron-based imaging techniques. The 2D XANES mapping for the oxidation states of manganese and nickel are shown in Figure 115c-d using the energy levels (color coded) near their K-edges. The results were collected at the same region of the sample by scanning the energies across the manganese K-edge (6539 eV) and nickel K-edge (8333 eV) separately in sequence. Figure 115d shows the uniform spatial distribution of Ni^{2+}, but manganese has slightly lower valance state than Mn^{4+} in Figure 115c. The 2D XANES obtained from TXM shows that $Mn^{3.7+}$ and Ni^{2+} are uniformly distributed throughout the bulk of pristine MNS sample with little variation of manganese. The magnitudes of the Fourier transform extended X-ray absorption fine structure (FT-EXAFS) spectra and their least square fit are shown in Figure 115e-f, reflecting the local environment around manganese and nickel in MNS and MN. The first peak at R=1.5-1.6 Å in Figure 115e-f represents the formation of six coordination in the nearest MnO_6 and NiO_6 octahedra, respectively. The Mn-TM_6 and Ni-TM_6 hexagon contributes to the second peaks around 2.6 Å on *a-b* plane in the second coordination shell, respectively. It should be noted that the FT-EXAFS spectra are not phase corrected, and the bond lengths shown in Figure 115e-f are about 0.3-0.4 Å shorter than the actual bond lengths.

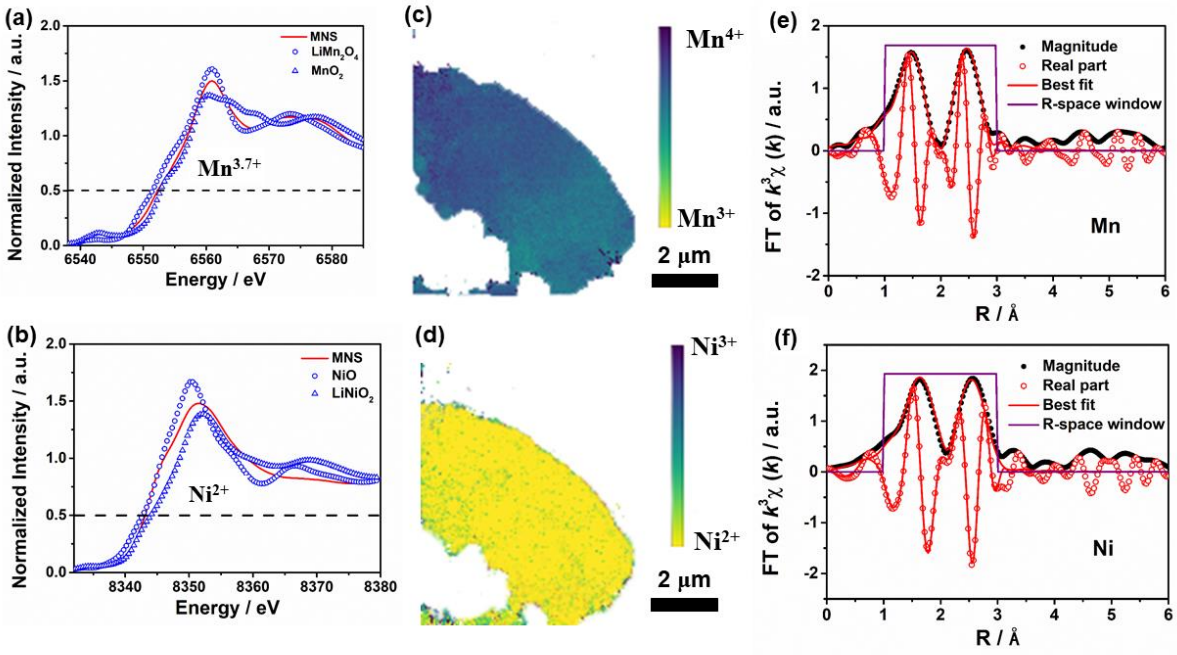

Figure 115. X-ray absorption near-edge spectroscopy (XANES) spectra of the (a) manganese and (b) nickel K-edges of pristine $Na_{0.67}[Mn_{0.61}Ni_{0.28}Sb_{0.11}]O_2$ (MNS) and standard metal-oxide references. The 2D XANES mapping of (c) manganese and (d) nickel in MNS. The least-square fits of the calculated Fourier transform extended X-Ray absorption fine structure (FT-EXAFS) phase and amplitude functions to the experimental EXAFS spectra for (e) manganese and (f) nickel in MNS.

Patents/Publications/Presentations

Publication

- Shin, K. H., S. K. Park, P. Nakhanivej, Y. Wang, P. Liu, S-M. Bak, M. S. Choi, D. Mitlin, and H. S. Park. "Biomimetic Composite Architecture Achieves Ultrahigh Rate Capability and Cycling Life of Sodium Ion Battery Cathodes." *Applied Physics Reviews* 7 (2020): 041410. doi: 10.1063/5.0020805; Publication Date (Web): December 8, 2020.

Task 7.2 – Development of a High-Energy Sodium-Ion Battery with Long Life (Chris Johnson and Khalil Amine, Argonne National Laboratory)

Project Objective. The project objective is to develop a high-energy Na-ion battery with long life. Moreover, the battery chemistry should utilize low-cost materials. The energy density target is 200 Wh/kg and/or 500 Wh/L, wherein the anode and cathode capacity targets are 600 $mAhg^{-1}$ and 200 $mAhg^{-1}$, respectively.

Project Impact. A Na-ion battery on par with the energy density of a Li-ion battery can have a high impact in the transportation sector with the assumption that the cost is significantly below $85/kWh and that the battery pack provides a 300-mile range. The consumer is not concerned about the battery chemistry employed if these metrics can be met. Development of these battery chemistries will situate the United States in a strong position as relates to new low-cost energy storage systems beyond lithium ion.

Approach. In a team approach, the Na-ion battery group will create a versatile Na-ion battery chemistry with beneficial advantages such as low cost, safety, recycling, and sustainability of materials used. The team will work synergistically so that the final design is the culmination of advances in phosphorus carbon composites mated with optimized lead or other highly dense metalloids, such as tin and/or antimony and derivatives thereof, for the recyclable anode. Synthesis and optimization of such blended composite anodes will be conducted in parallel to diagnostic characterization of structures, phase formation, and cycling stability. Cathode work will begin at the end of the first year and will involve gradient cathodes consisting of Fe-Mn compositions, as well as intergrowths of layer stacking sequenced oxides. If resources allow, the team also will attempt to stabilize cathode surfaces using ALD methods, particularly for the benefit of staving off dissolution of manganese and iron / electrolyte reactivity. Electrolytes will be partly procured from H. Li at PNNL.

Out-Year Goals. The state-of-the-art Na-ion battery in the literature has now been surpassed by this team, but performance is still too low for commercialization. Thus, the goal is to move forward and continually invent the most superior Na-ion battery chemistry that can compete worldwide through work output from this project.

Collaborations. Researchers from PNNL who are developing electrolytes for Na-ion batteries will provide this project with formulations to test with the various electrode combinations investigated at ANL.

Milestones

1. Doped RP anode with high specific capacity and stable cycle life. (Q1, FY 2021; Completed)
2. *In situ* characterization of layered cathodes during synthesis; synthesize Ni-based, Fe-based, and Mn-based sodium layered cathodes. (Q2, FY 2021; In progress)
3. Advanced characterization on developed cathodes and anodes during charge/discharge. (Q3, FY 2021; In progress)
4. Performance optimization of synthesized layered cathodes and demonstration of full-cell development using optimal phosphorus anode and developed/commercial cathodes. (Q4, FY 2021; In progress)

Progress Report

This quarter, the team reported that a hierarchical micro/nanostructured Sb-doped RP/carbon anode was developed (carbon type = Ketjenblack/MWCNTs; Figure 116a), which demonstrates extraordinary electrochemical performance with high ICE of ~ 90% and high areal capacity, together with good cycle stability and rate capability.

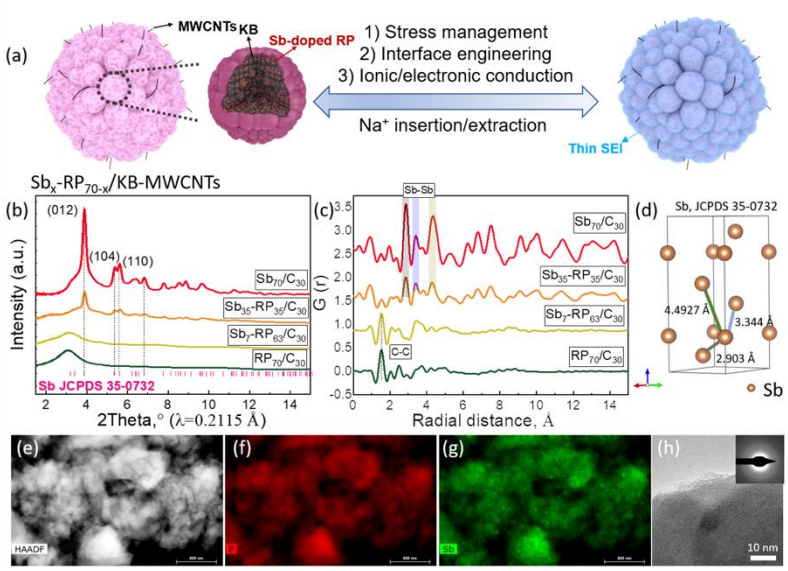

Figure 116. (a) Schematic illustration of the structure of hierarchical micro/nanostructured Sb_x-RP_{70-x}/C_{30} composite before and after cycling. (b) High-resolution X-ray diffraction and (c) pair distribution function data for Sb_x-RP_{70-x}/C_{30} composite. (d) Crystal structure of standard antimony (JCPDS 35-0732) with interatomic Sb-Sb distance index. (e) High-angle annular dark-field imaging transmission electron microscopy image. (f) Phosphorus elemental mapping. (g) Antimony elemental mapping. (h) Selected area electron diffraction pattern of Sb_7-RP_{63}/C_{30} composite.

A series of Sb_x-RP_{70-x}/C_{30} composites was synthesized using high-energy ball-milling (HEBM) process by tuning the weight ratio (x = 0, 7, 35, and 70) between antimony and RP. XRD characterization (Figure 116b) shows that both RP_{70}/C_{30} and Sb_7-RP_{63}/C_{30} composites exhibit amorphous structures, indicating that both RP and Sb_7-RP_{63} have very small particle sizes and are homogeneously distributed in the carbon matrix after HEBM. In contrast, the Sb_{70}/C_{30} and Sb_{35}-RP_{35}/C_{30} composites show obvious antimony diffraction peaks with slight peak broadening, indicating formation of individual antimony nanocrystalline particles in the composites. PDF was further conducted on the Sb_x-RP_{70-x}/C_{30} composites, as it can provide both local and long-range structural information independent of crystallinity. The results in Figure 116c show that both Sb_{70}/C_{30} and Sb_{35}-RP_{35}/C_{30} present clear oscillations and characteristic PDF peaks at 2.9, 3.3, and 4.49 Å, matching well with the interatomic distance of the Sb-Sb bond, as indexed in Figure 116d. In contrast, the RP_{70}/C_{30} and Sb_7-RP_{63}/C_{30} only show oscillations in the low radical distance range (< 6 Å), which confirms their amorphous structure and reveals that the coherent domain size of RP and antimony are smaller than 6 Å. In the case of Sb_7-RP_{63}/C_{30}, not any interatomic distance of Sb-Sb pairs can be observed, which indicates that the antimony exists as an atomic-level dopant in the RP. In a word, a low concentration of antimony could lead to formation of Sb-doped RP, while a high concentration of antimony would result in the formation of Sb/P mixtures. This can be confirmed by the TEM results for Sb_7-RP_{63}/C_{30}, in which both phosphorus and antimony were homogeneously distributed in the composite (Figure 116e-g). The high resolution TEM (Figure 116h) and selected area electron diffraction (SAED) pattern (Figure 116h, inset) further confirm its amorphous structures.

The team found that all of the Sb_x-RP_{70-x}/C_{30} composites demonstrated excellent cycle stability (Figure 117b-c), while the concentration of antimony significantly affected their specific capacity, average working voltage, and rate performance. Figure 117a shows the voltage profiles of the Sb_7-RP_{63}/C_{30} anode at C/3 within 0.02-2.0 V in the conventional carbonate-based electrolytes. Two sloping regions can be observed at about 1.0-0.5 V and below 0.5 V during the sodiation process, corresponding to the sodiation process from P to Na_xP and

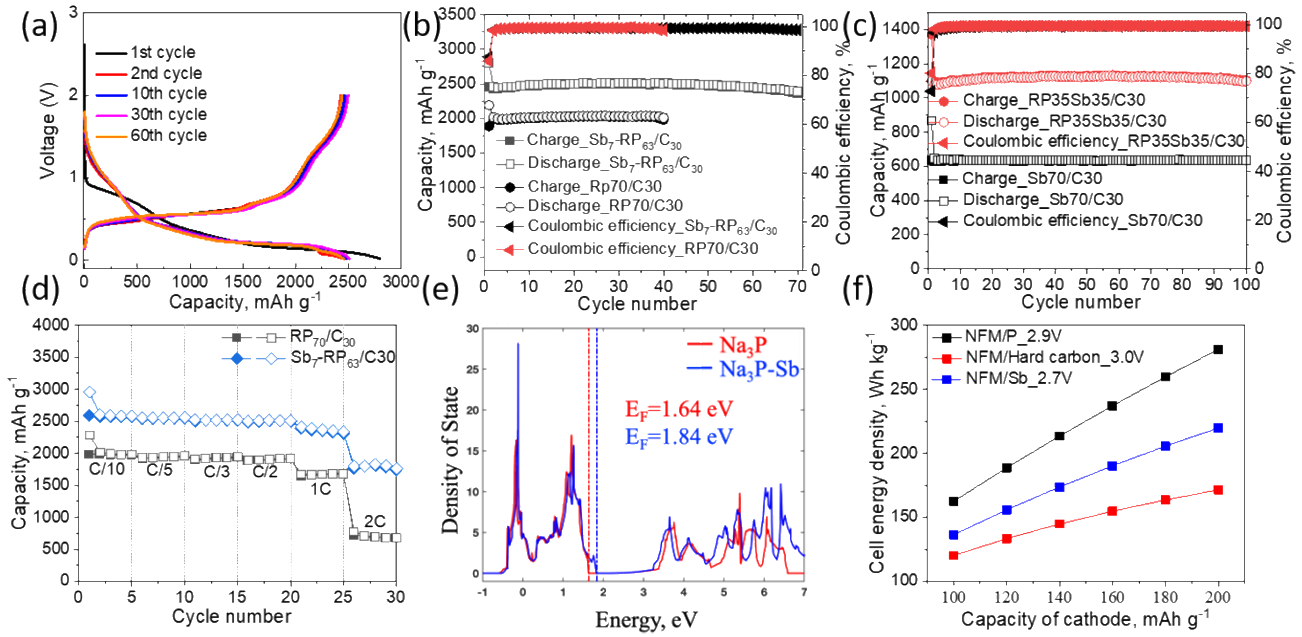

Figure 117. (a) Charge/discharge curves of Sb_7-RP_{63}/C_{30} anode at C/3. (b) Cycling performance of Sb_7-RP_{63}/C_{30} anode at C/3 and RP_{70}/C_{30} anode at C/10. (c) Cycling performance of Sb_{35}-RP_{35}/C_{30} and Sb_{70}/C_{30} anode at C/3. (d) Rate performance of Sb_7-RP_{63}/C_{30} and RP_{70}/C_{30} anode. Open and solid symbols represent discharge and charge capacities, respectively. (e) Density of states distribution of valence electrons for Na_3P and Sb-doped Na_3P. (f) Estimated cell energy density of Na-ion batteries with different anode materials using BatPaC.

eventually Na_3P. In the desodiation process, the charge curves consist of a sloping region at 0.02-0.4 V and an inclined plateau at 0.4-1.0 V, followed by a sloping region up to 2.0 V. The initial discharge and charge capacities of Sb_7-RP_{63}/C_{30} at C/3 were measured to be 2801.3 and 2456.1 mAh g^{-1}, manifesting a high ICE of ~ 88% and an extremely high phosphorus utilization of 95%. The initial irreversible capacity loss (~ 12%) was mainly attributed to decomposition of electrolytes to form the SEI on the surface of Sb_7-RP_{63}/C_{30}.

Sb_7-RP_{63}/C_{30} demonstrates superior cycle stability (Figure 117b), which can still maintain an ultrahigh reversible capacity of 2356.3 mAh g^{-1} (that is, 1650 mAh $g^{-1}_{composite}$) and a high capacity retention of 96% after 70 cycles. The areal phosphorus loading was controlled at around 0.6-0.8 mg cm^{-2}, resulting in an areal capacity loading up to ~ 2 mAh cm^{-2}. The tap density of Sb_7-RP_{63}/C_{30} composite was measured to be ~ 0.7 cc g^{-1}, which thus leads to a high volumetric capacity of 1155 mAh cc^{-1} (1650 mAh $g^{-1}_{composite}$ × 0.7 cc g^{-1}) based on the mass of Sb_7-RP_{63}/C_{30} composite (that is, 1650 mAh cc^{-1} Sb_7-RP_{63}).

As a comparison, the RP_{70}/C_{30} without antimony doping also demonstrates a high ICE of 86% and good cycle stability within 40 cycles at C/10 (Figure 117b). However, its reversible capacities (~ 2000 mAh g^{-1}) are lower than that of Sb_7-RP_{63}/C_{30}, which clearly illustrates that antimony doping can further boost the electronic transport of RP_{70}/C_{30}. As further shown in Figure 117c, Sb_{70}/C_{30} and Sb_{35}-RP_{35}/C_{30} can also deliver a highly reversible capacity of ~ 632 and 1100 mAh g^{-1} within 100 cycles at C/3, respectively. Despite the excellent cycle stability, increasing the content of antimony in the Sb_x-RP_{70-x}/C_{30} leads to decreased specific energy compared to atomic-level antimony doping in Sb_7-RP_{63}/C_{30}. Thus, it is essential to improve the electrochemical performance of an RP-based anode by atomic-level antimony doping.

Figure 117d further compares the rate capabilities of Sb_7-RP_{63}/C_{30} and RP_{70}/C_{30} with the charge/discharge rates ranging from C/10 to 2C. RP_{70}/C_{30} can deliver high specific capacities at low rates (C/10 to 1C). However, the specific capacity at 2C drops to ca. 800 mAh g 1, which is only 40% of that at C/10. On the contrary, the average capacities of Sb_7-RP_{63}/C_{30} at C/10, C/5, C/3, C/2, 1C, and 2C were calculated to be 2572.6, 2544.6, 2513.9, 2500, 2348.7, and 1779 (70% of that at C/10) mAh g^{-1}, respectively, which are all much higher than that of RP_{70}/C_{30}. The team has investigated the benefits of antimony doping on the redox reaction kinetics of RP during sodiation (Figure 117e). As the surface electronic structure of Na_3P is closely related to the sodiation chemistry

of RP, the density of states (DOS) of Na_3P and Sb-doped Na_3P was calculated. As shown in Figure 117e, the Fermi level is shifted up toward the conduction band from 1.64 eV to 1.84 eV through antimony doping. Therefore, it could significantly increase the electronic state to enhance the electron transfer and improve the electronic conductivity. The Argonne Battery Performance and Cost (BatPaC) model (Figure 117f) further showed that compared to hard carbon, the RP-based anodes can significantly increase the cell specific energy of Na-ion batteries. In addition, the cost of RP is cheap. All of the aforementioned results have provided a solid justification that the project's Sb-doped RP anode is a promising practical anode material for Na-ion batteries.

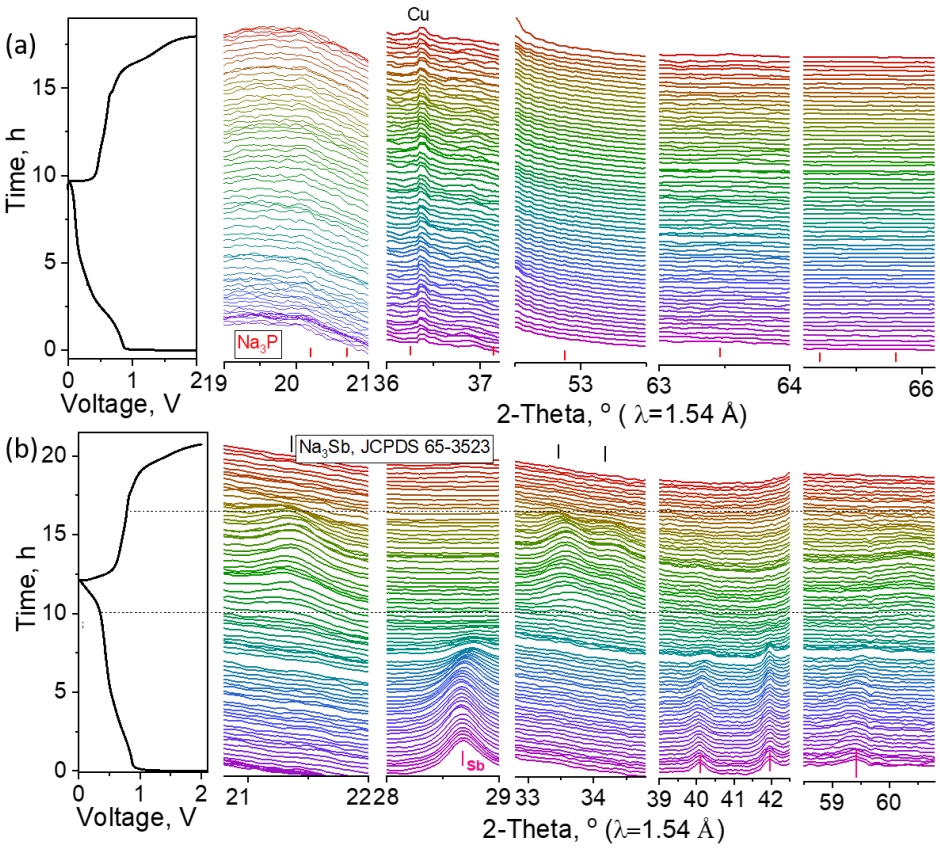

Figure 118. *Operando* high-energy X-ray diffraction (HEXRD) pattern of (a) RP_{70}/C_{30} and (b) Sb_{70}/C_{30} during charge/discharge at C/10 within 0.02-2.0 V. The original synchrotron wavelength (0.1173 Å) was converted into 1.54 Å for a better comparison with lab XRD results.

Phase transformation of alloying-based anodes and the induced parasitic reactions with the electrolytes are another critical factor that can affect electrochemical performance. Therefore, the team further conducted *operando* high-energy XRD to probe the structural evolution of RP_{70}/C_{30} (amorphous) and Sb_{70}/C_{30} (crystalline), the two end products of Sb_x-RP_{70-x}/C_{30} with distinct crystal structures. As shown in Figure 118a, the amorphous structure of RP_{70}/C_{30} was well maintained during the whole discharge/charge process. There is not obvious formation of any crystalline Na_3P during deep discharge of RP_{70}/C_{30} due to the absence of characteristic XRD peaks of Na_3P. In contrast, the crystalline Sb_{70}/C_{30} undergoes a phase transformation from pristine crystalline Sb to amorphous Na_xSb and further to crystalline Na_3Sb during discharge (Figure 118b). Three characteristic peaks of Na_3Sb (JCPDS no. 65-3523) can be clearly observed, which is consistent with the previous *in situ* XRD characterization on bulk antimony electrodes. The formed crystalline Na_3Sb during deep discharge of Sb_{70}/C_{30}, which is more reactive with the electrolytes, results in amorphization of electrode materials when charged back to 2.0 V. Therefore, the distinct phase transformation process of RP_{70}/C_{30} and Sb_{70}/C_{30} during the first charge/discharge has led to a significantly different initial irreversible capacity loss and ICE (86% versus 70%). Future work will focus on using optimal electrolytes and cathodes to develop full cells.

Patents/Publications/Presentations

Publication

- Deng, C., E. Gabriel, P. Skinner, S. Lee, P. Barnes, C. Ma, J. Gim, M. L. Lau, E. Lee,* and H. Xiong.* "Origins of Irreversibility in Layered $NaNi_xFe_yMn_zO_2$ Cathode Materials for Sodium Ion Batteries." *ACS Applied Materials & Interfaces* 12 (2020): 51397–51408.

Task 7.3 – High-Capacity, Low-Voltage Titanate Anodes for Sodium-Ion Batteries (Marca Doeff, Lawrence Berkeley National Laboratory)

Project Objective. The objectives are to understand differences in the sodium intercalation mechanism of various sodium titanate anodes through an array of synthetic, electrochemical, and structural characterization techniques, and to overcome practical impediments to their use, such as the high 1st cycle Coulombic inefficiencies that are currently observed. The ultimate goal is to produce a 200-250 mAh/g anode that cycles reversibly.

Project Impact. Although several suitable cathode materials for Na-ion batteries exist, there are few suitable anode materials due to low potential instabilities. Therefore, sodium titanate variations will be synthesized through different routes to develop materials with various morphologies and dopants. Decreasing the 1st cycle inefficiencies and improving cycling performance will allow enabling technology for a practical high-energy Na-ion battery.

Approach. Candidate stepped layered titanates will be synthesized by appropriate routes (hydrothermal, solid-state, etc.). Materials will then be characterized electrochemically and physically. Structure-function relationships will be built to correlate the effect of changing structure (for example, step size) on electrochemical properties.

Out-Year Goals. A series of synchrotron characterization techniques will be used to further develop sodium titanate anode materials with stable cycling while delivering high capacities.

Collaborations. TXM is done in collaboration with Y. Liu (SSRL). Synchrotron hard, soft XAS, and X-ray Raman efforts are in collaboration with D. Nordlund and D. Sokaras (SSRL). Electrolyte design is done in collaboration with K. Xu (ARL).

Milestones

1. Characterize lepidocrocite titanates. (Q1, FY 2021; Completed)
2. Optimize electrode. (Q2, FY 2021; In progress)
3. Assemble, test, and study full cells. (Q3, FY 2021; In progress)
4. *Go/No-Go Decision*: On lepidocrocite titanate, stop if problems are not solved. (Q4, FY 2021)

Progress Report

The team previously reported on the long-term cycling performance of lepidocrocite titanate $Na_{0.74}Ti_{1.815}O_4$, which showed 75.3% of the 2nd discharge capacity retention after 38 cycles. The capacity loss was attributed to the presence of residual structural and physiosorbed water. To check this hypothesis, this quarter, the $Na_{0.74}Ti_{1.815}O_4$ phase was dehydrated at elevated temperatures (ranging from 60°C to 800°C). XRD data show that, in addition to the water removal, the material gradually transforms into a new phase on heating to 600°C and eventually decomposes into $Na_2Ti_6O_{13}$ above 700°C (Figure 119a). FTIR-ATR spectroscopy reveals negligible hydroxyl groups in the 350°C-dehydrated sample and no hydroxyl groups for the 500°C-dehydrated and 600°C-dehydrated samples, suggesting that the dehydrated phase is not hygroscopic. Synchrotron XRD, Raman spectroscopy, and TEM analyses are ongoing to determine the structure of the dehydrated phase. Figure 119b presents the electrochemical performance of the 500°C-dehydrated sample (purely dehydrated phase). This phase needs to be discharged to lower voltages than the material dried at lower temperatures to ensure full electrochemical activation. When cycled between 0.1 and 2.0 V versus Na^+/Na, the discharge capacity is only 64 mAh g^{-1} on the 2nd cycle, but increases during subsequent cycles (cyan curve in Figure 119b). By lowering the discharge voltage cutoff to 0.05 V versus Na^+/Na from the 2nd cycle on, an increased capacity of
ca. 214 mAh g^{-1} is achieved by the 4th discharge. However, capacity fading is also noticeable, down to 90% of the 4th discharge capacity retention after 18 cycles (green curve in Figure 119b). Side reactions (for example, electrolyte decomposition) would be more drastic at low voltages; for this reason, the lower voltage limit was increased to 0.1 V from 0.05 V versus Na^+/Na after the 1st cycle. Notably, this protocol results in very stable cycling: full capacity retention of 185 mAh g^{-1} over 20 cycles (blue curve in Figure 119b). A comparison of the discharge capacity retention of $Na_{0.74}Ti_{1.815}O_4$ dehydrated at 60°C (purely the hydrated phase), 100°C (mainly the hydrated phase with small portion of dehydrated phase), 350°C (a mixture of dehydrated and hydrated phases) and 500°C (purely the dehydrated phase) is presented in Figure 119c. The results reveal that the hydrated phase offers higher initial capacities, but fades more rapidly; in contrast, the dehydrated phase cycles better, but has lower initial capacity.

Work the next quarter will be partly focused on determining the structure of the dehydrated phase. Synchrotron XRD, Raman spectroscopy, and TEM are in progress. Meanwhile, the possibility of directly synthesizing the dehydrated phase will be explored.

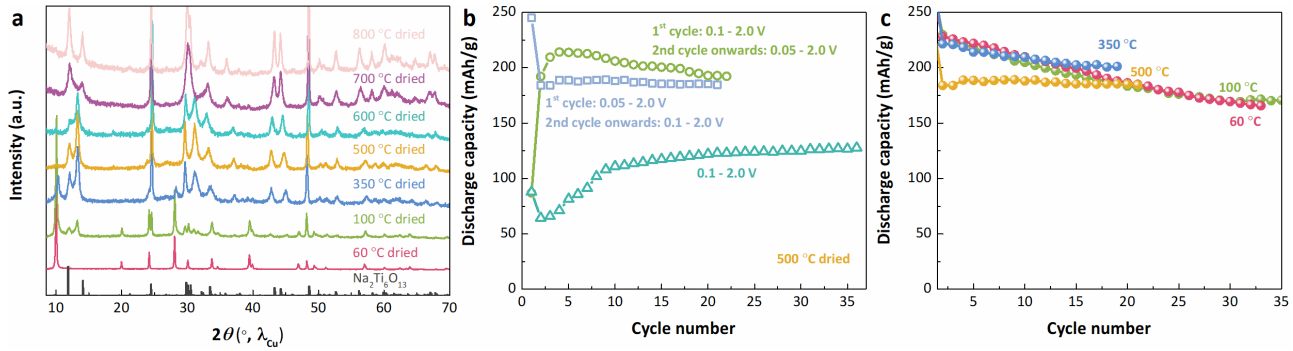

Figure 119. (a) Powder X-ray diffraction patterns of $Na_{0.74}Ti_{1.815}O_4$ annealed under air at different temperatures from 60°C to 800°C. (b) Discharge capacity of 500°C- annealed $Na_{0.74}Ti_{1.815}O_4$ cycled in different voltage regions. (c) Comparison of discharge capacity retention of $Na_{0.74}Ti_{1.815}O_4$ annealed at different temperatures. All the cells were cycled in sodium half-cell configurations at current rate of 8 mA g^{-1} with 0.5 M $NaPhB_4$/DEGDME electrolyte.

Patents/Publications/Presentations

Presentation

- MRS Spring/Fall 2020 Meeting, Virtual (November 27 – December 4, 2020): "Optimization of Titanate Anodes for Sodium Ion Batteries"; M. M. Doeff. Invited.

Task 7.4 – Electrolytes and Interfaces for Stable High-Energy Sodium-Ion Batteries (Ji-Guang Zhang, Pacific Northwest National Laboratory)

Project Objective. The Na-ion battery is a potential alternative energy source for EVs and grid applications due to the low cost and the natural abundance of sodium. The performance of Na-ion batteries largely depends on development of electrode materials and electrolytes. In recent years, a series of potential electrode materials has been developed. However, a fundamental understanding of the electrochemistry of Na-ion batteries, especially the stability of the electrode-electrolyte interface in these batteries, is still not well established. This project will develop innovative electrolytes to enable fundamental understanding on the interface between electrode and electrolyte for stable operation of high-energy Na-ion batteries. A high-capacity anode will also be developed. The proposed research will enhance the achievable capacities of both anode and cathode for Na-ion battery and improve the stability of electrodes/electrolyte interface, establish correlation (electrolyte design rule) between electrochemical performances of Na-ion batteries and the electrolyte/interface properties, and enable long cycle life and safe operation of high-energy Na-ion batteries.

Project Impact. Success of this project will provide a solid understanding on the electrolyte/electrode interphase of Na-ion batteries and significantly improve their energy density, cycle life, and safety. It will also accelerate the practical application of Na-ion batteries in both EV and stationary energy storage.

Approach. This project will optimize the electrolyte components and concentrations to develop innovative electrolytes and additives with improved electrochemical and physical properties. Ether-based electrolytes with different salt will be optimized toward both anode (sodium metal and hard carbon) and cathode. Phosphate-based LHCE will be optimized to improve cycling performance of Na-ion batteries. SEI/CEI components of Na-ion battery in ether and phosphate electrolytes will be studied using XPS and SEM/TEM techniques to reveal the fundamental mechanism behind the improved stable performance of Na-ion batteries. Electrolyte additives in carbonate electrolyte will also be investigated to improve the electrochemical cathode performance. These approaches will unravel the origin of the SEI at the dynamic interface, providing guidance for the electrolyte and interface design and enabling high capacity and long life of Na-ion batteries.

Out-Year Goals. This project will select the electrolyte compounds and identify the formation of interfacial SEI layer on hard carbon and CEI layer-on-layer oxide cathode and its effect on the electrode materials. It will also provide guidance on electrolyte optimization and to improve CE of sodium deposition/stripping to be more than 99%.

Collaborations. This project will collaborate with ANL, LBNL, and other leading scientists in the field of cathode and anode materials for Na-ion batteries. It will also collaborate with C. Wang and M. Engelhard of PNNL for TEM and XPS characterization.

Milestones

1. Develop high-capacity carbon anodes in Na-ion batteries with optimized electrolytes. (Q1, FY 2021; Completed, December 31, 2020)
2. Develop high-voltage electrolytes (≥ 4.2 V) to increase energy density of Na-ion batteries. (Q2, FY 2021)
3. Characterize CEI/SEI interphase properties in optimized electrolyte to probe the mechanism of high-voltage cycling stability of Na-ion batteries. (Q3, FY 2021)
4. Develop electrolytes that are compatible with conventional polymer separators. (Q4, FY 2021)

Progress Report

Last quarter, a novel carbon anode with a record specific capacity was developed by CVD coating of soft carbon (using acetylene precursor) on two porous carbon precursors with 1- and 2-nm pore size, respectively. Table 10 summarizes the preparation conditions, physical properties, and electrochemical properties of the anode samples prepared by this approach. With the same porous carbon precursor, the desodiation capacity and 1st efficiency of the final electrode material increase with the increasing CVD deposition temperature. The difference on pore size of precursor does not affect the 1st discharge capacity (489 mAh/g for AC-4b versus 487 mAh/g for PC-4b), although AC-4b sample exhibits lower sodiation potential than those of PC-4b (Figure 120a). However, the capacity retention of AC-4b at high rate is much poorer than that of PC-4b, as shown in Figure 120b. This is because the sodiation potential of AC-4b is too close to the cutoff potential (5 mV), and the sodiation step is consequently interrupted even at small polarization.

Table 10. Effect of synthesis conditions on the physical/electrochemical properties of carbon anode.

Sample	Pore size of carbon precursor (nm)	CVD temperature (°C)	Helium true density (g/cm^3)	Porosity (%)	1st desodiation capacity (mAh/g) (5 mV – 2 V)	1st Coulombic efficiency (%)
AC-2b	1	800	1.29	42.9	444	83
AC-3b	1	900	1.51	33.2	460	87
AC-4b	1	920	1.49	34.1	489	88
PC-4b	2	920	1.48	34.5	487	85

The carbon anode (PC-4b) with record capacity and excellent rate capability has been further evaluated in sodium full cells with NaNMC(O3- $NaNi_{0.68}Mn_{0.2}Co_{0.10}O_2$) cathode (85 wt% AM : 8 wt% SP : 7 wt% PVDF) and compared with the baseline cells with the commercial Kuraray carbon anode (type 2, particle size ~ 9 μm). A LHCE [NaFSI-TEP/TTE (1:1.5:2 in molar ratio)] is used to improve cycling stability of the cells. The cells with PC-4b anode demonstrate an initial discharge capacity of ~ 440 mAh/g, with the 1st CE of 79%; the cells with Kuraray hard carbon anode only deliver a reversible capacity of 202 mAh/g and a lower 1st CE value of 69% (Figure 121). A full cell using PC-4b anode exhibited a capacity of twice as much as that using Kuraray hard carbon anode (Figure 121b). After 400 cycles, PC-4b based full cell still retains a capacity of 70%, as compared to 65% capacity retention for the cells with Kuraray carbon anode. To explain the superior performance of the synthesized carbons developed in this work, its microstructure will be further characterized to have a deeper understanding on the electrochemical kinetics related to the Na-ion storage mechanism.

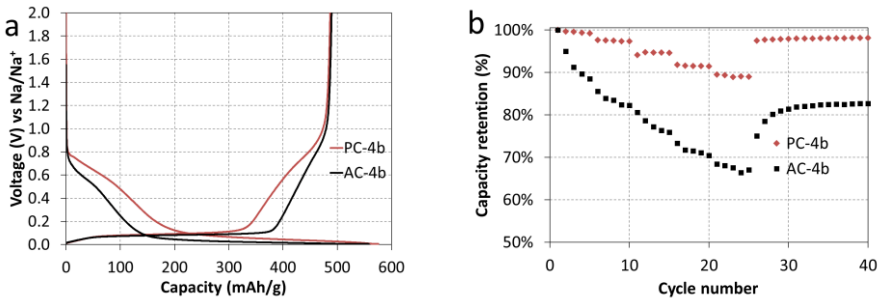

Figure 120. (a) 1st cycle voltage profile and (b) rate performance of PC-4b and AC-4b in sodium half-cell (90 wt% AM: 5 wt% SP: 5 wt% PAA) performed in a potential range of 5 mV - 2 V with 1 M $NaPF_6$ in EC/DMC (1:1 in weight) as electrolyte.

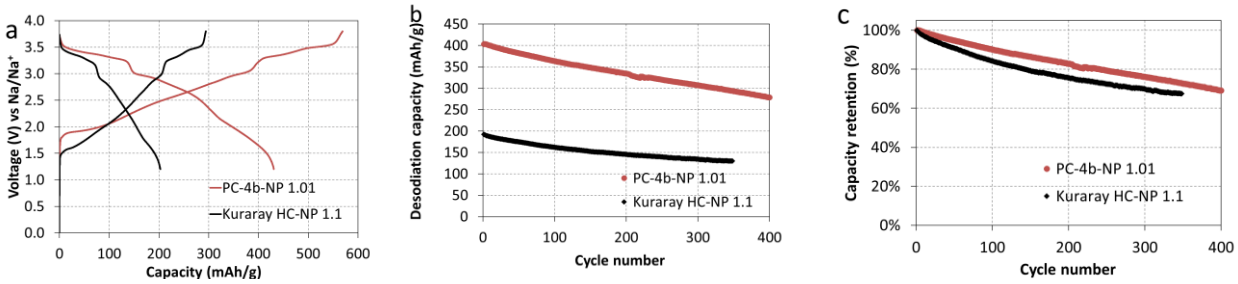

Figure 121. (a) Voltage profile. (b) Cycling capacity. (c) Coulombic efficiency of PC-4b||NMC full-cell (N/P = 1.01) compared to Kuraray HC||NMC full cells (N/P = 1.1), using NaFSI-TEP/TTE electrolyte (1:1.5:2 in molar ratio). Both pristine cathode and anode are used without any pretreatment or presodiation. The operated voltage window is 1.2-3.8 V; the 1st formation C rate is 0.1C, and cycling C rate afterward is 0.33C.

Patents/Publications/Presentations

The project has no patents, publications, or presentations to report.

Innovation Center for Battery500
(Jun Liu, Pacific Northwest National Laboratory; Yi Cui, Stanford University)

Project Objective. The project aims to develop commercially viable lithium battery technologies with a cell-level specific energy of 500 Wh/kg through innovative electrode and cell designs that enable the extraction of the maximum capacity from advanced electrode materials. In addition to achieving high specific energy, the project aims to be able to achieve 1,000 cycles for the developed technologies.

Project Impact. The Battery500 Consortium will develop next-generation lithium battery technologies that will significantly increase energy density, improve cycle life, and reduce cost. This will greatly accelerate deployment of EVs and reduce carbon emission associated with fossil fuel consumption. The consortium will utilize first-class expertise and capabilities in battery research in the United States and develop an integrated and multi-disciplinary approach to accelerate development and deployment of advanced electrode materials in commercially viable high-energy batteries. The advances made in this consortium will also benefit the improvement of current Li-ion battery technologies.

Approach. This project will utilize an assortment of national resources located at the national laboratory level and university level. The lithium anode combined with a compatible electrolyte system and two cathodes—one high-Ni $LiNi_xMn_yCo_zO_2$ and another sulfur—will be studied and developed to reach high energy density. The project focus is to design novel electrode and cell architectures to meet the 500 Wh/kg goal. The consortium will work closely with R&D companies, battery/materials manufacturers, and end users / OEMs to ensure that the developed technologies are aligned with industry needs and can be transitioned to production.

Out-Year Goals. This project aims for the following out-year goals. First, fabricate and test a pouch cell capable of 350 Wh/kg and 350 cycles. Second, fabricate and test a pouch cell capable of 400 Wh/kg and 100 cycles.

Collaborations. Collaboration among consortium team members will be well coordinated by the leadership team, which includes the keystone project leads and co-leads along with PIs at all member institutions. Collaboration with the community outside of this consortium and with industry will be facilitated by the executive committee, the advisory board, and the industry committee.

Milestones

1. Benchmark Li-anode architecture with 50-micron lithium anode using protocols for 350 Wh/kg cells, and achieve over 200 cycles in coins. (Q1, FY 2021; Completed)
2. Optimize pressure effect for Li-S from coin cells. (Q2, FY 2021; In progress)
3. Provide new electrolyte formulation for Li-S (PNNL). (Q3, FY 2021; In progress)
4. Demonstrate 350 Wh/kg pouch cell with > 450 cycles; 400 Wh/kg > 100 cycles; and > 450 Wh/kg pouch cell. Demonstrate good cycling of Li-S pouch cell 300 Wh/kg. (Q4, FY 2021; In progress)

Progress Report

Keystone Project 1: Materials and Interfaces

The goal of Keystone 1 is to provide the materials and chemistry support for Keystone projects 2 and 3. This quarter, a new baseline electrolyte, TTE-based LHCE of LiFSI-1.2DME-3TTE, has been recommended and adopted for the program (PNNL); it has been shown to work with a 94% nickel cathode under 4.4 V (UT Austin and PNNL), and its structure has been refined (SLAC). The LHCE with less DME has been demonstrated to be stable at 4.5 V on LCO cathode (PNNL). Another ether-based electrolyte has also been found to be effective and very stable (Stanford), and it was cycled against high-Ni NMC. Coatings on high-Ni NMC have been found to be effective for reducing both surface impurities and the 1st cycle loss (UT Austin and Binghamton). Lattice substitution has been found to be effective in capacity retention on long-term cycling (Binghamton). Next quarter, the impact of coatings and substitution will be evaluated in these two electrolytes.

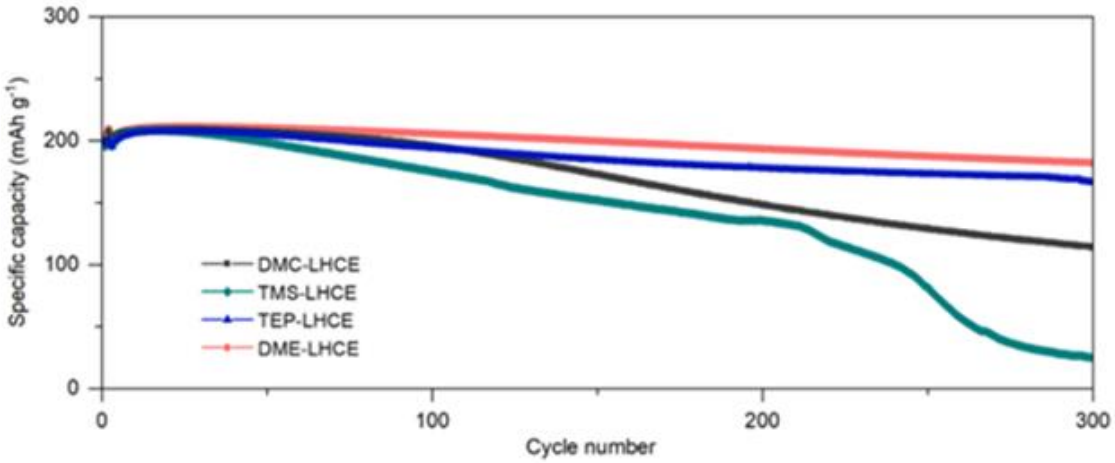

Figure 122. Comparison of cycling performances of Li||NMC-811 cells using localized high concentration electrolytes with different solvating solvents in the voltage range of 2.8-4.4 V at C/3 charge/discharge rates after two formation cycles at C/10 rate.

The PNNL group has identified the optimum solvating and diluting solvents for LHCEs. They found that DME was the preferred solvating solvent over organic phosphate (TEP), carbonate (DMC), and sulfone (TMS), as shown in Figure 122. After 100 cycles of NMC-811, it had the minimum population of cracked particles, and the least rock-salt layer formation and CEI formation [*Proceedings of the National Academy of Sciences of the United States of America* 117, No. 46 (2020): 28603]. They also found that the LHCEs with diluents TTE and TFEO formed the most effective CEI, while also producing the lowest cation mixing after 100 cycles. Based on cost and availability of TTE and TFEO, it was therefore recommended that the electrolyte LiFSI/DME/TTE can be used as a baseline electrolyte for high-Ni NMC cells in the consortium.

The PNNL group further evaluated the ether-based LHCE, LiFSI-DME-3TTE (by mol.), in Li||LCO batteries under the high charge cutoff voltage of 4.5 V and in a wide temperature range from -30 to 55°C, with the comparison to the baseline electrolyte. The LHCE allows the cells to maintain 92.9% of initial capacity after 300 cycles (or ~ 80% after 800 cycles) at 25°C, 83.6% after 300 cycles at 45°C, and 81.3% after 200 cycles at 55°C. However, the baseline electrolyte leads the cells to show continuous capacity fading at 25°C, only exhibiting a retention of 36% after 200 cycles. Significantly accelerated capacity decay is observed at 45°C, and the average cell CE is only 97.1% for the first 100 cycles, which means that the side reactions are more pronounced under the elevated temperature.

Recent work at SLAC and PNNL provides insight into the microscopic view of the LHCE and key interactions between electrolyte components by synchrotron X-ray scattering and AIMD (Figure 123). Although good miscibility between the solvating solvent (DME) and the diluent (TTE) is observed macroscopically during mixing, X-ray scattering reveals the presence of nanoscale phase segregation in pure solvent-diluent solutions. In contrast, when HCE is diluted with TTE, no such phase segregation is evident, highlighting the importance of considering interactions between free diluent and bound solvent molecules. These insights provide new information for further understanding the intermolecular interactions in advanced Li-metal battery electrolytes and will help guide the design of future LHCE systems.

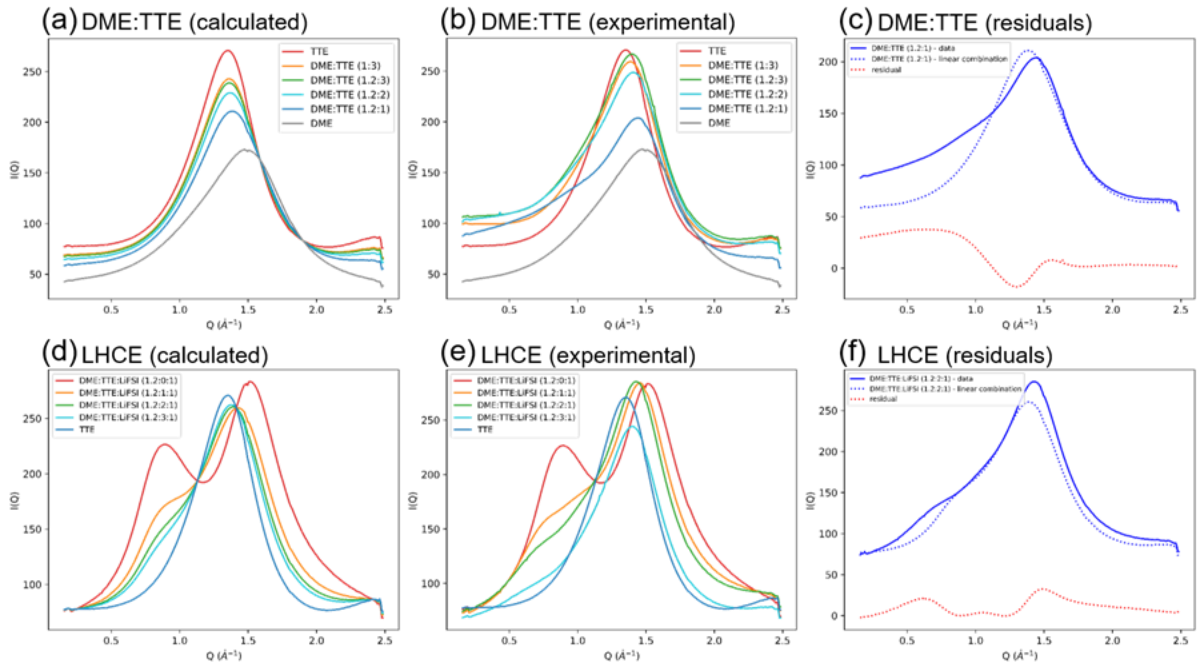

Figure 123. (a) Simulated X-ray scattering data for mixtures of DME and TTE generated using linear combinations of experimental scattering data for DME and TTE. (b) Experimental scattering data of mixtures of DME and TTE in different ratios. (c) Example of residual analysis for DME-TTE mixtures, where subtraction of simulated linear combination data (dotted blue line) from experimental data (solid blue line) shows excess scattering at low Q (dotted red line), indicative of nanoscale (ca 1-2 nm) phase separation. (d) Simulated scattering data for localized high concentration electrolytes (LHCEs) generated using linear combinations of experimental scattering data for HCE and TTE. (e) Experimental scattering data for different HCE:TTE ratios. (f) Example of residual analysis for LHCEs, where subtraction of simulated linear combination data (dotted blue line) from experimental data (solid blue line) shows no excess scattering at low Q (dotted red line), indicating no nanoscale phase separation in LHCE cycled at C/10 rate.

The Stanford group has identified a rationally designed electrolyte solvent ether molecule, FDMB, which is very stable relative to lithium metal and to high voltages such as those found in high-Ni NMC. The results are shown in Figure 124. The upper figure shows the excellent behavior of the electrolyte using LiFSI salt in FDMB, compared with that of using LiFSI in DMB and DME as well as of $LiPF_6$ salt in a carbonate electrolyte. The CE of this new electrolyte in Li||NMC-532 cell is over 99.98%. The lower figure shows excellent behavior for a range of high-Ni NMCs, 811, 622, and 532.

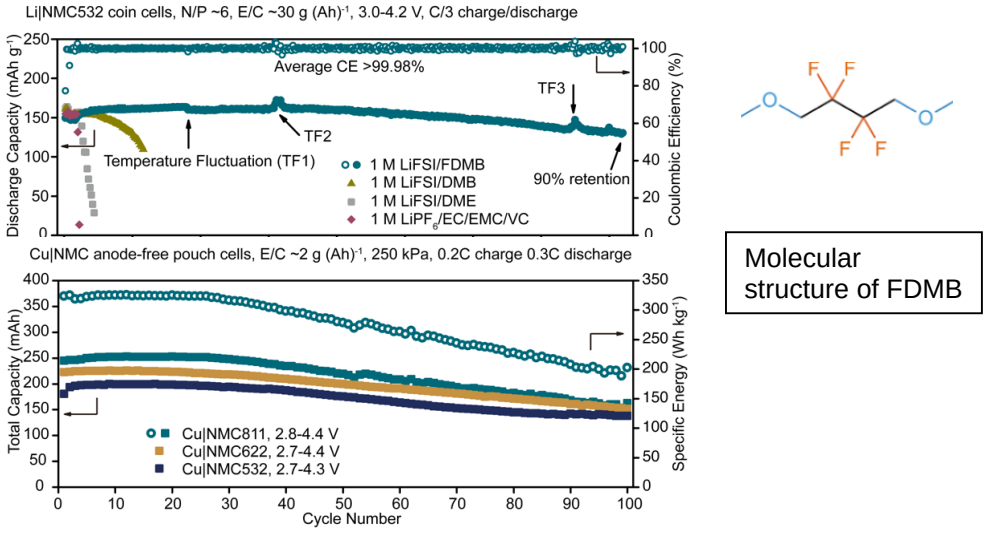

Figure 124. Behavior of the new FDMB ether electrolyte, showing (upper) relative to other electrolytes, and (b) for three high-nickel NMC cathodes.

Researchers at Binghamton studied a Li-free niobium oxide treatment of NMC-811 cathode to determine the impact of coating and lattice substitution. The use of a Li-free treatment allowed for removal of any surface carbonate species forming Li-Nb-O species. This treatment at a 1% niobium level decreased the 1st cycle loss, as shown in Figure 125a; it was found that the niobium was predominantly on the surface and in the surface layers when heated at 400°C and 500°C. In contrast, at higher temperatures it diffuses into the bulk of the material. For the latter, the impact is much less on the 1st cycle. Rate capability is also improved by this surface treatment (Figure 125b). However, long-term cyclability is improved when the niobium substitutes in the lattice, as shown in Figure 125c. These studies will be repeated using the newly adopted LHCE electrolyte system.

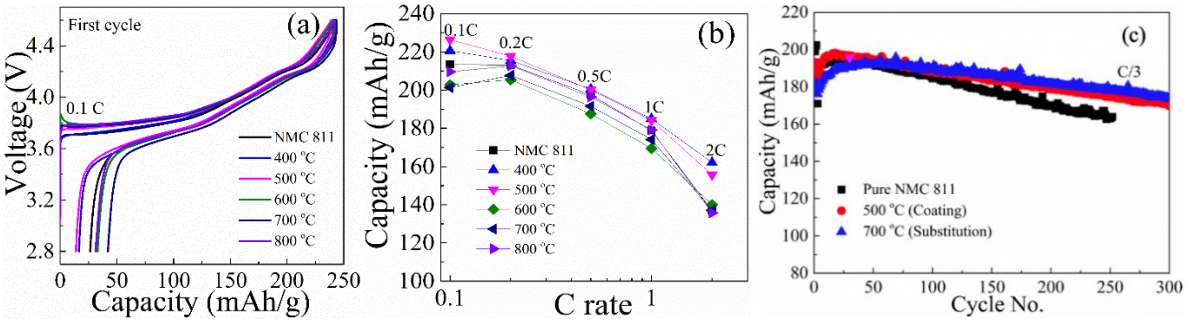

Figure 125. Impact of a NbO_y treatment of NMC-811. (a) Reduction of 1st cycle loss by surface treatment, 400°C and 500°C; (b) improved rate capability of surface treated material; and (c) bulk treated material, which shows the highest capacity retention. (a-b) Charged to 4.6 V. (c) Charged to 4.4 V.

Researchers at UT Austin have synthesized the very-high-Ni cathode $LiNi_{0.94}Co_{0.06}O_2$ (NC) and provided samples to the team. They found that a phosphoric acid treatment protected the surface from residual lithium formation on long standing in an air environment. The H_3PO_4 scavenges residual lithium species from the surface, as shown in Figure 126. The H_3PO_4-treated samples (PNC) maintain good morphology after exposure to air for 450 days compared to the untreated samples (NC), as indicated by SEM. The H_3PO_4-treated samples also show a thinner rock-salt layer (~ 3 nm) after long-term cycling than the untreated samples (~ 15 nm), as indicated by TEM. Treatment with ^{18}O isotope-labeled H_3PO_4 reveals the protection of the cathode surface by the formation of Li_3PO_4, as indicated by TOF-SIMS. Collaborators at PNNL have found that their new LHCE works very well with this high-Ni cathode at 1C rate, as shown in Figure 127; its behavior is much better than that in the former carbonate baseline electrolyte.

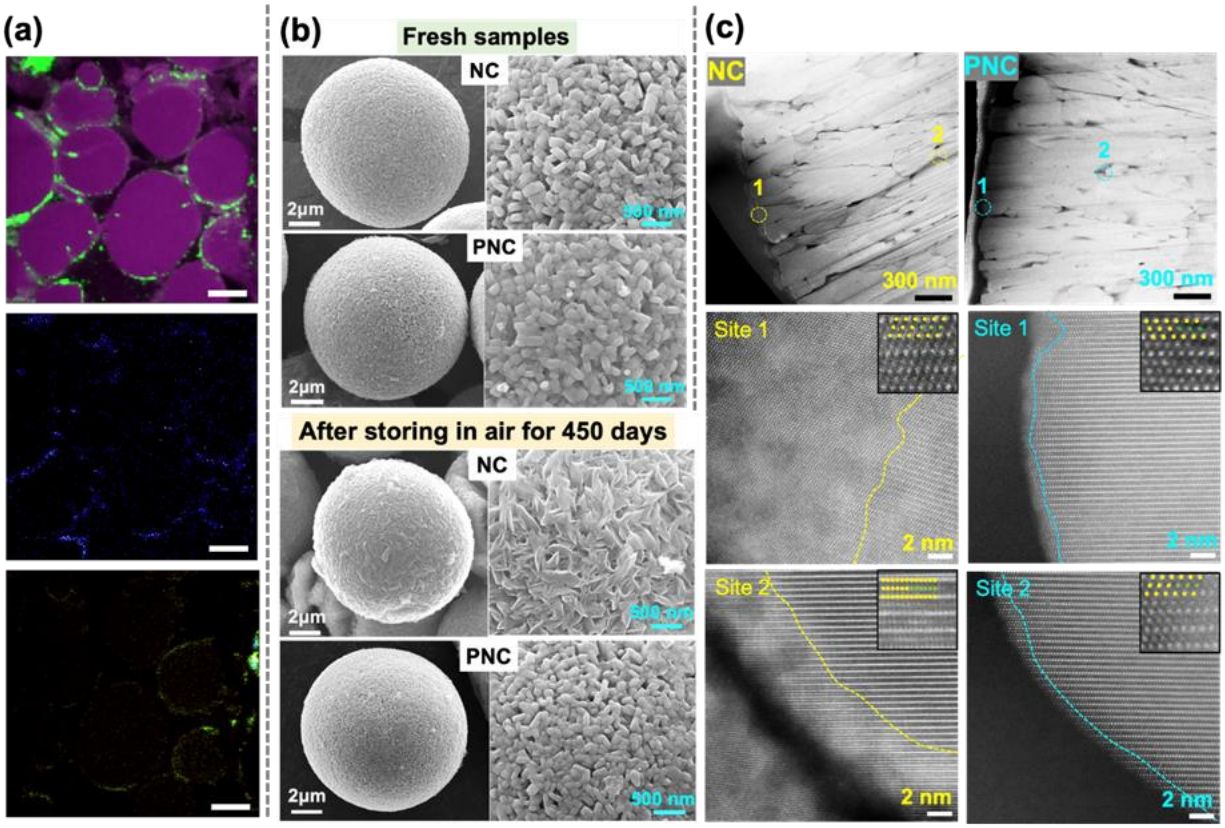

Figure 126. H_3PO_4 scavenges residual lithium and protects the surface with Li_3PO_4, as revealed by time-of-flight secondary-ion mass spectroscopy with ^{18}O labeling. The H_3PO_4-treated sample (PNC) forms a thinner rock-salt layer (~ 3 nm) than the untreated sample (NC) (~ 15 nm). The purple and green colors in the top of (a) represent, respectively, $^{16}O^-$ and $^{18}O^-$ species; the blue color in the middle of (a) represents $P^{18}O_2^-$ species; and the green color in the bottom of (a) represents $Li_2{}^{18}O^+$ species. The scale bar in (a) is 10 μm.

In collaboration with UT Austin, the Idaho National Laboratory (INL) team has used the electrochemical analytic diagnosis technique to analyze the capacity retention and fading behavior between two NMC-811 cathode active materials of different particle sizes and morphologies, as shown in Figure 128a. The larger 12-μm size particles are meatball shape with primary particles on the order of 200 nm, similar to those that constitute the small primary particles with intertwined coils of irregular shape. Figure 128b shows the IR-free voltage ($V_{IR\text{-}free}$) versus SOC curves in the charge regime at Cycle 15 for the two electrodes made of these two different types of NMC-811 particles with the same loading. Between 80-50% SOC, the two charging $V_{IR\text{-}free}$ profiles are in excellent agreement with the pseudo-OCV versus SOC curve. Such an excellent voltage versus SOC correspondence indicates that in this compositional range, the lithium intercalation kinetics is quite reversible and consistent with what the team would expect from a phase transition as depicted in the

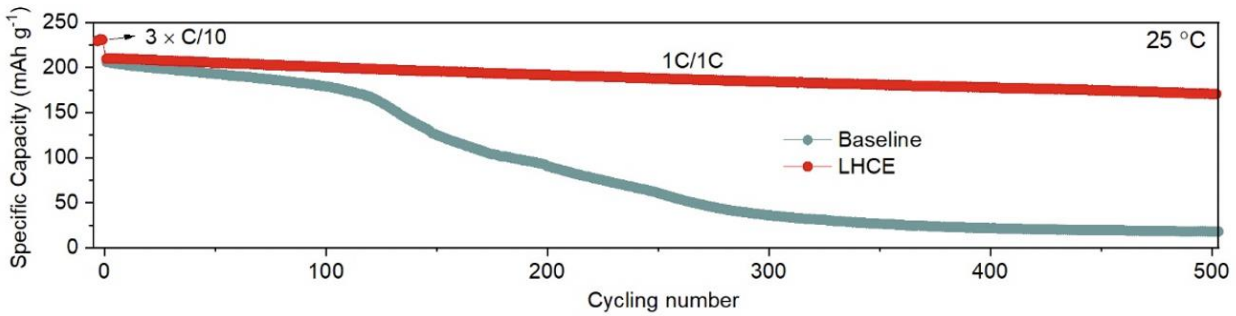

Figure 127. Cycling of $Li||LiNi_{0.94}Co_{0.06}O_2$ cells in prior baseline electrolyte compared with that in localized high concentration electrolytes.

pseudo-OCV versus SOC correlation, independent of particle size and morphology. Below 30% SOC, the charging profile of the electrode made of 12-µm size particles (the curve in red) deviated from this correlation, while the profile of the small particle electrode remains in accordance. The kinetics associated with lithium diffusion in NMC-811 particle in the low SOC region does exhibit particle-size dependence. This difference is represented in Figure 128c, where the initial capacity of the small particle electrode is larger than that of the 12-µm size particles in the formation process, indicating the small particles can release capacity in a more facile manner than the 12-µm particles. On 1st cycle aging, the small particles show a larger 1st cycle capacity loss than the 12-µm particles, as well as a high rate of capacity loss in charge retention. Although one can attribute this capacity fade to more SEI formation on the small particles, the incremental capacity (dQ/dV) analysis on the cycling behavior indicates that phase composition change and site occupancy rate may vary in the NMC-811 particles in the cycle aging, as well that caused the efficiency in charge retention in disparity with particle size dependence. The INL diagnostic and dQ/dV analyses could reveal critical information and provide much more detailed insight of the degradation of cathode active material to complement the physicochemical characterizations.

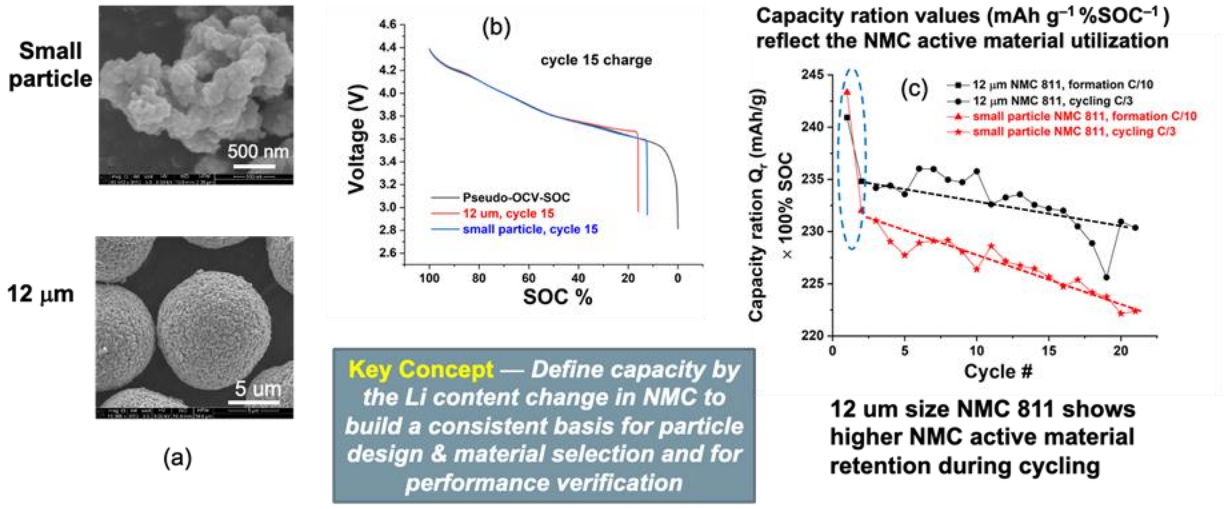

Figure 128. Electrochemical diagnostic analysis and characterization by Idaho National Laboratory to uncover utilization and degradation of cathode active material.

Highlights of Keystone Project 1

The highlights for this quarter are as follows:

- A TTE-based LHCE, with the formulation LiFSI-1.2DME-3TTE, has been recommended as the new baseline electrolyte for the Battery500 program (PNNL). It works very well with very-high-Ni cathodes. The analog LHCE with less DME can be stable at 4.5 V.
- A very stable (both to lithium and high voltages) ether-based electrolyte using the FMDB solvent has been discovered and tested against high-Ni NMCs (Stanford).
- Niobium substitution has been found to reduce the loss of capacity on extended cycling of high-Ni NMC (Binghamton).
- Phosphate and niobium coatings on high-Ni NMC have been found to be effective in reducing both the impact of surface impurities and the 1st cycle loss (UT Austin and Binghamton).

Keystone Project 2: Electrode Architecture

The aim of the Keystone 2 is to design, model, fabricate, and characterize the effects of electrode architecture on electrode and cell performance to achieve the goal of 500 Wh/kg specific energy at cell level. Included in this report for Keystone project 2 are lithium concentration profiling in cathodes (INL and BNL), electrode characterization and electrolyte optimization for polymeric sulfur (UCSD and PNNL), and the evaluation of carbon-based host for lithium metal (University of Washington, UW). Highlighted this quarter are recent advancements in the demonstration of electrochemical analytic diagnosis (eCAD) in lithium concentration profiling in the cathode active materials, compositional characterization and electrolyte evaluations for polymeric sulfur, and the electrolyte effects on the performance of carbon-based host for lithium metal.

Lithium Concentration Profile in the Cathode Active Materials

The INL eCAD and BNL *in situ / operando* synchrotron XRD characterizations have been used to understand how variants in the electrode architecture design affect cell performance, to understand utilization and degradation of cathode active material, and to identify barriers in electrode design.

BNL has developed an *in situ / operando* characterization method with the capability to use synchrotron XRD techniques to probe the lithium concentration profile in the cathode active materials during charging and discharging process over the electrode surface area (lateral mapping) or along the thickness of the electrode (depth profiling). With the lattice parameters refinement, the lithium concentration profile can be determined as a function of the location on the cathode surface and/or along the thickness. The lithium concentration profile can be further inferred as SOC dependence with spatial resolutions.

In collaboration with BNL, the INL team has used the eCAD technique to analyze the BNL charging-discharging voltage profiles, as shown in Figure 129a, for the lateral mapping of the lithium concentration distribution on the cathode surface at three different degrees of discharge in capacity or SOCs. The SOC values so determined by the XRD lattice parameters refinement and eCAD showed excellent agreement, within the resolution of the experiments and the precision in methods of determination. Figure 129b shows (1) the cell configuration for the depth profiling, (2) comparison of the voltage profiles of the discharge curves obtained in the depth profiling experiments versus the pseudo-OCV versus SOC curve used in the eCAD analysis to align the lithium concentration profile for the SOC determination using eCAD technique, and (3) SOC profiles during charge-discharge cycles in the formation process at C/10, cycle at C/5 rate, and cycle at 0.4C rate. During the formation, the C/10 rate SOC profiles determined by eCAD and XRD refinement, respectively, are in great agreement. The agreement indicates that the two methods, as shown in the lateral mapping, are complementary to each other with excellent accuracy. At C/5, a small but noticeable disparity began to appear. Such a discrepancy becomes substantial at 0.4C, as the lithium concentration distribution in the depth profiling broadens. Despite such a discord in the SOC inferences, the complementary information from each technique provides better perspective on how electrochemical information would be affected by the electrode architecture and design, and how the physicochemical information from characterizations can enhance the understanding of the underlying mechanism in affecting the cell performance, which is critical to success in achieving Battery500 project goals.

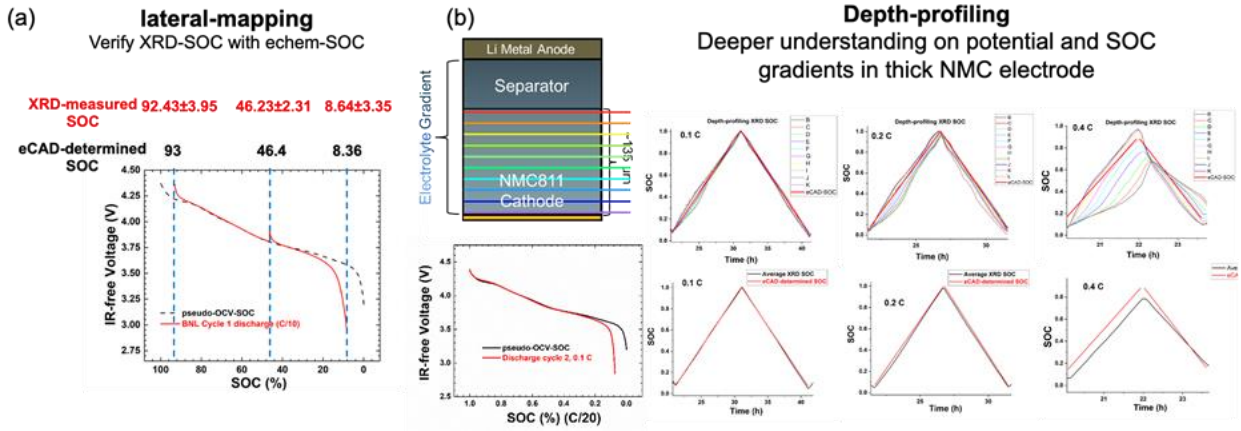

Figure 129. The Idaho National Laboratory completed electrochemical analytic diagnosis (eCAD) characterizations to understand the utilization and degradation of the cathode active material, as revealed in the electrode architecture and design. (a) Determination of the state-of-charge (SOC) of the NMC electrode based on the discharging profile and comparison of the SOC values derived from the lattice parameters using the Brookhaven National Laboratory synchrotron X-ray diffraction (XRD) data obtained during a surface lateral mapping experiment on the NMC electrode at three depths of SOC. (b) Similar analysis on charge-discharge cycles at different rates in the depth profiling along the thickness of the cathode. Discrepancies at higher rates were shown between the SOC values determined by XRD inference and eCAD method.

Analysis of Sulfurized Polyacrylonitrile

Y. S. Meng's group at UCSD used UCSD STEM EELS to probe the bonding environment evolution of nitrogen, sulfur, and carbon in sulfurized polyacrylonitrile (SPAN) cathode at the pristine, 1-cycle discharged and charged states. It was found that all three elements were actively participating in the electrochemical reaction. The 10-cycled SPAN sample was studied by STEM EDS to see whether long-term cycling would affect the structure as well as the elemental distribution in the SPAN particles.

Pristine SPAN. The pristine SPAN particles were studied here as the baseline reference. The elemental distributions of sulfur, carbon, and nitrogen were obtained by STEM EDS (Figure 130a-d). It was shown that the SPAN particles have a diameter ~ 500 nm, and all three elements are uniformly distributed in the whole particle. The 'U' shape C signal comes from the lacey carbon supportive film on the TEM grid. There is no evidence of sulfur clusters in all the SPAN particles, which further confirms that sulfur element is bonded to the SPAN polymer backbone and elemental sulfur particle does not exist in the sample.

10-Cycle Discharged SPAN. The pristine SPAN particles were studied to see if there would be any significant redistribution of elements after cycling. It is still under debate whether the sulfur element is detached from the SPAN polymer after cycling. By studying the elemental distribution in the SPAN particles by STEM EDS after 10 cycles, the team can gain some useful insights about how the elements, especially sulfur, are participating in the electrochemical reaction. The cycled sample lamella is prepared by cryo-FIB, which thinned the samples to ~ 100 nm to make sure that thickness was strictly controlled across different samples. Figure 130e shows the morphology of the 10-cycle discharged SPAN particles, which still have a diameter of ~ 500 nm. Overall, the structure of the SPAN did not change much compared to the pristine one. As shown in Figure 130f-h, there was not much redistribution of carbon and nitrogen elements in the sample, which could suggest that the SPAN polymer backbone is still intact after cycling. Although a small portion of the sulfur started to accumulate on the surface of the particle, most was still uniformly distributed in the whole particle. The result shows that while a small portion of sulfur would leave the SPAN particle after cycling, most would stay in the SPAN particle, which could be evidence of the ultra-stability of the SPAN cathode.

10-Cycle Charged SPAN. Similar results were observed in the 10-cycle charged SPAN as the discharged SPAN. Figure 130i shows the morphology of the 10-cycle charged SPAN particles, which also did not change much compared to the pristine and discharged ones. As shown in Figure 130f-h, all three elements were still

uniformly distributed in the SPAN particles. The results shown in Figure 130 suggest that the electrochemical reaction of SPAN will not create a large-scale elemental redistribution. Most importantly, the sulfur element did not segregate much and form clusters after cycling, which could be a key reason for the stability of the SPAN/Li electrochemical reaction.

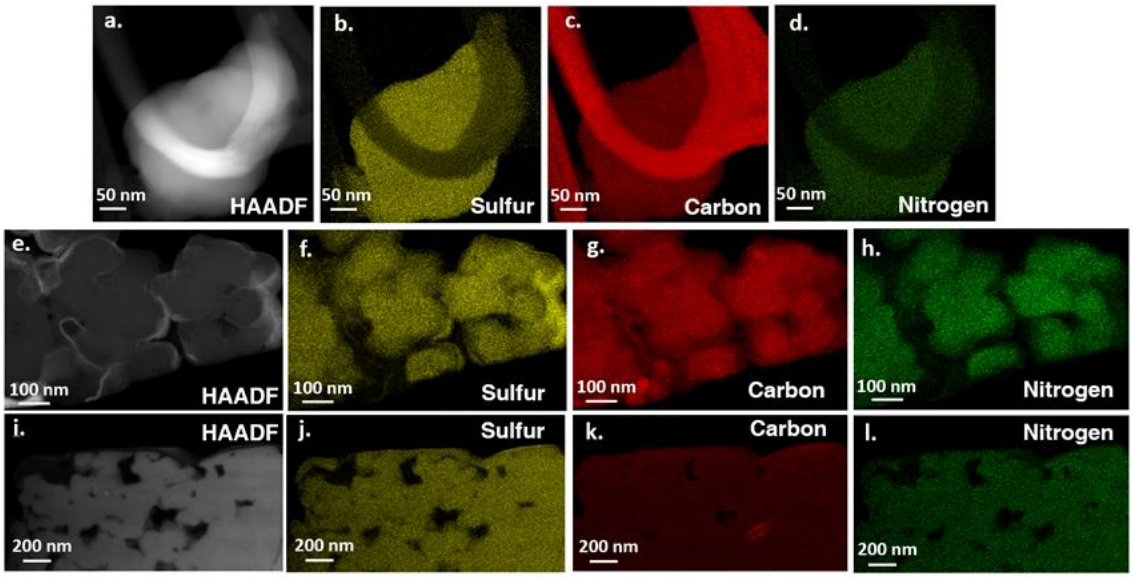

Figure 130. Scanning transmission electron microscopy (STEM) energy dispersive X-ray spectroscopy mapping of: (a-d) pristine sulfurized polyacrylonitrile (SPAN); (e-h) 10-cycle discharged SPAN; and (i-l) 10-cycle charged SPAN.

The PNNL team further evaluated the Li||SPAN cells with two electrolytes, LHCE (LiFSI-1.2DME-3TTE, by mol.) and baseline electrolyte [$LiPF_6$/carbonate (1 M $LiPF_6$ in EC-EMC (3:7 by vol.) + 2 wt.% VC)], about the high-temperature (60°C) cycling stability, room-temperature discharge rate capability, and low-temperature discharge performance. The SPAN electrode had an areal capacity loading of ~ 6 mAh cm^{-2}, and was obtained from the UCSD team. As shown in Figure 131a, the Li||SPAN cell with $LiPF_6$/carbonate exhibits an abrupt capacity drop after about 10 cycles. In contrast, the cell with LHCE maintains an available capacity of 6.4 mAh cm^{-2} after 100 cycles at C/5, corresponding to a high-capacity retention of 92.1%. From Figure 131b, the cell using LHCE exhibits superior discharge rate capability up to 3C and zero capacity loss when the discharge rate is set back to C/5 after the high-rate discharge. In contrast, the cell with $LiPF_6$/carbonate shows fast capacity decay after 5 cycles at C/5 and limited reversible capacity after 20 cycles at different discharge rates. Figure 131c-d presents the charge/discharge curves of Li||SPAN cells with $LiPF_6$/carbonate and LHCE, respectively, under various discharge temperatures (from 25 to -30°C). Obviously, the LHCE enables higher capacity retentions and average voltage outputs as well as better capacity recovery (Figure 131d) than the $LiPF_6$/carbonate (Figure 131c), where the reversible capacities at -20 and -30°C can be maintained at 4.86 and 4.68 mAh cm^{-2}, corresponding capacity retentions of 81.3% and 78.3%, respectively. When the temperature is back to 25°C, only 2% capacity is lost compared to the initial discharge capacity of 5.98 mAh cm^{-2} at 25°C. The much-improved high-temperature cycling stability, rate capacity, and low-temperature discharge performance in cells using LHCE suggest that the electrode/electrolyte interface layers are more conductive than those with $LiPF_6$/carbonate, thus benefiting superior Li^+ ion transfer kinetic.

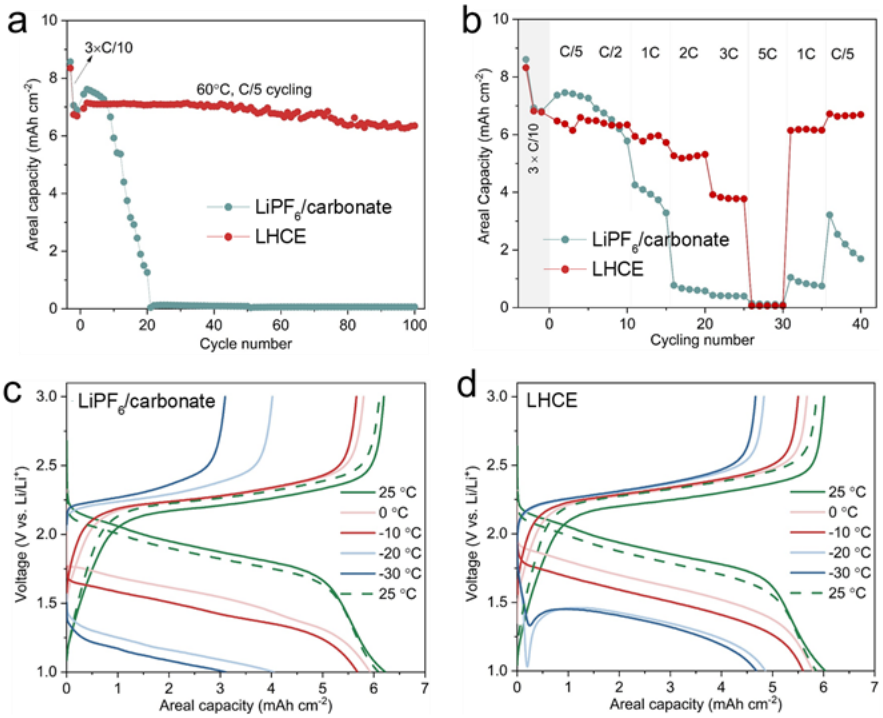

Figure 131. Electrochemical performances of Li || sulfurized polyacrylonitrile (SPAN) batteries with $LiPF_6$/carbonate and localized high concentration electrolyte (LHCE) between 1.0-3.0 V. (a) Cycling stability under 60°C. (b) Cell discharge rate capability tests at 60°C after 3 formation cycles at 25°C, with a constant charge rate of C/5 and different discharge rates from C/5 to 5C. (c-d) Low-temperature discharge tests at C/5 with (c) $LiPF_6$/carbonate and (d) LHCE, where the operating temperature for all charging processes was 25°C and discharging was conducted at 25, 0, -10, -20, and -30°C, respectively, and then back to 25°C. In all cell tests in (a-d), 1C = 6.0 mA cm^{-2}.

Evaluation of Carbon Hosts for High Energy Rechargeable Lithium Metal Batteries

The UW group demonstrated the key factors determining the performance of carbon hosts. They chose three typical carbon materials, commercial hard carbon (pore size < 1 nm, surface area < 100 $m^2\ g^{-1}$), mesoporous carbon (pore size 1~10 nm, surface area 100~500 $m^2\ g^{-1}$), and functionalized mesoporous carbon (pore size, 1~10 nm, surface area > 500 $m^2\ g^{-1}$), as well as a carbon host loaded with silver nanoparticles. The chosen materials covered a wide variety of pore size, from micro- to meso-porosity, surface area, surface functionality, and potential catalytic-effect of the metal particles.

The CE and cyclability of lithium plating and stripping were evaluated for different carbon-based materials in different electrolytes. The same amount of lithium metal is plated on the carbon electrode and then stripped with a cutoff voltage of 1 V versus Li/Li^+. Figure 132a shows a plot of CE versus cycle number for lithium plating and stripping on the carbon-based materials in 1.0 M $LiFP_6$ in EC/EMC (3:7 by wt) + 2.0 wt% VC. The deposition capacity is 1 mAh cm^{-2} at a current density of 1 mA cm^{-2} with a volume of 60 mL for each coin cell. The ICEs of 81.7%, 83.9%, 71.7%, 74.6% are obtained for hard carbon, hard-carbon/Ag, mesoporous carbon, and surface-oxidized mesoporous carbon, respectively. These ICEs cannot be readily compared because different types of carbon are expected to have different properties. However, after 40 cycles, the CEs of all carbons decline to almost zero. Figure 132b shows the electrochemical performance of lithium plating/stripping on four kinds of carbon materials in the ether-based electrolytes of 1.0 M LiTFSI in DOL:DME (1:1 by vol.) with 5 wt% $LiNO_3$ additives. All of these carbon anodes display similar trends that the CE is significantly increased and maintains at 97% before the 80th or 100th cycles, and degrades rapidly after the 100th cycles. In contrast, these four kinds of carbon anodes show an excellent electrochemical performance when they are tested

in LHCE that consists of 1.49 M LiFSI in DME:TTE (molar ratio of 1.2:3), shown in Figure 132c. The average CE of all four carbons increases to 99.0% and remains very stable over 200 cycles in this LHCE. These results are a little surprising, but they have very important implications. Although the types of carbon, surface properties, and compositions should be relevant, the nature of electrolytes plays the most critical role by far. The different carbon materials tested all behave poorly in the conventional $LiPF_6$/carbonate electrolyte. The conventional ether-based electrolyte was better, but not adequate. More stable electrolytes, such as LHCEs, must be developed. Therefore, developing advanced electrolytes is critical to extending the cyclability of the Li-metal anode and should be studied further.

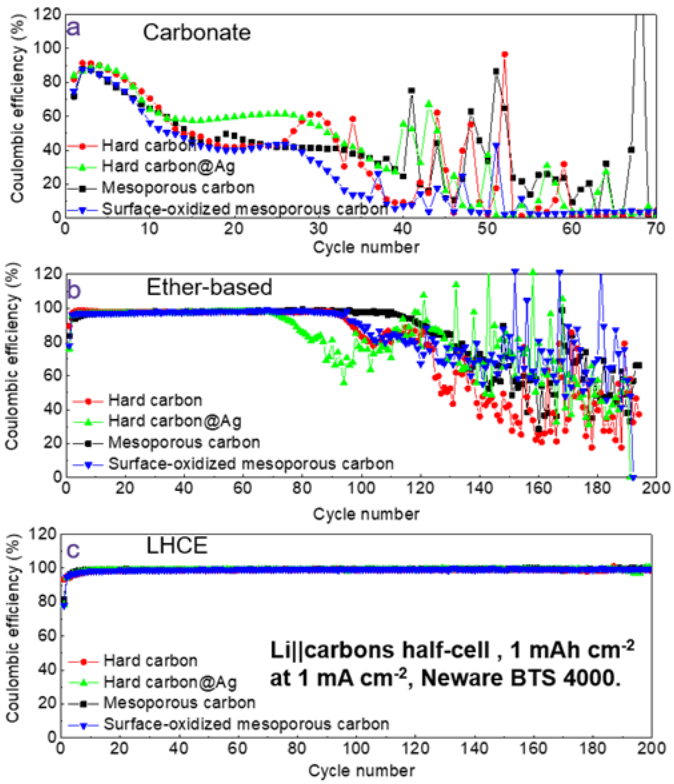

Figure 132. Coulombic efficiency versus cycle number of lithium plating/stripping on hard carbon, hard-carbon/Ag, mesoporous carbon, and surface-oxidized mesoporous carbon in (a) carbonate-based electrolyte, (b) ether-based electrolyte, and (c) localized high concentration electrolyte.

Highlights of Keystone Project 2

The highlights for this quarter are as follows:

- The eCAD and *operando* synchrotron XRD techniques are coupled to probe lithium concentration profiling in the cathode (INL, BNL).
- The elemental distribution of SPAN electrode after long cycling was studied by STEM-EDS (UCSD).
- SPAN electrode cycled in DME-LHCE was evaluated at various cycling rates and temperatures (PNNL).
- The performance of carbon hosts was strongly influenced by electrolytes (UW).

Keystone Project 3: Cell Fabrication, Testing, and Diagnosis

This quarter, the modeling team at UT Austin modified the reaction scheme for the 1D lithium sulfur discharge model.[1] Electrolyte engineering is important to control speciation and minimize degradation through inhibiting the polysulfide shuttle mechanism. Studies have found that the speciation changes depending on the system of additives and solvent. Many Raman and UV-Vis spectroscopy studies have noted the presence of a radical species $S_3^{\bullet-}$ in lithium sulfur systems. (1)

With this work, the aim was to more accurately align model reaction schemes to the speciation suggested by spectroscopic studies. To that end, the $S_3^{\bullet-}$ radical species was incorporated in the model as an assumed to be electrochemically inactive species that serves as a sink for the S_6^{2-} species.

The new homogeneous reaction is assumed to be reversible and elementary; the forward and backward reaction rates are $R_f = k_f \left[S_6^{2-} \right]$ and $R_b = k_b [S_3^{\bullet-}]^2$. An equilibrium reaction, when the forward and backward rates are equal, is then defined as:

$$K_{S3} = \frac{k_f}{k_b} = \frac{[S_3^{\bullet-}]^2}{[S_6^{2-}]} \quad (1)$$

In addition to modifying the reaction scheme, the geometric parameters of the model have been updated to reflect high-energy density lithium sulfur pouch cells taken from the work by Lu, et al.[2] The cathode and separator thicknesses and sulfur content have been calculated according to the values from a 300 Wh/kg cell. The new parameters along with other values taken from the group's recently published Tanks-in-Series model[3] reflect experimentally relevant trends like higher voltages and rate-dependent capacity.

Results of Reaction Scheme Modification

The equilibrium constant sets the ratio of $S_3^{\bullet-}$ to S_6^{2-}, and the k_f controls how quickly the reaction comes to equilibrium. By looking at a range of these parameters, it is possible to begin to connect the solvent effects on speciation to the battery performance. Figure 133 below shows the effect of K_{S3} with fast dissociation kinetics (a) and slow dissociation kinetics (b).

With fast dissociation kinetics, the homogeneous reaction reaches equilibrium instantaneously. The equilibrium constant K_{S3} is varied from 100 to 10^5 mol/m^3. With a low equilibrium constant, the curve is the same as without the dissociation chemistry since there is negligible radical $S_3^{\bullet-}$ species. As the equilibrium constant increases, more of the S_6^{2-} species is converted to $S_3^{\bullet-}$ radical species, which does not participate in the reduction scheme. The higher values of K_{S3} can be equated to electrolyte systems that favor stabilization of the radical $S_3^{\bullet-}$ species, while the lower values of K_{S3} are due to the solvent favorably stabilizing the S_6^{2-} species. The overall voltage is affected by the stabilization of the $S_3^{\bullet-}$ radical species by an increase in the first plateau voltage and then a depression of voltage up to 200 mV through the end of discharge.

For Figure 133b with the slow dissociation kinetics, the k_f value is 0.001 s^{-1}, which means the reaction occurs over thousands of seconds and on the order of the discharge curve. The beginning of the voltage curve is unchanged through the first plateau under these conditions. During the transition between the plateaus, the curves start to deviate. With slow kinetics, the $S_3^{\bullet-}$ radical species does not accumulate significantly until much later than Figure 133a. With the highest value of K_{S3}, the cell experiences significant capacity loss, about 25%, due to trapped sulfur in the $S_3^{\bullet-}$ radical species. Depending on the reaction timescales and the solvent

interactions with the speciation, highly stabilizing electrolytes may lead to reversible capacity loss following this mechanism of trapped polysulfide species. The inclusion of this simple homogeneous dissociation reaction of a radical species that does not participate in the reduction scheme dramatically affects battery performance. This work represents an important step forward in understanding and modeling the complex speciation within Li-sulfur batteries and incorporating important experimental insights into full-cell models.

The PNNL pouch cell team prepared and evaluated multiple high-energy cells using either a bare copper current collector or thin lithium anode and an NMC-622 cathode. Three of the cells were comprised of a Li-metal anode (denoted as Cell 1-3) and one with Li-free copper anode (denoted as Li-free cell). The charge-discharge cycling data and charge retention curves were analyzed by the INL team using detailed eCAD analysis. The eCAD analyses and the results are reported in Figure 134 as a summary report of the NMC-622 cathode active material's utilization and the impact on charge retention and cycle life. Figure 134a shows the NMC-622 utilization efficiency $e_{C/n}$ at C/3 cycling as a function of cycle number. The utilization efficiency $\varepsilon_{C/n}$ was calculated according to

$$\varepsilon_{C/n} = QR_{C/n} / QR_T \quad (2)$$

where QR is the "capacity ratio" expressed as mAh g^{-1} $\%SOC^{-1}$. $QR_{C/n}$ is the capacity ratio measured at C/n rate, and QR_T is the theoretical capacity for the NMC composition. A reliable way to obtain the $QR_{C/n}$ is shown in Figure 135. The capacity ratio QR can be calculated by a general equation as

$$QR = \Delta Q / \Delta SOC \quad (3)$$

In Figure 135, several discharge curves as a function of cycle number were transformed into IR-free voltage versus SOC profiles using the eCAD method, and they are aligned with a universal pseudo-OCV versus SOC curve that represents the proper OCV versus lithium content in NMC-622. The region highlighted by the blue dashed circle shows that the IR-free voltage versus SOC profiles from the C/3 polarization aligned very well with the universal pseudo-OCV versus SOC curve, implying the SOC and lithium content in NMC correlated very well. In this region, the group can arbitrarily select two points A and B to illustrate how QR and $\varepsilon_{C/n}$ can be derived. For $QR_{C/n}$, they can determine the capacity difference $\Delta Q_{C/n}$ between A and B from the

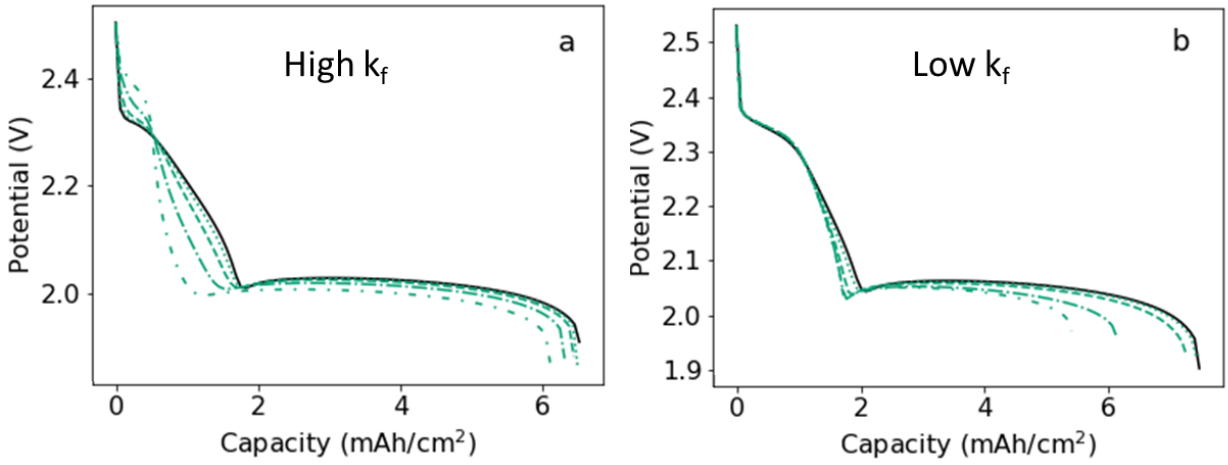

Figure 133. (a) 1C discharge curves for fast dissociation kinetics k_f = 1000 s^{-1} and increasing equilibrium coefficients K_{S3} = 10^2 mol/m^3 (• • •), 10^3 mol/m^3 (– – –), 10^4 mol/m^3 (— • — • —), and 10^5 mol/m^3 (- • - • -) are compared to the base case without any dissociation chemistry (k_f = 0, ——). (b) 0.5C discharge curves for slow dissociation kinetics (k_f = 0.001 s^{-1}) and increasing equilibrium coefficients K_{S3} = 10^2 mol/m^3 (• • •), 10^3 mol/m^3 (– – –), 10^4 mol/m^3 (— • — • —), and 10^5 mol/m^3 (- • - • -) are compared to the base case without any dissociation chemistry (k_f = 0, ——).

capacity measurements in the discharge curve, while the eCAD analysis will give the ΔSOC. Thus, $QR_{C/n}$ can be derived from Equation 3. Likewise, they can calculate the ΔQ_T between A and B from the lithium content and Faraday's law and use the same ΔSOC to calculate the QR_T. The utilization efficiency $\varepsilon_{C/n}$ can readily be obtained by Equation 2, as exhibited in Figure 134a. The results shown in Figure 134a are quite informative. Despite the cell design differences, the NMC $\varepsilon_{C/n}$ values among the four are rather consistent, sharing the same trend. The NMC utilization can hold up well in the first 200 cycles. The variations in kinetics, including mass transport in different porous electrode structures, do not affect NMC utilization during this period, indicating that NMC utilization is mostly governed by the NMC's bulk property itself. After 200 cycles, the utilization began to decrease by 6-8 % across the four designs, again consistently. The group shall infer that this is likely due to the change in the charge retention ability internally by NMC lattice structure. The capacity variations among them that are exceeding the internal effect by NMC identified above must then come from the transport properties in the porous media and the kinetic polarization hindrance at the interface.

Figure 135b compares the measured capacity $Q_{C/3}$ versus the one determined from the capacity ratio obtained from the highlighted region in Figure 135, as $QR_{C/3}$ ´ 100%SOC. The ratio of $Q_{C/3}$ / ($QR_{C/3}$ ´ 100%SOC) will represent the utilization loss due to kinetic origins outside the NMC bulk or those that come from the transport properties in the porous media and the kinetic polarization hindrance at the interface. Such an identification and separation of the kinetic effects by careful quantification of the NMC utilization in the polarization shall provide valuable information for cell design improvements and for gap analysis of kinetic issues to improve performance.

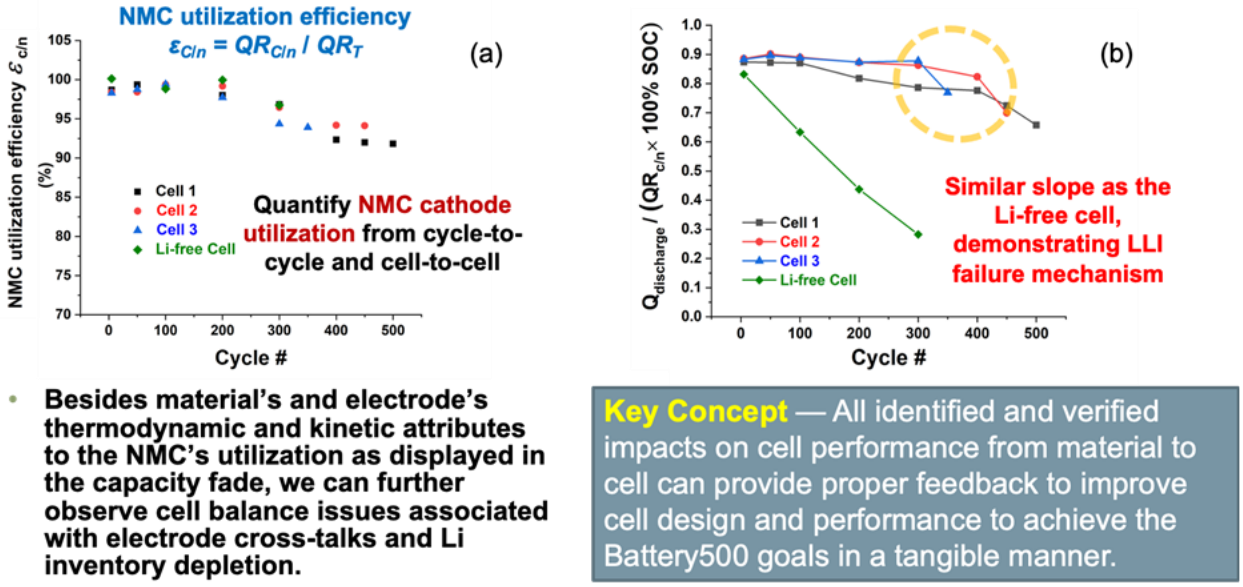

Figure 134. Electrochemical analytic diagnosis (eCAD) characterizations to analyze cell performance based on utilization and cell degradation of the cathode active material due to lithium inventory loss at the lithium anode. (a) NMC-622 cathode utilization variations as a function of cycle number among four different cells of design. (b) Capacity retention presented as a function of the ratio of capacity Q versus capacity ratio QR under the same test protocol at C/3.

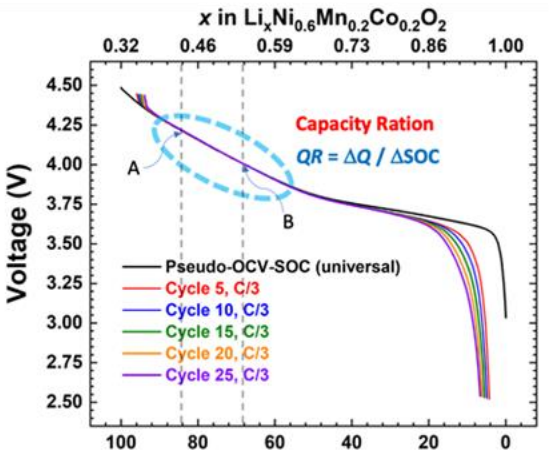

Figure 135. IR-free voltage versus state-of-charge profiles derived using the electrochemical analytic diagnosis (eCAD) method to show the open circuit voltage versus lithium content in the NMC.

The Battery500 also continues to develop, evaluate, and characterize high energy, long cycle life cells as well. Several different designs for both sulfur and NMC cathodes are being evaluated.

References

[1] Kumaresan, K., Y. Mikhaylik, and R. E. White. *Journal of the Electrochemical Society* 155 (2008): A576.

[2] Lu, D., et al. *ACS Applied Materials & Interfaces* 10 (2018): 23094–23102.

[3] Parke, C. D., A. Subramaniam, S. Kolluri, D. T. Schwartz, and V. R. Subramanian. *Journal of the Electrochemical Society* 167 (2020): 163503.

Highlights of Keystone Project 3

The highlights for this quarter are as follows:

- Development of a model to understand the impact of non-participating radical species dissociation reaction that impacts Li-S battery performance (modeling team, UT Austin).
- Electrochemical analysis providing insight into electrode utilization regardless of kinetic impacts associated with different cell designs (INL).

Patents/Publications/Presentations

Patent

- Provisional patent on niobium oxide treatment of NMC materials has been filed by Binghamton.

Publications

- Xin, F., and M. S. Whittingham.* "Challenges and Development of Tin Based Anode with High Volumetric Capacity for Li-ion Batteries." *Electrochemical Energy Reviews* 3 (2020): 643–655. doi: 10.1007/s41918-020-00082-3. Publication Date (Web): October 1, 2020.
- Huang, Z., S. Choudhury,* H. Gong, Y. Cui,* and Z. Bao.* "A Cation-Tethered Flowable Polymeric Interface for Enabling Stable Deposition of Metallic Lithium." *Journal of the American Chemical Society* 142, no. 51 (2020): 21393–21403. doi: 10.1021/jacs.0c09649. Publication Date (Web): December 14, 2020.
- Gao, N., A. W. Abboud, G. S. Mattei, Z. Li, A. A. Corrao, C. Fang, B. Liaw, Y. S. Meng, P. G. Khalifah, E. J. Dufek, and B. Li.* "Fast Diagnosis of Failure Mechanisms and Lifetime Prediction of Li Metal Batteries." *Small Methods* (2020): 2000807. doi:10.1002/smtd.202000807. Publication Date (Web): November 3, 2020.
- Zhang, J-G.,* W. Xu, J. Xiao, X. Cao, and J. Liu. "Lithium Metal Anodes with Nonaqueous Electrolytes." *Chemical Reviews* 120, no. 24 (2020): 13312–13348. doi:10.1021/acs.chemrev.0c00275. Publication Date (Web): November 11, 2020.
- Ren, X., X. Zhang, Z. Shadike, L. Zou, H. Jia, X. Cao, M. H. Engelhard, B. E. Matthews, C. Wang, B. W. Arey, X-Q. Yang, J. Liu, J-G. Zhang,* and W. Xu.* "Designing Advanced *In-Situ* Electrode/Electrolyte Interphases for Wide Temperature Operation of 4.5-V Li||$LiCoO_2$ Batteries." *Advanced Materials*, 32, no. 49 (2020): 2004898. doi: 10.1002/adma.202004898. Publication Date (Web): November 4, 2020.
- Ren, X., P. Gao, L. Zou, S. Jiao, X. Cao, X. Zhang, H. Jia, M. H. Engelhard, B. E. Matthews, H. Wu, H. Lee, C. Niu, C. Wang, B. W. Arey, J. Xiao, J. Liu, J-G. Zhang,* and W. Xu.* "The Role of Inner Solvation Sheath within Salt-Solvent Complexes in Tailoring Electrode/Electrolyte Interphases for High-Voltage Lithium Metal Batteries." *Proceedings of the National Academy of Sciences of the United States of America (PNAS)* 117, no. 46 (2020): 28603–28613. doi:10.1073/pnas.2010852117; Publication Date (Web): November 17, 2020.
- Parke, C. D., A. Subramaniam, S. Kolluri, D. T. Schwarz, and V. R. Subramanian.* "An Efficient Electrochemical Tanks-in-Series Model for Lithium Sulfur Batteries." *Journal of The Electrochemical Society* 167 (2020): 163503. Publication Date (Web): December 3, 2020.
- Uppaluri, M., A. Subramaniam, L. Mishra, V. Viswanathan, and V. R. Subramanian.* "Can a Transport Model Predict Inverse Signatures in Lithium Metal Batteries Without Modifying Kinetics?" *Journal of The Electrochemical Society* 167 (2020): 160547. Publication Date (Web): December 29, 2020.
- Li, Z., L. Yin, G. S. Mattei, M. R. Cosby, B-S. Lee, Z. Wu, S-M. Bak, K. W. Chapman, X-Q. Yang, P. Liu, and P. G. Khalifah.* "Synchrotron *Operando* Depth Profiling Studies of State-of-Charge Gradients in Thick $Li(Ni_{0.8}Mn_{0.1}Co_{0.1})O_2$ Cathode Films." *Chemistry of Materials* 32 (2020): 6358–6364. doi: 10.1021/acs.chemmater.0c00983. Publication Date (Web): July 5, 2020.
- Oyakhire, S. T., W. Huang, H. Wang, D. T. Boyle, J. R. Schneider, C. de Paula, Y. Wu, Y. Cui,* and S. F. Bent.* "Revealing and Elucidating ALD‐Derived Control of Lithium Plating Microstructure." *Advanced Energy Materials* 10, no. 44 (2020): 2002736. doi: 10.1002/aenm.202002736. Publication Date (Web): October 11, 2020.

Presentations (Invited)

- ECS PRiME 2020, Virtual (October 4–9, 2020): "Status of Battery500 Consortium"; J. Liu.
- Science and Technology in Society (STS) 17th Annual Meeting, Kyoto, Japan (October 6, 2020): "We Owe Future Generations a Cleaner and Sustainable World"; M. S. Whittingham.
- Indian Institute of Technology (IIT) Banaras Hindu University (BHU) with IIT Madras and IIT Roper (October 6, 2020): "Battery Energy Storage Past, Present and Future Directions"; M. S. Whittingham.
- Tobin Marks Lecture in Discovery Chemistry, UMD (October 13, 2020): "The Origins of the Lithium Battery and Future Challenges/Opportunities"; M. S. Whittingham.
- World Laureates Forum on Science and Technology for the Common Destiny of Mankind, Shanghai, China (October 29, 2020): "Li-Ion Battery Storage with Renewable Energy: A Solution to Cleaning the Environment and Mitigating Global Warming"; M. S. Whittingham.
- MSE Seminar, Imperial College, London, England (November 4, 2020): "The Origins of the Lithium Battery and Future Challenges/Opportunities"; M. S. Whittingham.
- National Institute of Standards and Technology (NIST) (November 4, 2020): "The Origins of the Lithium Battery and Future Challenges/Opportunities"; M. S. Whittingham.
- International Battery Association (IBA), Bled, Slovenia (November 17, 2020): "Pushing the Limits of Intercalation Reactions: Two Li vs Higher Ni NMC"; M. S. Whittingham.
- Bay Area Battery Summit 2020, Virtual (November 18, 2020): "Li-Ion Batteries: The Journey from an Idea to Commercialization to Domination"; M. S. Whittingham.
- Microsoft, Richmond, Washington, Virtual (November 24, 2020): "Past, Present and Future Directions of Battery Energy Storage"; M. S. Whittingham.
- European Battery Association, Berlin, Germany (November 25, 2020): "How I Created a Rechargeable World"; M. S. Whittingham.
- International Green Energy Summit, Virtual (December 4, 2020): "Energy Storage: Key for a Greener Economy"; M. S. Whittingham.
- ACS: Advancing Energy Conversion, Capture, and Storage, Virtual (December 4, 2020): "Energy Storage: Present Status, Future Challenges and Key Role in a Greener Economy"; M. S. Whittingham.
- Storage X International Virtual Symposium, Stanford University (November 13, 2020): "Molecular Design for Electrolyte Solvents and Artificial SEI for Stable Lithium-Metal Anodes"; Z. Bao.
- ECS PRiME 2020, Pacific Rim Meeting on Electrochemical and Solid State Science, Virtual (October 4–9, 2020): "Intercalation Chemistry of Oxides"; A. Manthiram.
- Thermo Fisher – UT Austin Battery Seminar, Austin, Texas (October 14, 2020): "Next Generation Battery Technologies"; A. Manthiram.
- CBMM Webinar Series – Towards Extreme Fast Charging and High Energy Batteries, Austin, Texas (October 20–22, 2020): "High-Energy Cobalt-free Lithium-ion Batteries"; A. Manthiram.
- MRS Spring/Fall 2020 Meeting, Virtual (November 28 – December 4, 2020): "Pairing Lithium-Metal Anode with High-Nickel NMC and Sulfur Cathodes: Fundamental Understanding and Engineering Solutions"; A. Manthiram.
- Northeastern University, Boston, Massachusetts (December 9, 2020): "Near-Term and Long-Term Perspective of Electrical Energy Storage"; A. Manthiram.
- IBA 2020, Virtual (November 17–18, 2020): "Quantitative Cell Qualification to Enable Long Life Rechargeable Li Metal Batteries"; B. Liaw, et al.

- ECS PRiME 2020, A-01-0034, Symposium of Intercalation Chemistry for Electrochemical Energy Storage Technologies: In Honor of M. Stanley Whittingham, Virtual (October 4–9, 2020): "How Well Cathode Materials are being Used in Rechargeable Li Batteries?"; Y. Zhang, B. Liaw,* E. J. Dufek, and B. Li.
- Battery Safety Council Forum 9, Virtual (November 17–18, 2020): "INL's Battery Diagnostic and Prognostic Approach for Failure Mode and Effect Analysis (FMEA)—Identify Cell Quality through Better Qualification"; B. Liaw.
- BESSY III Expert Workshop, Energy Storage and Batteries, Virtual (November 4, 2020): "Ion Transport in Electrolytes"; M. F. Toney.
- PETRA IV Workshop, Materials and Processes for Energy and Transport Technology, Virtual (October 21, 2020): "Challenges and Opportunities in Electrochemical Energy Storage Technologies"; M. F. Toney.
- ECS PRiME 2020, Virtual (October 4–9, 2020): "Direct Observation of the Sulfur-Based Chemical Species in Li-S Batteries by Spatially-Resolved X-Ray Fluorescence Microscopy and X-Ray Absorption Spectroscopy"; S-M. Bak, Z. Shadike, L. Shi, H. Liu, P. Liu, P. Northrup, Y. Du, Y. S. Chu, D. Lu, J. Xiao, and X-Q. Yang. Invited.
- ECS PRiME 2020, Virtual (October 4–9, 2020): "Multi-Dimensional Multi-Scale Diagnostic Study on Layered Cathode Materials"; R. Lin, S-M. Bak, Y. Shin, Z. Shadike, Q. Wang, S. Tan, E. Hu, and X-Q. Yang.*
- ECS PRiME 2020, Virtual (October 4–9, 2020): "Probing the *In-Situ* Surface Chemistry of $LiNi_{0.94}Co_{0.06}O_2$ and $LiNi_{0.92}Co_{0.06}Al_{0.02}O_2$ Cathode Materials using Synchrotron-Based Ambient-Pressure XPS"; Z. Shadike, S-M. Bak, E. Hu, S. Tan, Q-C. Wang, R. Lin, and X-Q. Yang.*
- AIChE Battery and Energy Storage Conference, Virtual (October 2020): "Clockwork Inside Cathodes – Unparalleled Insights into Defects and Inhomogeneities"; P. Khalifah.
- ECS PRiME 2020, Virtual (October 8, 2020): "Designing New Electrolytes for High-Energy Lithium Metal Batteries"; W. Xu,* X. Ren, X. Cao, P. Gao, and J-G. Zhang.
- Materials Today Award Presentation (December 14, 2020): "Integrating Materials Science, Electrochemistry and Engineering in Energy Storage Technologies"; J. Xiao.
- ECS Webinar (November 11, 2020): "Electrochemistry in Rechargeable Lithium Metal Batteries"; J. Xiao.
- ECS PRiME 2020, Virtual (October 4, 2020): "Integrating Materials Science, Electrochemistry and Engineering in Energy Storage Technologies"; J. Xiao.
- 20th Annual AABC, Virtual (November 3, 2020): "Battery 500 Consortium: Understanding and Addressing the Fundamental Challenges in Rechargeable Lithium Metal Batteries"; J. Xiao.
- ECS PRiME 2020, Virtual (October 6, 2020): "Enhanced Electrode/Electrolyte Interphases in Fluorinated Orthoformate Electrolytes for Stable High-Voltage Lithium Metal Batteries"; X. Cao,* W. Xu, and J-G. Zhang.
- MRS Spring/Fall 2020 Meeting, Virtual (October 27, 2020): "Advanced Diagnostic Tools for Characterizing Lithium Metal and Solid-State Batteries"; Y. S. Meng. Invited.
- 8th International Renewable Sustainable Energy Conference (November 25–28, 2020): "Advanced Diagnostic Tools for Characterizing Lithium Metal and Solid-State Batteries"; Y. S. Meng. Invited.
- ECS PRiME 2020, Virtual (October 4–9, 2020): "High Coulombic Efficiency Electrolyte Enables Li||Span Batteries with Superior Cycling Performance"; P. Liu. Invited.